Translational evaluation of electrospun drug delivery systems: fabrication, pharmacokinetics, and tissue-specific host responses

Jamie L. Hernandez

A dissertation

submitted in partial fulfillment of the

requirements for the degree of

Doctor of Philosophy

University of Washington

2021

Reading Committee:

Kim Woodrow, Chair

Buddy Ratner

Ying Zheng

Program Authorized to Offer Degree:

Bioengineering

University of Washington

Abstract

Translational evaluation of electrospun drug delivery systems: fabrication, pharmacokinetics, and tissue-specific host responses

Jamie L. Hernandez

Chair of the Supervisory Committee:
Kim A. Woodrow

Department of Bioengineering

Pre-exposure prophylaxis (PrEP) is an oral regimen of antiretroviral (ARV) drugs for the prevention of HIV. However, near-perfect adherence to PrEP is needed to maintain protective drug concentrations in the lower female reproductive tract (FRT). To address issues of adherence to medications like PrEP, we investigate the use of drug-loaded electrospun materials as a long-acting drug delivery vehicle. Electrospinning has previously demonstrated the ability to formulate physiochemically diverse ARV drugs into stable solid dispersions. Here, we investigate various formulations of drug-loaded electrospun materials and further demonstrate the scalable potential of electrospinning. Electrospinning is used to formulate long-acting triple-drug releasing material as an adherence-independent subcutaneous implant, and we assess the pharmacokinetics and biocompatibility of these implants in mice. Finally, towards the development of adherence-independent and topical electrospun devices, we probe local tissue hosts responses in the FRT in baboons. Research from this thesis provides new insight into drug release kinetics and material biocompatibility resulting from drug delivery systems specifically within subcutaneous and FRT tissue environments.

TABLE OF CONTENTS

LIST OF FIGURES

LIST OF TABLES

ACKNOWLDEGEMENTS

I would like to thank my advisor and mentor Kim Woodrow for all her guidance and time spent training me. Throughout my time in your lab, I have been inspired by all the support you provide your students, and the human-centered focus you bring back to bioengineering. I have grown so much as a scientist and a woman because of my time here. Thank you for seeing my potential.

I would also like to acknowledge all the members of my committee: Buddy Ratner, Ying Zheng, Kelly Stevens, and Paul Drain. Thank you for taking the time to provide me with your valuable input. Your comments have provided me with greater insight into drug delivery, device translation, and HIV prevention in the clinic. I always appreciated getting the chance to see the unique perspectives you all had as scientists. Further, I would like to specifically thank my reading committee for taking your time to review this thesis; I hope you can find some joy in reading it.

As an unofficial member of my committee and a collaborator, I would also like to thank Jeffrey Jensen. I am so glad I had the opportunity to collaborate with OPERM on such interesting projects right as I started graduate school. The research experiences I had at OHSU for this work are definitely the most memorable of my entire PhD.

This work was supported by grants to Kim from NIH/NIAID (R01-AI-145483), grants to Kim and Jeff from the Gates Foundation (OPP1006248) and NIH/NIAID (R01-AI-150325), and the HHMI Gilliam Fellowship for Advanced Study to me and Kim. I was further supported by the ARCS Foundation.

I would also like to thank all my fellow lab mates in the Woodrow Lab for all their technical guidance and advice throughout graduate school; I have learned so much from all of you. Jaehyung Park, thank you for your mentorship and all that you have taught me about animal work and

immunology. Ian Suydam, thank you for all your scientific expertise and enthusiasm, it was continuously motivating. Thank you to Shijie Cao, Hannah Frizzell, and Rachel Creighton who all supported me in my onboarding as a new researcher in the lab and all inspired me as fellow students. Finally, thank you to Peter Chien, My-Anh Doan, Hannah VanBenschoten, and Hienschi Nguyen – it was wonderful to have the opportunity to work so collaboratively with all of you.

I would also like to thank all my friends who also lifted me up throughout this process. Thank you to my fellow Bioengineering Graduate Representative Meilyn Sylvestre – I have always admired your abilities to bring people together and build communities. Memories of our lunches together are the first thing I think of when I reflect on my grad school experience. Thank you to Sara Keller and your inspiring sense of adventure – I'm so glad I got the chance to explore Seattle and some of the Washington state wilderness with you. Thank you to Alexander Prossnitz for your endless positivity, infectious excitement for science, and climbing gym pep talks. Finally, thank you to Elliot Claveau for being a force of good in the world – you brought so much joy to our house, even in quarantine.

Thank you to my family who have continuously supported me to pursue my education. To Mom and Dad – I am here today as a product of your hard work ethic. I feel so empowered knowing that I am making you proud. To my sister Kellie Hernandez, who always inspired me to be a good student and who was a role model for me and my interests in math and science. Thank you for all your visits to Seattle, they were highlights of my time here.

To Christopher Everson – I wouldn't be the same person or scientist without your love and support. Thank you for listening, always inspiring me to be a thoughtful researcher, being my champion, helping me learn how to make plots with Python, and being the best partner that I could ever ask for – you are my light.

Chapter 1. SUMMARY AND SPECIFIC AIMS

Oral pre-exposure prophylaxis (PrEP) has been a powerful tool for reducing the impact of HIV, where uninfected individuals follow a daily pill regiment of antiretroviral (ARV) drugs as prevention.[1,2] However, due to low partitioning of drug in the female reproductive tract (FRT), near perfect adherence to PrEP is required to achieve protective dosages at this potential entry point of infection.[1,3–7] Therefore, issues of disproportionate protection by oral PrEP are not a problem of ARV efficacy. Rather, issues of adherence and drug partitioning are a matter of drug delivery and could be addressed with the development of novel drug delivery systems (DDS).

Long-acting injectables (LAIs) of PrEP have been developed to reduce the need for daily adherence by the patient, but these treatments are not readily reversible and can still have sub-optimal dosing.[8–10] Solid nanocrystalline forms of ARVs compose these LAIs and show promise for controlling drug release rates, but there are currently few ARV candidates capable of stable nano-formulation.[11] Subcutaneous implants have shown promise for long-acting, adherence independent drug dosing, and further have the benefit of being removable in case of adverse reaction.[12] The subcutis is an ideal location for long-acting DDS as this tissue space is rich with capillaries and lymph vessels to enable drug uptake, and device placement is relatively non-invasive.[11,13,14] For these reasons, subcutaneous implants have already clinically available for uses such as contraception.[13,15,16] Topical DDS also show promise to circumvent drug partitioning issues, as topical ARV delivery can achieve a drug concentration 1000-times higher in the relevant tissue.[17] Topical PrEP systems have been investigated, including vaginal gels and rings, but these methods have shown to have low adherence by patients.[18,19]

In pursuit of developing novel DDS which can practically address these issues observed with PrEP, the capability of scalable production must be considered. Further, novel subcutaneous

implants fabricated from such scalable methods should be investigated for long-acting potential. Towards the development of long-acting and topical systems in the FRT, we also propose the need to assess the biocompatibility of intrauterine fibrous materials. For these reasons, electrospinning was used to (1) develop scalable and uniform solid dosage forms, (2) develop long-acting subcutaneous implants, and (3) probe the comparable foreign body reaction between the subcutis and the FRT.

Electrospinning is hypothesized to be the ideal material fabrication method for its ability to encapsulate physiochemically diverse, highly insoluble agents, and ability to fabricate nanofibrous materials composed of polymers with various drug release properties. **The goal of this proposed thesis work is to develop electrospun ARV drug delivery materials capable of scalable fabrication, long-acting pharmacokinetics, and biocompatibility.** Research for this thesis investigates the following:

1.1 AIM 1: TO INVESTIGATE FORMULATION AND SCALABLE ELECTROSPINNING METHODS FOR UNIFORM AND CONTROLLED ARV DOSING

Electrospinning was employed to develop materials with varied drug release kinetics. Scalability was considered a major determining factor for material translatability. Specifically, we define scalable materials to be capable of high basis weight deposition, mass uniformity, and drug dose consistency between samples in a single material. For long-acting release and materials designed to probe fibrotic responses, we use low-throughput needle electrospinning to screen various polymers and drugs. Within this aim we also characterize the resulting material features and *in vitro* agent release rates. The investigation of fiber formulations will be investigated through the following subaims:

Subaim 1.1: Optimize free-surface electrospinning methods to generate materials with scalable, controlled regions of mass consistency

Prior work has developed rapidly dissolving fibers containing three physicochemically diverse ARV agents including etravirine (ETR), maraviroc (MRV), and raltegravir (RAL), or collectively referred to as the 3ARV combination. For this formulation, studies have optimized the free-surface electrospinning parameters for material throughput. Continued work focused on methods to study the mass deposition of different polymer solutions using dynamic substrate movement during the free-surface electrospinning process. Simple simulations and experimental data are used to predict and validate the parameters needed to achieve defined regions of consistent mass deposition. A discussion of these electrospinning methods, and the resulting drug-loading consistency, is found in Chapter 3 with supporting information for this research found in Appendix A.

Subaim 1.2: Modify and formulate fiber implants for months scale ARV delivery

Materials with extended-release timeframes were investigated through screening various polymers with diverse properties for 3ARV encapsulation and release rates. In addition to traditional release study models, the release of physicochemically diverse agents within the protein-rich, low-fluid environment of the subcutis were modeled through an adapted release study platform. Results from this subaim can be found in section 4.4.1 and Appendix B.

Subaim 1.3: Formulate electrospun materials to probe host responses

Electrospun fibers were also used as a model biomaterial to probe the comparative foreign body response between the subcutis and in the FRT. To select the ideal material for provoking fibrotic tissue growth in the subcutis, three known sclerosing agents were used including

doxycycline, silver nitrate, and polidocanol. Further, we assessed polymers which can achieve burst or extended release of these drugs. We also studied the effect of added gelatin to promote cell binding. Sections 5.4.1 and 5.4.2 discuss these fiber formulations and release rates.

Innovation: The present work provides novel assessment and simulation strategies for predicting uniform fiber mass distribution. Materials generated from dynamic free-surface electrospinning methods have the highest basis-weight mass electrospun fiber deposition to our best knowledge. Additionally, release models adapted here can be used as a valuable tool for predicting drug release from the subcutis, especially for drugs with low solubility. Sclerosing agent fibers further demonstrate the adaptability of electrospinning and create formulations which support various pathways of scar tissue growth.

Impact: Such high-basis weight materials show proof-of-concept capabilities for high and consistent solid-dosage formulation. Further, simulated methods are described across two unique fiber formulations, thereby providing amendable methods applicable across different polymer solutions. In this study, we also demonstrate proof-of-concept capabilities for consistent drug loading congruent with United States Pharmacopeia (USP) standards. Needle-electrospun 3ARV materials also provide insight to polymer properties which dictate drug release rates.

1.2 Aim 2: To measure the pharmacokinetics for HIV preventative efficacy of electrospun ARV materials

HIV efficacy will be evaluated in this thesis research through pharmacokinetics (PK). All drugs that will be used in these studies are already FDA approved, and therefore efficacy of the achieved drug concentrations can be estimated. Drug concentrations in the blood represent a

measurement of relative homogeneity of drug across the body. Further, blood samples can be quantified overtime. However, ARVs are known to be heterogeneously distributed in tissues.[20,21] Localized drug concentrations in the lower-FRT and the rectum are important for viral inhibition at these frequent sites of initial infection. Further, poor ARV partitioning to lymphoid tissues reduces the protection to vulnerable immune cells, especially in HIV treatment. [22,23] Both fiber and film implants were formulated from MVC, RAL, and ETR within the optimal polymer identified in subaim 1.2. Comparative study of implants with differential surface topologies was intended to demonstrate the effect of material architecture on drug delivery rates. Further, we characterize burst release of drug as an effect of material surface drug association, as well as the long-acting effect of this initial drug release. Therefore, in the following subaims we characterize agent release rate and specific partitioning of these physicochemically diverse drugs over an extended timeframe:

Subaim 2.1: Quantify blood serum drug levels for drug release kinetics using murine subcutaneous implant model

Materials developed in subaim 1.2 were investigated via subcutaneous implantation in mice. After implantation, blood serum samples were measured overtime and out to an extended, 120-day endpoint. Using various blood collection techniques – including diluted tail-prick samples for the initial, high-frequency timepoints – samples could be safely collected from each individual mouse across the full study. Results from this subaim are included in sections 4.4.2, 4.4.3, 4.4.5 and Appendix B.

Subaim 2.2: Characterize tissue drug concentrations following long-acting, subcutaneous implant placement

At the end of these extended implant studies, tissues were harvested to estimate remaining drug in the implant pocket. These samples included excised implants and local skin biopsies. Organ tissues were also collected for studies of long-acting drug partitioning, including the lower FRT, the rectum, lymph nodes, spleen, lungs, liver, and kidneys. Tissue 3ARV concentration results are discussed in sections 4.4.3 through 4.4.5 and Appendix B.

Innovation: This study represents the first electrospun ARV subcutaneous implant, and the implant which simultaneously delivers the greatest quantity of different ARVs to our best knowledge.
Impact: PK studies of all proposed routing strategies and release timeframes provide important information for both the fields of HIV prevention and drug release in general. Specifically, these studies will provide insight to the impact of drug and implant properties on long-acting release from the subcutaneous environment, and how these properties impact the heterogeneity of different tissue drug concentrations.

1.3 AIM 3: TO ASSESS TISSUE-SPECIFIC HOST-RESPONSES AND BIOCOMPATIBILITY OF ELECTROPSUN SOLID DISPERSIONS

Safety is a necessary measurement when characterizing new combinations of drugs and materials in new tissue spaces. Implanted materials could pose a risk of fibrous capsule formation, inflammatory cell migration, and potential reproductive damage in application to the FRT. New

materials designed for long-acting drug release rates will be assessed for biocompatibility *in vivo* using a subcutaneous implant mouse model, and *in vivo* in baboons for FRT studies.

Subaim 3.1: Assess foreign body reaction toward subcutaneously implanted ARV/fibers in mice

Biocompatibility of 3ARV-implants were measured in parallel with PK studies through behavioral observations, weight measurements, and at endpoint histology of the implant sites. Fiber implants were also compared to smooth, film implants as a more traditionally studied material fabrication method. Masson's trichrome stain was used to visualize fibrotic growth and presence of immune cell infiltration. Section 4.4.4 and Appendix B discusses the biocompatibility of ARV-loaded implants.

Subaim 3.2: Characterize the inflammatory response towards fibrosis-provoking electrospun materials in vitro cell and murine subcutaneous models

To characterize the host response towards materials created in subaim 1.3, materials were studied *in vitro* with macrophages to characterize the cytokine response, and with fibroblasts to measure material adhesion. Since the murine subcutaneous implant model is the standard for measuring implant compatibility, these materials were screened as subcutaneous implants in mice, and assessed via histology. Research for *in vitro* inflammatory profiles is available in section 5.4.3, cell adhesion is discussed in section 5.4.4, and subcutaneous implant studies tested in mice is included in section 5.4.5.

Subaim 3.3: Investigate safety and reproductive impacts after transcervical placement of integrated fiber/IUDs in NHPs

Intrauterine application of novel materials pose risk for reproductive damage in addition to general biocompatibility. Considering uterine anatomy, a baboon model must be used to enable transcervical methods. General safety will be evaluated with behavioral assessments following placement procedures. Fallopian tubal occlusion is known to occur from inflammatory agents within the uterine cavity under acute stimuli. Reproductive safety was therefore assessed via patency of fallopian tubes visualized with x-ray imaging and perfused contrast dye. Sections of the utero-tubal junction were also assessed by histology. Results are included in section 5.4.6 and Appendix C.

Innovation: Research conducted in this aim is novel in illustrating the relatively dampened fibrotic host response within the upper FRT.

Impact: Safety studies provide value to this thesis research by confirming 3ARV implants have no major adverse side-effects. This is especially valuable with the unidentified properties of ARVs dosed in the subcutis.

Chapter 2. INTRODUCTION TO RESEARCH

Sections adapted from: Hernandez, J.L. & Woodrow, K.A.. (2021) Medical applications of porous biomaterials: features of porosity and tissue-specific implications for biocompatibility. Under Consideration by Advanced Healthcare Materials.

2.1 ABSTRACT

Drug delivery systems (DDS) can be used to target the delivery of pharmaceutical agents, and control the release kinetics of drugs, thereby enabling greater therapeutic responses and overcoming barriers due to human application. HIV prevention is one application which could especially benefit from the development of novel DDS, as HIV continues to be a global issue that disproportionately effects young women worldwide. Pre-exposure prophylaxis (PrEP) is a daily oral regimen that has shown great efficacy in preventing HIV infection in at-risk patients, but this treatment is disproportionately less protective for young women. Here, we will discuss the history of PrEP and identify short comings of the various developed ARV preventative systems, including oral PrEP, topical tenofovir gel, the dapivirine ring, and long-acting injectables. Further, we discuss the wide variety of DDS that are clinically available for contraception. Using knowledge from these clinically assessed DDS and from research, we also cover the strategies for achieving controlled drug release including polymer selections, nanocrystalline drug formulations, and the effect of implant morphology on drug release. The material fabrication method electrospinning is discussed as a system for controlled drug delivery and specifically how electrospun materials have served the delivery of ARVs. Finally, we discuss the effect of material morphology on biocompatibility, including the host response and biofilm formation. Specific responses towards subcutaneous implants and within the unique environment of the female reproductive tract are

further assessed. We conclude that new DDS are needed to improve the protective potential of HIV prophylactic strategies, and that the drug release kinetics and biocompatibility of the system must be equally considered to determine acceptability of the technology.

2.2 INTRODUCTION TO RESEARCH MOTIVATIONS

2.2.1 *History and efficacy of pre-exposure prophylaxis (PrEP)*

Treatments of antiretroviral (ARV) drugs have proven to effectively prevent HIV transmission from mother to child during pregnancy, birth, and breast feeding.[24] This success at protecting HIV exposed individuals inspired the concept of preventing HIV infection in at risk adults using ARV treatments. PrEP is a daily oral drug regimen of ARVs tenofovir disoproxil fumerate (TDF) and emtricitabine (FTC). The first clinical trial for PrEP was the multi-national Preexposure Prophylaxis Initiative (iPrEx) trial, which followed 2,499 HIV-negative men or transgender women who have sex with men (MSM). The treatment of FTC-TDF showed reduction in HIV risk by 44% over those on the placebo drug.[25] Due to this efficacy, oral PrEP is now the recommended standard of prevention for high HIV risk individuals by the World Health Organization (WHO).[4] However the study FEM-PrEP, which included 2,120 HIV-negative women in Kenya, South Africa, and Tanzania was ended early due to lack of efficacy.[26] Evidence from this study showed that PrEP had more protective efficacy in MSM than heterosexual women. Measurements of drug concentrations in rectal and vaginal tissues revealed that orally delivered PrEP partitions in lower concentrations to the female reproductive tract (FRT). Due to this, protective dosages for MSM can be achieved with talking the pill as little as four non-consecutive days. Conversely, protective dosages in women are achieved after perfect daily adherence.[4] Additionally, it is reported that two to 3 doses per week can be 75-90% effective in men, but

ineffective at protecting against HIV in women.[6] As will be discussed in section 2.2.2, this is especially an issue because of the high global prevalence of HIV in young women.

2.2.2 *Global burden of HIV infection on women*

In 2020, 1.5 million people worldwide became newly infected with HIV.[27] Although medical interventions have decreased rates of infection, HIV is still a global problem and continues to have high prevalence in regions like sub-Saharan Africa. Furthermore, the HIV/AIDS epidemic is the leading cause of disease burden in sub-Saharan Africa.[28] The highest HIV-seropositive population is reported in eSwantini, where approximately 27.4% of the total adult population lives with HIV.[29] This disparity of HIV impact on this region is illustrated in Figure 2.1, a map of global HIV prevalence across the world.

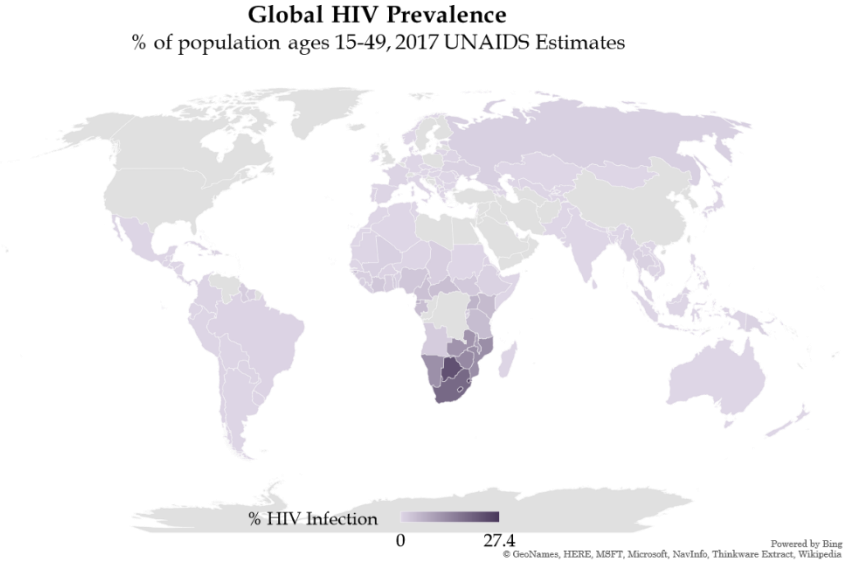

Figure 2.1. Map of percent total HIV infected population between ages 15-49, estimated for 2017 [29]

Data was obtained using published data sets available by the World Bank Group [29]*. Values are estimated by UNAIDs, for the total percent of HIV infected population between ages 15-49. Reported values on the map above are based on 2017 estimates.*

It is estimated that 4 million young people (below 25 years old) are HIV-seropositive in sub-Saharan Africa. Amongst these people, 3 million are women.[30] On average worldwide, young women have twice the risk of HIV infection compared to young men.[31] Additionally it is estimated that the HIV transmission through the FRT has accounted for 12.6 million infections, while 10.2 million cases were transmitted through the male genital tract, 3.9 million acquired through the rectum, and 2.6 million via direct blood stream contact.[22,23] Therefore it is known that young women in Africa carry a large burden of the HIV epidemic. Figure 2.2 maps the ratio of HIV-seropositive women per HIV-seropositive men within a country's total population. In comparison to Figure 2.1, it is clear that women are the most impacted by HIV where HIV most impacts the world.

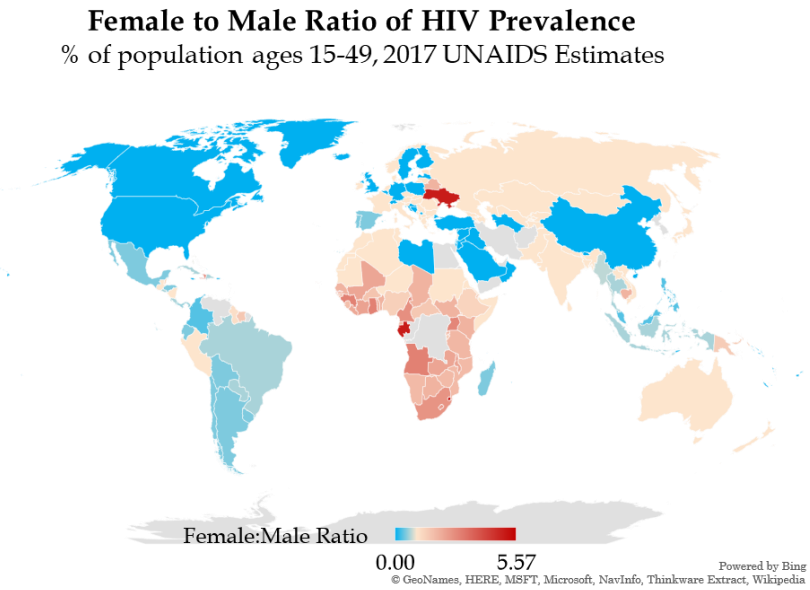

Figure 2.2. Map of the ratio of HIV infected female population per infected male population, estimated for 2017 [32,33]

Values reported on the map above were determined via datasets published by the World Bank Group, based on UNAIDs estimates[32,33]*. Ratio values were calculated using 2017 percent HIV infected population estimates for females per males in each reported country, ages 15-49.*

Societal factors such as the lack of an ability for young women to negotiate the terms of protective methods in which her partner partakes in is thought to be a main contributing factor in increased cases of HIV. Younger sexual debuts for women also are thought to contribute to HIV prevalence.[30] Effective HIV prevention therefore must address the burden in young women and must solve the issues of treatment feasibility. Due to the rigorous dosing regime and the small margin for failure, the daily PrEP pill is considered to not be feasible or acceptable for young women worldwide.[34] This is additionally demonstrated by the low uptake by young women observed in PrEP trials.[26] In section 2.3 we will discuss alternative, female-focused PrEP and contraception solutions tested clinically and their assessed shortcomings.

2.2.3 *HIV infection via the female reproductive tract (FRT)*

The pathology of HIV and pharmacokinetics of ARVs provide special implications for a successful, long-acting drug delivery system. By sexual contact, HIV can be transmitted through the various epithelial surfaces in the lower FRT. Specifically this can occur via squamous surfaces of the vagina or ectocervix, or the single-layered columnar epithelium that composes the endocervix. Additionally the creation of abrasions from intercourse provides access for HIV uptake.[22] Considering the vulnerability of these tissues, and that the vaginal route is estimated to have the largest contribution to HIV cases worldwide,[22,23] it is essential that protection includes the FRT if an impact is to be made on the HIV/AIDS pandemic. Unfortunately, as discussed in section 2.2.2, current technologies do not yet appropriately dose the FRT.

$CD4^+$ T-cells are the main host-cell that harbors HIV. Among multiple possible infection routes, HIV can infect other species of human immune cells, which enables mucosal uptake of the virus. These cell populations include stromal dendritic cells, Langerhans cells, and macrophages.[22] Evidence from Pena-Cruz, *et al.* shows that $CD1a^+$ DCs in the vaginal epithelium are an early

target for HIV and continue to remain infected after viral suppression.[35] After infection, macrophages are also known to act as reservoirs for the virus thereby preserving the infection even after antiviral treatments.[36,37] HIV virions can enter the vaginal epithelium alone or in infected donor cells through abrasions and by transcytosis through epithelial cells.[22] Various targets exist for HIV in the vaginal epithelium, and therefore treatments that can provide universal protection are required.

2.3 Clinically Investigated Drug Delivery Systems (DDS)

2.3.1 *DDS examples used for emerging PrEP technologies*

Due to both the measured successes of oral PrEP and the shortcomings of patient uptake (as described in section 2.2.1), researchers have acute interest in creating novel PrEP alternatives. These alternatives have used engineered drug delivery systems to address two main deficiencies of the oral form. First, technologies have focused on the issue of inadequate efficacy in women. To address this, topical formulations of ARVs have been developed, which circumvents the issue of low drug partitioning of oral PrEP in the FRT.[4,30,38] Gels and rings have been the first vehicles for intravaginal ARV delivery. Multiple ARVs have been investigated within topical gels, but tenofovir, an active ingredient in oral PrEP, has shown the most promise.[7,38–40] Additionally, multiple ARV rings have been developed, but the dapivirine (DPV) loaded ring has had the highest impact in phase 3 clinical trials.[18]

The second issue that the new generation of PrEP technologies have attempted to address is inadequate patient adherence to the daily pill. The main breakout technology to improve adherence is long-acting injectable (LAI) ARVs. Crystalline forms of rilpivirine (RPV) and cabotegravir (CAB) have been investigated in these treatments. These injectable forms have shown

efficacy for up to 8 weeks.[41–43] Intravaginal rings additionally aim to improve patient adherence by reducing the dosing frequency to 4 weeks.[18] A summary of these clinically studied PrEP alternatives is included in Table 2.1. The dosing frequency, reversibility, requirement for frequent adherence, and if the technology provides potent intravaginal delivery is compared for all options. Further descriptions of these technologies, and the results concluded from their clinical trials, will be addressed in the following sections.

Table 2.1. Summary of clinically studied PrEP delivery technologies.

Technology	Dosing Frequency	Reversible?	Adherence Independent?	Intravaginal Topical Delivery?
Oral PrEP	Daily	Y	N	N
Tenofovir Gel[38,39]	12 hr before sex, within 12 hr after sex	Y	N	Y
Dapivirine Ring[18,44,45]	4 weeks	Y	N	Y
Long-acting Injectable Cabotegravir & Rilpivirine [10,41–43,46,47]	4-8 weeks	N	Y	N

2.3.1.1 Pharmacokinetics of FRT drug partitioning

PrEP has been found to be less effective at protecting against vaginal transmission of HIV. As previously discussed, this is due to lower TFV drug partitioning to the FRT after oral administration of drug. Although adherence is still an ongoing issue, topical delivery of ARVs have shown improved pharmacokinetics in the FRT. As demonstrated in clinical studies by Abdool Karim, *et al.*, oral tenofovir disoproxil fumerate (TDF), a prodrug of TFV, was found to enable

rectal tissue TFV concentrations of 2000 ng/g, but just 10 ng/g TFV in vaginal tissue and 70 ng/mL in CVF after 24 hours. Comparably, topically delivered TFV gel created vaginal tissue drug concentrations of approximately 10^3-10^4 ng/g and 10^5-10^6 ng/mL TFV in CVF samples.[38] Other clinical studies estimate that perfect adherence of 300 mg daily oral TDF only results in estimated FRT tissue concentrations of 0.56 µmol/L TFV, while perfect adherence to daily topical TFV gel is estimated to enable tissue concentrations of 1.8 µmol/L.[48] These studies confirm that oral TDF unfavorably protects the FRT, but the issue of low local concentrations can be successfully circumvented by direct delivery to the FRT. The success of topical delivery systems has been recapitulated in other studies as well. Topical delivery therefore proves to be an effective solution to improving PrEP for women, as further described in sections 2.3.1.2 and 2.3.1.3.

2.3.1.2 Tenofovir gel

Tenofovir (TFV) gel was the first technology developed as a solution to low FRT drug partitioning following the disappointing results in female focused clinical trials of oral PrEP. The agent TFV was selected from being previously used as one of the ARV agents used in oral PrEP.[39] Additionally, Dumond, *et al*. previously verified favorable TFV exposure in the FRT as compared to other ARVs.[49] The TFV gel first differs from the oral PrEP formulation by topical delivery, which a patient self-administers using a pre-filled vaginal applicator. Each dose contains 40 mg of gel containing 1% TFV. The gel vehicle was formulated with 9-[(R)-2-phosphonomethoxy) propyl] adenine monohydrate (PMPA) in a solution of purified water with edetate disodium, citric acid, glycerin, methylparaben, propylparaben, and hydroxyethycellulose (HEC). Unlike oral PrEP, the gel additionally does not require daily use. Rather, patients use the TFV gel in a coitally dependent regime: one dose is given 12 hours before sex and a second dose is given within 12 hours after sex, with no more than 2 doses administered within 24 hours.[39]

The Center for the AIDS Program of Research in South Africa (CAPRISA) 004 trial was conducted to assess the efficacy of the TFV gel in comparison to a placebo gel. Women uninfected with HIV were enrolled in May 2007 through January 2009 in both rural and urban Kwa-Zulu Natal, South Africa. In total 1,085 women ages 18-40 years old were enrolled, and 889 were included in the analysis of the trial, reported by Abdool Karim, *et al.*.[39] Earlier trials showed great promise for a gel system. Rosen, *et al.* reported that 94% of women surveyed in the phase 1a trial would "probably" or "definitely" use a TFV gel for HIV prevention.[50] Unfortunately, this adherence was not reflected in the CAPRISA trial. In the patients that remained HIV seronegative, the overall median adherence to the TFV gel was reported to be 61.3%, while HIV seroconverted patients had an overall median adherence of 59.2% to the gel.[39]

Overall, the TFV gel was shown to reduce HIV acquisition by 39%, or by 54% in patients with greater than or equal to 80% adherence to the treatments.[7,38] Pharmacokinetic (PK) studies of this trial indicate that TFV concentrations lower than 1,000 ng/mL in cervicovaginal fluids (CVF) resulted in comparable risk of seroconversion as the placebo gel treatment, further highlighting the importance of dosing adherence.[38] Analysis conducted by Kashuba, *et al.* reported that TFV concentrations in the CVF of 100 ng/mL resulted in 65% HIV protection, while 1,000 ng/mL correlated to 76% protection.[7] Although the TFV gel achieved this moderate success, other experts in the field conclude that this coitally dependent treatment is not an acceptable strategy for a large population of women.[30] Possibly the largest impact of the CAPRISA trial has been the identified need to simplify the PrEP regime. This need has informed the development of alternative technologies including the DPV ring and LAIs.

2.3.1.3 Dapivirine ring

The need for topical PrEP technologies for women, and additionally the need for simplified methods for adherence contributed to the development of the DPV ring. Much like the contraceptive device NuvaRing, the DPV ring is placed within the vagina for four consecutive weeks. Patients are therefore only required to remove and replace this device every 28 days.[18,45,51] These rings are made from a flexible silicone elastomer. DPV is distributed throughout the matrix and is cured by platinum catalysis.[45,51] Human scale devices had an outer diameter of 56 mm and a cross-sectional diameter of 7.7 mm.[51]

Initial phase I clinical trials of ARV rings included rings loaded with DPV, MVC, and both DPV/MVC.[51] Non-nucleoside reverse transcriptase inhibitors (NNRTIs), like DPV, have been found to enable higher drug concentrations in the FRT by systemic administration. This is the same rationale for use of the NNRTI Nevirapine for the prevention of mother-to-child HIV transmission.[49,51,52] Unfortunately DPV is not effective against less commonly transmitted HIV-2. For this reason, and concerns over creating NNRTI resistant HIV, MVC was also investigated. MVC is a CCR5 receptor antagonist that protects against both HIV-1 and HIV-2.[51] It was therefore hypothesized that a dually loaded device would provide broad protection. Chen, *et al.* showed that DPV had favorable release kinetics from the ring and enabled local drug concentrations greater than 1,000-times the plasma concentration. MVC was dosed four-times greater than the dose of DPV, but could not be detected in blood plasma.[51]

A Study to Prevent Infection with a Ring for Extended Use (ASPIRE) was the phase III clinal trial that assessed the efficacy of the DPV ring over a placebo ring in 2,629 enrolled patients. Women were ages 18 to 46, and resided in Malawi, South Africa, Uganda and Zimbabwe. Within this trial, the rate of HIV incidence overall was 3.3 in 100 in the active ring group, and 4.5 per 100 in the placebo group, meaning that overall the DPV ring reduced HIV incidence by 27%.[18] Baeten,

et al. concludes that ring efficacy was varied for different age groups as a product of adherence. The DPV ring was determined to be 56% effective for women more than 21 years old and 61% effective in women more than 25 years old. For women 18 to 21 years of age, the efficacy of the DPV ring was -27%.[18] The lack of preventative efficacy in this age group is especially unfortunate as women younger than 25 years old in sub-Saharan Africa have one of the highest incident rates of HIV worldwide.[30] Although this device was developed to simplify adherence, it is clear that the method was still found to be unfavorable with young women, many whom chose to remove the device. From this study it is additionally clear that new dosage forms require discreetness in addition to a simplified dosing schedule.

2.3.1.4 Long-acting injectable cabotegravir and rilpivirine

Diverging from female specific PrEP technologies, LAIs are delivered by an intramuscular injection and therefore can treat people regardless of reproductive anatomy. Currently there are two ARVs that have been investigated as LAIs in clinical trials: CAB and RPV. Long-acting release of these agents is achievable by nanocrystalline formulation of drug particles. Theory of drug release from nanocrystalline suspensions will be described in greater detail in section 2.4.3. Briefly, the crystallinity makes the drug particle more insoluble, therefore resulting in slow release rates. These drug crystals are then broken down into nanoscale particles, which increases drug surface area and solubility.[11] Additionally, the nanoscale allows for simple injection. The balance of the impacts on crystallinity and length scale results in a formulation that can provide a protective drug dose for up to 8 weeks.[10,11,43]

The two most advanced clinical trials testing LAIs are ECLAIR and LATTE-2. ECLAIR was a phase IIa trial that assessed the use of LAI-CAB for the prevention of HIV in men. Participants were enrolled from March 2014 to February 2016, and in total tested 127 men, mostly

who identified as MSM. The study began with an oral lead-in phase, then tested a total of three injections, administered every 12 weeks of either LAI-CAB or saline. As reported by Markowitz, *et al.*, this study concluded that the injections were well tolerated, and the only case of seroconversion occurred after the final injection, during the follow-up period. Adverse reactions were commonly reported, mainly being injection site pain. Amongst the LAI-CAB group, 80% of participants reported experiencing an adverse reaction of grade 2 or higher (on a scale to 4), as opposed to 48% in the placebo injection group. Additionally, the given 800 mg dose was determined to be suboptimal for a 12-week protective timeframe.[47] LAIs still have promise as a PrEP solution, but would likely require a more frequent dosing regimen or reformulation.

The LATTE-2 trial is a phase IIb that tested both CAB and RPV in HIV positive men and women as a treatment. A total of 309 patients were enrolled across the USA, Canada, Spain, France, and Germany from April 2014 to November 2016. Patients were either placed in a (1) four-week treatment group with 400 mg CAB and 600 mg RPV, eight-week treatment group with 600 mg CAB and 900 mg RPV, or (3) oral CAB, abacavir, and lamivudine. Mild injection site pain was reported in 84% of injections, moderate in 15%, and severe enough to result in discontinuation of the treatment in 2 of 230 patients. Therefore, the treatments were considered well tolerated. Margolis, *et al.* also claims that the both the four-week and eight-week dosing regimens maintained HIV-1 viral suppression as effectively as the daily oral therapy group. Long lasting treatment groups also reported higher rates of satisfaction at the end of the 96 week study as compared to those given the oral treatment.[42] Kerrigan, *et al.* compiled testimonials from patients in the LATTE-2 trial, again highlighting the positive reception of the compliance independent option.[53]

Although this study has realized the future for long-acting HIV treatments, the application for HIV prevention still requires prototyping to enable more realistic timeframes for frequency of hospital visits. Additionally, the ECLAIR trail was not assessed in women, so the efficacy of establishing protective drug concentrations in the FRT by systemic CAB dosing has only been assessed in smaller cohorts.[8] Although LATTE-2 included women in the study, the use of the LAIs for antiretroviral therapy does not address the issue of intravaginal infection. For these reasons, there still exists a need for new PrEP technologies that can serve young women.

2.3.2 *DDS systems used for contraception*

Availability of contraceptive methods not only supports the basic human right of family planning, but has implications for population health, the economy, and the environment. Because of this, governments across the world have had interest in supporting family planning programs since the first contraceptive revolution hit Europe in 1880.[54] The history of these government family planning plans range from controversial to highly successful. Community involvement has proven to be essential in the success of these programs, especially in rural regions or regions with higher rates of literacy. Bangladesh employed a program that included visits from literate women from the community to act as family welfare assistants. From 1979 to 1996, the use of contraception by in-union women in Bangladesh rose from 12% to 49%.[54] Visits from community health workers, or relais, were used in a 2016 study in The Republic of Niger. Brooks, *et al.* reports that these visits were shown to increase the use of modern contraception in the young married women studied.[55] In urban communities, social media has shown to influence perspectives on family planning, and media such as soap operas are credited with influencing desire for smaller family sizes in places like Brazil.[54]

Public health initiatives concerning contraception in the modern era are now emphasizing the importance of long-acting reversible contraceptives (LARC), such as intrauterine devices (IUDs) and implants. Such technologies are preferable for their extended period of action, high efficacy, and the elimination of potential improper use by the patient. In the United States, 43% of unintended pregnancies are reported to be from inconsistent or incorrect use of a contraceptive use.[56] IUDs are already widely used across the world, and are currently the most commonly used method in Asia, and specifically countries like China.[54,57,58] Across all IUD or intrauterine contraceptive (IUC) users surveyed by the United Nations in 2011, women in Asia account for 83%.[57] This is shown in Figure 2.3, a map of the most prevalent contraceptive methods used by country.

In Africa, the most commonly used contraceptive method is the injectable intramuscular DMPA-IM or commercially known as Depo-Provera.[58,59] Although less effective than the LARCs, DMPA-IM is still highly effective for multiple months after a single injection (see Table 2.2). The use of DMPA-IM in Africa has also been controversial, as qualitative studies suggested the use of DMPA-IM increases a woman's risk of contracting HIV.[59–61] The ECHO trial provided evidence that contraceptive methods do not directly contribute to HIV risk. Rather, the population that uses contraception the most are independently also the population that carries the highest rate of new HIV infections.[59] Evidence from this study further proves the importance of these contraceptive methods worldwide. Overall, it has been reported that an unmet need exists for contraception for women in places like Africa.[62,63]

The urgency of implementing family planning programs has been reported to be in a lull in recent history. Partially, this is due to a re-centered focus on the AIDS epidemic over the issue of over population.[54] One qualitative study conducted in Rwanda indicated that stakeholders would

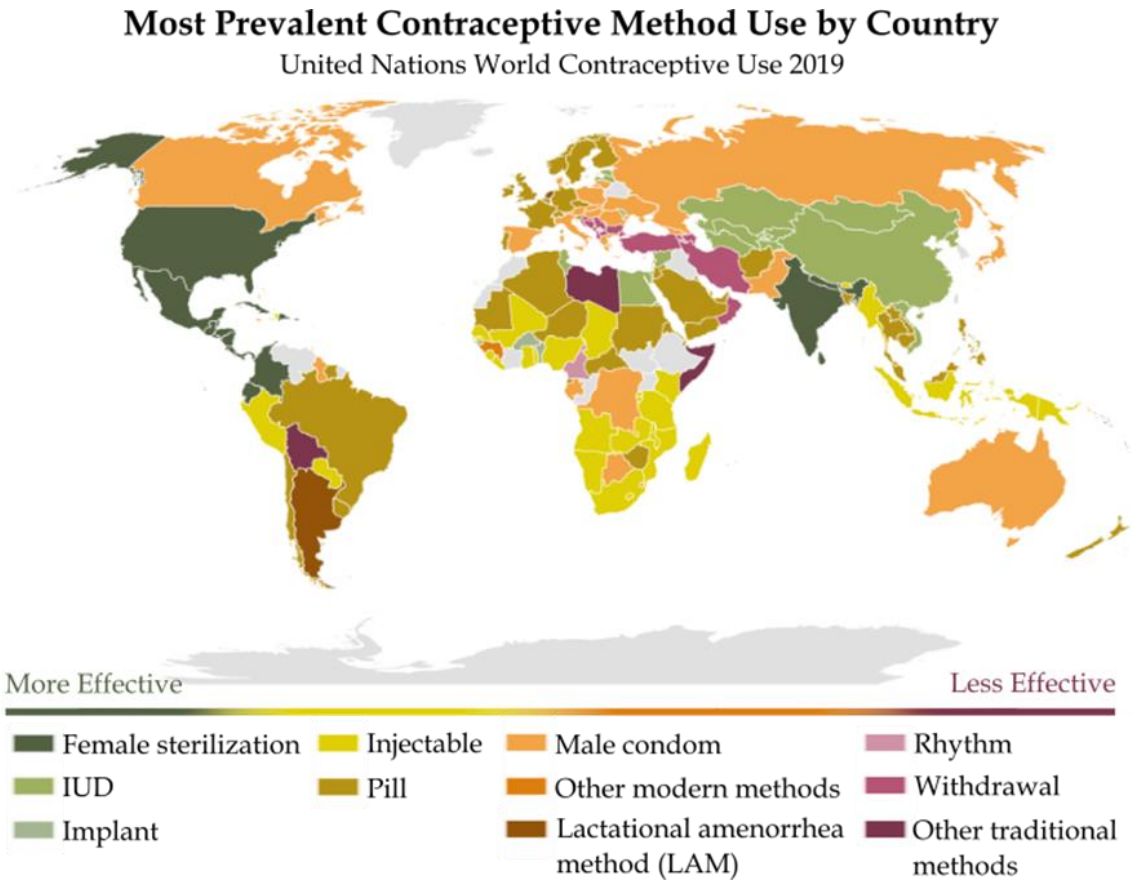

Figure 2.3. Map of most popular contraceptive method use per country [64,65].

Data for method popularity provided by the United Nations World Contraceptive Use report for 2019 [64]. Values for contraceptive use are reported as percent of married or in-union women that utilize the method, as measured by survey-based estimates. The most popular contraceptive method was determined for each reported country based on the most recent survey reported. Color-coding for efficacy of methods are grouped approximately based on The U.S. Centers for Disease Control and Prevention "Efficacy of Family Planning Methods" chart.[65]

prefer to allocate more money to family planning resources than is currently distributed. Wall, *et al.* concludes from these surveys that new policies must support the integration of HIV preventative services with family planning resources.[66] Conclusions from the ECHO trial reflect this as well, further promoting the need for technologies that can integrate both HIV prevention and contraception.[59] Various drug delivery options for contraception exist, and all have shown near

100% efficacy. A summary of currently FDA approved contraceptive methods are detailed in Table 2.2. In the following sections, the contraceptive technologies IUDs (section 2.3.2.1) and implants (section 2.3.2.2) further explored. For the application of compliance independent DDS, we determine that these technologies will have the most relevance to the proposed thesis research.

Table 2.2. Summary of clinically available female contraceptive technologies in the U.S.

Agent Delivery Technology	Efficacy [65]	Route of Dosing	Frequency of Dosing	Year First FDA Approved
Copper IUD (Paragard)	99.2%	Intrauterine	12 years	1984 [67]
Hormonal IUD (Mirena, Kyleena, Liletta, Skyla)	99.8%	Intrauterine	3 - 7 years	2000 [68]
Implant (Nexplanon, Implanon)	99.9%	Subcutaneous	3-5 years	2006 [69]
Injectable (Depo-Provera)	96%	Intramuscular	3 months	1959 [70]
Ring (NuvaRing)	93%	Intravaginal	Monthly	2001 [71]
Pill	93%	Oral	Daily	1960 [72]

2.3.2.1 Intrauterine devices

Intrauterine devices (IUDs) have been investigated since the early 1900s. The first report of such a device was by Dr. Richard Richter in 1909, who created a ring-shaped IUD fashioned from silkworm gut. Revival of the pursuit of IUD development occurred in the 1960s, leading to the discovery of copper as a highly contraceptive agent by Dr. Jaime Zipper.[73] This era invented clinically viable devices such as the Copper-T IUD still used today, but also included the

development of devices that set back the field, like the Dalkon Shield (see section 2.8.2). Despite this failure, IUDs and other LARC options are becoming more widely accepted, with the prevalence of use per country ranging from 2% to 80% of the population of contraceptive users.[74] Topical delivery of contraceptive agents allows for low dosages, and sustained delivery of these agents allows for adherence independent use. IUDs are therefore becoming a more desirable option for their reduced hormonal side-effects, near 100% efficacy, and the reduced frequency of treatment uptake.

In the United States, the Paragard Copper-T and hormonal levonorgestrel (LNG) options including Mirena, as well as its lower dose versions, are the IUD options on the market.[57,74] The ParaGard, also referred to as the T380 Cu-IUD, consists of 380 mm^2 of copper on a plastic frame.[75] This device was FDA approved in 1988,[67] and is currently the only copper IUD approved for the US market.[75] Larger than the other IUDs in the US market, Paragard is 32 mm by 36 mm.[76] Hormonal options have been developed more recently, being first marketed in Finland in 1990,[77] and FDA approved in the US in 2000.[67] Mirena, the LNG-IUD, has the dimensions of 32 mm by 32 mm and requires an insertion tube that is 4.75 mm in diameter.[78] With a release rate of 20 µg per day, the Mirena is protective up to seven years.[78,79] In 1991, a clinical trial with 2,244 women showed high efficacy of both these devices, where the LNG-IUD resulted in a pregnancy rate of 1.1% and the copper TCu380 device had a pregnancy rate of 1.4% after seven years.[78]

The VeraCept® is an emerging copper IUD that is currently going through phase III clinical trials.[80] This device includes 175mm^2 of copper on a frame made of nitinol wire, a nickel alloy that has shape-memory properties. The device dimensions are 32 mm by 30 mm.[81] This results in a device that has a thinner profile than the other IUDs.[81,82] In clinical trials comparing this new IUD to the already approved T380S copper IUD, the VeraCept was found to result in less

pain, fewer incidences of expulsions, and higher rates of continuation.[81] IUDs continue to be one of the most effective solutions to unintended pregnancies and are further innovating as a modern option.

2.3.2.2 The contraceptive implant

The subcutaneous implant is relatively one of the newest contraceptive options available in the clinic. The first generation of the contraceptive implant was Norplant®, which was first approved in Finland in 1983, and FDA approved in 1990. This system composed of six rods, 34 mm in length and 2.3 mm in diameter. Each rod was designed as a capsule which contained 36 mg of the hormone levonorgestrel (LNG). Tubing made of polydimethylsiloxane (PDMS) and methyl vinyl siloxane copolymer coated the drug reservoir. The system was found to release approximately 80 µg LNG per day, then 30 µg per day in later years for a total of five approved years of use.[16] With the state-of-the-art shifted towards single rod systems, the Norplant is no longer clinically used.

Implanon® was the initial version of a single rod device, which uses progestogen etonogestrel (ENG) as the active hormone released. A total of 68 mg of ENG is contained within a ethylene vinyl acetate (EVA) core and membrane.[16] For the first 3 months, the implant releases 60 µg per day, then to 30 µg per day until the end of the second year, and is effective for three years.[83] Nexplanon®, now the most modern iteration of the subcutaneous device, is different from Inplanon by being radio-opaque and with a new applicator. The addition of 3% barium sulphate enables x-ray imaging of the implant in case of deep insertion. New insertion methods additionally aim to eliminate problems with non-insertion that were the cause of 50% of pregnancies with the device.[84,85] Nexplanon is reported to have the same pharmacokinetics as Implanon, and beyond the use of the radio dye, is completely the same in composition.[84]

Economics is largest hurdle for the ENG implant, as well as the other LARC options. Both the implantation procedure and IUD placement requires trained personnel and adequate clinics to conduct procedures. Between the cost of the device, training, and potential costs for post-procedure care in the case of adverse events, it is unclear to some professionals how much the implant saves financially over taking a daily pill.[85] Patient preference and efficacy at preventing unintended pregnancies should still be factored into public policy. One study reported by Wong, *et al.* compared the patient perspectives of 439 women on the various LARC options: the ENG implant and IUD (hormonal or copper). Overall, more participants reported to be satisfied with the IUD over Implanon, with 74.3% of IUD users reporting satisfaction after 6 months versus 57.5% of Implanon users. This study concludes that counseling is a valuable aspect of patient uptake with LARC.[86] Despite this report of relative disappointment with the implant, there exists value in having options. For people with abnormalities that prevent intrauterine placement of an IUD, or any other personal rationale, the implant serves as a highly effective option for contraception.

2.4 STRATEGIES FOR LONG-ACTING DRUG DELIVERY

2.4.1 *Factors controlling long-acting drug deliveries from polymeric systems*

Drug delivery systems (DDS) can take on various forms and mechanisms. In application to this proposed thesis research, drug delivery systems that we discuss refer to polymer systems that passively release drug. Mechanisms of drug release by the discussed systems are therefore dictated by diffusion of drug through polymers, erosion of drug from the DDS matrix, and chemical degradation of polymer which releases encapsulated drug.[87] Passive polymeric drug delivery systems can also have various geometries. Matrix systems incorporate drug

homogeneously throughout the polymer system. Reservoir systems are composed of a drug core with a polymer rate limiting membrane.[87] For our purposes, the designed system should (1) release drug for a long period of time, (2) have effective daily doses maintained, and (3) rapidly provide protective drug concentrations after placement.

Considering a system where the geometry is fixed, the polymer and drug selections must be rationally considered. Degradation rates are impacted by polymer and drug solubility as well as by diffusion.[87] Diffusion rates are controlled by the size and structure of drug molecules, polymer chain mobility, and the interaction between drug molecules and polymer chains.[88] Polymers can be selected to be more or less permissible to diffusion. Additionally, polymers can be selected and formulated in a spectrum of being non-erodible, slowly or selectively biodegradable, and rapidly dissolving. With multiple drug options, an active ingredient should be prioritized that can potently provide treatment. Potency of an agent can be determined through reported factors such as the half maximal effective or inhibitory concentrations (EC_{50}/IC_{50}). Pharmacokinetic factors such as clearance rates from the body will also impact needed release rates and possible timeframes of drug delivery systems. Factors that control drug release by polymers will be further discussed in section 2.4.2. Additionally, the factor of drug crystallinity is explained in theory and in application to serving HIV therapies in section 2.4.3.

2.4.2 *Polymer properties to control drug release*

Effects on drug release by polymers alone are dependent on the solubility of polymers and the chain mobility.[88] Parameters that impact these factors are the degree of crystallinity, glass transition temperature, and molecular weight. Polymers can be fully amorphous or semi-crystalline. The organized orientation of polymer chains in regions of semi-crystalline polymers makes degradation less energetically favorable and materials less permissible to diffusion.

Amorphous polymers have a greater degree of chain mobility, thereby having higher rates of diffusion.[88–91] All polymers also have glass transition temperature (T_g) as a property, being the temperature at which a polymer will shift from a glassy, brittle state to being more rubber-like. Molecularly, this occurs due enhanced chain mobility. An implanted biomedical polymer with a T_g higher than body temperature will have slower drug release, while polymer with a T_g lower than body temperature will have enhanced diffusion and faster drug release rates.[88–90] Various molecular weights are additionally available for a polymer, as determined by the average chain length. Higher molecular weight options will have reduced chain mobility, lower rates of diffusion, and therefore are more favorable for sustained drug release. Chain length will also impact polymer chain orientation, therefore also impacting the crystallinity of the material.[89,91] A long-acting drug delivery system then would theoretically be highly crystalline, have a high T_g, and high molecular weight, but the interactions of these factors may not act in synergy. However, the specific molecular behaviors of the system will be dependent on drug selection.

2.4.3 *Drug properties to control release rates*

Along with the stated polymer factors that will impact a long-acting drug delivery system, properties of the drug will also impact release kinetics. Further, the compatibility of drug and polymer will impact the dose of drug which can be delivered.[90] Solubility of the drug will greatly impact rates and the quantities at which the drug is released because of drug diffusion rates. Drugs with greater hydrophobicity will have lower drug release rates into aqueous interstitial fluids and blood.[90] The acceptability of low concentrations of released drug is dependent on the potency of the drug. Measures of half maximal effective concentration (EC_{50}) or inhibitory concentration (IC_{50}) are quantified *in vitro* or *in vivo* and can give relative insight to the comparative potency of drug. However, *in vitro* data is most commonly available for drugs, and can be determined with

different cell types or assays, so these measurements are not perfectly translatable to *in vivo* blood or tissue drug concentrations.[92] Individual drug potency can be increased through co-delivery with other agents which have synergistic potency. Therefore delivering multiple drugs simultaneously can be an effective method for increasing the efficacy greater than the sum of individual agents.[93,94] Pharmacokinetic measurements of agents also commonly report the half-life ($t_{1/2}$) of drugs. Drugs with low half-lives will be rapidly cleared from the body, and therefore require greater release frequencies to replenish active drug concentrations.[95]

2.4.3.1 Drug protein binding

To translate *in vitro* EC_{50} or IC_{50} values to relevant concentrations *in vivo*, research commonly compares blood or secretion concentrations to protein-adjusted values (PA-IC_{50}). Such measurements consider the quantity of drug which associates with off-target proteins, like albumin, and therefore is not free to bind to the drug target. Albumin is one of the most common proteins available in the body – especially in blood – and is a common off target protein which drugs bind to.[96] Drug protein affinity percentages can therefore also provide insight to the complex interactions which drugs will have in biological systems. Although the off-target bound drug is inactive, drug binding is typically reversible to maintain an equilibrium of protein-bound and free drug.[97]

Interestingly, albumin binding has been used as a drug carrier which can increase drug half-lives and enable specific tissue portioning. Albumin is larger than the threshold for renal clearance and undergoes neonatal Fc receptor (FcRn) mediated recycling, which enables long, 19-day circulation times.[95,98,99] Drugs such as Levemir® and Victoza®, which are FDA approved to treat diabetes, non-covalently bind to albumin, which increases the active agent half-life from up to 6 minutes to 7 hours, and 2 minutes to 15 hours, respectively.[95,98] While these active agents are

proteins, such albumin binding is also a potential strategy applicable to small molecule drugs.[95] In addition to half-life extension, albumin binding can effectively target drug release to tumors and lymph nodes, as well as intracellular uptake by antigen presenting cells.[99–101] For these reasons, agents have been designed to have affinity to endogenous albumin as tumor and lymph node dyes.[99,100] Further, albumin affinity has shown to be an effective strategy for targeted vaccination, increased T-cell priming, and with reduced systemic delivery and toxicity.[101] Therefore, albumin binding can improve long-acting release, as long as the active agent can dissociate at effective dosages.

2.4.3.2 Drug crystallinity and drug crystal particle scale

Keeping the chemical structure of a selected drug constant, solubility of a drug can be controlled by crystallinity, as well as the scale of the drug particle. Crystalline structures are typically more insoluble due to high structure stability and lattice energy. To improve the bioavailability, excipients have been commonly used to formulate drugs in amorphous forms.[102] For drug delivery, crystalline morphologies can be used to slow drug release rates, but large drug crystals can be too insoluble for practical use. Therefore, nanocrystalline formulations of drugs have been used to achieve desired pharmacokinetic properties. By decreasing the crystal particle size, the solubility, and release rate of the drug particle will increase. This can be seen using the Ostwald-Freundlich equation, which describes saturation solubility as a function of particle size [2.1]:

$$\log\left(\frac{C_S}{C_\infty}\right) = \frac{2\sigma V}{2.303RT\rho r} \quad (2.1)$$

In this equation, C_S is the saturation solubility of the drug particle, or the solubility of the drug particle. The radius of the drug particle, which is reduced to nanoscale, is represented as r. C_∞ is the solubility of a large particle, σ is the interfacial tension between drug particle and the

environment, V is the volume of the drug particulate material in moles, and ρ is the density of the solid. Standard variables include the gas constant R, and absolute temperature T. Therefore it can be seen that a decrease in particle size will cause a decrease in solubility by this law.[103–105] Drug particle scale, along with this decrease in saturation solubility, is also shown to effect the rate at which drug is dissolved, which is described by the Noyes-Whitney equation [2.2]:

$$\frac{dX}{dt} = \frac{DA}{h_D} \times (C_S - C_t) \quad (2.2)$$

Decreasing the size of the drug particle decreases the particle surface area, A. As before, C_S is the saturation solubility of the drug particle, but C_t is the concentration surrounding the drug particle. The dissolution rate of the drug into its environment is dX/dt, the diffusional distance is h_D, and the coefficient for diffusion is represented by D.[103–105] This equation clearly illustrates the impact the reduction of drug particle size has on the rate at which the drug will be released into the environment, especially considering the previously discussed decrease in saturation solubility.

Beyond theory, this effect has shown to have clinical relevance by the example of LAIs. The long-acting injections of RPV and CAB, tested in the LATTE-2 and ECLAIR trials are formulated to be nanocrystalline.[10,46] In addition to having optimized properties for extended efficacy, the nanoscale of the drug particles are small enough for injection. Other FDA approved ARVs show promise as LAIs, but additional work will be required to make stable, non-aggregated forms.[11] Additional options for nanocrystalline ARVs (ncARVs) could provide benefit in case of HIV drug resistance and for synergistic potency.[93] Alternative delivery routes, such as topical administration ncARVs, would be an innovative use of these drug forms and could provide improved dosing frequencies. Incorporating these ncARVs into new delivery vehicles, such as electrospun fibers, could be a simple solution to stabilize the drugs, further tune release rates, and

enable new methods of administration. Nanocrystalline formulations are therefore an interesting solution for manipulating drug release and have various innovative and unexplored applications.

2.5 Effect of material microarchitecture on DDS

2.5.1 *Definitions and measurements of porous materials*

Porosity is defined as the void of material, and is further characterized by the interconnections, or throats, between these pores, and walls or struts of the medium which forms the 3D structure (*Figure 2.4*).[106] Features of pores, throats, or struts are characterized by their size, shape, organization, density, and homogeneity. Traditionally, pore scale is delineated as macroporous when greater than 50 nm, mesoporous between 2 nm and 50 nm, and microporous when smaller than 2 nm.[107–109] Nanoporosity is also used to describe materials within the nano-scale range, with pore diameters between 1 and 100 nm.[108] Spherical, tubular, and random pore structures are commonly observed in porous materials, but novel fabrication methods are continuing to develop complex, high-resolution geometries,[110–113] and even materials with transforming topologies.[114] The geometry of these pores and interconnections are further defined as either closed, open, or blind-ended.[106]

Materials with porous features are mainly characterized by pore size or by the percent or ratio of porosity in the medium. For fibrous porous materials, strut or fiber diameter is also an important feature to characterize. Pore and strut size is most commonly estimated using imaging.[106] Methods such as optical microscopy, scanning electron microscopy (SEM), and transmission electron microscopy (TEM) can capture sections or regions of the material, then image analysis software can measure the pore or strut size features within the region of interest.[106] While these

methods are simple, intuitive for assessing the material morphology, and avoid preparation methods that may modify native microstructures, imaging methods fail to capture the complete 3D structure of the material.[106] Other methods such as mercury and flow porosimetry can also quantify pore size as measured by the differential gas pressure of mercury or the measured pressure of a wetting fluid (P). However, these methods cannot measure closed pores and may have variable accuracy depending on surface and wetting fluid interactions.[106,107] Using the Washburn equation [2.3] or similarly the Young-Laplace formula, pore diameter (D) is calculated as a function of the surface tension of mercury or the wetting liquid (γ), and the contact angle of mercury or the wetting liquid and the sample (θ).[106]

$$D = \frac{-4\gamma\cos(\vartheta)}{P} \quad (2.3)$$

Measurements of porosity, or void fraction, are reported as either a percent or ratio (ε) of the pore volume (V_P) to the total bulk volume of the material (V_T). Materials are considered to have low porosity when $\varepsilon < 30\%$.[115] Pore volume is typically calculated using the density of the material used (ρ_m) and the mass of the sample (m_S).[106,107] Another simple way to calculate porosity uses Archimedes principle, which states that the volume of a fully emersed body is equal to the volume of water displaced. Pore volume can be calculated by the difference of wet and dry material weight, while total volume can be calculated by the difference of wet and fully submerged material. However, this method is not accurate for hydrophobic materials due to poor water penetration.[106] Equation 2.4 shows these calculations of percent porosity.

$$\%\, Porosity = 100 \times \varepsilon = 100 \times \frac{V_p}{V_T} = 100 \times \left(V_T - \frac{m_s}{\rho_m}\right) \Big/ V_T \quad (2.4)$$

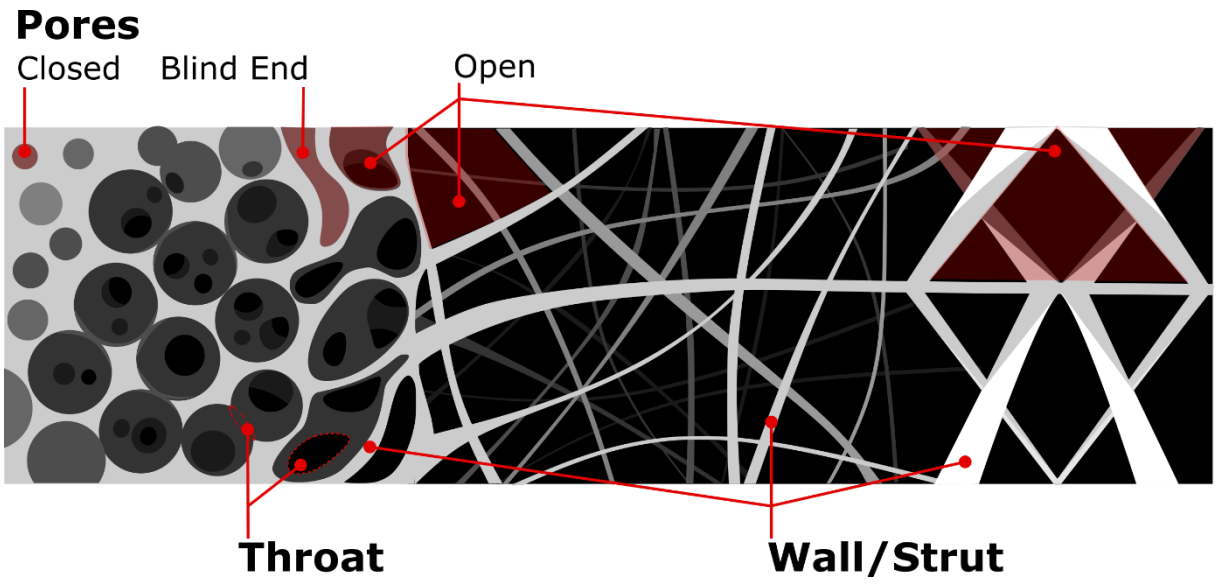

Figure 2.4. Example architectures and relevant features of porous materials.

2.1.2 Implications of porosity on biomaterial properties

When considering material porosity, context is important for evaluating porosity effects on performance outcomes. For implants and tissue engineering scaffolds, voids are typically intended to permit cell migration, the influx of oxygen and nutrients to sustain these cultures, and the outflux of metabolic wastes.[116,117] For drug delivery, these voids are intended to be saturated with biological fluids, thereby enabling drug release by modes of outward drug diffusion or hydrolysis mediated material erosion.[109,118,119] Thus, permeability is an important effect of porosity and influenced by pore size and their interconnections, bulk material dimensions, surface characteristics of the material such as hydrophilicity, and pressure differences.[106,107] Capillary action is one mechanism of permeability, which mediates uptake of fluids within pores due to pore size and surface tension of the solution with the material walls.[120,121] While decreased pore or throat size may limit permeation of agents such as cells via size exclusion,[117,122] capillary action dictates an increased fluid permeation distance with smaller pore diameters.[121] Therefore, the

impact of pore size on biological fluid permeation depends on the target permeating agent and the surface interactions of the fluid and material walls.

Porosity also impacts material surface-to-volume ratios – as greater percent porosity increases material surface area, and larger pores with constant percent porosity decreases material surface area.[119] Wall or strut size is therefore also a determinant of the surface-to-volume ratio. Materials with larger surface-to-volume ratios can enable greater access for cell attachment,[118,123] or increase drug release rates (described in section 2.1.3).[119] The presence of pores and walls also implies the presence of texture or roughness at the material surface, which additionally impacts cell attachment, protein absorption, inflammatory responses, platelet activation, and bacterial adhesion.[124–129] Increased porosity also decreases scaffold support which can inversely affect the mechanical integrity of the material.[130]

While attachment, drug release, and mechanical properties are impacted relatively by porosity, the specific selection of the material will also have a critical impact on these attributes. To delineate the contribution of porosity alone, research commonly assesses chemically identical materials with multiple pore sizes,[131–134] or screens various materials and assesses the correlation of pore size effects in addition to the composition.[135–138] The effect by pores as opposed to wall structure has also been studied by compressing porous materials after identical fabrication methods.[132]

2.1.3 Effects of porosity on drug release rates

Drug delivery is one important application of biomaterials and is impacted in various ways by porosity. The release of drug into biological solution requires both drug dissolution and diffusion. Within a polymer matrix, drug release can occur by the erosion of the encapsulating polymer or by diffusion through a polymer matrix - both of which may be impacted by porosity.[139]

The Higuchi Equation separately considers non-porous and porous drug release systems [2.5], is widely used, and simply estimates the flux of total drug release (Q) over time (t) per unit area (A) considering drug dissolution and diffusion.[139,140] Further, this equation is modeled one-dimensionally for a rate-limiting ointment film releasing drug into skin under sink conditions, where D is the diffusion coefficient of drug into the biological solution, ε is the porosity of the material, τ is the tortuosity – or the size and branching of the interconnected pores, C_0 is the initial concentration of drug, and C_S is the drug solubility within the matrix.[141]

$$Q = A\sqrt{\left(\frac{D\varepsilon}{\tau}\right)(2C_0 - C_S)C_S t} \quad (2.5)$$

This form of the Higuchi equation accounts for a change in the effective diffusion constant for porous mediums, which increases with higher porosity and lower tortuosity, thereby also increasing drug release.[140,142] The diffusion coefficient also changes dynamically in response to matrix swelling.[140] In the case of porous mediums, swelling alters pore size and tortuosity overtime.[142] The presence of porosity in a drug delivery system described by the Higuchi equation also modifies the drug solubility factor (C_S), which accounts for the partition of drug concentrated inside and outside of the pores.[139,140]

Factors of porosity such as the increased surface area, decreased path of diffusion within the matrix, and greater inward or outward flux may increase drug release rates, and specifically drug release mediated by polymer scaffold erosion.[109,119] Experimentally, materials with larger surface-to-volume ratios – like materials with high porosity – have shown faster, diffusion mediated release.[109,119] However, this correlation is material dependent, as polymers with acidic byproducts such as poly(lactic acid) (PLA) and poly(lactic-co-glycolic acid) (PLGA) show increased drug release for materials with lower porosity, lower permeability, and thicker material walls. Accumulation of carboxylic groups within pores accelerates the hydrolysis of these

degradable polymers.[143–145] Higher porosity can also imply a decreased deliverable dose or a reduction of the polymer which controls agent release.[118] Therefore, the release kinetics of drug delivery systems are heavily influenced by both material composition, material pore morphology, and the interaction of these factors.

2.6 ELECTROSPUN FIBERS

2.6.1 *Summary of electrospun fiber use in research*

Electrospinning is a material fabrication method that is relatively simple in laboratory settings, and robust enough to be used with almost any synthetic or natural polymer. For these reasons, electrospinning has found medical research applications in fields such as tissue engineering and drug delivery.[90,146] To create an electrospun fabric, polymers are dissolved into solvent which can rapidly evaporate. Additional agents, such as drugs or biologics, can be added into this solution prior to spinning as well. There are various methods which this solution can then be electrospin into a solid material. The two relevant methods to this research are the typical needle electrospinning and wire electrospinning conducted by the commercial device, the Elmarco Nanospider®. Diagrams of these methods are illustrated in Figure 2.5. In typical needle electrospinning, this polymer solution is extruded from a syringe with a charged needle across from an oppositely charged target. Wire electrospinning replaces the needle with a wire that is coated with the polymer.[147] With an applied electric field, conical structures are formed from the liquid polymer droplet from the needle or on the wire, known as the Taylor cone. At high enough voltages, the electric force overcomes surface tension, thereby creating fibers at the Taylor cone which collect onto the target.[148,149]

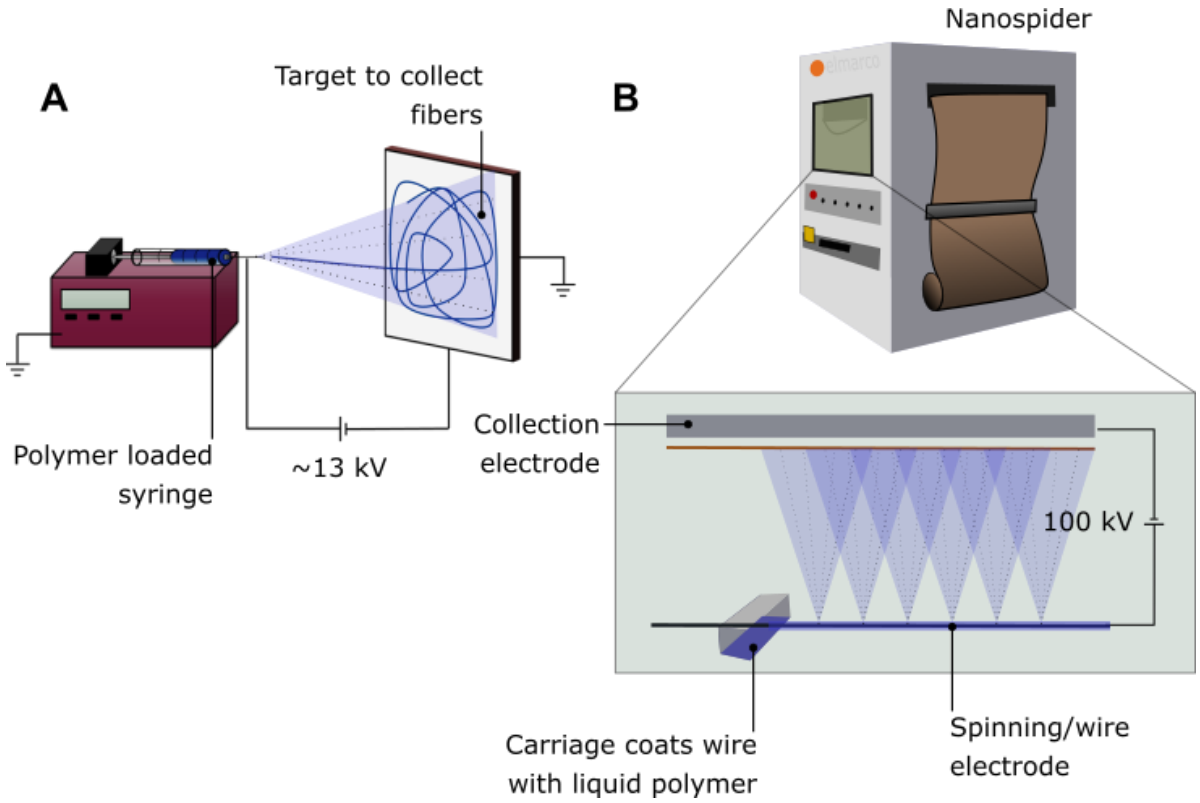

Figure 2.5. Diagram of electrospinning methods

The two methods used in this research are detailed, including (A) single-needle electrospinning and (B) wire electrospinning with the Elmarco Nanospider.

The resulting material from electrospinning is non-woven, and fabric or plastic like in texture. Polymer selections provide various functions to the material, such as biodegradability, cell attachment, or mechanical matching. Fibers that compose the material are in the micro or nano scale, of which the scale is known to be impacted by electrospinning parameters such as solution viscosity, conductivity, distance between electrodes, room temperature, and humidity.[148] The structure of fibers provide function to the field of tissue engineering as an extracellular matrix mimic.[146] For drug delivery, the agents are encapsulated within the fiber. Therefore, fiber scale has shown to have impact on release rates through control over material swelling and degradation.[90]

Sheets of fibers are additionally conducive to surface functionalization, which enables more properties like improved biocompatibility and additional agent delivery.[150]

Additionally interesting to biomedical applications of electrospun fibers is the ability to form these fibrous materials in various geometries. In a review compiled by Chen, *et al.*, electrospun materials have shown potential uses as 1D, 2D, or 3D structures. One-dimensional materials are referring to fiber particulates, which can serve applications such as agent injections.[146] Two-dimensional materials are spun onto a flat collector and serve directly as a drug delivery patch or as a skin scaffold. Electrospun skin scaffolds and wound dressings have been intensively researched from various polymers and including various antimicrobial agents.[151] Three-dimensional electrospun materials are spun onto shaped or molded structures to result in more complex geometries. For example, rotating rods can be directly spun onto to form a fibrous vessel in application to vascular grafts.[152] Electrospinning onto larger rotating rods has also been used by Ball, *et al.* in forming tampon-like structures for vaginal delivery of preventative agents for herpes simplex virus, HIV, and also providing contraception.[153] Through the various options for materials, fine scale control, additional functionalization, agent addition, and use with different geometries, electrospinning proves to be a desirable fabrication method for widespread applications.

Electrospun meshes are commonly used in biocompatibility studies of porous features as these materials are truly porous, thin, tunable, and are clinically relevant to tissue support and hernia repair surgeries.[154] Various factors including polymer concentrations, flow rate, voltage, solvent, and modified collection targets with perforations or rotation can be altered to change the dimensions and alignment of the electrospun fibers, and therefore pore size and porosity.[63,132,155,156] However, the resulting porosity from electrospun fibers is typically lower than other scaffold

fabrication methods, but the process can be adapted with subtractive methods like porogen leaching and freeze casting to improve porosity.[112,157,158]

Despite extensive research with this platform, few electrospun technologies have reached the clinic. Skin scaffolds have advanced the most from the electrospinning platform, making up the majority of electrospun clinical trials. These include treatments of surgical wounds after non-melanoma cancer removal,[159] diabetic ulcers, nitric oxide release for the treatment of cutaneous leishmaniasis.[160] Additionally, electrospun technologies have been studied clinically as a treatment for immature necrotic teeth[161] and as a vascular graft.[160] Although there are only a handful of in-human studies, it is clear that electrospinning is beginning to have applicable success and biomedical potential in the approaching future.

2.6.2 *ARV loaded electrospun fibers*

Electrospinning has served many iterations of researched HIV prevention methods. Along with the properties explored in section 2.6.1, physiochemically diverse agents can be encapsulated by electrospinning. ARV drugs, which can be very hydrophobic, have shown high drug loading capabilities in electrospun materials.[90,162] In application to HIV prevention, Huang, *et al.* developed electrospun cellulose acetate phthalate (CAP) to capture human seminal fluid. CAP was used for its innate anti-HIV properties and also shows potential for drug loading to eliminate vaginal HIV infection.[163] Hua, *et al*. iterated upon this platform via coaxial electrospinning, with CAP spun as a fiber core. Polyurethane is spun as the shell, reinforcing the materials for improved delivery.[164] Ball, *et al.* similarly showed the development of HIV preventative fiber formulations using rapidly dissolving polymers and the ARV maraviroc both by a single needle method[165] and co-axially.[166] Rapidly dissolving materials are important for serving on-demand protection. Longer acting materials could enable longer timeframes of protection. Sustained release of ARV agents

was achieved by Carson, *et al.*, who used hydrophobic polyester polymers for greater than 30 day dosing of TFV.[167] Electrospinning therefore shows potential to serve the fabrication of rapid and sustained drug delivery materials.

A composite ARV and contraceptive fiber system was developed by Blakney, *et al.*, which used the hydrophilic polymer polyvinyl alcohol to encapsulate the ARV tenofovir and the contraceptive agent levonorgestrel in layered methods, interwoven, and combined spinning.[168] This research illustrates the various modalities that electrospinning can dually protect against HIV and unintended pregnancies. The methods for this are shown in Figure 2.6, where agents can be co-formulated, co-electrospun, or potentially integrated onto existing contraceptive devices. In our example in Figure 2.6C, we illustrate possible physical wrapping of fibers onto existing devices such as the VeraCept® IUD.

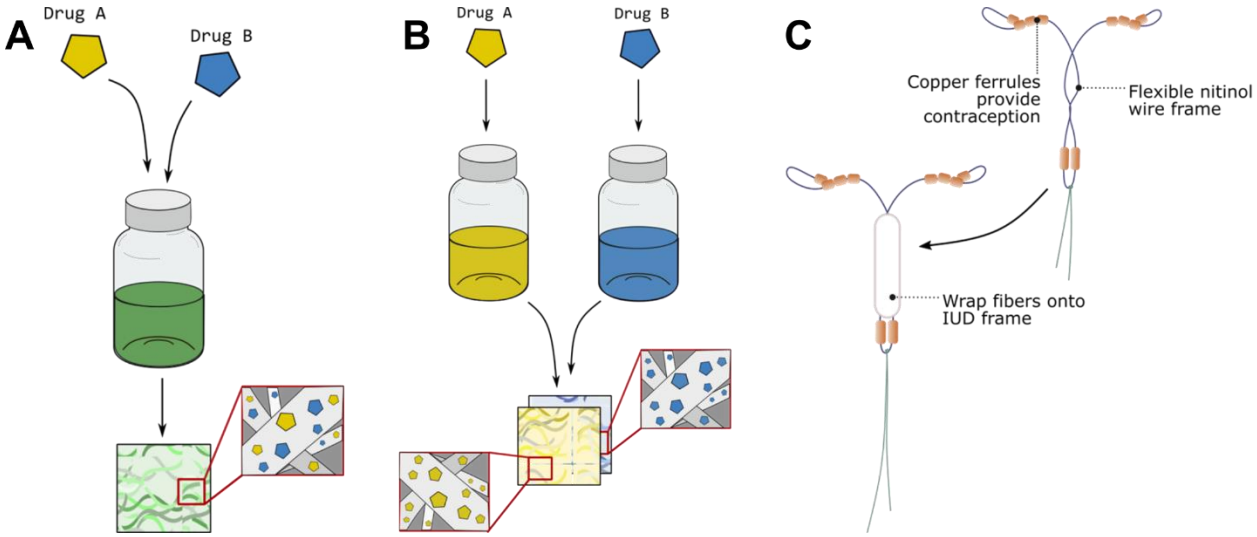

Figure 2.6. Diagram of potential methods of co-delivery of agents with electrospun fibers. *Methods outlined to create dual protective technologies from (A) electrospun mats with co-formulated agents, (B) separately formulated, but co-spun agents, and (C) physical integration of ARV loaded fibers onto existing devices, such as an IUD pictured.*

2.7 BIOCOMPATIBILITY IN RESPONSE TO POROUS MATERIALS

A modern definition of biocompatibility put forth by Crawford *et al.*, is "the ability of a material to locally trigger and guide the proteins and cells of the host toward a non-fibrotic, vascularized reconstruction and functional tissue integration."[169] The effect of material porosity on biocompatibility has been extensively studied, repeatedly showing that porosity improves tissue healing responses and decreases scar tissue growth.[113,131,132,170–176] Considering our tissue-specific focus here, we have broadened our definition of biocompatibility to consider the other factors which are critical to the success of the medical device. In addition to the FBR, we discuss biofilm formation and the nuanced impacts by porosity. Table 2.3 and Figure 2.7 includes a summary of porosity effects on the various aspects of biocompatibility discussed in this section.

2.7.1 *The foreign body reaction*

2.7.1.1 Protein adhesion

The FBR can be characterized by five phases.[169,170,177] First, local tissue and blood proteins will adhere to the material surface within an order of seconds following implantation. In this first phase, a provisional matrix is formed around the implant, including clotting proteins like fibrinogen, fibronectin, and vitronectin, as well as opsonins such as proteins belonging to the classical complement system pathway and immunoglobulins (IgG).[170,177] This provisional matrix develops rapidly into a thrombus composed mainly of fibrin.[170] The composition of the provisional matrix changes dynamically over time following the Vroman Effect, as proteins absorb and desorb on the surface.[169,170,178] Bioactive agents in the provisional matrix – including cytokines, growth factors, and chemoattractants – can promote the activation, migration, proliferation, and polarization of immune cells and fibroblasts, thereby impacting the subsequent stages of the FBR.[178]

Table 2.3. Summary of porosity effects on various features of biocompatibility

Response	Ideal pore size (μm or ↓/↑)	Ideal Porosity (Value or ↓/↑)	Model Tested	Ref
Reduction of fibrous capsule	30 - 40	↑	*in* vivo: C57BL/6 mouse percutaneous and subcutis, BAT-gal mouse subcutis, Sprague-Dawley rat abdominal wall	131,173,176,179–181
Macrophage polarization	M1: ≤20 or ≥60 (at surface), 34 (intrapore) M2: 30-50 (at surface), ≥360	M1: ↓ M2: ↑	*in vitro:* C57BL/6 mouse bone marrow-derived macrophages, human monocyte-derived macrophages *in vivo*: BAT-gal mouse subcutis	113,131,132,177,179,182
FBGC formation	<75	↓ for subcutaneous PU; ↑ for intramuscular PLA	*in vitro*: RAW 264.7 macrophages *in vivo*: BAT-gal mouse subcutis, male Wistar rat subcutis, male Lewis rat intramuscular	134,183,184
Angiogenesis	≥5, ~40	↑	*in vivo*: BAT-gal mouse subcutis, C57BL/6 mouse subcutis, male Wistar rat subcutis, Lewis or Sprague-Dawley rat subcutis and abdominal wall	117,131,134,136,169,177,180,181
Biofilm Prevention	15-25 × 10^{-6} for anodic surface, ≥100 for infection 14d after implantation	↓ for infection at time of implantation; ↑ for infection after implantation	*in silico:* extended Derjaguin and Landau, Verwey and Overbeek model in vitro: E. coli O157:H7, E. coli K12, L. monocytogenes, S. aureus, S. epidermidis *in vivo:* female outbred mouse subcutis with *S. aureus* injection, male Sprague-Dawley rat subcutis with *S. aureus* injection.	126,138,185–187

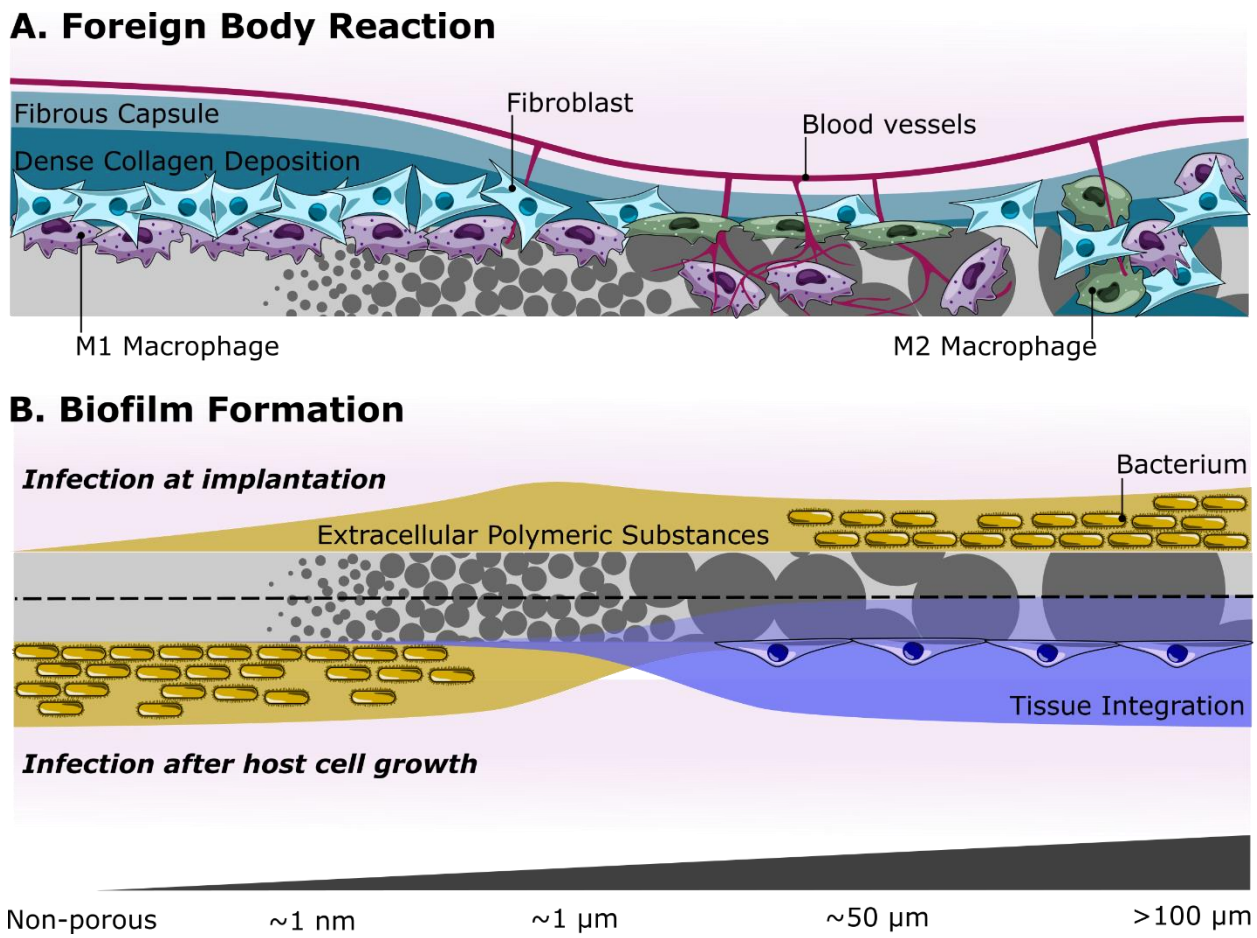

Figure 2.7. Schematics summarizing biocompatibility trends reported in respect to biomaterial pore size.

(A) In the FBR, non-porous materials induce thick fibrous capsule formation. Pores approximately 30-40 µm in diameter generate less of a capsule, greater angiogenesis, M1 macrophages within pores, and elongated M2 pores at the material surface. Larger pored materials generate mixed macropage populations and intrapore fibrosis.[113,131,132,177,181] *(B) If infection occurs at time of implantation, greater biofilm formation occurs in materials with larger pores, but also in pores which are small enough to permit bacterium yet size exclusionary to immune cells. However, larger pores also allow for faster tissue integration which inhibits biofilm formation if infection occurs after host tissue growth.*[138,186–188]

The magnitude of protein absorption is highly dependent on the type of material used, but is also increased by surface roughness.[170] Increased absorption is likely a factor of a greater surface

area to volume ratio.[189] Greater porosity can therefore induce greater protein adhesion as well as the specificity of proteins that adhere to the surface. Jansson, *et al.*, showed that titanium surfaces with pores between 0.2-0.3 μm absorbed two to eleven times more albumin and IgG than smooth titanium surfaces. While IgG may activate immune cells, albumin reduces platelet and neutrophil activation.[190] However, this effect is altered at the scale of protein-size, as was shown in a study by Richert, *et al*.. Nanoporous titanium surfaces with a mean pore diameter of 0.011 μm promoted fibrinogen, lysozyme, and human growth/differentiation factor-5 (GDF-5, osseogenic cell promoter) binding, and decreased absorbance of bovine serum albumin, IgG, fibronectin, and collagen as compared to non-porous surfaces.[191] The dimensions of IgG and fibronectin surpass this pore diameter, which likely explains this difference in absorption.[191]

Beyond pore size, the protein adhesion is also dependent on the geometry of the material walls or struts. Woo, *et al.* demonstrated that porous poly(L-lactic acid) (PLLA) scaffolds with nanofibrous walled pores (diameter = 0.05-0.5 μm) absorbed 4.2 times the protein compared with materials with solid walled pores (diameter = 250-420 μm). Additionally, these nanofibrous materials specifically absorbed greater quantities of proteins implicated in cell attachment including albumin, fibronectin, vitronectin, and laminin.[192] Stochastic roughness, which may be created from materials with random pore morphology, has shown to increase absorbance of fibronectin, an ECM protein that promotes macrophage attachment.[178,189] Although informative to understand early mechanisms of the FBR, studies of protein adhesion alone are conducted *in vitro*. These studies therefore exclude competitive protein binding dynamics that will have determining effects on immune cell signaling and the final host response.

2.7.1.2 Acute inflammation

Following protein adhesion, the FBR enters the second phase known as acute inflammation.[169,170,178] Neutrophils are the first immune cells to infiltrate the material surface and act as the primary cell population during acute inflammation, along with mast cells, for a period of hours or less than a week.[170,178] Tissue damage from implantation, recognition of the provisionary matrix, recognition of the foreign body and/or bacterial infection may initiate neutrophil migration.[169,170] Studies have rarely focused on the biomaterial impact on acute inflammation, therefore not much is known about the effect of porosity or topography on this phase.[170] One study by van Tienen, *et al.* distinguished the one-week acute inflammatory response towards materials with porosities of 73% or 86% – both with pores 150-300 μm in diameter but varied by the throat diameter. A similar magnitude of neutrophil infiltration was observed towards both materials, despite differences in tissue ingrowth at later timepoints.[193] These studies focused on quantifying cell accumulation, but additional information on the cytokine release profile by neutrophils may better inform the factors that recruit, activate, and direct macrophage phenotypes.[170]

2.7.1.3 Chronic inflammation and macrophage polarization

Chronic inflammation defines the third phase of the FBR, and persists for two to three weeks with notable local responses from macrophages.[170] Macrophages have been characterized as the primary arbiter of the FBR, and are activated by cytokine signaling and by adhesion to the provisional matrix. Activated macrophages are described to exists in two main polarization states: the pro-inflammatory M1 phenotype and the anti-inflammatory M2 phenotype.[169,170,177] M1 macrophages kill pathogens, activate T-cells, degrade ECM proteins, are implicated in T helper 1 cell (Th1) responses to intracellular pathogens, and are associated with a FBR that has greater

acute and chronic inflammation. M2 macrophages are further divided into M2a, M2b, M2c, and M2d phenotypes. All M2 subtypes are implicated in Th2 responses to extracellular pathogens, ECM synthesis, angiogenesis, and control over acute and chronic inflammation.[169,177,194] Although, M2b macrophages may also promote inflammation and M2d macrophages are implicated in wound healing as opposed to fibrosis.[194] Table 2.4 includes known inducers of these phenotypes, and factors which are secreted from these cell types.

These subtype delineations are known to be an oversimplification of macrophage behavior *in vivo*.[169,194] Additionally, absence or over-abundance of either pro-inflammatory and anti-inflammatory macrophages can lead to unfavorable FBR.[194] Beyond macrophages, cells of the adaptive immune system also play a role in the FBR.[179,195,196] Regulatory T-cells (Tregs) have been implicated in pro-healing responses. Th1 cells increase inflammation and inhibit collagen deposition, while Th2 cells induce fibrosis and inhibit inflammation.[179,195] Further, T-cells may act on macrophages and influence their polarization through the release of cytokines, or by antigen presentation.[195]

The macrophage response to porous materials has been extensively studied. Sussman, *et al.* characterized macrophage phenotypes in response to sphere templated poly(hydroxyethyl methyacrylate) (pHEMA) materials with either 34 μm or 160 μm pores as well as non-porous pHEMA. Inflammatory infiltrate was significant at the surface of non-porous implants but was minimal at the surface of either 34 or 160 μm porous materials. Within the fibrous capsule at the material interface, non-porous materials had M1 dominated responses, whereas porous materials had M2 dominated responses. Within the 34 μm pores, macrophages were more significantly M1 phenotypes, but were associated with greater vascularization and lower intrapore fibrosis. This distinction was not observed significantly in 160 μm-porous materials.[131] Sphere-templated

pHEMA pores 100 μm in diameter have also been found to induce greater gene expression for inflammatory Th1 cells in comparison to 40 μm pores.[179]

Garg, *et al.* used electrospun polydioxanone materials with randomly conformed pore diameters averaging approximately 2, 22 and 30 μm, which increase with strut diameter. Macrophages seeded onto materials with larger pore and strut diameters resulted in greater M2 macrophage attachment. Additionally, compressed materials with equivalent strut size, but reduced pore diameter, had reduced M2 attachment, indicating that the pore size is indeed the main contributor to macrophage polarization in these materials.[132] Using 3D printed polycaprolactone (PCL) box-shaped pores, Tylek, *et al.* illustrated that M2 differentiation is accompanied by macrophage elongation. Further, elongation is promoted with smaller, 40 μm pores.[113] The observations made from these studies are illustrated in Figure 2.7A.

Bartneck, *et al.* also studied the effect of electrospun porosity on macrophage polarization, and inversely found 20 μm porous materials induced more M1 polarization and 100 μm materials induced greater M2 polarization as measured by 27E10+ and CD165+ surface markers, respectively. However, the cytokine profiles suggest the 20 μm materials initiate greater pro-angiogenic signaling, while greater pro-inflammatory expression is measured in response to 100 μm materials.[197] These results are still consistent with the consensus of work, as signaling ques have the largest downstream effect on the FBR, and illustrates the over simplification of the polarization model for macrophages. Moving to even larger pore size, Yin, *et al.* found increased M2 polarization and VEGF expression in response to materials with 360-μm pores as compared to 160-μm pores.[182] Combined with existing research, this suggests that a window of unfavorable immune responses may exist for pore sizes around 100 – 160 μm. In studies of meshes with pore diameters ranging between 460 μm and up to 4000 μm, more favorable responses have been seen

with larger pores.[198,199] Pores larger than 1000 µm are said to prevent contact between filament associated inflammatory infiltrate, and therefore prevents the bridging of scar tissue.[199] However, the capability of having large scale pores is dependent on the three-dimensional thickness of the scaffold and the required mechanical properties. Overall, existing research suggests that despite difference in polymers, fabrication methods, and architecture, pore sizes approximately 30-40 µm in diameter yield greater pro-healing immune cell responses at the material surface, and have been further associated with greater vascularization, a reduced fibrous capsule, and greater tissue integration.[131,132,171–173,179,181,200–202]

2.7.1.4 Foreign body giant cell formation

The fourth phase of the FBR is foreign body giant cell (FBGC) formation. Multi-nucleated FBGCs form by the fusion of macrophages at the biomaterial surface.[169,170] This is a result of frustrated phagocytosis, where adherent macrophages attempt and fail to phagocytose the large implant, and is thought to be a mechanism to avoid apoptosis.[169,170,203] Cytokines IL-4 and IL-13 are implicated in FBGC formation and are considered to be derived from M2 macrophages, but distinctively express both pro-inflammatory and anti-inflammatory cytokines (Table 2.4).[170,194] Further, pro-healing growth factors, such as VEGF, are secreted by FBGCs,[204,205] as well as reactive oxygen species (ROS) and enzymes which contribute to material degradation and device failure.[170] The function of FBGCs in either a pro-healing or destructive FBR is not clearly defined, although these cell types likely contribute to both pathways depending on material features and time.[184,204,205]

In comparison to macrophage polarization, the relationship between pore size and FBGC formation is less consistent in the literature. Saino, *et al.* showed greater FBGC formation *in vitro* on PLLA non-porous films as opposed to electrospun nanofibrous and microfibrous materials.[183]

Similarly, a study of highly porous (~85%) sphere templated polyurethane (PU) materials by Bezuidenhout, *et al.* found significantly reduced FBGC formation on materials with larger pore diameters (150-180 μm) when implanted subcutaneously in rats.[134] However, Lucke, *et al.* showed greater FBGC formation on porous electrospun PLA mesh surfaces than non-porous membranes, which were implanted intramuscularly in rats.[184] At early timepoints, the macrophage populations within and surrounding porous materials are consistent with the observations made by Sussman, *et al.* describing high M2 populations at the surface and high M1 populations within pores. However, after 56 days, the FBGC response was seen to be greater towards porous mesh materials, as compared to smooth, membrane implant controls.[131,184]

The discrepancy in the FBGC response towards porosity across these different studies could be confounded by additional factors which may influence the FBR. First, pore size is not reported for PLA meshes with high FBGC adhesion, and highly porous PU materials with low FBGC adhesion are not compared to a non-porous control.[134,184] Therefore, a window of high FBGC adhesion may exists for porous materials with small void diameters, as is observed for macrophage polarization. Second, FBGCs effect degradable PLA and bio-stable PU differently, and the release of lactic acid from PLA materials is known to promote inflammation.[184] However, reported FBGC responses from other *in vitro* studies of PLLA contradict what is observed *in vivo* for PLA electrospun materials, although differences in chirality and resulting changes in polymer crystallinity may confound this comparison.[183,184] Finally, the difference in implant site may also contribute to FBGC responses. Indeed, greater inflammatory responses have been observed towards materials implanted intramuscularly, as compared to materials implanted subcutaneously.[206] Thus, the effects of porosity on FBGCs, and the effects of FBGCs on the FBR, are not simply positive or negative for wound healing. Future assessments to clarify the role of

porosity on FBGCs and the resulting FBR should consider additional factors like material and local tissue environment.

Table 2.4. Macrophage phenotypes, inducers, and secretion signatures

Macrophage Phenotype	Inducers [a]	Elevated Expression/Secretion [a]	Ref
M1	LPS, IFN-γ, TNF-α, GM-CSF	TNF-α, IL-1β, IL-6, IL-12, IL-23, ROi	169,177,194,207
M2a	IL-4, IL-13	IL-10, TGF-β, IL-1ra	169,177,194,207
M2b	IC, TLR, LPS	IL-10, TNF-α, IL-1, IL-6, RNi, ROi	169,177,194,207
M2c	IL-10, TGF-β	IL-10, TGF-β, MMP9	169,177,194,207
M2d	IL-6, Adenosine	IL-10, IL-12, TNF-α, TGF-β, VEGF-A	194,207
FBGC	IL-4, IL-13, MMP9	ROS, MMP9, IL-1α, IL-6, IL-8, TNF-α, IL-10, TGF-β, MCP-1, TIMP-1, TIMP-2, VEGF	170,178,194,204,205

[a] abbreviations: IL = interleukin, TNF = tumor necrosis factor, GM-CSF = granulocyte macrophage colony-stimulating factor, IFN = interferon, LPS = lipopolysaccaride, IC = immune complexes, TLR = toll like receptor, ROi = reactive oxygen intermediates, RNi = reactive nitrogen intermediates, ROS = reactive oxygen species, TGF = transforming growth factor, VEGF = vascular endothelial growth factor, MMP = matrix metalloproteinase, MCP = monocyte chemoattractant protein, TIMP = tissue inhibitor of metalloproteinases

2.7.1.5 Fibrous capsule formation, wound healing, and angiogenesis

In the final stage of the FBR, collagen rich scar tissue growth, known as fibrous capsule, commonly develops around biomaterials. In response to factors such as TGF-β released from cells

like M2 macrophages, fibroblasts migrate to the surface of the biomaterial and generate ECM proteins like collagen which forms the fibrous capsule.[169,170] Macrophages may also secrete other factors such as matrix metalloproteinases (MMPs), which degrade ECM proteins as needed for tissue remodeling at the implant site.[170,194] Biomaterials become encapsulated by this largely acellular tissue, which can act as a barrier in applications like drug delivery, sensors, or electrodes, and additionally can alter local tissue mechanics and therefore tissue function.[169] Further, fibroblasts may differentiate into myofibroblasts, which can contract the tissue surrounding the biomaterial, potentially causing patient pain and device damage.[169,170]

In contrast to fibrous capsule formation, the desired outcome for most implanted biomedical materials is to functionally integrate into the surrounding tissue environment. Beneficial wound healing responses promote the regeneration of local tissue cell types, and the ingrowth of new vasculature, known as angiogenesis, to support the transport of oxygen and nutrients into developing tissue.[117,169,170,208] Angiogenesis is especially important in biomaterial scaffolds for tissue engineering, where cells must functionally inoculate the material structure. Without supporting capillaries, oxygen and nutrients can penetrate a distance of approximately 150-200 μm.[117]

A reduction in fibrous capsule size in response to porous materials was first observed by Karp, *et al*., where a difference in FBR was demarcated between commercial Millipore filters with pores 0.025-0.1 μm and 0.22-8.0 μm. In the materials with larger pores, a less developed fibrous capsule was observed with cells found inside the pores, more non-adherent macrophages between the implant and capsule, and many FBGCs.[133] Cells have been found to penetrate materials with pores as small as 0.8 μm, but an increase in pore size up to 9 μm further promoted vascularization.[136]

Studies of larger pore-size materials have indicated that the benefit of increased pore size on pro-healing and angiogenic responses has an upper limit. Sussman, *et al.* found that porosity overall reduced fibrosis. However, materials with 34 μm pores were permeated by cells with minimal collagenous growth and a greater density of blood vessels, while 160 μm pores contained a greater fraction of fibrotic tissue.[131] In a study by Bezuidenhout, *et al.*, materials with pore sizes ranging from 63 to 180 μm showed no statistical difference in vascularization.[134] Overall, porosity and pore sizes approximately 30-40 μm in diameter significantly impact the acceptability of local tissue responses when studied in rodent models. Interestingly, this pore size is near twice the size of relevant cells – with rodent macrophages and fibroblasts measuring approximately 13 and 18 μm, respectively.[209,210] A summary of the effects from pore size on fibrous capsule formation and angiogenesis is illustrated in Figure 2.7A.

2.7.2 *Biofilm formation*

Biomaterials can also initiate adverse responses by creating a new niche for foreign pathogens within the body. Indeed, the bacterial colonization of medical devices, known as biofilm formation, is one of the most frequent complications of clinical biomaterial use.[188,211] While the host immune system might normally clear invading bacteria, the local fibrous capsule generated in response to the biomaterial creates an immune depressed environment, and bacterial colonies within a biofilm are protected by extracellular polymeric substances (EPS).[188,212] Thus, biomaterial surfaces can enable the persistence of bacteria like *Staphylococcus aureus* within the body that lead to device failure and chronic disease.[188]

Biofilms are formed through a cycle with four stages. First, motile bacterial cells adhere to the material surface.[188,212] Bacterial cells can adhere reversibly, with non-specific forces or irreversibly with specific interactions with lectin or adhesin.[188] Next, adhered cells form a colony

and secrete EPS. These bacterial colonies continue to grow and form into a mature biofilm, where cells can remain dormant until favorable conditions for infection arise. Dormancy, along with the colony structure, make biofilms characteristically resistant to antibiotics.[188,212,213] Finally, the biofilm disperses as aggregates or sessile bacterium to escape regions of accumulated bacterial waste and to start new regions of infection.[212]

Overall, implants with greater porosity have been implicated with a higher risk of biofilm formation. This is especially true for small-scale porous materials that may be size exclusionary towards leukocytes but not bacteria.[188] On titanium surfaces, Braem, *et al.* found greater bacterial adhesion to materials with pore sizes up to 150 μm or porosities greater than 15% because of greater surface roughness.[186] Antibiotic prophylaxis can reduce the risk of infection, as well as using materials surface modified with nonadherent properties, anti-microbial agents, or specific topographies.[188,213,214] Feng, *et al.* also studied the effect of pore size on biofilm formation towards alumina materials with 0, 15, 25, 50, and 100 nm pore diameters *in vitro* and via computational modeling. Materials with either 15 or 25 nm pore sizes were found to reduce bacterial attachment through repulsive forces from the densely packed vertical pore sidewall within the anodic surfaces.[185] This effect of porosity on bacterial attachment is therefore also dependent on pore geometry and chemical composition of the material.

The correlation between porosity and infection is not as simple when studied in complex biological systems. The “race for the surface” describes the competition between host tissue and bacterial communities for space on the implant surface.[154,214] Tissue integration is therefore one of the most effective mitigation strategies for biofilm formation.[154,188,214] Although porous mediums with large available surface areas can promote the adherence of biofilms, these porous materials also encourage tissue ingrowth, as described in section 2.6.1.

In an investigation of biofilm formation towards various dense and porous implants with 100 - 200 μm pores, Merritt, *et al.* found that porous materials were more susceptible to biofilm formation if the material became contaminated before or at the time of implantation. However, the porous materials were more resistant than dense materials if the infection occurred after 28 days, when the tissue had integrated into the material.[187] Sclafani, *et al.* assessed biofilm formation towards high-density polyethylene (PHDPE, Medpor) materials with pores 100 - 250 μm and ePTFE with internodal pore sizes ranging from 10 - 30 μm. For both materials, implants became infected when inoculated with *S. aureus* immediately following surgery. When inoculated 14 days after implantation, PHDPE materials with larger pores were found to be more resistant towards infection due to faster tissue integration. Other studies have shown tissue integration with ePTFE materials, so infection may not arise with these implants at later timepoints. Specific material composition may also confound the effect by pore size alone.[138] While porosity does increase the risk of biofilm formation, porous materials still provide benefits for tissue ingrowth which can decrease the risk of infection (Figure 2.7C). Therefore, surface treatments can be an effective strategy to control pathogen growth while still gaining the other advantages of biocompatibility that porous materials provide.

2.8 TISSUE SPECIFIC RESPONSES

As reiterated throughout this review, porosity can yield a more favorable host response, and many different methods exist to engineer biomaterials with precise porous architecture. Yet, medical devices are not always composed of porous materials. This is because various tissues have unique functions and necessitate different aspects of biocompatibility, which impacts the design requirements for materials attempting to achieve local homeostasis. Further, tissues have unique

microenvironments with different local immune cell populations that contribute to known variations in tissue specific host responses.[206,215–217]

2.8.1 *Subcutaneous implants for material study and clinical uses in drug delivery*

The subcutis exists as an adipocyte rich layer of tissue just beneath the skin surface, and primarily serves the body for thermal regulation, energy storage, and for protection from injuries.[14] Due to the presence of blood capillaries,[13] lymphatic plexus,[14] and the minimally invasiveness of accessing this compartment, the subcutis is widely used as a model to study the biomaterial FBR.[125,131,133,179,216,218–220] As detailed above (Section 2.7.1), porous materials with pore sizes approximately 40 μm in diameter show low fibrotic encapsulation, higher vascularization, and pro-healing responses from local immune cells, such as M2 polarized macrophages.[125,131,132,179,200,221]

The vascularization and peripheral location of the subcutis makes this tissue compartment ideal for long-acting drug delivery implants for applications such as contraception, treatment of schizophrenia, management of opioid addiction, and HIV prevention.[13,15,222–225] Subcutaneously implanted porous devices have also shown greater fibrotic encapsulation than devices implanted in the intraperitoneal space or the epididymal fat pad in mice.[215] Although porous materials demonstrate improved biocompatibility over dense, non-textured surfaces,[133] some subcutaneous drug delivery systems are intentionally designed with low porosity to reduce drug release rates, as described in Section 2.3.[226,227] Sustained, long-acting drug release is critical for implantable drug delivery systems to improve patient adherence compared to a frequent daily dosing schedule, and fibrous capsule formation can impede drug release.[13,169,219,228] Implant re-insertion is also not practical in a timeframe of approximately less than six months.[15] Biocompatibility is also essential for enabling patient compliance towards these drug delivery systems, as patients will discontinue use of elective devices that cause discomfort.

Contraceptive implants (section 2.3.2.2) – such as Nexplanon and its precursor Implanon, or Jadelle and its precursor Norplant – are the most widely used intradermal systems.[15,223] Nexplanon is a single cylindrical implant (2x40 mm) made of an ethylene vinyl acetate (EVA) polymer core loaded with the contraceptive agent etonogestrel and a drug-free EVA rate-controlling membrane, which has an effective duration of three years.[15,85,223,229] Jadelle is composed of 2 rods (2.5x43 mm each) that release the contraceptive levonorgestrel for up to five years within a polymer core and silicone rate-controlling membrane.[15,223] Information concerning the porosity and surface topography of these implants is limited. However, similar hot-melt fabricated, drug-free EVA membranes exhibit microtextured but non-porous features.[230–232] Additionally, silicone implants have been described as smooth and solid, as opposed to porous.[233] Therefore, surface features of these implants lack microporous features which are associated with improved healing responses. Although adverse reactions have been reported,[234] such contraceptive implants have largely proven to be safe and tolerable.[235] In a study of tolerability of both levonorgestrel and etonogestrel subdermal implants, López del Cerro, *et al.* found one non-tolerable case of a FBR, out of 221 implants, which resulted in implant expulsion.[235] In another assessment of local side effects of Norplant by Alvarez, *et al.*, 108 (35.6%) patients reported local hyperpigmentation of the skin, and 68 (22.4%) patients reported skin depression at the site of the implant due to a loss of subcutaneous tissue,[234] both which may be attributed to a FBR.[236]

A study of HIV preventative implants by Barrett, *et al.* indeed showed that dense implants created by hot-melt extrusion could achieve long-acting release of the investigational antiretroviral drug MK-8591 beyond 6 months. Interestingly, the implants became more porous over time, developing from the implant surface eroding into the core, with pores being created and increasing to ~2 μm wide with random geometry after full drug release. The mechanism of drug release was

therefore said to be mediated by solution permeation through voids evacuated by solubilized drug. The study does not include an assessment of the local tissue response.[226] In fact, another HIV implant study by Su, *et al.* describes overall lack of FBR assessment across other HIV implant studies, and reports an unacceptably adverse inflammatory reaction towards their tenofovir alafenamide fumarate loaded polyurethane membrane implant, despite lower inflammation observed against placebo implants.[237] Pharmaceuticals can contribute to adverse host responses, and therefore specific material and drug combinations must be assessed for their biocompatibility. Although porosity is not the sole arbiter of biocompatibility, material microarchitecture has shown to have a robust effect on resulting tissue outcomes and has been extensively studied in the subcutis. Therefore, surface features such as porosity – and the balance of its effects on pharmacokinetics and biocompatibility – should be considered in the development of safe, long-acting devices.

2.8.2 *Porous materials in the FRT*

Like the eye and brain, both the male and female reproductive systems are immune privileged. For both these reproductive systems, this privileged state is necessary to prevent immune recognition of haploid germ cells as non-self.[238–240] The FRT is especially interesting regarding the FBR, as tolerance towards paternal haploid cells, and embryos is required for fertility, and balanced tolerance towards the commensal vaginal microbiota is essential for general wellbeing and protection against disease.[240–242] Tregs are implicated as the primary mediator of this privileged state, especially during early pregnancy.[240,241] Ovarian steroids like estrogen and progesterone are known to regulate immune cell responses either directly or indirectly through cytokine signaling, and immune cell populations change temporally during the menstrual cycle.[240]

Other factors like MMPs are also known to change in response to the menstrual cycle and pregnancy, and contribute to the immune state of the FRT.[243,244]

The FRT is also interesting in the study of the FBR, as it is a common compartment for device placement – including tampons, diaphragms, and vaginal rings for drug delivery in the vaginal cavity, and contraceptive intrauterine devices (IUDs) in the uterus. Immune tolerance is observed towards medical implants like IUDs, which do not undergo fibrotic encapsulation, yet do induce inflammation as one mechanism of contraception.[245–248] However, intrauterine fibrosis can arise, and is especially studied in cases of fallopian tubal occlusion. The occurrence of tubal occlusion has been observed to occur under acute stimuli such as material and mechanical stress from permanent contraceptive devices such as Essure,[249] large and repeated administration of chemical sclerosing agents,[250,251] or by chronic *chlamydia tachomatis* infection.[250,252] Considering that tissue integration is uncommon in the FRT and even detrimental to tissue function, as well as the bacteria tolerant nature of the FRT, biofilm formation is perhaps the most significant risk against material biocompatibility. Device biofilm formation can promote pathogen proliferation in the FRT, and potentially inhibit drug release for devices like contraceptive vaginal rings.[212] Thus, porous materials can cause negative health effects when resident in the FRT.

Tampon use is a known risk factor for menstrual toxic-shock syndrome (mTSS).[253,254] Common use of extra-absorbent tampons starting in 1976 created a new niche for the common bacteria *Staphylococcus aureus* to interact with the human host environment, thereby contributing to the 1979-1980 epidemic of mTSS.[253,254] However, mTSS can arise without device use,[254] and reports of pessary use to treat uterine prolapse as early as the 19th century also describe possible cases of mTSS.[253] As a result of the porous structure which enables device absorbency, it is thought that a tampon with absorbed menses increases oxygen content within the typically anaerobic

vaginal environment. This can allow for *S. aureus* growth, which releases TSS toxin 1 (TSST-1).[254,255] TSST-1 binds to vaginal epithelial cells, which induces chemokine signaling to macrophages and CD4+ T-cells. Consequently, these immune cells release a cytokine storm which manifests as mTSS – causing fever, hypotension, gastrointestinal effects, and/or alterations in consciousness.[254] However, incidence of mTSS with tampon use is rare. Efforts to reduce mTSS cases have included a standardization for labeling device absorbency, as well as recommendations for reduced wear time and use of the lowest needed absorbency rating.[254]

The IUD Dalkon shield is another interesting case of the possible detrimental effects of porosity in the FRT. The Dalkon shield was clinically available from 1971 until 1974 and varied from other IUDs in its shield-like shape of the device body. Most importantly, the Dalkon Shield also uniquely had a porous, multifilament removal string, which was needed as the larger body of the device required greater force to remove.[256–259] Unlike other IUDs, which feature a monofilament removal string, the tail was found to wick bacterial species from the vaginal cavity into the uterus by capillary force.[256,257] Further, the small pore size between filaments excluded the passage of polymorphonuclear leukocytes through the IUD tail, so bacteria within the string remained protected against host immune responses.[257] In the United States, 11 deaths from generalized sepsis and 209 cases of septic spontaneous abortion were reported for women using the Dalkon shield, as well as a fivefold increase in pelvic inflammatory disorder cases as compared to other IUDs of the time.[256,259] Despite setbacks from this device, modern IUDs are safe and are the most effective contraceptive method available, with less than a 1% failure rate.[259]

Regardless of the history concerning porosity related health issues in the FRT, research on porous devices have been studied to address various FRT tissue disorders. Asherman syndrome is one uterine tissue disorder which causes abnormal endometrial tissue growth which causes the

lining of the uterus to adhere. One strategy to mitigate this tissue growth is the placement of a biomaterial barrier within the uterus, such as an IUD.[260–262] To improve local coverage, a compressible porous scaffold was developed by Cai, *et al.* and studied in an intrauterine adhesion rat model. Scaffolds enabled the delivery of basic fibroblast growth factor (bFGF), which together led to statistically equivalent endometrium and gland growth as undamaged uterine tissue, and greater neovascularization. However, the porous scaffold alone initiated low endothelium and gland growth, and higher fibrosis – all comparable to the intrauterine adhesion group.[261] The added growth factor therefore appears to be the main contributor to healthy endometrial regeneration, rather than the porous scaffold.

Surgical mesh is another example of porous material commonly used to provide tissue reinforcement. In the case of pelvic organ prolapse, where pelvic organs herniate into the vagina, reinforcement with transvaginal mesh was previously a solution. However, due to mesh erosion and material exposure from chronic inflammation and poor tissue integration, the use of transvaginal mesh – but not intra-abdominal mesh – is now banned countries like the United States, United Kingdom, and Australia.[263,264] Mukherjee, *et al.* proposes the use of ECM-mimicking electrospun meshes seeded with endometrial mesenchymal stem cells (eMSCs) to improve vaginal tissue integration. Although electrospun meshes with eMSCs promisingly increase gene expression associated with angiogenesis, cell adhesion, and ECM regulation, these implant studies were conducted subcutaneously due to limitations of mouse FRT size.[264] Therefore, these results are not truly indicative of the FRT response. Accurate models of the human FRT are limited, but the specific microenvironment is necessary to capture this nonstandard host response which has been frequently misunderstood in the past.

2.9 CONCLUSION

This review of the state of HIV prevention research confirms that current methods do not adequately serve young women. Although new female focused PrEP methods have been developed and clinically studied, these methods still fall short of practical use by young women world-wide. These clinical studies do give evidence that PrEP technologies would optimally provide protection if (1) the ARVs are topically delivered, (2) the woman has control over use, (3) the method requires low frequency of adherence, (4) the system could integrate with contraceptive methods, and (5) the system can be used discreetly. All these issues can be addressed by the development of novel biomaterials for drug delivery. Such novel DDS must be assessed for practical manufacturability, pharmacokinetics, and biocompatibility. In this thesis proposal we will investigate electrospun drug delivery vehicles, the capacity to manufacture multi-ARV loaded materials, achieve long-acting release as an implant, and study the resulting host response in the subcutis and FRT.

Chapter 3. SCALE-UP OF DRUG ELUTING FIBERS

Adapted from: Hernandez, J.L., Doan, M.A., Stoddard, R., Chien, S.T., Suydam, I.T., & Woodrow, K.A.. Scalable production of high basis weight and uniform drug eluting fibers by free-surface electrospinning. *In preparation.*

Supporting figures are available in Appendix A.

3.1 ABSTRACT

Electrospinning is a material fabrication method which has been extensively researched for pharmaceutical dosage forms, filters, and tissue engineered scaffolds. Despite this interest, electrospinning methods have failed to create high basis weight materials with consistent fiber deposition. Here, we show that free-surface electrospinning methods can generate materials with high throughput, high basis weight, and controllable deposition as relevant to scalable solid-dosage form production. Optimized free-surface electrospinning parameters, and the interaction of parameters, which significantly increase fiber throughput and disperse deposition were identified using design of experiments. Using the identified optimal settings – including a lower polymer concentration, higher carriage speed, larger orifice size, and higher electric field – fibrous materials could be generated at 12.9 g/hr. Fibers were observed to collect with a gaussian distribution, and the standard deviation factor of this distribution was measured to change dependent on the specific polymer formulation. Simulations of material collection utilized this mass distribution value to predict material collection with oscillating, dynamic movement of the spinning substrate. Dynamic spinning methods allowed for a larger collection area, greater surface density, and uniformity. Using simulated and experimental data, a defined region of consistent, 100 g/m^2 basis weight fiber deposition could be achieved dependent on the dynamic path length and specific polymer

formulation. Finally, these free-surface electrospinning methods were used to efficiently encapsulate three physicochemically diverse pharmaceutical agents, with less than a 10% coefficient of variation in mass or drug dosing across a representative sheet. These data provide new proof-of-concept potential for electrospinning to manufacture medical biomaterials.

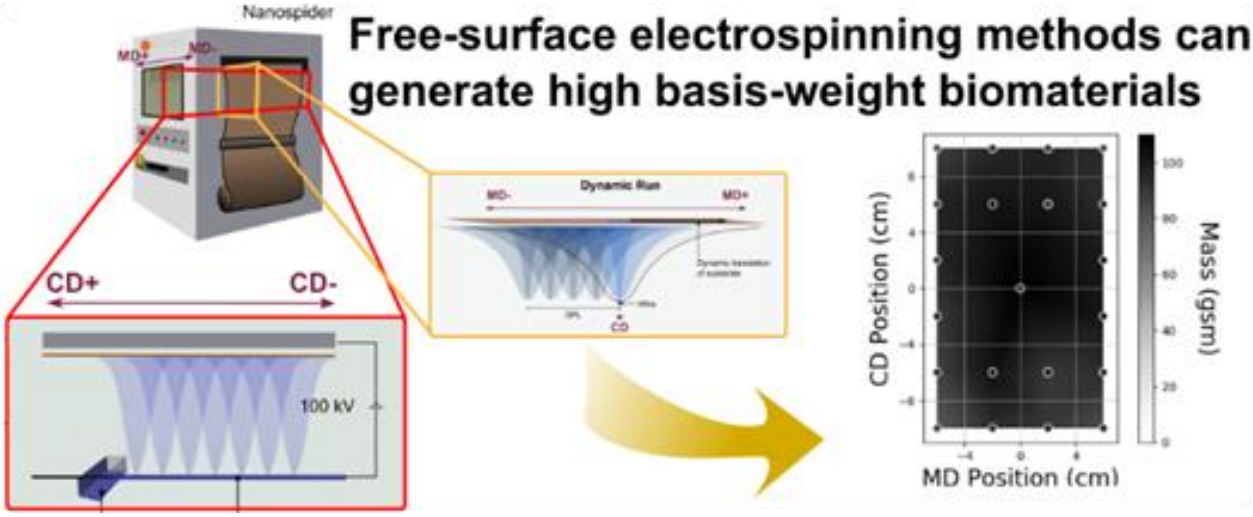

Figure 3.1. Graphical abstract for the scaled-up drug eluting fiber methods using free-surface electrospinning

3.2 INTRODUCTION

Nonwoven textiles have broad applicability for biomedical research. Electrospinning is a notable nonwoven fabrication method that shows high utility due to processing of versatile polymers, incorporation of physicochemically diverse agents, and control of fiber structures and topography such as size and alignment.[90,146,265–269] Due to these benefits, electrospun materials have been investigated for applications in drug delivery, tissue engineering, and diagnostics.[147,265,268–270] Within the drug delivery field, electrospun fibers have had significant clinical impact as wound dressings. In research, electrospinning has shown broad applicability for

topical drug delivery, including intravaginal solid dosage-forms for on-demand HIV protection[162,165,271] and contraception,[153,168,272,273] as well as a topical ocular glaucoma treatment to reduce dosing required by eye drops.[274] Drug-loaded fibers have also been investigated in oral drug delivery applications such as dissolving membranes for rapid dosing,[275,276] as a high-surface area vehicle for improving the release kinetics of insoluble drugs,[277,278] and as a pH responsive vehicle for the controlled delivery of biologics.[279]

Despite the simplicity and adaptability of electrospinning, sufficient productivity of these nonwoven materials remains a hurdle for practical translation.[270,280,281] Electrospinning is commonly conducted with low-throughput methods using a single charged needle containing the polymer solution and a negatively charged or grounded target for the materials to collect. This method therefore yields a relatively small area where the materials collect and a slow rate of material collection, reported to be only 1-100 mg/h.[282] Free-surface electrospinning improves material throughput by using a charged surface, like a wire or cylinder, coated in the polymer solution in place of the needle which allows for numerous polymer jets, or Taylor Cones, to form.[271] Industrial free-surface electrospinning equipment, such as the Nanospider™ by Elmarco, are therefore capable of productivity rates up to 278 g/h.[282] As compared to other nonwoven methods, electrospinning is reported to yield materials with a lower area density, with basis weight range of approximately 0.02-10 g/m^2 (gsm). [270,280,282] However, electrospinning remains the ideal method for creating fibers with the smallest diameters,[280] enabling high drug loading up to 60% of the total mass, encapsulating pharmaceutical agents with up to 100% drug loading efficiency, co-formulating various agents, and controlling agent release kinetics.[90]

Here, we establish a method for creating large scale, high basis weight nonwoven fabrics using free-surface electrospinning. In pursuit of scalable medical materials, we first optimized the

electrospinning parameters using design of experiments (DOE) which can assess individual factors and two-factor interactions that contribute to fiber throughput and deposition range. We additionally modeled the deposition consistency of the materials by controlling the dynamic movement of the collection substrate. Finally, we assessed the dosage uniformity of three physicochemically diverse antiretroviral drugs delivered within a throughput optimized excipient formulation. Additionally, we ambitiously demonstrate the capability for electrospinning to uniformly co-formulate multiple physicochemically diverse agents into a single dosage form without volatile solvents. The method described here yields the highest basis weight electrospun fibers for drug delivery to our best knowledge.[280,282–284] Through this investigation, we highlight the importance of optimizing materials using scalable fabrication methods to enable realistic translation of medical technologies.

3.3 Materials and Methods

3.3.1 *Materials*

Polymers polyvinyl alcohol (PVA, 87-90% hydrolyzed, Mw=30,000-70,000, Sigma Aldrich), polyethylene oxide (PEO, Mw=400,000, Scientific Polymer Products, Inc.), and polylactic-co-glycolic acid (PLGA, 50:50 L:G, carboxylate terminated, inherent viscosity =0.55-0.75 dL/g, Lactel Absorbable Polymers) were electrospun with either deionized water or hexofluoroisopropanol (HFIP, Oakwood Chemical). Antiretroviral (ARV) agents were purified using methods from Jiang, *et al.*, from tablets of Selzentry® (300 mg, ViiV Healthcare), Insentress® (400 mg, Merck), and Intelence® (200 mg, Janssen) for maraviroc (MVC), raltegravir (RAL), and etravirine (ETR), respectively.[94] Sieved Tenofovir (TFV, Particle Sciences, gift from

CONRAD) was used as obtained. Dimethyl sulfoxide (DMSO, BDH/VWR Analytical), acetonitrile (HPLC grade, Sigma-Aldrich), and potassium monophosphate (Fisher Chemical) were used for quantification.

3.3.2 *Methods*

3.3.2.1 Polymer formulation and characterization

Unless otherwise specified, PVA/PEO was formulated at 84:14 (w/w) PVA and PEO and 17.4% (w/v) in deionized water. Polymers were mixed using a stand mixer (Eurostar 20 digital, IKA) at 1000 RPM for 10 min, then 100 RPM overnight. PLGA fibers were electrospun from a 15% (w/v) PLGA solution in HFIP and mixed with a stir bar overnight. For drug loaded formulations, each agent was homogenized (T25 digital Ultra-Turrax, IKA) into the solvent prior to addition of polymer, at the specified loading percentage.

3.3.2.2 Free-surface electrospinning

All electrospinning was conducted using a Elmarco Nanospider (Liberec, Czech Republic) with an oscillating carriage spinning electrode. In this method, fibrous materials are generated from a polymer solution which is coated onto a wire electrode by an oscillating carriage. The carriage holds a reservoir filled with the polymer solution and coats the wire through an interchangeable orifice piece which the wire passes through. Solid fibers are formed from this solution by an applied voltage gradient across the wire electrode and collection electrode. The collection electrode is covered by the collection substrate to allow for simple collection of the material. This substrate can undergo dynamic movement during the spinning process.

Unless specified, solutions were coated onto the wire electrode through a 0.7 mm orifice at a rate of 350 mm/s. Additionally, the collection electrode was maintained at a distance of 200

cm, and electrospun across a 100 kV voltage difference. Chamber humidity was controlled at approximately 10% using compressed air. Industrial brown waxed paper (24" x 1500', 30 lb) was used as the collection substrate. Under static spinning conditions, the collection substrate remined stationary. Under dynamic spinning conditions, the collection substrate was translated at a rate of 155 mm/min. This movement oscillates over a defined distance, labeled to start (marker 1) and end (marker 2) directly above the wire spinning electrode, and continuously pass over this defined distance. A single pass is defined when the first marker labeled on the collection substrate and aligned directly above the wire electrode (Material direction (MD) axis=0), is translated until the second marker, at specified dynamic path length (DPL) away from the first marker, is aligned with MD=0. The next pass is performed with the reversed movement of the collection substrate until the first marker has returned to the starting position. Electrospinning was conducted until the center fiber mass reached a target basis weight of 100 gsm. This target was determined through periodic sampling of the center-most 4x4 cm fiber section, which was removed, weighed, and replaced for further spinning. Additional spinning time or pass number was then determined by linear interpolation.

3.3.2.3 Throughput, mass distribution analysis, and simulations

Throughput was measured by the mass of the fibers collected on the pre-weighed substrate divided over time. Samples of the fiber mats were collected with a 1 cm arch punch tool (7.85×10^{-5} m^2) at specified locations and weighed with a microbalance (Meddler Toledo). The value σ_s is determined from gaussian line fitting from n=5 samples which were collected across the carriage direction (CD) averaged at both edges. To determine gaussian line fits across the material direction (MD) of the fiber mat, statically spun materials were sampled. Using these gaussian line fits, simulations were created to model dynamic spinning conditions, where the spinning substate

translates to increase the collected surface area of fibers. In addition to gaussian line fit equations, simulations also accounted for the spinning substrate winding rate and approximate fiber deposition per pass. Simulations of mass deposition and correlations to measured mass deposition were conducted using MATLAB (MathWorks Inc., Natick, MA, USA, version R2019b).

3.3.2.4 Quantification of drug content using HPLC

Fiber samples were dissolved in DMSO at a concentration of 1 mg fiber/mL. Samples of the solutions were filtered with 0.22 µm syringe filters (Millex Durapore, Millipore) prior to quantification. High-performance liquid chromatography (HPLC, Shimadzu Prominence) was then used to measure the concentrations of the three drugs in tandem with a diode array detector (Shimadzu Prominence SPD-20A). Samples were analyzed at 35 ºC at a flow rate of 1 mL/min, and a gradient of 38 - 73% acetonitrile (ACN) and 25 mM monopotassium phosphate in water (KH_2PO_4 buffer) was used as the mobile phase. Specifically, the mobile phases begin at a ratio of 62:38 KH_2PO_4 buffer/ACN, then ACN increases to 73% of the mobile phase over 8 min, and then is returned to 38% by the end of the 20 min sample run. A C18 column (5 µm, 100 Å, 250 x 4.6 mm, Phenomenex Kinetex) is used as the stationary phase. Detection wavelengths and approximate retention times were 193 nm and 4.3 min for MVC, 300 nm and 7.1 min for RAL, and 234 nm and 15.3 min for ETR.

3.3.2.5 Statistical Analysis

DOE planning and analysis was conducted using StatEase Design-Expert (Minneapolis, MN, USA, version 9.0.4.1). Linear and gaussian line fits, as well as determinations of statistical significance were made using GraphPad Prism (San Diego, CA, USA, version 9). Significant differences were determined using repeated measured two-way ANOVA, or repeated measures

one-way ANOVA for overall drug loading comparisons, with Geisser-Greenhouse correction and with Tukey's multiple comparisons test.

3.4 RESULTS

3.4.1 *Assessment of electrospinning parameters on fiber throughput and distribution*

Free-surface electrospinning is amenable to scale-up, but the process has been used primarily in low-basis weight coatings for industrial filtration. Therefore, we first set out to optimize processing parameters for free-surface electrospinning that would achieve the high basis weight and uniformity required for pharmaceutical manufacturing of biomedical materials. Design of experiments (DOE) was used to efficiently identify process and solution parameters that would significantly affect fiber yield and distribution (Figure 3.2A). Factor inputs included two polymer solution variables: polymer concentration (0.174-0.196 g/mL) and drug loading of a model agent tenofovir (0-28.57%, or 0-10M). We also investigated the effect of four process variables: speed of the carriage that coats the polymer solution onto the charged wire (125-250 mm/s), distance between the charged spinning wire and oppositely charged spinning substrate (180-220 mm), applied electric field (0.35-0.45 kV/mm), and size of the orifice which coats the polymer solution onto the charged wire (0.6-0.8 mm). The specific polymer formulation used for parameter optimization was composed of PVA and PEO. These polymers were selected due to their hydrophilicity and relevance to rapid drug release. The specific 84:14 ratio of PVA to PEO was determined via hill-climbing optimization.[285]

Electrospinning experiments with the specified factor input settings were performed on an Elmarco Nanospider (Figure 3.2B). The location of the collected material was defined with respect

to the carriage direction (CD) and the material direction (MD) of the instrument. CD is defined as the axis parallel to the wire spinning electrode, where the carriage translates across to re-coat the wire with polymer spinning solutions (Figure 3.2B). MD is perpendicular to the CD-axis and defined as the direction in which the electrospinning substrate is translates. We determined that a scalable method for producing medical materials will require dense and uniform accumulation of material within a reasonable time frame. As such, we focused on fiber throughput (units of g/m^2, or gsm) and fiber distribution measured along the CD-axis (σ_s, in cm) (Figure 3.2 C&D).

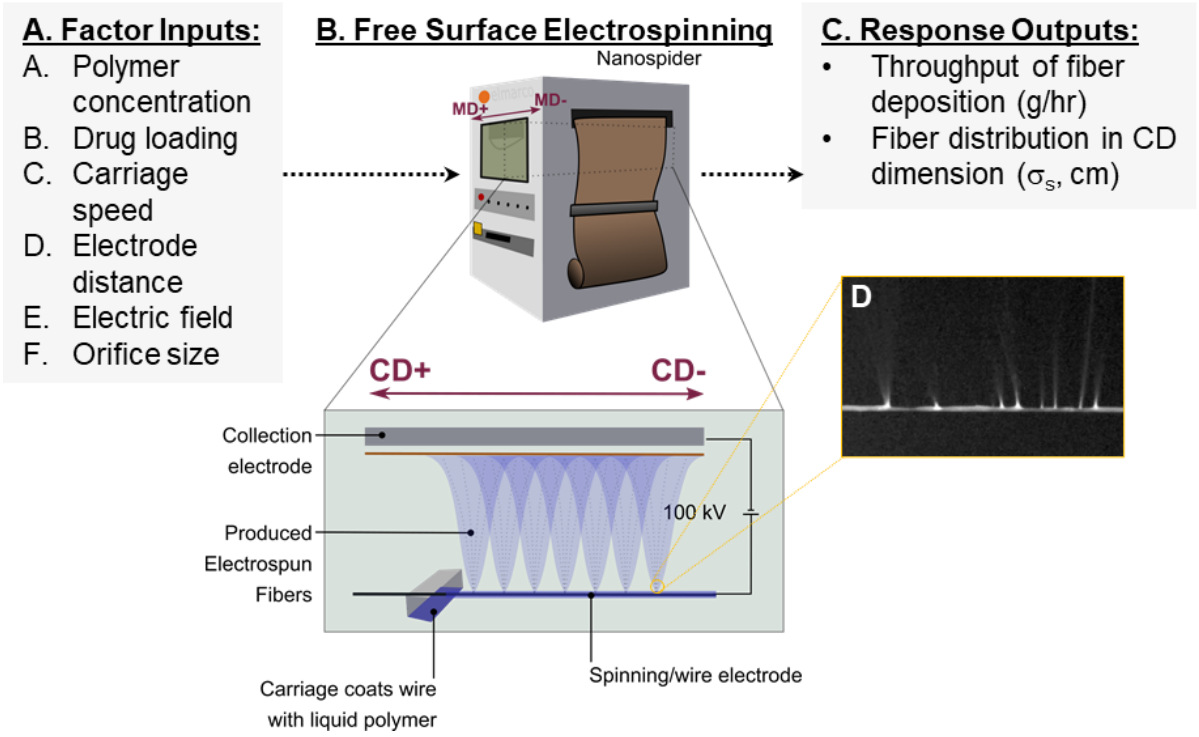

Figure 3.2. Design of experiments (DOE) is employed to assess free-surface electrospinning parameters.

Parameter diagram for the (A) DOE investigated settings adjusted for (B) free-surface electrospinning, and (C) investigated for responses in fiber production. (D) An image of the charged wire shows the liquid polymer jets which form the collected solid fibers.

Carriage speed, polymer concentration, orifice size, and electric field all significantly impact fiber throughput (Figure 3.3A, Appendix A Figure A.1A). Indeed, low polymer concentration, high carriage speed, larger orifice size, and high electric field yielded the greatest throughput of 12.9 g/hr. Fiber distribution was most significantly affected by carriage speed, electric field, and electrode distance (Figure 3.3B, Appendix A Figure A.1B). With a high carriage speed, high electrode distance, and low electric field, the greatest σ_S value of 5.11 cm was achieved. Several two-factor interactions showed to significant effects on the throughput and distribution response outputs (Appendix A Table A.1 and Table A.2). Throughput significantly increased with the interaction of increased drug loading and decreased polymer concentration (Figure 3.3C), decreased polymer concentration and a higher carriage speed (Figure 3.3D), as well as a higher carriage speed and larger orifice (Figure 3.3E). Several two-factor interactions were found to significant effect σ_S (Appendix A Figure A.1B and Table A.2). The σ_S value increased with interactions between low polymer concentration and high carriage speed (Figure 3.3F), as well as a decreased electric field and larger electrode distance (Figure 3.3G). We conclude that the optimal spinning parameters for our experiment would have a lower polymer concentration (0.174 g/mL), higher carriage speed (250 mm/s), an electrode distance of 200 mm, an applied 100 kV voltage difference, and an orifice size of 0.7 mm. Since the electric field had opposing impacts on throughput and distribution, we opted to use a higher electric field to prioritize productivity and compensate for deposition consistency by controlling substrate movement.

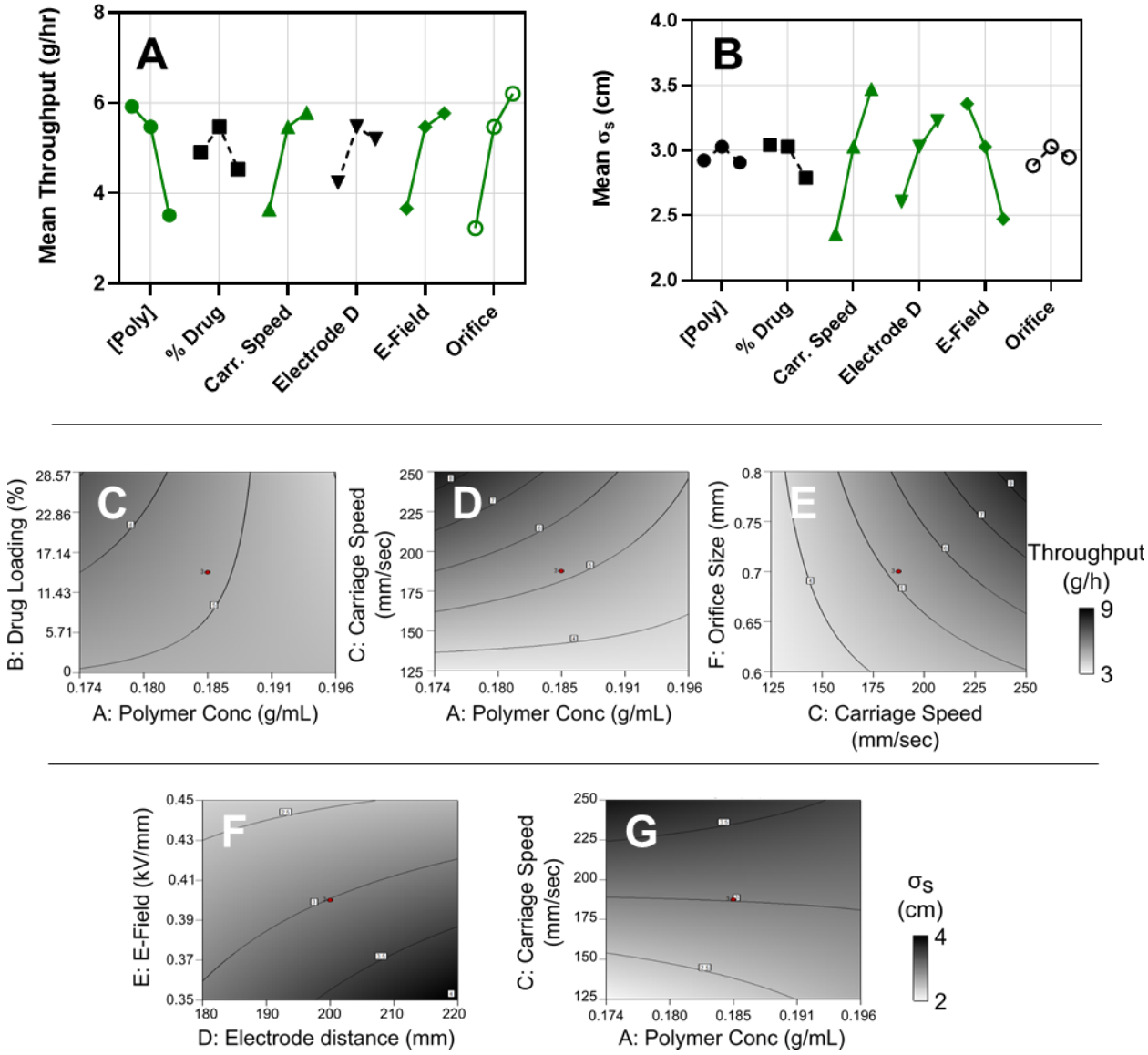

Figure 3.3. Electrospinning settings and the interaction of parameters control fiber throughput and distribution patterns.

Plots of the mean effect from all factors on (A) throughput and (B) σ_s. The significant factor interactions that impact throughput are additionally shown in the contour plots for (C) drug loading vs polymer concentration, (D) polymer concentration vs carriage speed, and (E) carriage speed vs orifice size. Contour plots for the interactions that most impact σ_s are shown as (F) polymer concentration vs carriage speed, and (G) electric field vs electrode distance.

3.4.2 *Dynamic substrate movement for controlling uniform fiber deposition*

Free-surface electrospinning supports greater scalability of fiber production due to the higher density of fiber jets and adaptability for roll-to-roll processing. We took advantage of the ability to control the movement of the collection substrate along the MD axis to obtain high-basis weight and uniform materials. By controlling the residence time and substrate movement relative to the electrospinning wire, we could precisely tune fiber collection in specific areas. Figure 3.4 A&B illustrate the difference in fiber deposition under spinning conditions with a static or dynamic collection substrate, respectively. We hypothesized that longer residence times achieved by repeated "passes" of the collection substrate across a specified dynamic path length (DPL) could increase the basis weight or accumulation of fibers across a larger area. Here, we define the DPL as the distance of the collection substrate that repeatedly and directly passes over the wire spinning electrode (Figure 3.4B). In addition to the polymer blend previously optimized for fiber throughput, we assessed a polymer solution composed of 15% (w/v) PLGA in HFIP. We selected this material for the differential use of an organic solvent, common use of HFIP with electrospinning, and the common use of PLGA in biomedical applications. We expect the use of these different polymer solutions illustrates the resulting differences in electrospinning, as well as the general application of these simulations as a tool to account for differences in fiber deposition.

Electrospun fibers collect with variable deposition along the MD and away from the spinning electrode, as seen under static spinning conditions (Figure 3.4A). For a fixed position on the CD-axis, electrospun fibers were found to deposit with a gaussian distribution across the MD-axis, centered at the wire spinning electrode (MD=0 cm). Simulating material deposition can therefore inform necessary electrospinning parameters needed to achieve defined areas with

consistent fiber basis weight. Therefore, the resulting fiber basis weight (A, in gsm) as a function of MD position (x_{MD}, in cm) under static conditions can be described in the equation below [3.1].

$$A(x_{MD}) = A_{Target} e^{-\frac{1}{2}\left(\frac{x_{MD}-\mu}{\sigma_{MD}}\right)^2} \quad (3.1)$$

The maxima of fiber deposition is equivalent to the target fiber basis weight (A_{target}), which we set to 100 gsm, and controlled for during electrospinning by periodic sampling of the centermost 4x4 cm square of material. Due to this method for controlling material deposition, samples with coordinates at the edge of this testing region (MD=±2 cm, CD=±2 cm) could not be accurately collected. We additionally maintained center coordinates during dynamic electrospinning such that the MD position of the mean basis weight (μ) is equal to zero. Most interestingly, we found that the standard deviation of this Gaussian fiber-mass distribution (σ_{MD}, in cm) – or the spread of fiber deposition across the MD-axis – varies based on the polymer formulation. Under static electrospinning conditions, the observed spread of fiber deposition was found to be smaller, or narrower, for PVA/PEO (σ_{MD} = 3.787 cm) than PLGA (σ_{MD} = 6.443 cm) (Figure 3.4 C, Appendix A Table A.3).

It might be hypothesized that a formulation with a larger σ_{MD} value, and therefore wider fiber distribution, may yield fiber mats with a larger region of consistent fiber deposition at the target basis weight under dynamic electrospinning conditions. However, fiber deposition simulations do not reproduce this expectation. Simulated data was produced using the expression below [3.2] where p is the pass number of the substrate above the wire electrode, DPL is defined as the difference of the starting position ($l_{p,st}$) and the ending position ($l_{p,ed}$) centered at MD=0, r_{sub} is the rate of substrate movement (155 mm/min), t_{stat} is the time to 100 gsm determined from the static run, and k is the step in MD position away from the center of the wire electrode. With a shorter DPL such as 12 cm, the PVA/PEO formulation with the lower σ_{MD} indeed yields a fiber

sheet with a smaller uniform area than the PLGA formulation (Figure 3.4D). However, DPLs approximately 16 cm and larger can be seen to have a larger uniform area for formulations with a lower σ_{MD} compared to higher σ_{MD} values (Figure 3.4 E&F). This is because the target 100 gsm basis weight is controlled for in all materials at the center of the mat. Therefore, as the path becomes increasingly large, formulations with larger σ_{MD} values achieve the target basis weight at the center with fewer passes, and have a shorter electrospinning time for fibers to accumulate.

$$\max_{p=1}\left\{p \times \sum_{k=l_{p,st}}^{l_{p,ed}} \left(\frac{1}{r_{sub} t_{stat}}\right) A_{Target} e^{-\frac{1}{2}\left(\frac{x_{MD}-k}{\sigma_{MD}}\right)^2}\right\} \leq 100\ gsm \qquad (3.2)$$

Simulations proved to be a useful tool for predicting fiber deposition patterns of different polymer formulas, and especially the region in which mass deposition plateaus. We found experimental data to be highly correlated to simulated dynamic run data, with high correlation coefficient (r) (Appendix A Table A.3). Additionally, in plotting experimental data versus the simulated data (Appendix A **Figure A.2. Linear relationships between simulated and experimental results show that mass deposition patterns can be roughly predicted.**Figure A.2), we found the relationship to be highly linear with coefficient of variation values also near to 1 (Appendix A Table A.3). Quantile-quantile (QQ) plots also indicate that the distributions of simulated and experimental data are comparable, as seen by linear relationships of plotted quantile values individually comparing PVA/PEO and PLGA formulations under 12 or 16 cm dynamic run conditions (Figure 3.4 G&H).

While we conclude these simple simulations can be predictive of actual material deposition, some discrepancies do exist between the theoretical and observed data. These differences may be due in part to the manual method of controlling electrospinning time to achieve the target basis weight, or from the underlying inconsistency of electrospun fiber deposition in this process format.[280,286] Root mean square error (RSME) measurements between the experimental

and simulated results show that the error is relatively consistent between the tested formulations and dynamic path lengths, except for 16cm dynamic run PLGA results which have comparatively lower error (Appendix A Table A.3). Despite some error, formulation-specific simulations are a valuable tool to determine the required electrospinning parameters needed to achieve the desired area of material at the target basis weight. The methods are especially informative in ensuring sufficient production of drug dosages or devices, while minimizing material waste.

While fibers deposit with gaussian distribution across the MD axis, centered at the wire electrode, the same pattern is not observed across the CD axis. Fibers are generated across the length of the wire (Figure 3.2B), and therefore the deposition is relatively linear across this length when measured at fixed MD positions (Figure 3.5). Further, the linear deposition has a near-zero slope. For all linear line fits of mass deposition versus CD position at fixed MD positions, slopes do not significantly deviate from zero with the exception at MD = -4 cm for the PVA/PEO 16 cm dynamic run and for MD = -6 cm for the PLGA static run. Inconsistencies in this linear trend are especially observed for MD cross-sections furthest from the wire, as seen by low basis weight values for samples collected for MD=6 or 8 cm at CD=0 for PVA/PEO 16 cm dynamic run (Figure 3.5B). This is likely due to sampling outside of the uniform area, where mass deposition dramatically decreases (Figure 3.4E). Plots of fiber surface density across the CD-axis further illustrate the differences in spread between the two formulations under static conditions, as seen by the differences in the spread of y-intercept values (Figure 3.5 A&C). Improved consistency under dynamic electrospinning conditions can also be observed as measured by the reduction in y-intercept range in comparison to statically electrospun materials (Figure 3.5).

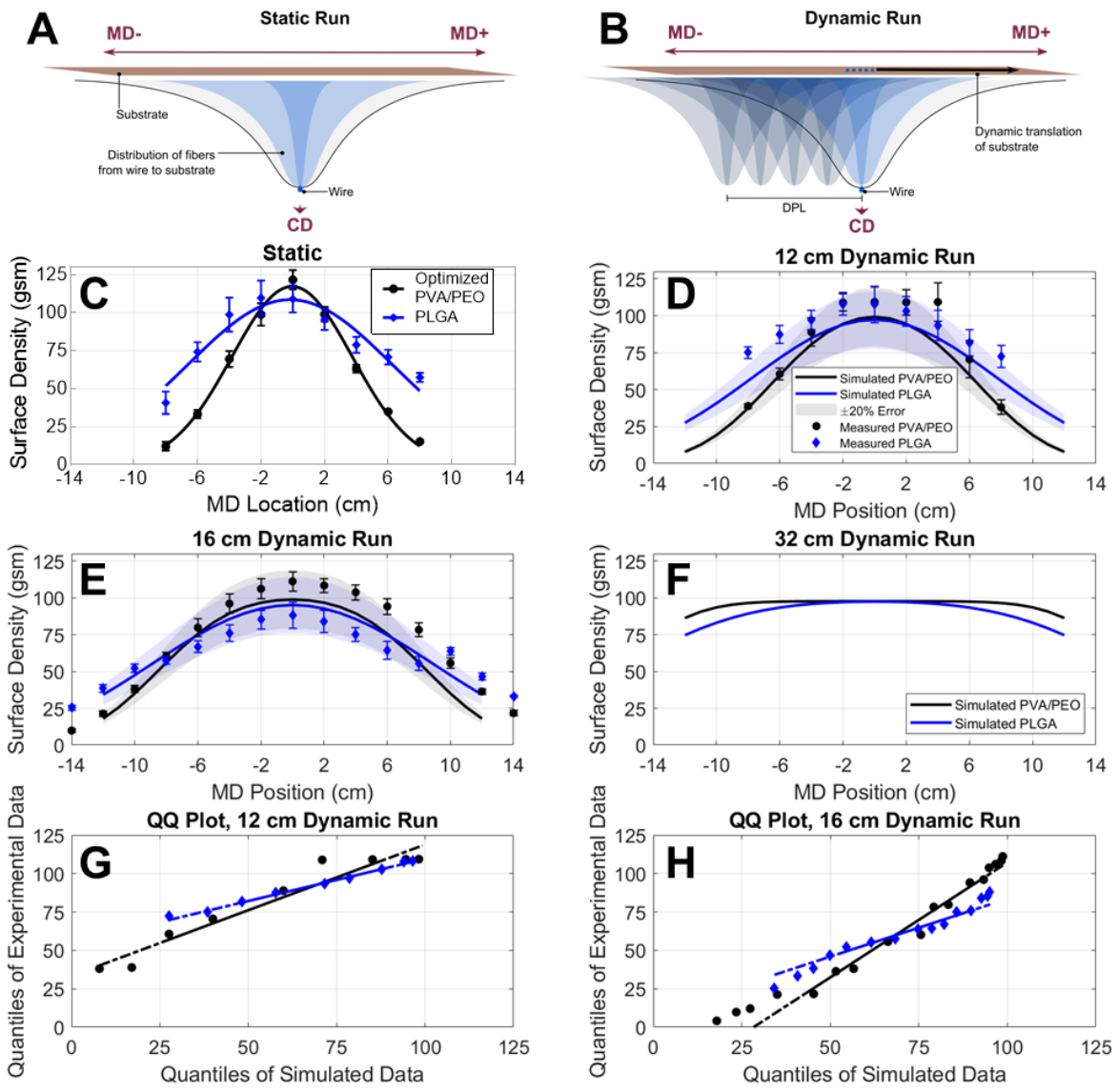

Figure 3.4. Sensitivity of mass distribution to dynamic path length (DPL).

Figures of (A) a static substrate (static run) shows the gaussian distribution of fiber mass across the MD-axis and (B) the collection of fiber mass distribution under substrate movement (dynamic run). (C) Measurements of the surface density of static run fibers could be fit with a gaussian model. The distribution of surface density for dynamic runs with DPLs of (E) 12 cm and (F) 16 cm was captured with simulated and measured data. (D) Simulated dynamic runs with a longer, 32 cm DPL demonstrate the production of larger areas of consistency. Experimental samples are plotted as average ± standard deviation and were measured across n=1 sheet of material and n=4-5 samples collected at CD=-8, -4, 0, 4, and 8 cm. QQ plots for (G) 12 cm and (H) 16 cm

(Figure 3.4 continued) dynamic runs show linear relationships indicating similar distributions between simulated and experimental data, with lines representing the full theoretical distribution and with solid regions connecting the first and third quantiles of data.

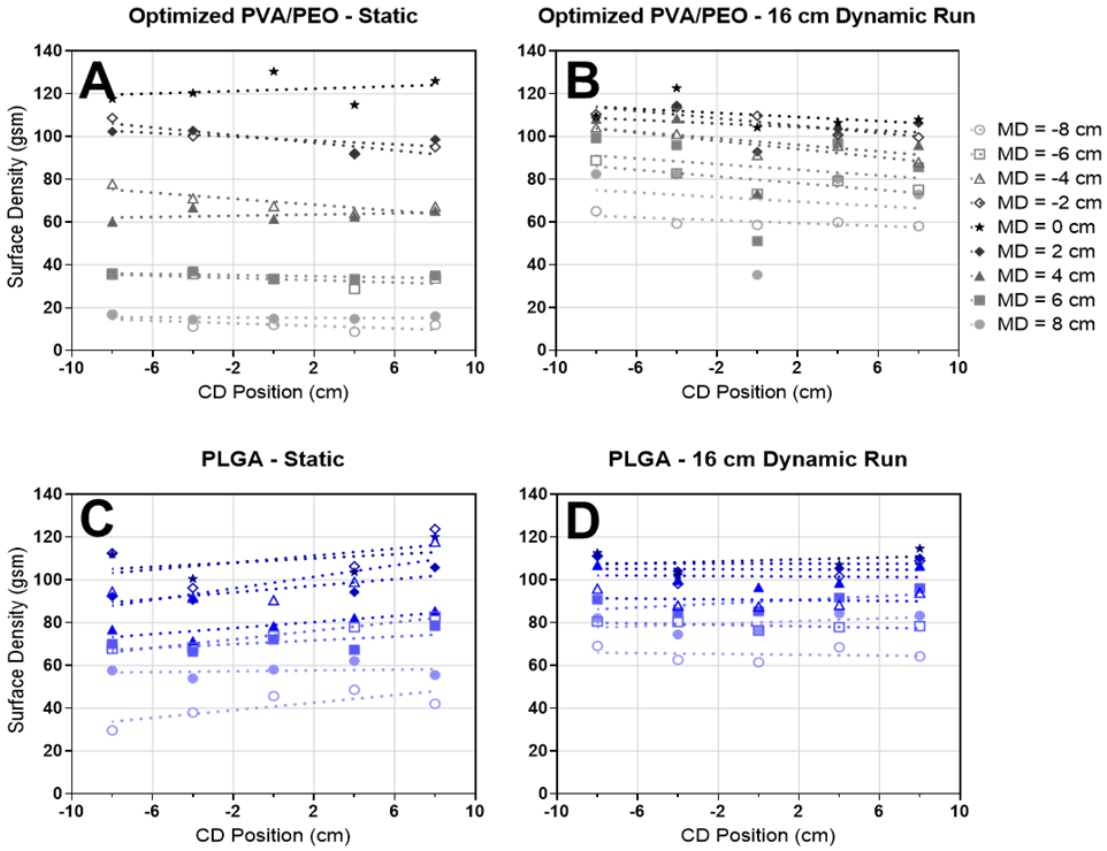

Figure 3.5. Fiber deposition is relatively linear across the CD-axis.

Measured surface density from samples taken from the (A & B) optimized PVA/PEO formulation and (D & E) PLGA fiber mats, spun under (A & D) static and (B & E) 16 cm DR conditions.

3.4.3 *Drug uniformity across the sampling area*

Pharmaceutical solid dosage-formulation and agent delivery is one promising application for electrospun biomaterials. Scalable methods of electrospinning would be required for the

generation of multiple dosages across a single fiber mat. Further, materials with high basis weight could deliver larger dosages within a smaller material area. We therefore sought to assess the uniformity and encapsulation efficiency of physicochemically diverse pharmaceutical agents within these high basis weight materials. Here, we use three different pharmaceutical agents as model drugs: maraviroc (MVC), raltegravir (RAL), and etravirine (ETR). These drugs are all antiretroviral agents, but have differences in water-solubility ranging from 53.9 mg/mL,[287] 0.011 mg/mL,[287] and 0.00397 mg/mL[288] for RAL, MVC, and ETR, respectively. These drugs also have a range of reported partition coefficients (logP) of 4.3 for MVC,[289] 0.4 for RAL,[287] and >5 for ETR.[288] Therefore, we expect these agents to represent an interesting challenge for formulation consistency. We prioritized using the optimized PVA/PEO formulation, which are common excipients in many drug delivery systems and where drug dissolution is nearly instantaneous following contact with water. Each drug was loaded into the polymer solution at 5% (w/w), representing a total 15% (w/w) theoretical drug amount within the fibers. Since the target basis weight is 100 gsm, full encapsulation of drug is theoretically equivalent to 5 gsm for each ARV drug. Measurements of percent drug loading approximates drug basis weight but is not necessarily equivalent. We hypothesized that dynamic, free-surface electrospinning could yield multi-drug loaded materials that had uniform basis weight across a defined target area, determined through simulation, and therefore uniform drug basis weight from a single batch process.

Using simulated data, we selected a DPL of 20 cm to create a minimum, proof-of-concept 4 cm MD by 20 cm CD area of fiber uniformity (Figure 3.6A). The measured mass distribution across multiple replicate fiber sheets correlates to simulated 20 cm dynamic run results (Sheet 1: Pearson r = 0.976; Sheet 2: r = 0.981; Sheet 3: r = 0.971) (Figure 3.6A). This electrospinning method also proved to be capable of efficiently formulating the three agents into a solid dosage-

form, with an average loading efficiency across all measured samples of 82% for MVC, 71% for RAL, and 97% for ETR (Figure 3.6B). Although highly efficient, specific drug loading is significantly different for the three agents. These differences indicate that hydrophobic drugs formulate more efficiently in this particular formulation. In the predicted uniform area, there is also no significant variation in fiber mass or specific drug loading dependent on location (ex. Center (MD=0, CD=0 cm) versus corner (MD=2, CD=10 cm)), as determined by comparing averaged replicate values of coordinate defined replicate samples (all $p>0.16$). Therefore, dynamic free-surface electrospinning can produce uniform drug-loaded materials at the target 100 gsm basis weight.

Representative maps of fiber and drug basis weight distribution are shown for a region encompassing the defined target area and surrounding region within 10% of the simulated target 100 gsm basis weight (Figure 3.6 C-F, all distribution maps are shown in Appendix A Figure A.3). Some differences in fiber basis weight and drug loading can be observed for each measurement, however these maps show an overall homogeneity in fiber mass and in each drug across each fiber sheet (Figure 3.6 C-F). While some regions of low drug basis weight may be due to overall reduced mass (Appendix A Figure A.3 A-D), mass is not the only driver of drug variation. In some locations, lower drug loading appears to be independent of overall mass deposition (Appendix A Figure A.3 E-F). Further, some maps indicate lower drug loading across all samples from sheet (Appendix A Figure A.3D). However, all measured differences are minimal as determined by a coefficient of variation (CV) of less than 10% for all measurements in the representative fiber mat, and less than 15% for drug measurements in all other replicates (Table 3.1). These data show the capabilities of the electrospinning process to generate multiple, uniform, and high basis weight solid dosage-forms from a single process.

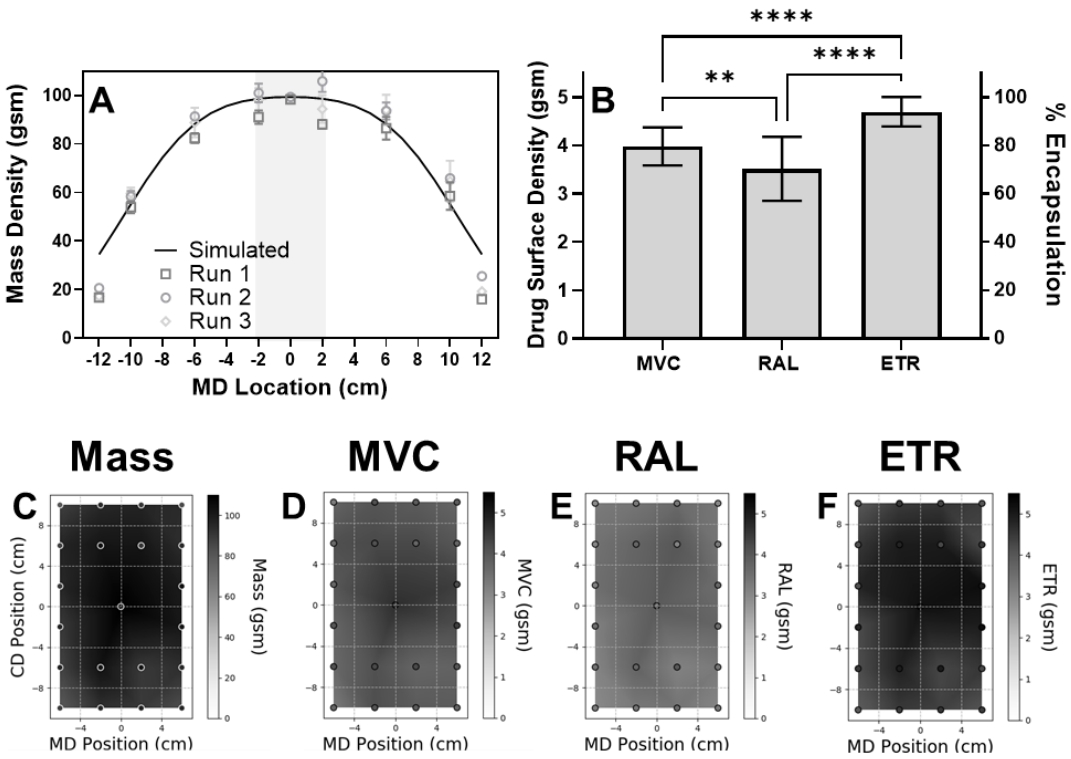

Figure 3.6. Optimized drug-loaded PVA/PEO fibers deposit without location-based defects in the simulated consistent zone, and with efficient loading of various physiochemically diverse drugs.

*Plots of (A) fiber basis weight and simulated data. Multi-drug consistency across the material is shown for (B) drug loading in the consistent region across all replicates (n=3 fiber mats, n=9 samples). Representative maps (sheet 3) of linearly interpolated (C) mass, and the co-formulated drugs (D) MVC, (E) RAL, and (F) ETR show fiber and drug basis weight across a representative 20cm dynamically spun fiber mat. Statistical significance is represented by **: $p<0.01$ and ****: $p<0.0001$.*

Table 3.1 Mass and drug loading averages across a fiber mat and between fiber mat replicates

	Fiber Sheet 1	Fiber Sheet 2	Fiber Sheet 3	Overall
Fiber Mass (gsm)	90.57 ± 3.83	103.0 ± 4.53	97.76 ± 6.81	97.11 ± 7.21
Range (gsm)	85.7- 98.3	96.9-111.5	89.6 -110.1	85.7-111.5
Range in % Error from Target	-14.3 – +1.7	-3.1 – +11.5	-10.4 –+10.1	-14.3 – +11.5
% CV	4.231	4.393	6.967	7.429
MVC Loading (gsm)	3.88 ± 0.24	3.95 ± 0.58	4.11 ± 0.58	3.98 ± 0.39
MVC Range (gsm)	3.55 – 4.26	2.89 – 4.55	3.72 – 4.65	2.89 – 4.65
Range in % Error from Target	-28.9 – -14.8	-42.2 – -8.9	-25.6 – -7.0	-42.2 – -7.0
% CV	6.312	14.74	6.458	9.883
RAL Loading (gsm)	2.74 ± 0.19	4.22 ± 0.27	3.59 ± 0.29	3.52 ± 0.66
RAL Range (gsm)	2.46 – 3.07	3.83 – 4.63	3.14 – 4.00	2.46 – 4.63
Range in % Error from Target	-50.8 – -38.6	-23.4 – -7.5	-37.2 – -19.9	-50.8 – -7.5
% CV	7.012	6.294	8.050	18.83
ETR Loading (gsm)	4.66 ± 0.25	4.75 ± 0.36	4.68 ± 0.32	4.70 ± 0.30
ETR Range (gsm)	4.27 – 5.01	4.23 – 5.25	4.28 – 5.16	4.23 – 5.25
Range in % Error from Target	-14.7 – +0.1	-15.3 – +4.9	-14.4 – +3.3	-15.3 – +4.9
% CV	5.381	7.620	6.750	6.461

Target values are equal to 100 gsm for mass and 5 gsm for each drug.
Mass and drug measurements reported as average ± standard deviation.
Range values reported as min – max.
% CV = coefficient of variation.
All values determined for just the $-2 < MD < 2$ uniform area (n=9 per mat)

3.5 DISCUSSION

To address the known short comings of electrospinning in application to biomaterial manufacturing, we aim to demonstrate proof-of-concept capabilities for high basis weight production and control over the region of uniformity. Studies of scalability typically focus on faster rates of material production; therefore, we also assess the parameters which contribute to high throughput production methods in our study. Throughput and consistency are known challenges for electrospinning, potentially due to non-homogenous collection of surface charge, which generates repulsive forces at regions of the material surface.[286] Low throughput also increases the time and associated cost for material fabrication, thereby limiting the practical clinical translatability of the electrospinning method.[270]

To first assess the impact of free-surface electrospinning parameters on the production of high basis weight materials, we prioritized the factors (A) polymer concentration, (B) drug loading, (C) carriage speed, (D) electrode distance, (E) electric field, and (F) orifice size (Figure 3.2). Polymer concentration significantly impacts fiber production as adequate polymer entanglement is required to form electrospun fibers, rather than an electrospray. However, high viscosity due to high polymer density can also prevent the ability for fibers to form, yet some viscosity is needed to retain polymer solution onto the wire electrode in our studied electrospinning configuration.[290] Here, we found that a lower, 0.174 g/mL polymer concentration yielded greater fiber throughput. Drug loading is calculated from the total solid material mass, so increasing drug loading decreases the quantity of polymer available to entangle and form fibers. While drug concentration did not significantly affect either fiber throughput or distribution alone, the interaction between high drug loading and low polymer concentration contributed to greater fiber throughput (Figure 3.3C). This

suggests that drug loading of the model agent TVF at ~28% (w/w) did not disrupt polymer entanglement.

In the wire spinning-electrode configuration of the Nanospider, the size of the orifice controls the quantity of polymer solution which can coat the wire and the carriage replenishes this polymer coating. Therefore, both orifice and carriage speed affect the volume of solution available to electrospin. Increasing both parameters increased fiber throughput, as well as the interaction of these factors, while carriage speed alone increased the distribution of fibers. In a similar free-surface electrospinning configuration, the rate of rotation into a polymer bath to replenish the liquid polymer coating also showed significant impacts on productivity.[291] This study additionally showed that greater applied potential also contributes to greater fiber productivity.[291] We also observe greater throughput with a larger electric field, and confirm that the interaction between polymer concentration and electric field are likely significant, with t-values above the t-value limit (Appendix A Figure A.1). Increased electric field decreases fiber distribution, which can be rationalized through greater focused attraction of the fibers towards the collection electrode. The distance of the collection electrode, and the interaction between low electric field and increased electrode distance, increases fiber distribution. This can be explained by considering fiber generation from a single jet as an inverted bell curve, with the Taylor Cone at the curve minima. When the substrate is further from the origin of the jet, the width of the distribution increases.

Using the ideal settings of the factors which significantly impacted the assessed outputs, we achieved a maximum fiber throughput rate of 12.9 g/h. Previous research with free-surface electrospinning has focused on fiber throughput as a measure of scalability. The free-surface electrospinning device used in this study, the Nanospider, has been described to achieve a production rate up to 278 g/h.[282] Free-surface electrospinning has also been described to be

capable of up to 1 kg/h production rates.[291] However, we are using water as a solvent, which has lower productivity due to a slower evaporation rate compared to organic solvents.[292] Despite this, aqueous solvents have benefits such as lower cost, compatibility with sensitive agents like biologics, and reduced toxicity from potential residual solvent.[292] In a similar study using an aqueous solution of PVA and TFV, Krogstad, *et al.* report a throughput rate of up to 7.6 g/h with wire free-surface electrospinning, while traditional needle electrospinning could only achieve a throughput rate of up to 0.14 g/h.[271] In another free-surface electrospinning study of an aqueous PVA solution, Bhattacharyya, *et al.* measured a maximum productivity of approximately 0.5 mg/min per cm of the electrode when characterizing the effect of rotation rate of the electrode on productivity. Our productivity across a 25 cm wire length with our ideal settings is 8.6 mg/min per cm. Therefore, our achieved throughput with an aqueous solvent has relatively acceptable scalable potential.

While production rate is important to characterize for scalability, our focus in this study was to assess the capability of electrospinning to achieve a defined region of high basis weight fiber deposition. The production of high basis weight materials is a challenge for electrospinning due to throughput decay potentially caused by the buildup of residual charges on the collected material surface which can repel fibers,[286] and from solvent evaporation in solution reservoirs, known as solution aging.[291–293] In a study by Forward, *et al.*, solution aging limited electrospinning times to only 10 minutes.[291] We achieved a target basis weight of 100 gsm and show that dynamic electrospinning can create materials with consistent regions of fibers which achieve this high surface density. In our experiments, the run was terminated once the target basis weight was achieved, so this achieved surface density does not represent a maximum limit of this electrospinning method. In the literature, free-surface electrospinning has been reported to achieve

a basis weight range of only 0.002-10 gsm.[270,280,282] Electrospun materials are commonly characterized as having low basis weight,[294–296] and reported values commonly only measure as high as approximately 25 gsm.[297–300] The greatest electrospun surface density found was by Zhang, *et al.*, who report the use of 60 gsm electrospun, acrylonitrile-butadiene materials.[284] Therefore, we present a strategy which yields the highest reported basis weight from electrospinning to our best knowledge. Our achieved basis weight is within the range of other non-woven fabrication methods like meltblowing, spunbond, and carding, which are capable of larger basis weights approximately 5-500, 10-800, or 10-2000 gsm, respectively. However, electrospinning is also capable of nanosized features, which are approximately 10-100 times smaller than fiber diameters achieved with these alternative methods.[280]

Other studies of electrospun fibers have mostly focused on controlling the distribution of collected fibers via controlling the electric field with collector design.[301–304] Rather than modifying existing commercial electrospinning equipment to control fiber collection, we present a strategy to regulate the electrospinning process and yield predictable materials. We show that we could control the region of consistent fiber deposition by a simulation-determined DPL, which was dependent on the specific σ_{MD} parameter of the polymer formulation. Simulations used here proved to be a useful tool for determining the minimal run needed to collect the necessary area of consistent material. Methods which can minimize the total run length also minimize the waste of material, drug, and time needed to create the fiber mat. Therefore, the capability to simulate fiber deposition further supports the potential for scalable electrospinning.

We interestingly observed that ETR, which has the lowest water solubility (0.00397 mg/mL[288]), also had the highest drug loading (encapsulation efficiency ~97%), and lowest dose variation between all samples (CV ~6.5%) when electrospun in this aqueous solution (Figure 3.6B,

Table 3.1). Hydrophilic drugs have shown poor compatibility with polymers, which has caused known complications for electrospun formulations.[90,167] We therefore consider the >70% encapsulation of hydrophilic RAL to be reasonable. Further, depending on the application, significant differences in loading between drugs may not be a concern or could be accounted for depending on the required relative dosages or specific formulation.

According to United States Pharmacopeial (USP) standards, drug tablets or suppositories are acceptably uniform by content uniformity tests if 10 samples measure within a range of ±15% of the label claim and have a CV ≤6%, or if all but one in 30 samples falls outside the ±15% range, but all samples are within ±25%,and have a CV ≤7.8%.[305] In Table 3.1 we compare error in drug loading to the full drug loaded into the material as a rigorous measurement of method efficiency, however the label claim refers to the quantity of drug intended for dosing.[305] Although sampling quantities here do not meet the requirements for this assessment, comparisons to these standards can help determine if uniform dosing is possible with electrospun materials, and drug properties which may be the most conducive to uniformity. Across all collected samples, MVC and RAL are not congruent with USP standards, especially when considering dosing error with theoretical loading as the label claim. However, if drug loss is acceptable, and the label claim for MVC is defined as 4.1 gsm (0.32 mg per 1 cm diameter punch), the first and last runs could be considered acceptably uniform for MVC loading. RAL loading shows homogeneity per mat, but inconsistencies per run. Acceptable uniformity would require the label claim to be approximately 2.75 gsm (0.22 mg) RAL for the first run, but 4.25 gsm (0.33 mg) RAL in the second run. The most hydrophobic drug ETR does not exhibit these nonuniformity issues. Even when considering the label claim to be the theoretical loading (5 gsm), ETR dosing in samples across each individual sheet and cumulatively have error within ±15% for all but one sample (at 15.3% error), and a CV

≤7.62% (Table 3.1). Therefore, these electrospun materials do show the capability of uniform drug loading comparable to rigorous USP standards.

Although the error of drug encapsulation could be acceptable for some applications, a major shortcoming of this current method is inconsistency across multiple runs potentially due to the manual control over total fiber deposition. Observationally, we found that electrospinning throughput rates could be dependent on specific volume of polymer within the carriage and environmental factors like humidity.[286] Further study into such factors could mitigate this error. Variability of hydrophilic drug loading could also be optimized in future studies. Alternative formulations should be assessed if a hydrophilic drug is the target agent for formulation. However, if multiple candidate drugs exist, the selection of a hydrophobic drug may intrinsically improve loading and uniformity in similar electrospun materials. Alternatively, the mapping and interpolation methods presented here could be used to mitigate these issues, as the specific material area could be determined by integrating these measurements to achieve a target dosage.

3.6 CONCLUSIONS

Electrospinning is a material fabrication method which has interesting applications for biomedical purposes due to its ability to be used with nearly any polymer, the capacity to formulate physicochemically diverse agents, and the resulting fiber microgeometry which mimics the native architecture of the tissue extracellular matrix.[90,147,265,268–270,280] However, current reported electrospinning methods lack the capacity to fabricate materials with consistent, high basis weight fiber deposition.[270,280,281] For medical applications, high surface density is required to deliver clinically relevant dosages within a reasonable material surface area, or to create scaffolds with greater three-dimensional structure. Further, consistency of this high basis weight material is

necessary to control drug dosages across the material and enable scalable production of such medical technologies.

This study provides in depth characterization of electrospinning parameter effects on throughput and distribution. Further, we show that dynamic electrospinning methods could be used to control fiber deposition, and to have a defined region with a consistent target basis weight of 100 gsm. This achieved basis weight is also more than 1.6 times greater than the highest reported surface density for electrospinning to our knowledge.[284,297–300] While such high-basis weight materials may be ideal for drug delivery, materials with such density may lack the required porosity for cell permeation into the depth of the material for applications like cell seeding.[117,286,290] Therefore, future alterations to this method, such as porogen loading, could make these electrospun materials further amendable to tissue scaffold relevant biomaterial fabrication.

Using the PVA/PEO polymer solution optimized in DOE study, three physicochemically diverse agents were found to be efficiently formulated in the consistent, high basis weight electrospun fibers. Specific drug loading was found to have relatively low variation across samples within the defined region of consistent fiber deposition (CV <20% for all, <10% across samples in the representative fiber mat). Further, we demonstrate that the agent with the greatest hydrophobicity also can achieve uniformity across all samples congruent with USP standards. We believe this work presents proof-of-concept capabilities of the electrospinning process to manufacture medical materials. Future work could build upon these methods to further improve particular drug loading and consistency, as relevant to a specific application.

3.7 ACKNOWLEDGEMENTS

We would like to acknowledge the University of Washington Statistical Consulting Service for input on statistical methods. We would also like to thank R. Edmark for all his help with the Nanospider and the electrospinning protocols used here, H. VanBenschoten and P. Nguyen for their supporting work with dynamic electrospinning, and C. Everson for his initial guidance with Python.

Chapter 4. ANTIRETROVIRAL DRUG PROPERTIES DICTATE LONG-ACTING RELEASE AND TISSUE PARTITIOINING BEHAVIORS IN MULI-DRUG LOADED SUBCUTANEOUS IMPLANTS

Adapted from: Hernandez JL, Chien ST, Suydam IT, Woodrow KA. Antiretroviral drug properties dictate long-acting release and tissue partitioning behaviors in multi-drug subcutaneous implants. *In Preparation.*

Supporting figures are available in Appendix B.

4.1 ABSTRACT

Subcutaneous implants can provide patients with long-acting, compliance independent drug dosing. For this reason, subcutaneous implants have shown emerging interest for HIV prevention. However, any successful long-acting HIV preventative device will require multi-drug dosing, which poses a challenge for formulation considering the physicochemically diverse selection of antiretroviral (ARV) candidates. As a method which has shown the capacity of efficient multi-drug delivery, we assessed electrospun fiber implants composed of three-synergistically potent ARVs and a biodegradable polymer selected by *in vitro* release studies. In mice, subcutaneous electrospun fiber implants exhibit burst release of the more hydrophilic drugs maraviroc (MVC) and raltegravir (RAL), which could be reduced via simple pre-wash treatments of the implants. Over an extended, 120-day timeframe, fiber implants show drug-specific differences in release timeframes and magnitudes in blood serum. However, endpoint drug tissue concentrations show that the most hydrophobic drug etravirine (ETR) remains in high

concentrations within the implant and in local skin tissue biopsies. Further, ETR is found to be capable of significant partitioning into lymph nodes, the lower-female reproductive tract, and the rectum. Topologically smooth film implants also exhibit the same drug-dependent trends. Therefore, we illustrate that drug release and drug tissue portioning is largely dictated by drug properties. Further, we find that the properties of ETR enable significant drug quantities within the tissues most relevant to HIV protection. Evidence from this work emphasizes the need for greater focus on drug properties and prodrug strategies to enable relevant, extended, and targeted drug release.

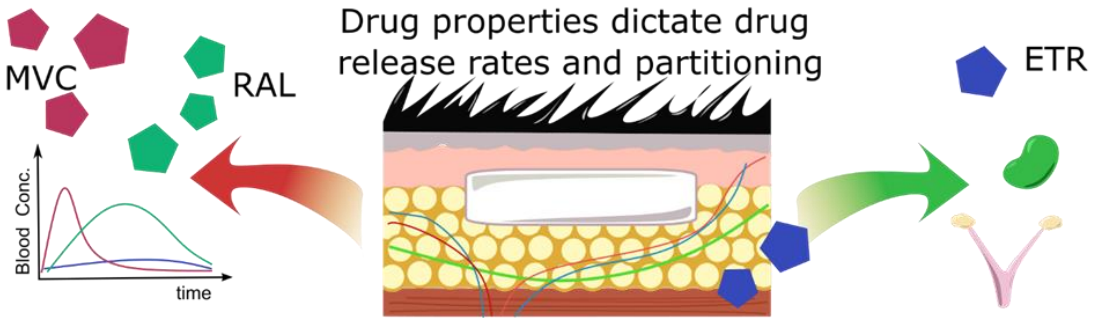

Figure 4.1. Antiretroviral drug properties dictate long-acting release and tissue partitioning behaviors in multi-drug subcutaneous implants

4.2 INTRODUCTION

Long-acting drug delivery systems (LA-DDS) offer patients multi-month therapeutic dosing without the need to take pills daily, thereby improving adherence to treatments regardless of patient compliance.[15] Extended drug release has been used for localized drug delivery in devices such as intrauterine devices (IUDs)[223,306] and drug eluting cardiac stents.[307] However for more generalized purposes, LA-DDS are often implanted sub-dermally or within the subcutis.[13] The

subcutaneous space lies just under the skin or dermis, and just above muscle tissue.[14] This superficial location provides a minimally invasive location for device placement, which can be implanted via trocar rather than by surgery.[16,308] As a adipose-rich tissue, the subcutis mainly functions as insulation, energy storage, and protection against injury.[14] In addition to adipocytes, the subcutis also contains connective tissue, as well as a network of capillaries and lymphatic vessels which enable pharmaceutical uptake into the blood supply.[11,14] For these reasons, subcutaneous implants have been developed for contraception, treatment of opioid addiction, delivery of schizophrenia medication, and have an emerging interest for HIV prevention.[15,226]

Daily oral regimens of antiretroviral (ARV) drugs are clinically used to prevent HIV infection, known as pre-exposure prophylaxis (PrEP).[4] However, the requirement of daily adherence to PrEP has limited its efficacy. Due to low partitioning of drug to the female reproductive tract (FRT), near perfect adherence is required to enable protective dosages at this potential site of infection where the majority of global HIV cases arise.[4,6,22,23,26] While pharmacokinetics are typically reported for the blood, various ARVs have shown poor and heterogenous distribution in tissues, including the lymph nodes which harbor immune cell populations vulnerable to HIV infection. In cases of HIV treatment, this unfavorable drug partitioning is thought to enable the development of viral sanctuary sites, and therefore viral rebound.[21,309] While subcutaneous LA-DDS have the potential of overcoming adherence issues, the application of HIV prevention presents a large design challenge. In addition to the need for a sufficient drug reservoir which maintains protection for at least 6 months, quantities of drug must have appropriate drug partitioning from the subcutis into tissues like the lower FRT, rectum, and lymph nodes. Further, for effective protection, implants would also need to deliver a combination of at least two ARVs to ensure vial inhibition.[11] Many of the ARVs which have synergistic potency

also have physicochemically diverse properties, therefore further research is needed to assess LA-DDS which can co-deliver ARVs at fixed-dose ratios for effective therapy.

Electrospinning is a material fabrication method which has shown interest as a drug delivery vehicle due to the capabilities to formulate physicochemically diverse agents into a solid dosage form, co-formulate agents, encapsulate drugs with high drug loading and high efficiency, and the compatibility of the method with nearly any polymer.[90,167] Drug release rates can be controlled by the use of polymers with different properties. Properties like hydrophilicity, crystallinity, glass transition temperature, and molecular weight can impact the inward flux of water into the implant as well as the outward flux of drug into the surrounding tissue.[109,310,311] For biodegradable materials, properties including hydrophilicity, crystallinity, and importantly the presence of hydrolysable or enzymatically cleavable functional groups are all known to control the erodibility of the material which can therefore release drug.[87] Material architechture can also impact these drug release rates. Electrospinning yields sheets of materials with nano or micro-scaled fibrous features, and are therefore porous, with high surface-to-volume ratios.[109,119] Increased surface area can increase release rates by permitting water influx and maximizing the bioavailable surface area of the implant.[16,223,226,229,237] Even for long-acting applications, increasing these drug release rates can be favorable especially for agents with low solubility. While low solubility can enable long-acting release, drugs with low solubility can also have low bioavailability and therefore non-therapeutic dosages.[312]

Here, we assess electrospun implants which simultaneously elute three physicochemically diverse ARVs, including Maraviroc (MVC), Raltegravir (RAL), and etravirine (ETR). Using both *in vitro* release methods and *in vivo* murine implant studies, we compare ARV partitioning into blood serum, local tissues or mimics, and remaining in the implant. Using the optimal polymer for

sustained release, we create electrospun triple-ARV implants which we study out to 120-days. Further, we assess the contribution of surface associated drug to burst release through wash treatments. Throughout this study we quantify blood serum concentrations, and we collect endpoint tissue concentrations. While serum measurements indicate that most drugs are cleared by the end of the study, tissue measurements find large remaining concentrations of ETR in the implant and local skin tissue. Further, for some samples, ETR is partitioned in very high concentrations in the lymph node, FRT, and the rectum. We additionally find that this drug behavior is recapitulated for topologically distinct film implants with a decreased material surface area. These results suggest that drug release here is primarily mediated by the properties of the pharmaceutical agents. These data support that different drugs require different strategies to best control the release of bioavailable drug. Further, interesting tissue partitioning properties of ETR may make this drug a promising candidate for LA-DDS.

4.3 MATERIALS AND METHODS

4.3.1 *Materials*

Poly(lactic-co-glycolic acid) (PLGA, Lactel Absorbable Polymers) materials used four different PLGAs. PLGA1 was defined to be 50:50 L:G, carboxyl terminated, and IV=0.55-0.75 dL/g. PLGA2 was 50:50 L:G, ester terminated, and IV=0.95-1.2 dL/g. PLGA3 was 75:25, ester terminated, and IV=0.55-0.75 dL/g. PLGA4 was 50:50 L:G, ester terminated, and IV=0.55-0.75 dL/g. Additionally, polycaprolactone (PCL, Mw=80,000, Sigma-Aldrich) and poly-L-lactic acid (PLLA, IV= 0.67 dL/g, Lactel Absorbable Polymers) are used. Poly(vinyl alcohol) (PVA, 87-90% hydrolyzed, Mw=30,000-70,000, Sigma-Aldrich) for glue. All electrospun polymer solutions used

hexofluoroisopropanol (HFIP) as a solvent. Solvent cast films used dichloromethane (Fisher Scientific) and Sylgard Elsatomer (Dow Inc.). Maraviroc (MVC), raltegravir (RAL), and etravirine (ETR) were used as the assessed pharmaceuticals purified as described in Jiang, *et al.* from tablets of Selzentry® (300 mg MVC, ViiV Healthcare), Insentress® (400 mg RAL, Merck), and Intelence® (200 mg ETR, Janssen).[94] Radiolabeled ARVs (maraviroc-d_6, raltegravir-d_6, and etravirine-$^{13}C_6$, Alsachim, Inc.) were used for LC/MS quantification. Release studies utilized fetal bovine serum (FBS, heat inactivated, Gibco), agarose (Sigma-Aldrich), and Dulbecco's phosphate buffered saline (PBS, Corning). Quantification used dimethyl sulfoxide (DMSO, DH/VWR Analytical), potassium phosphate monobasic (Fisher Chemical), and acetonitrile (ACN, HPLC-grade, Fisher Chemical). Tissues were prepared for histology using formaldehyde solution (10% formaldehyde, Macron Fine Chemicals), ethanol (Decon Laboratories, Inc), and sucrose (Macron Fine Chemicals).

4.3.2 *Electrospinning to create multi-drug fiber implants*

Electrospun fibers were first created from a polymer solution using the specified polymer dissolved at 15% (w/v) HFIP. Each pharmaceutical agent was added to this polymer solution at 5% (w/w) for a total drug loading of 15% (w/w) in total fiber. The polymer solution was electrospun from a 1 mL glass syringe and 23 G needle, with 1 mL per sheet, and extruded at a constant rate of 10 µL/min. Fibers were collected on brown waxed paper on a metal target across an applied voltage of ~13 kV.

4.3.3 *Solvent casting to create multi-drug film implants*

Solvent cast films were created using methods adapted from Catiker, *et al.*.[313] Briefly, PLGA was dissolved in dichloromethane at 6% (w/v) along with drugs at 5% (w/w) to polymer.

The polymer solution was then added to a petri dish lubricated with Sylard Elastromer and allowed to air dry for 24 hours. The PLGA films were subsequently placed onto a high vacuum line overnight to remove residual solvent.

4.3.4 *Material characterization*

Scanning electron images (SEM, Apreo Variable Pressure, ThermoFisher Scientific) were collected for both fiber and film surfaces. Fiber and pore measurements were collected from these images using ImageJ (FIHI/ImageJ 1.51s, National Institutes of Health, USA).[314] Contact angle measurements were collected using a contact angle goniometer (Model A-100, Ramé-hart, Inc.).

4.3.5 *Tandem, multi-drug detection using HPLC*

High-performance liquid chromatography (HPLC, Shimadzu Prominence) was used to quantify drug concentrations within a range of approximately 0.0001-0.1 mg/mL using a linear standard curve for *in vitro* assessments, excised implants, local tissue samples, and organ tissues when the signal was within this detection range. To individually detect MVC, RAL, and ETR a gradient of 38 - 73% ACN and 25 mM monopotassium phosphate in water as the mobile phase. A C18 column (Phenomenex Kinetex) was used as the stationary phase. Detection wavelengths and approximate retention times were 193 nm and 4.3 min for MVC, 300 nm and 7.1 min for RAL, and 234 nm and 15.3 min for ETR.

4.3.6 *LC/MS detection of drug concentrations*

Liquid chromatography-mass spectrometry (LC/MS) was used to quantify smaller concentrations in blood serum, and organ biopsies less than 100 ng/mL. Methods were used as previously described by Blakeney, *et al.*.[315] Briefly, equipment used included an I-Class Acquity

UPLC (Waters Corporation) coupled with a Waters Xevo TQ-S tandem quadrupole mass spectrometer (Waters Corporation), a Micromass Zspray Atmospheric Pressure Ionization Source, and a Chromolith Performance RP-18e 100-3 mm analytical column (Merck) for sample separation. For sample preparation, serum was centrifuged at 10 kG for 10 min, then 10 µL of the sample supernatant was added to 20 µL ACN with 15 ng/mL of each of the labeled drugs. Samples were then vortex mixed, centrifuged at 10 kG for 10 min, and filtered through a 0.22 µm spin column. Radiolabeled ARVs were spiked into the serum samples at a final concentration of 10 ng/mL. Blank ACN was repeatably measured throughout the run as a negative control, and to remove background signal. Concentrations, with background subtracted out, were calculated as a ratio of the ARV signal in the sample to the signal of the radiolabeled ARV channel, then multiplied by the known 10 ng/mL concentration, and dilution factors. MassLynx software (version 4.2, Waters Corporation) was used to analyze LC/MS data.

4.3.7 *Drug Encapsulation and release studies*

To determine actual drug loading, materials were sampled using a 1 cm diameter die and dissolved at 1 mg fiber per 1 mL DMSO. Drug concentrations are quantified by HPLC as described in section 4.3.5. Encapsulation efficiency was calculated as a percent per theoretical loading of 0.05 mg/mL drug in the solution. Release studies were conducted either in PBS as a conventional experimental format and with a gel and protein-supplemented format as a subcutis mimic. At specified timepoints ranging between 15 min to 28d or 1176d, 100 µL samples were collected with replacement of media.

Polymers were screened using conventional *in vitro* release studies using PBS at calculated sink conditions for a 1 cm punch of material for a final concentration of 3.825 mg/mL fiber per release media. Hybrid release studies were conducted with 40 mg of materials rolled into 1 cm-

long cylinders, placed via 7 G trocar needle into 10 mL of 2% (w/v) agarose gel solidified in a 50 mL conical tube, with 40 mL protein enriched release media consisting of 50:50 FBS/PBS. To aspirate any protein-bound drug 100 µL cold ACN was added to release samples, vortex mixed, centrifuged at 10 kRPM for 10 min, and filtered prior to measurement. Quantities of drug remaining in implants tested either *in vitro* or *in vivo* were measured by dissolving implants in known volumes of DMSO. Drug concentrations within the agarose gel, tissue mimic were measured by homogenizing the gel with 10 mL ACN at 10 kRPM, mixing overnight, then centrifuging at 4kG for 5 min to separate out gel particulates.

4.3.8 *Subcutaneous murine implant studies and sample collection*

Sheets of material were prepared into implants by cutting the materials into 2 cm strips, which were trimmed to a length resulting in a fiber mass equal to 200 mg/kg theoretical dosing per drug, as determined by mouse weights measured three days prior to surgery. All materials were ultra-violet (UV) sterilized for 30 min per side prior to implantation. Sterilized sheets were then rolled and secured into cylindrical implants using sterile 20% (w/v) PVA/water glue. Implants specified to undergo a "washing" step the day prior to implantation were added to sterile PBS at 37ºC and 300 mL for 8 hours.

Animal research was approved by the Institutional Animal Care and Use Committee (IACUC) at the University of Washington. All guidelines for animal care were followed. Surgeries were conducted using 8-week-old female C57BL/6J mice (Jackson Laboratory). Mice were anesthetized using isoflurane delivered via a precision gas vaporizer and administered 0.05 mg/kg buprenorphine as an analgesic. The implant site – placed intrascapularly at the midline of the dorsum – was shaven and sterilized using altering swabs of betadine solution (Purdue Products) and ethanol (Fisher). One incision was made, followed by a single pocket created via blunt

dissection where the implant was placed. Incisions were secured using surgical staples (7mm, Reflex).

Throughout the 120-day study, blood samples were collected from mice at varying frequencies. To capture initial burst release, blood was sampled from mice at 30 min, 1 hr, 2 hr, 4 hr, 8 hr, 24 hr, 3 d, and 7 d using tail prick in order to say beneath blood collection limits of 10% of the mouse weight within any 2-week period. Tail prick samples were collected using a 21 G needle. Quantity of blood collected was quantified via pipette and diluted in 15 µL PBS to obtain a minimum quantifiable volume of serum by LC/MS and a maximum dilution factor of 4x. Samples were collected weekly from 2 to 5 weeks, then every 10 days using submental bleeds, collected using a 5 or 6 mm lancet (Goldenrod). If submental bleeds yielded serum samples less than 10 µL, samples were diluted with 10 µL PBS, or samples were collected via submental bleed. At the study endpoint (120 days) final blood samples were collected using cardiac puncture procedures, using a 27 G needle and syringe. To isolate blood serum, all blood samples were allowed to clot at 4ºC overnight. Samples were centrifuged at 2.3 kG for 10 min, supernatant was collected, then centrifuged again to yield the final serum samples.

4.3.9 *Tissue and implant preparation for drug concentration measurements*

Following sacrifice, lymph nodes (inguinal, lumbar), the female reproductive tract, GI tract, spleen, lungs, kidneys, and liver were collected. The remaining implant was identified within the skin, and a 2x2 cm samples surrounding the implant were excised. For drug concentration measurements, the sample was cut in half, and the remining implant was removed and dissolved into 400 µL DMSO. Half of the remaining tissue was then saved for histology (see section 4.3.10) and 3 mm biopsy samples were taken from the other half, with three replicate samples taken at the implant site, and approximately 1 cm above or below the implant midline (n=9 samples total).

Implant tissue samples reserved for histology reserved the center most 1 cm of tissue for histology and sampled tissues approximately 1 cm on each side of the implant for n=6 samples total. Tissue samples were frozen at -80ºC until time of measurement. Samples of tissue were weighed and added to a prepared 2 mL Precellys tube with 250 µL ACN. All samples were then homogenized (Precellys 24, Bertin Technologies) at 3x at 6500 RPM for 20 s. Homogenzied solutions were then centrifuged at 10 kG for 10 min, and supernatant was passed through a 0.22 µm filter prior to quantification.

4.3.10 *Histological analysis*

For histological analysis, samples were fixed in 4% (v/v) formaldehyde/PBS solution for 24 hours, then transferred to 70% ethanol for at least 24 hours, and finally a 5% (w/v) sucrose/PBS solution following final tissue trimming until embedding to prevent implant dissolution. Samples were sectioned and stained using Masson's Trichrome stain. Images were taken using brightfield microscopy at 10x (Nikon Eclipse Ti) or using a stereoscope (Nikon Model C-LEDS) for images at 2x. Capsule and inflammatory cell layers are measured using ImageJ (FIJI/ImageJ 1.51s, National Institutes of Health, USA).

4.3.11 *Statistical analysis*

All statistical analyses were conducted using GraphPad Prism (version 9.2.0). Comparisons between *in vitro* and *in vivo* data were assessed by 2way ANOVA and Šídák's multiple comparisons test. Comparisons between fiber and film implants and differences between drug concentrations per timepoint were further assessed as repeated measures. Comparisons between drugs per material used Tukey's multiple comparisons test. Comparisons including

washed material treatments were analyzed using 3way ANOVA mixed-effects model with Tukey's multiple comparisons test.

4.4 Results and Discussion

4.4.1 *Physicochemically diverse agents can be co-formulated, and the resulting materials can release ARVs over 28-days when studied in a protein-enriched in vitro model.*

For long-acting HIV prevention to be successful from any subcutaneous implant, it is known that a combination of antiretroviral agents would need to be simultaneously delivered.[11] In pursuit of developing such a device, we selected three physiochemically diverse agents to probe the capacity to co-formulate and co-deliver these drugs via electrospinning. These drugs include maraviroc (MVC), raltegravir (RAL), and etravirine (ETR) which are further known to be synergistically potent (Figure 4.2).[93,94] MVC is a C-C chemokine receptor type 5 (CCR5) inhibitor, which blocks HIV-1 entry via this viral co-receptor, and is comparably the least potent when delivered alone.[94,316] RAL is the most hydrophilic drug within this combination, and acts as an integrase inhibitor which prevents the insertion of viral DNA into the host genome.[94] Finally, ETR is a non-nucleoside reverse transcriptase inhibitor (NNRTI) which prevents reverse transcription of viral RNA to DNA. ETR is also nearly aqueously insoluble, has high protein binding affinity, and is comparably the most potent of the three assessed drugs.[94,317,318] Considering these divergent properties, as well as their practical applicability to HIV prevention, we believe these drugs capture an interesting range of properties to probe long-acting behaviors within electrospun implants.

Table 4.1 Properties and predicted agent efficacy of studied physicochemically diverse ARVs

ARV:	MVC	RAL	ETR	Refs.
Molar mass (g/mol)	513.7	444.4	435.3	[287–289]
Solubility in water (mg/mL)	0.011	53.9	0.00397	[287–289]
logP	4.3	0.4	>5	[287–289]
Blood plasma protein binding	76%	83%	99.9%	[319]
IC_{50}	17.4 nM (8.94 ng/mL)	6.9 nM (3.07 ng/mL)	1.4 nM (0.61 ng/mL)	[94]

IC_{50} = half maximal inhibitory concentration
logP = partition coefficient

To formulate electrospun materials which could most ideally sustain the release of the three physicochemically diverse ARVs, biodegradable polymers including polycaprolactone (PCL), poly-L-lactic acid (PLLA), and various forms of poly(lactic-co-glycolic acid) (PLGA) were screened using *in vitro* release studies. These specific polymers were selected due to their variety of properties which are known to mediate drug release (Table 4.2). PLGA is an amorphous polymer, while PCL and PLLA have been described to be semi-crystalline.[313,320,321] Greater structural order requires greater energy to degrade polymer bonds for erosion-mediated release. Further, amorphous polymers have greater polymer chain mobility, allowing for greater water influx for both erosion and diffusion-mediated drug release.[89–91] These polymers also have differences in glass transition temperature (T_g), or the temperature which a polymer shifts from a glass-like state to a state that is more rubber-like. Again due to greater polymer chain mobility, drug diffusion rates are theoretically greater when at temperatures greater than the polymer T_g.[88,90] Considering these materials will be implanted at body temperature, reported T_g values for PCL dictate that the polymer will be more rubber-like, PLLA will be more glass-like, and PLGA will be near-to or just below the transition state within the subcutis.[313,320,321] Across the various PLGAs,

we also assess different terminal functional groups, molecular weights, co-polymer ratios, and blends of PLGA with both PCL or PLLA. These properties can further impact material hydrophobicity, outward drug flux from the matrix, and polymer entanglement needed for electrospun fiber generation.[90,322] Considering these factors – and the interaction of factors which may impact release – *in vitro* release methods were necessary to determine the polymer selection best suited for controlled, diverse ARV delivery.

Table 4.2 Properties of polymers screened for triple-ARV release from electrospun fibers

Polymer [a]	**Semi-crystalline or Amorphous (C/A)?**	**T_g (°C) ↑/↓ body temp?**	**M_W (kDa) (IV (dL/g))** [a]	**Refs.**
PLGA 1 (50:50, carboxyl term)	A	↓	21.1 – 43.5 (IV = 0.55-0.75)	313,323
PLGA 2 (50:50, ester term)	A	↓	73.7 – 111.5 (IV = 0.95-1.2)	
PLGA 3 (75:25, ester term)	A	~	76.0 – 119.9 (IV = 0.55-0.75)	
PLGA 4 (50:50, ester term)	A	↓	21.1 – 43.5 (IV = 0.55-0.75)	
PLLA	C	↑	~140	91,313,320,323
PCL	C	↓↓	~ 80	321

[a] *Values referenced from manufacturer.*

All triple-ARV polymer combinations could be successfully electrospun into solid dosage-forms, and all combinations show high encapsulation efficiency of the three drugs, except for RAL in PLLA or PCL materials in comparison to PLGA1 (Appendix B Figure B.1). Drug release rates from each material formulation was first studied across an 8-week timeframe using a more

traditional PBS release study platform. For these biodegradable systems, biphasic release behavior can be expected.[320] An appropriate material selection will have minimal drug burst release, followed by pseudo-linear period with sufficient dose per day release. Across our various formulations, drug release rates primarily follow trends of polymer T_g – where PCL and PCL/PLGA materials show significant burst release of MVC and RAL within the first day, and PLLA materials exhibit a pseudo-linear release rate insufficient for consistent dosing (Figure 4.2 A&B). While all assessed polymers are biodegradable, electrospun materials which have increased surface-to-volume ratios have also been characterized to have primarily diffusion-controlled release, which is consistent with T_g mediated observations.[88,109,119]

Across the different PLGA materials, observations in release rates were dependent on the drug. For MVC, carboxyl terminated PLGA (PLGA1) and higher molecular weight PLGA (PLGA2) exhibited greater burst release, while the PLGA with a greater lactic acid content behaved similar to PLLA materials (Figure 4.2A). Interestingly, RAL exhibited greater burst from each of these three PLGAs (Figure 4.2B). Ester-terminated, lower molecular weight PLGA (PLGA4) however exhibited the most sustained pseudo-linear release of both MVC and RAL (Figure 4.2 A&B). Likely, the ester terminal group makes the material more hydrophobic thereby slowing drug diffusion.[90] Extended release of both MVC and RAL from the lower molecular weight PLGA (PLGA4 vs PLGA2) is inconsistent with the consensus of work which rationalize that greater molecular weight polymer materials will have reduced chain mobility, and have more linkages which would more time to degrade the polymer chain for release.[320] Extended release of drug here with reduced molecular weight PLGA may be due to specific RAL- and MVC-polymer interactions, and potentially due to differences in fiber surface partitioning of these drugs which would alter burst release.[90] Due to the extended release of these drugs, we selected PLGA4 as the

optimal polymer for continued assessments of these electrospun implants. While typically these studies are conducted under sink-conditions, the insolubility of ETR would require such large volumes that drug detection would fall far below detectible concentrations. Therefore, ETR was predictably indetectable from any sample for any material across this study (Figure 4.2C).

To enable ETR detection needed to characterize the deliverability of this hydrophobic, high protein affinity drug, an alternative release model was needed. Indeed, previous studies have characterized these issues with highly insoluble drugs and have promoted the use of alternative *in vitro* release models which can more accurately quantify drug release and better represent physiological environments.[324] Inspired by a study by Abouelmagd, *et al.* where 50:50 FBS/PBS release media was used to significantly solubilize hydrophobic drug[324] – as well as Peschka, *et al.* where a layer of agarose gel was used to embed liposomal DDS within the release media[325] – we composed a release study model which could more accurately capture the protein-rich and low-fluid environment of the subcutaneous space. In this *in vitro* model, materials could be implanted into the agarose gel as a tissue mimic using a trocar device, and FBS/PBS medium could supply serum proteins such as albumin, which ETR is known to extensively bind to.[317] Using this model, release of MVC and RAL was greater than the PBS model at endpoints near to 28-days (Figure 4.2 D&E). Importantly, ETR could be detected, although in low levels, in the FBS/PBS medium overtime (Figure 4.2F). In comparing ETR release of the same implants in serum samples after implantation in mice, similar concentrations and release trends confirm the acceptability of this model as a predictor for ETR release (Figure 4.2F). Although protein-bound ETR may not be the active form of the drug, these quantifications still represent drug quantities which can be released from the implant, and also quantities which are likely in equilibrium with free-drug in solution.[326] This model also could be employed to predict drug concentrations remaining in the implant and in

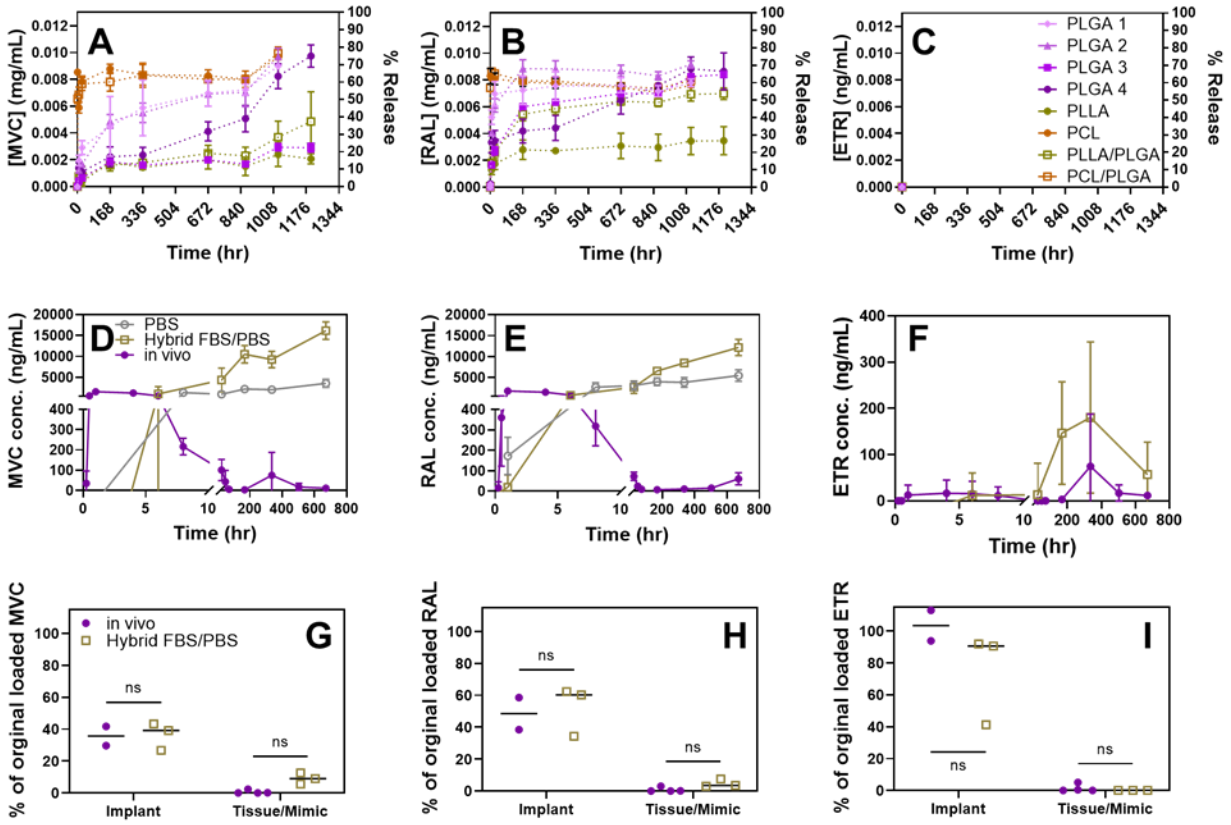

Figure 4.2. In vitro release models find optimal ARV release from lower Mw, ester-terminated PLGA, and a model which captures the protein-rich, low fluid environment of the subcutis can enable the detection of ETR release.

PBS release studies were used to screen various electrospun materials for the release of (A) MVC, (B) RAL, and (C) ETR. To detect highly insoluble ETR, drug release studies from PLGA4 fiber materials were also conducted using a release model with agarose tissue mimic and FBS/PBS release medium. Release of (D) MVC, (E) RAL, and (F) ETR is shown for the PLGA4 fiber materials in this new model system, in comparison to results from the PBS study, and a 28-day in vivo study. Plots represent mean ± standard deviation for n=3 replicates. To further demonstrate the improved capacity to predict subcutaneous drug release with the agarose/FBS model, we measure the remaining (G) MVC, (H) RAL, and (I) ETR after 28-days in the excised implant and agarose tissue mimic in comparison to in vivo data. Individual values are plotted, with lines representing the mean, for n=3 in vitro samples, n=2 in vivo implants, n=4 in vivo tissue biopsies.

the surrounding tissue mimic (Figure 4.2 G-I). Drug specific trends between this *in vitro* model and *in vivo* results at 28-days further show congruency, with non-significant differences detected between the two assessments (Figure 4.2 G-I). These data show after 28-days MVC has the lowest quantity of drug remaining at approximately 40%, RAL with only 50%, and ETR with approximately the full drug loading still available. The high insolubility of ETR may therefore promote its use for extended release, as long as relevant dosages can release into the necessary tissues over time.

4.4.2 *Surface association of MVC and RAL lead to burst release of drug from fibers which does not alter long-acting drug release*

Although in vitro characterizations proved to be useful tools for selecting candidate materials, we next conducted in vivo implantation studies in mice to best study pharmacokinetics (PK) and biological responses to the fiber implants. Blood serum measurements enable the study of drug concentrations overtime and represent a bioavailable drug dosage to blood bound immune cells in regions across the body. Initial blood samples were collected frequently and in small volumes by tail prick in order to track the PK for each mouse across the entire study (Figure 4.3A). To meet sample volume requirements for LC/MS and to enable extractable serum volumes, whole blood samples were diluted for these initial samples, and this known dilution factor was used for the final concentration calculation. Therefore, these measurements of serum are theoretically an under approximation, but the high concentrations in the first day, and the sensitivity of LC/MS enabled sufficient detection appropriate for material and drug comparisons.

For the more hydrophilic drugs MVC and RAL, electrospun fiber implants showed large burst release of drug into the serum (Figure 4.3 B&C). Initial concentrations of ETR were comparably lower (Figure 4.3D). While it is important for a LA-DDS to rapidly achieve relevant

drug dosages for immediate efficacy, burst release of agents can cause toxicity issues, and can decrease the quantity of drug available in the reservoir. To probe the source of burst release of the fiber materials, we also implanted prewashed fiber materials. Washing the samples proved to be a simple method which successfully diminished initial burst drug release, as washed fiber samples show reduced burst release of MVC and RAL (Figure 4.3 B&C and Table B.2). This significant decrease in drug release with wash treatments can be especially seen for MVC at one hour ($p=0.0034$), four hours (0.0378), and eight hours (0.0097) (Figure 4.3B). For RAL, washing significantly decreases drug concentrations at two hours ($p=0.0418$) (Figure 4.3C). Further, values for the area under the curve within the first 24 hours (AUC_{24}) and the maximum concentration in the first 24 hours ($C_{max,24}$) for MVC and RAL for all implant and washing treatments are decreased in comparison to standard fiber materials (p-values near or less than 0.05, Figure 4.3). Washing did not have a significant impact on ETR release at any time or by any PK measurement (Figure 4.3D and Table B.2). These data suggest that this burst release of drug from electrospun materials is likely due to MVC and RAL associated on the fiber surfaces, which is a known complication of hydrophilic drug loading in electrospun fibers.[90] Interestingly, washing treatments do not appear to effect long-acting release of these implants (Appendix B Table B.2, Table B.3). Washing implants can therefore prove to be an effective method to reduce burst release of such materials in case of toxicity issues.

Table 4.3 Summary of pharmacokinetic (PK) quantifications for initial (≤24 hours) ARV release comparing standard and wash-treated electrospun fiber implants.

Fiber Treatment	AUC (h·ng/mL)			C_{max} (ng/mL)		
	MVC	RAL	ETR	MVC	RAL	ETR
Standard	6672.3 ± 699.4	9687.0 ± 2749.7	96.33 ± 166.85	1527.40 ± 163.41	1852.45 ± 608.39	8.421 ± 14.586
Washed	1147.0 ± 107.3	1097.7 ± 1065.3	3590.4 ± 5643.3	171.5 ± 90.1	85.6 ± 62.0	431.1 ± 641.2
p-value (Standard vs Washed)	0.0541	0.0005	0.5287	<0.0001	<0.0001	0.7527

Values reported as the mean ± standard deviation, or p-value for significance, for n=3 mice per group.

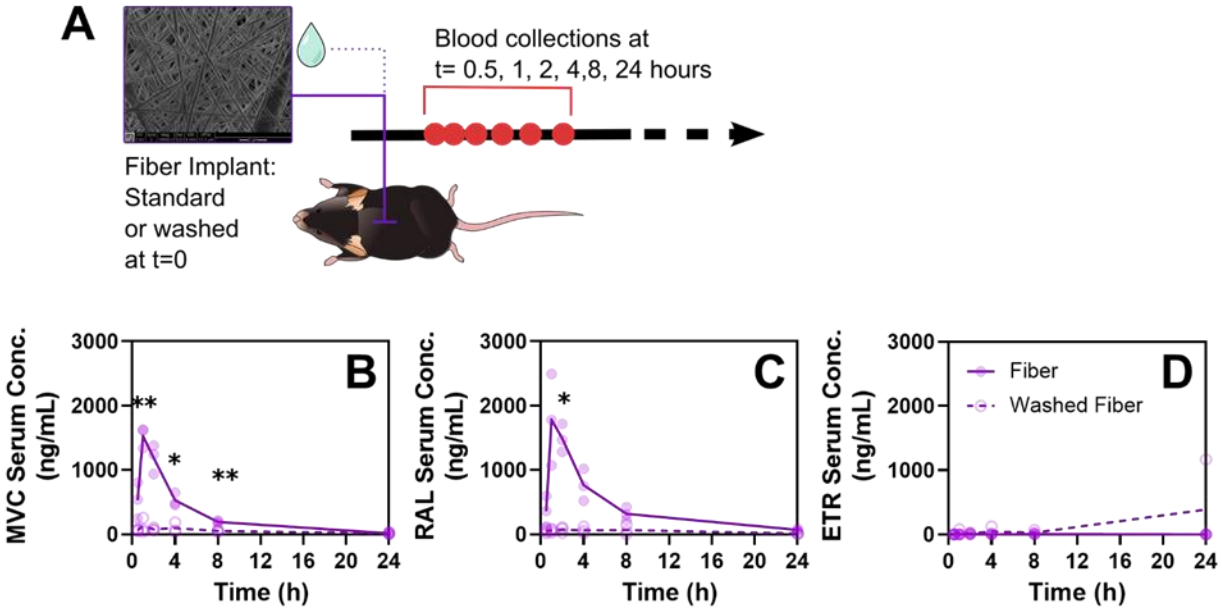

Figure 4.3. Fiber implants have high burst release of MVC and RAL due to surface association of drug, which can be mitigated by simple washing.

*(A) Blood serum was collected by tail prick and quantified across the first 24 hours for initial release of (B) MVC, (C) RAL, and (D) ETR. Individual measurements plotted and lines representing the mean for n=3 mice. Significant differences in concentrations between standard and washed fibers are denoted by * for p<0.05 and ** for p <0.01.*

4.4.3 *Physicochemically diverse ARVs show different long-term serum release kinetics*

Across the long-acting release period, defined to be 7 to 120 days (Figure 4.4A), MVC, RAL, and ETR serum concentrations show drug-dependent differences in release rates and magnitude (Figure 4.4 B-D). At the earlier time points and at 65 days (1560 hours), serum concentrations of the different ARVs show some significant differences. RAL concentrations are greater than ETR at one week ($p=0.0353$), 3 weeks ($p=0.0421$), and 65 days ($p=0.0042$). MVC concentrations are greater than ETR at four weeks ($p=0.0296$), but ETR is significantly greater than MVC at 65-days ($p=0.0319$). At 65 days, RAL is also significantly greater than MVC ($p=0.0059$). MVC appears to be mostly cleared by 75 days, however, reliable concentrations are detected in serum intermittently, and even at 120 days in washed fiber samples (Appendix B Figure B.3 B). RAL is mostly cleared by 95 days, although one fiber-treated mouse has detectible RAL serum concentrations at 115 days (Figure 4.4C).

Low and intermittent ETR serum concentrations are measured throughout the study. At 95 days, ETR appears to be mostly cleared from blood serum (Figure 4.4D). However, reliable measurements are detected in washed fiber implants (9.9 ± 2.2 ng/mL, ~22.7 nM) at 120 days (Figure 4.4D and Appendix B Figure B.3 F). It should also be noted that the half maximal inhibitory concentration (IC_{50}), which we use here as an approximation of a relevant drug concentration, is often below reliable signal from this LC/MS method. Although this method can achieve a lower limit of detection as low as 0.05 ng/mL,[315] some presence of background signal and error introduced by sample dilution led us to employ rigorous standards for defining the drug signal as significant. Specifically, sample signal was determined to be non-zero if the LC/MS peak was at least four-times the background signal from the most recent ACN standard. Disregarding these standards, the average quantities of serum ETR from standard fiber implants at 120 days

would measure to be 1.2 ± 1.3 ng/mL (~2.8 nM). Comparably, in a subcutaneous implant study by Barret, *et al.,* plasma concentrations of the investigational ARV MK-8591 were measured to be approximately 10 nM at nearly 120 days,[226] which is greater than measured concentrations here, but of a comparable magnitude.

PK studies have been used as a prediction for efficacy, including for HIV-preventative LA-DDS.[226] Although some LA-DDS study probable efficacy as compared to known half maximal effective concentrations (EC_{50}) or IC_{50} values,[226] protective dosages are often determined by four times the protein adjusted IC_{90} (4x PA-IC_{90}), or even known protective dosages when available.[8,10,12,47,327,328] While we compare IC_{50} values here for a consistent comparison, MVC is known to be protective in humans with a minimum plasma concentration of 50 ng/mL.[329] RAL is likely protective at 40.88 ng/mL 4x PA-IC_{90}.[327] To our best knowledge, equivalent values for ETR are not reported. For our data, this suggests that fiber implants deliver likely protective dosages of MVC nearly immediately through 21 days, RAL from approximately 28 to 70 days, and relevant dosages for ETR are uncertain despite knowing ETR has greater potency (Table 4.1). Although serum concentrations are important for assessing efficacy of the LA-DDS, it is also important to measure drug concentrations in relevant tissues and drug potentially remaining in the implant to gain better insight for the long-acting potential of these materials.

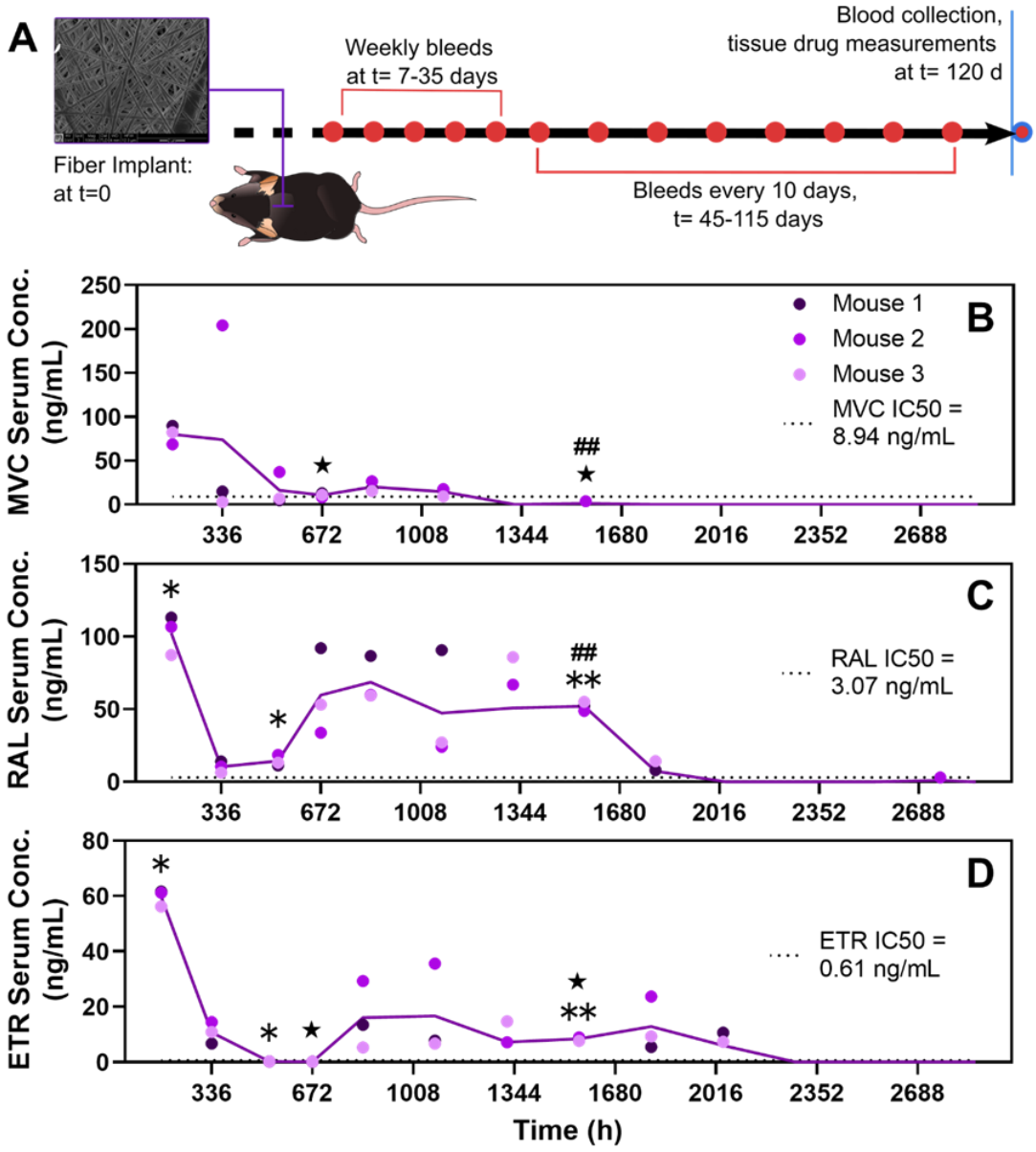

Figure 4.4. ARVs release with different rates and magnitudes over the extended timeframe.

*(A) Following fiber implantation, blood serum samples are collected at specified timepoints across the 120-day study. (B) MVC, (C) RAL, and (D) ETR serum concentrations are quantified overtime, for n=3 replicates. Individual data points are plotted per mouse unless drug concentrations were below detection, and the mean concentration calculating non-detectible values to be zero is plotted as a line. Significant serum concentration differences at each time point between drugs are denoted: MVC/RAL as ## for p<0.01; MVC/ETR as ★ for p<0.05, or ★★ for p<0.01; and RAL/ETR as * for p<0.05, or ** for p<0.01.*

4.4.4 *High concentrations of hydrophobic, high-protein affinity ETR remain in the implant, local tissue, and tissues relevant to HIV-protection*

To assess the remaining potential for drug release, implants were excised from the subcutis at the 120-day endpoint, and biopsies were collected at defined locations surrounding the remaining material. All assessed implants were significantly reduced in size and paste-like in consistency. In each assessed group, the direct implant site for one mouse was saved for histology (Appendix B Figure B.5). Therefore, implant drug concentrations are collected for just two implants, and six biopsies were collected from one animal, to not include the biopsies coordinated inline with the implant. Histology indicates some anticipated magnitude of foreign body reaction to the implants, with loosely accumulated collagen deposition and adhered immune cells less than 200 μm in thickness (Appendix B Figure B.5).

Detected drug within the remaining implants were quantified to be approximately 0.4%, 0.1%, and 69% of the original delivered dose of MVC, RAL, and ETR, respectively (Figure 4.5A). Specifically, ETR measures to be 86.3% and 51.8% in these implants. These remaining drug concentrations could indicate some potential for greater than 6 months of drug release. However, from measurements of blood serum PK which find ETR concentrations below reliable detection, it is unclear the exact magnitude which drug is released near the end of this study. Considering the low solubility of ETR compared to the other drugs, it might be hypothesized that the drug is nearly too insoluble to effectively release from the implant. It could also be hypothesized that fibrous encapsulation could be inhibiting drug release. Indeed, other studies of LA-DDS have shown that a non-biocompatible reaction can act as a barrier for drug diffusion.[169,330]

However, measurements of skin tissue biopsies outside of the implant show that ETR has eluted beyond the site of the implant (Figure 4.5B). Skin biopsies are sampled as an array varying

in locations ranging from the site of the implant to further than two cm away. Detection of drug does not appear to be correlated with sample location (Appendix B Figure C.4 C). Rather, the magnitude of ETR concentration follows a trend of the specific mouse. Interestingly, the second fiber treated mouse has significantly higher ETR skin tissue concentrations than either of the other subjects (Mouse 1 vs 2: $p=0.0008$; Mouse 2 vs 3: $p=0.0067$; Mouse 1 vs 3: $p>0.9999$). This increase in ETR in this mouse's tissues is also balanced by a lower percentage of ETR remaining in the implant (Figure 4.5A). Although there exists some subject-to-subject variation, drug specific trends are relatively consistent across samples, with only a single biopsy detecting either MVC or RAL at values approximately 174x and 717x less than ETR concentrations within the same biopsy, respectively. As seen in serum concentrations, implant and tissue drug concentrations appear to be highly dependent on drug properties. While implant and local skin ETR concentrations provide insight to the existence of a drug reservoir, the localized concentrations of ETR have minimal utility for HIV prevention.

At 120-days, we additionally collected the FRT, gastrointestinal tract, inguinal and lumbar lymph nodes, spleen, lungs, liver, and kidneys. Regions of the lower FRT, including the vagina and cervix were especially of interest considering the high global incidence of HIV infection specifically through these tissues, and for the known issues of FRT drug partitioning with systemically delivered ARVs.[4,6,22,23,26] The rectum is also an important tissue location for ARV partitioning, as this tissue site has the greatest estimated probability of HIV transmission per exposure.[22] High ARV partitioning in these tissues should be the priority in any HIV-preventative LA-DDS. While poor ARV partitioning has been observed in the FRT for PrEP, studies have also shown heterogenous ARV partitioning for HIV treatment.[20] Low ARV partitioning is especially observed in lymph nodes in comparison to peripheral blood concentrations.[309] This partitioning is

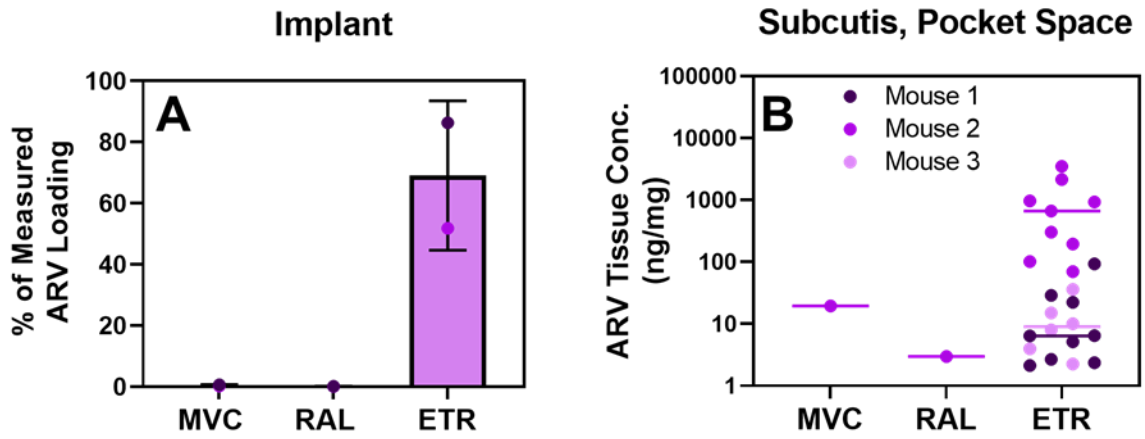

Figure 4.5. ETR remains in high concentrations in the implant and in the local tissue. *Quantities of drug detected in (A) the excised implant and (B) biopsies of the surrounding skin are reported as individual values when detectable, and bars representing the average ± standard deviation. Implant drug concentrations are measured as a percent of the original drug loading of the specific material sample and with n=2 implant samples. Biopsy samples are collected within approximately 1 cm of the implant site, with either n=6 or 9 biopsies per animal and plotted on a log scale.*

especially concerning considering the density of immune cells, and specifically CD4+ T cells, which reside in lymphoid tissues.[20,21] Further, lower drug partitioning in lymph nodes and secondary lymphoid tissues like the spleen is associated with the persistence of HIV infection and the development of viral sanctuary sites.[20] Therefore high partitioning of ARVs in these tissues could have interesting implications for both HIV treatment and prevention. Finally we assessed drug concentrations in the lung, liver, and kidney as tissues associated with drug clearance.[331,332]

Although serum concentration measurements indicate that drug may mostly be cleared at 120 days (Figure 4.4), large concentrations of ETR and some concentrations of MVC can be detected across the assessed tissues of interest (Figure 4.6). RAL was not detected within any of the tissue samples. It should be noted that detectible concentrations were not found consistently across all treated mice, except for comparatively low ETR concentrations in the liver (78.4 ± 47.3

ng/g, Figure 4.6B). However, ETR is also commonly detected in these tissues from washed fiber implants with similar trends in tissue-specific partitioning and the magnitudes of drug concentrations within these tissues (Appendix B Figure B.5, Table B.3). Most interestingly, for one fiber-treated mouse (Mouse 3) ETR was detected at 247469.2 ng/g in lymph node tissue, 14316.4 ng/g in rectal tissue, and 3035.7 ng/g in lower-FRT tissues. Further, these high drug concentrations are greater than the concentrations detected in the lung, liver, or kidney. For the lymph node sample, these ETR concentrations were approximately 1458x, 2054x, and 215x greater than the lung, liver, and kidney, respectively. For the FRT sample, concentrations are 18x greater than the lung, 25x greater than the liver, and 2.6x greater than the kidney. In other long-acting ARV studies, reported tissue concentrations are comparably lower than this study. In a study of cabotegravir implants studied in non-human primates, rectal drug concentrations ranged from less than 50 ng/g to less than 150 ng/g at 12 weeks.[333] Studies of a long-acting dolutegravir system in mice found that drug concentrations partitioned more significantly in blood plasma than in the female reproductive tract, which measured to have less than 400 ng/g of drug at approximately 12 weeks.[12]

While further assessments would be required to improve consistency, or to track the tissue distribution of ETR over time, these results importantly prove that ETR is indeed capable of distribution beyond the implant site. Further, ETR has some preferential distribution to our specific tissues of interest. However, since we are collecting tissues from just the 120-day timepoint of this study, it was unclear if these observations in tissue drug concentrations were due to the specific properties of the drug, or if this was an artifact of the timing of release from the electrospun materials. Indeed, RAL and MVC release is measured to be more rapid, and in part we know this is due to greater surface association of these drugs on the material surface through our washing

experiments. We therefore decided to further probe the effect of drug segmentation within the electrospun materials, and specifically the contribution of this greater material surface area on long-acting drug behaviors.

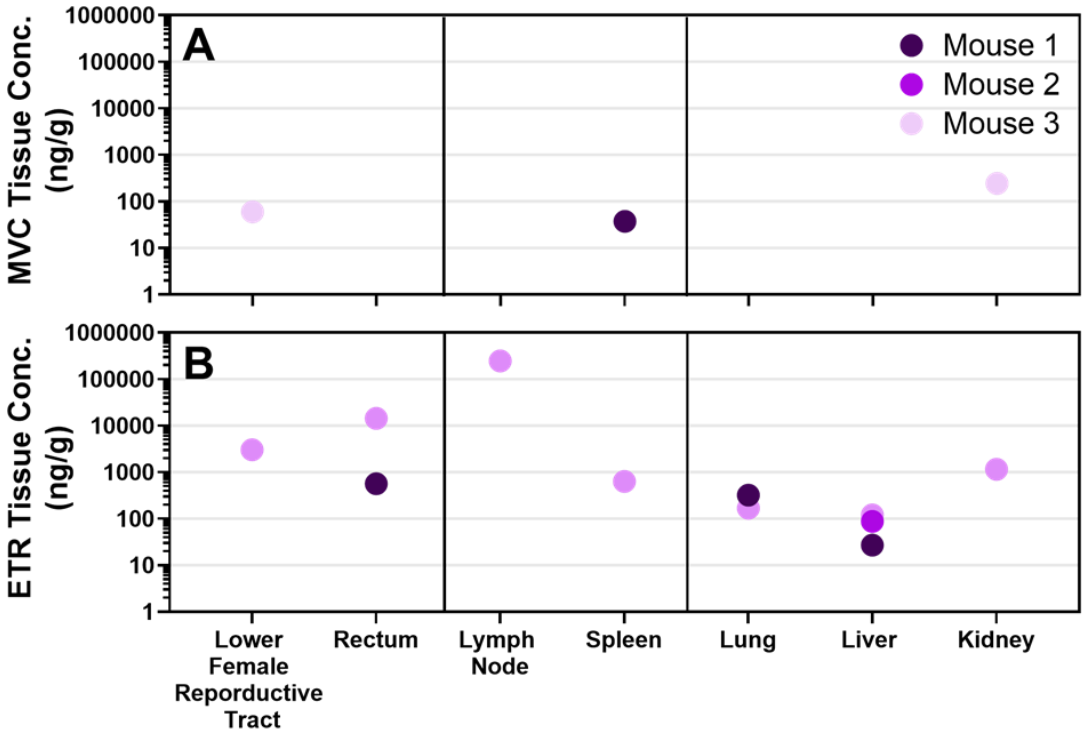

Figure 4.6. ETR can be detected in especially high concentrations in lymph nodes, rectum, and lower-female reproductive tract, while RAL is not detected in any tissue sample.

Detectible concentrations of (A) MVC and (B) ETR are plotted individually per tissue and represented for each individual fiber-treated mouse. Samples with ARV signal below the limit of detection are excluded from this plot.

4.4.5 *Alteration of DDS morphology does not alter drug-specific release or tissue partitioning*

One of the defining characteristics of electrospun materials is a greater surface-to-volume ratio. While this surface topography can provide functional attributes, the increased surface area also increases the exposure of the drug-delivery matrix to the surrounding environment. In a

homogeneous matrix system, this increased surface area would intrinsically increase the amount of drug at the surface. For electrospun fibers, hydrophilic drugs may specifically have increased surface association due to incompatibilities within hydrophobic polymers.[90] Rapid release of drug, even within the seven to 120-day timeframe may be an artifact of this increased surface area. Further, specific drug segmentation within these fiber features could be contributing to the timing of ARV detection in blood and tissues. To assess if the effect of drug release rates and endpoint tissue partitioning was due to the electrospun materials, we formulated and implanted additional triple-drug loaded, PLGA implants via solvent casting (Figure 4.7A, Appendix B Figure B.2). Solvent casting successfully created materials without pores or other surface features, and could highly encapsulate the triple-ARV formulation (Appendix B Figure B.2, Table B.2). However, encapsulation efficiency of ETR and especially MVC is significantly reduced compared to the electrospun materials (Appendix B Figure B.2). Despite this, if the material was having a significant impact on long-acting release, we would hypothesize that the rates of drug release would be shifted or extended over a longer period of time.

Despite these characterized differences between fiber and film materials, implant studies showed comparable pharmacokinetics between these two implants. While film implants did not have significant burst release like the standard fiber implants, initial release in the first 24 hours was comparable to the washed fiber implants, as quantified by comparable AUC_{24} measurements for MVC ($p>0.9999$), RAL ($p=0.8719$), and ETR ($p=0.8710$). (Appendix B Figure C.3, Table B.2). Washed films were also assessed and showed minimal differences in AUC_{24} values as compared to standard films ($p>0.9999$ for all drugs) suggesting that the three drugs within the films are minimally surface associated (Appendix B Table B.2). In comparing long-acting release, PK measurements show similar drug-dependent trends between standard fiber and film implants

(Table 4.4). The only quantifiable difference between the materials is a significantly greater average RAL C_{max} released by the films (Table 4.4), although both dosages would be significantly above estimated ~41 ng/mg protective dosages for RAL.[327]

Although all drug AUC_{LA} values between fibers and films are statistically comparable, the average AUC_{LA} for MVC is approximately 2.2x lower from films implants which is consistent with a 1.7x decrease in MVC encapsulation within the films (Appendix B Figure B.2). While the total quantity of MVC delivered by fibers is greater, most of this release is within the first few weeks. RAL shows the greatest release into blood serum from all materials. For films, this can be measured by significantly greater AUC_{LA} values compared to both MVC (p=0.0179) and ETR (p=0.0168). Films also achieve clearance times of approximately 75 days for MVC, 95 days for RAL, and 85 days for ETR, although significant quantities (87.0 and 1.9 ng/mL) of ETR are detected in serum for film treated mice at the 120-day endpoint (Figure 4.7B).

Table 4.4 Summary of pharmacokinetic (PK) quantifications for long-acting ARV release (7 days ≤ t ≤ 120 days).

	AUC (h·ng/mL)			C_{max} (ng/mL)		
Treatment	**MVC**	**RAL**	**ETR**	**MVC**	**RAL**	**ETR**
Fiber	32346.3 ± 24503.9	74322.7 ± 8294.6	22534.0 ± 8132.0	125.2 ± 68.3	102.4 ± 13.5	59.7 ± 3.0
Film	14907.0 ± 3983.2	98278.0 ± 10507.8	28174.0 ± 13259.5	37.47 ± 16.4	156.7 ± 9.9	76.8 ± 55.0
p-value (Fiber vs Film)	0.7157 (NS)	0.1122 (NS)	0.9208 (NS)	0.3852 (NS)	0.0187 (*)	0.9548 (NS)

Values reported as the mean ± standard deviation, or p-value for significance, for n=3 mice per group.

Within the remaining implant at 120 days, films also follow the same drug specific trend, where MVC and RAL are nearly depleted from the material, and approximately 60% of ETR remains in the implant (Figure 4.7C). Further, no MVC or RAL can be detected in local skin biopsies, however ETR is found in high concentrations across various distances from the implant site (Figure 4.7D). Drug-specific trends are further retained across the other measured tissues as well. As was observed for fiber implants, some detectable quantities of MVC could be calculated in liver and kidney tissues (Figure 4.7E), RAL was not detected for any tissue sample, and ETR could be detected in high concentrations in lymph nodes, the lower-FRT, and rectum (Figure 4.7F). ETR is again found in significant quantities within lymph node samples, with an average concentration of 346772 ng/g, which is 73x, 2972x, and 3749x greater than average values detected from the lung, liver, and kidney, respectively. Favorable partitioning of ETR in the lower-FRT is again observed, being on average 1.9x greater than lung, 77x greater than liver, and 98x than kidney concentrations (Appendix B Table B.3).

Our drug-specific observations across these different implant materials are consistent with what is known about the partitioning of these ARVs when delivered orally. In a study of cross-species ARV lymph node partitioning, Burgunder, *et al*. also characterized RAL as a drug which preferentially partitions into blood plasma rather than lymph nodes for both mice and non-human primates. MVC also shows some preferential partitioning into plasma for mice, but not for primates.[21] In a clinical trial of ETR for HIV treatment, preferential lymph node partitioning was also observed, with four-fold greater concentrations than in blood plasma. Further, this targeting was considered to be the source of ETR's effective viral reduction within the first week.[317] Interestingly, other reports have stated that extensive penetration of ETR outside blood plasma would not be expected due to the drug's high protein binding affinity.[334] Indeed, as illustrated in

our *in vitro* release studies, ETR binds extensively to serum proteins like albumin. However albumin drug binding is also associated with longer drug half-lives, and greater lymph node partitioning as seen with lymph node tracking dyes and even for targeted vaccination strategies.[95,98–101] Considering this, future studies could investigate the activity of free ETR in these tissues.

Results from this study demonstrate the determining role which drug properties have in long-acting drug release. Specifically, here we note the possible effects due to drug hydrophobicity and protein binding affinity. While the selection of a different polymer, or the design of rate limiting membrane may slow release and can be effective for specific agents, some drug behaviors like the solubility, and preferential blood or lymphatic uptake of drug from the implant site, are not controlled by simply engineering the implant. These findings further promote the need for careful drug selection – and likely prodrug modification of existing ARVs – in order to co-deliver diverse agents with similar dosing timeframes. Prodrugs with increased molecular weight are another strategy which can increase preferential lymphatic uptake of drugs from the subcutis.[335] While we show ETR has the potential for favorable partitioning, prodrug modification could further improve the consistency of this behavior when formulated within polymer vehicles like electrospun implants.

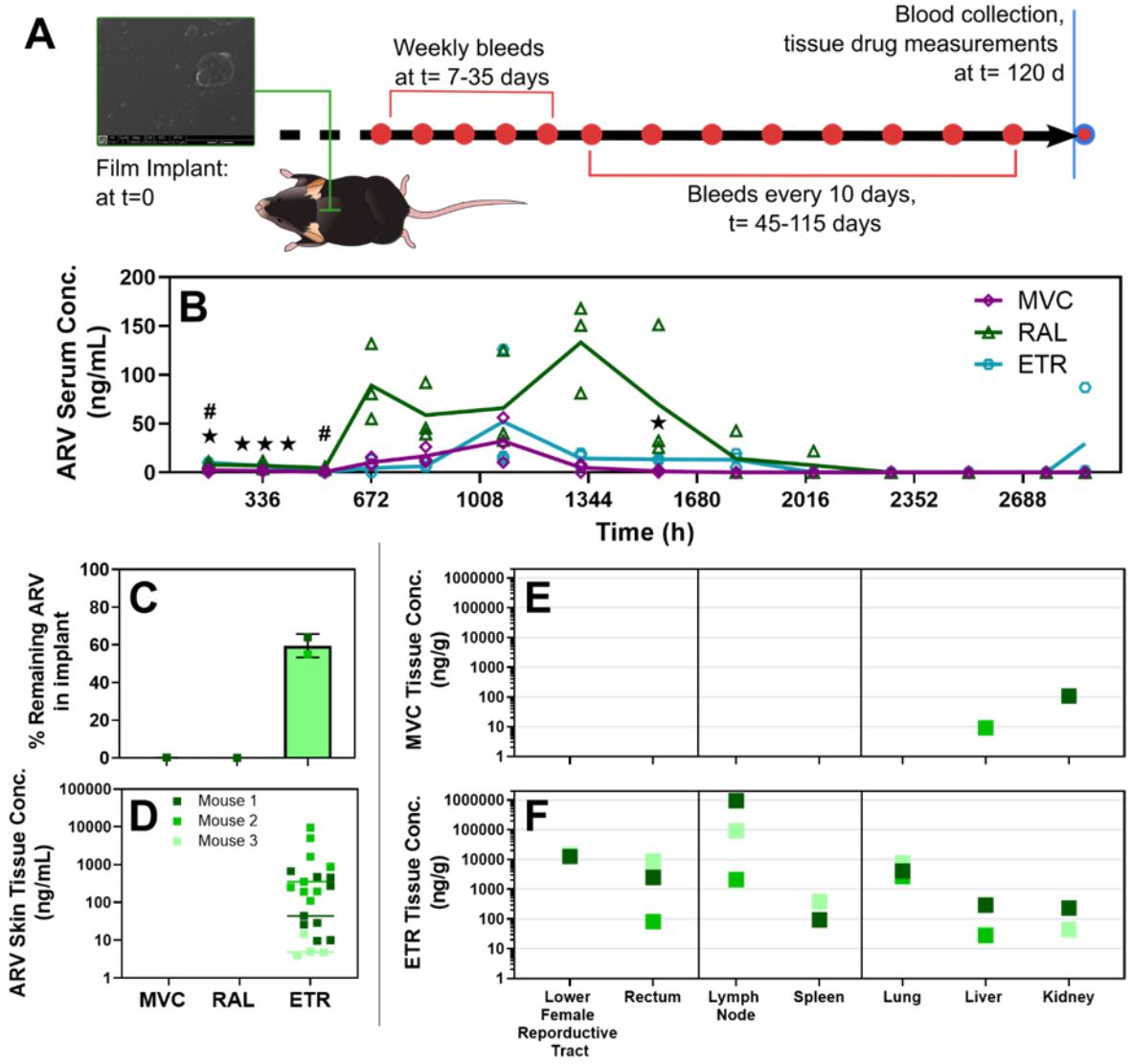

Figure 4.7. Surface topology does not alter drug-specific trends in ARV release rates or tissue partitioning.

(A) Solvent cast films are subcutaneously implanted in mice using the same experimental timepoints as the electrospun fiber implants. (B) All ARV concentrations are measured in blood serum overtime, with individual measurements plotted and lines representing the mean value for n=3 mice. Significant differences in mean serum concentrations are represented for: MVC/RAL as # for p<0.05; and MVC/ETR as ★ for p<0.05, or ★★★ for p<0.001. Remaining drug concentrations are measured at 120-days for (C) remaining film implants (n=2) and (D) skin tissue biopsies (n=2 mice and n=9 biopsies, and n=1 mouse with n=6 biopsies). Organ tissue biopsies with detectible (E) MVC and (F) ETR are plotted individually per mouse.

4.5 CONCLUSION

In the pursuit of multi-drug dosing, long-acting subcutaneous implants, we assessed the PK properties and tissue partitioning of three-physicochemically diverse ARVs co-formulated within electrospun materials. Electrospinning could successfully encapsulate the three-ARV agents together in a variety of polymer materials. Through *in vitro* polymer screening studies, acceptable drug release behaviors were observed from ester-terminated, low molecular weight PLGA fibers. Further, the insoluble and high-protein affinity properties of ETR required protein-enriched study conditions to attain predictive measurements. Through studies of this optimal material subcutaneously implanted in mice, burst release of the more hydrophilic drugs MVC and RAL were observed within the first 24-hours. Simple washing treatments were found to mitigate these excessive dosages and provided insight to the mechanism of this release likely being due to the greater surface association of drug on the fiber surface. Further, the large burst release of these drugs did not contribute to long-term PK measurements. In the extended-release timeframe, the physicochemically diverse ARVs exhibit drug-specific differences in blood serum uptake overtime. Interestingly, we also see drug-specific differences in tissue partitioning at 120 days. Finally, we found that the release and partitioning behaviors of these three ARVs were not dependent on increased surface area features of the electrospun materials. Rather, drug-specific PK observations were maintained when studying topologically smooth, solvent-cast film implants.

These results illustrate that specific drug properties here are the primary arbiter for release and tissue partitioning behaviors. Future studies can build upon this study to tailor the design of the DDS for the drug – or most importantly – the selection or modification of the drug. For MVC, a DDS which slows agent diffusion may better enable extended serum concentrations and further enable relevant tissue accumulation. For RAL, prodrug modification may be required to extend

release and facilitate tissue partitioning. Here we find that ETR may be a promising agent for long-acting delivery via the subcutis, as seen by the capacity for high lymph node, FRT, and rectal partitioning. By selecting for multiple agents with properties that together allow for extended release, protective dosages, and targeted tissue trafficking, a subcutaneous device could sufficiently meet the requirements for compliant-independent HIV protection.

4.6 ACKNOWLEDGEMENTS

Research was conducted at the University of Washington Mass Spectrometry Center and we specifically would like to thank D. Whittington for his help. We would also like to thank S. Braswell for SEM images collected at the University of Washington Molecular Analysis Facility, K. Wu and the B. Ratner lab for goniometer use, as well as B. Johnson and O. Korohod at the University of Washington Histology core. Research is supported by NIH/NIAID [R01-AI-150325 to KAW]; the Howard Hughes Medical Institute (HHMI) [Gilliam Fellowship for Advanced Study to JH and KAW], and ARCS (Achievement Rewards for College Scientists) foundation [to JH].

Chapter 5. EFFECT OF TISSUE MICROENVIRONMENT ON FIBROUS CAPSULE FORMATION TO BIOMATERIAL-COATED IMPLANTS

Adapted from: Hernandez, J. L., Park, J., Yao, S., Blakney, A. K., Nguyen, H. V, Katz, B. H., Jensen, J.T, & Woodrow, K.A.. (2021). Effect of tissue microenvironment on fibrous capsule formation to biomaterial-coated implants. Biomaterials 273, 120806.

Supporting figures are available in Appendix C

5.1 ABSTRACT

Within tissue exposed to the systemic immune system, lymphocytes and fibroblasts act against biomaterials via the development of a fibrous capsule, known as the foreign body reaction (FBR). Inspired by the natural tolerance that the uterine cavity has to foreign bodies, our study explores the role of microenvironment across classical (subcutaneous) and immune privileged (uterine) tissues in the development of the FBR. As a model biomaterial, we used electrospun fibers loaded with sclerosing agents to provoke scar tissue growth. Additionally, we integrated these materials onto an intrauterine device as a platform for intrauterine biomaterial study. Polyester materials in vitro achieved drug release up to 10 days, greater pro-inflammatory and pro-healing cytokine expression, and that the addition of gelatin enabled greater fibroblast attachment. We observed the material that induced the greatest FBR in the mouse, had no effect when inserted at the utero-tubal junction of non-human primates. These results suggest that the FBR varies across different tissue microenvironments, and a dampened fibrotic response exists in the uterine cavity, possibly due to immune privilege. Further study of immune privileged tissue factors on

biomaterials could broaden our understanding of the FBR and inform new methods for achieving biocompatibility in diverse tissues.

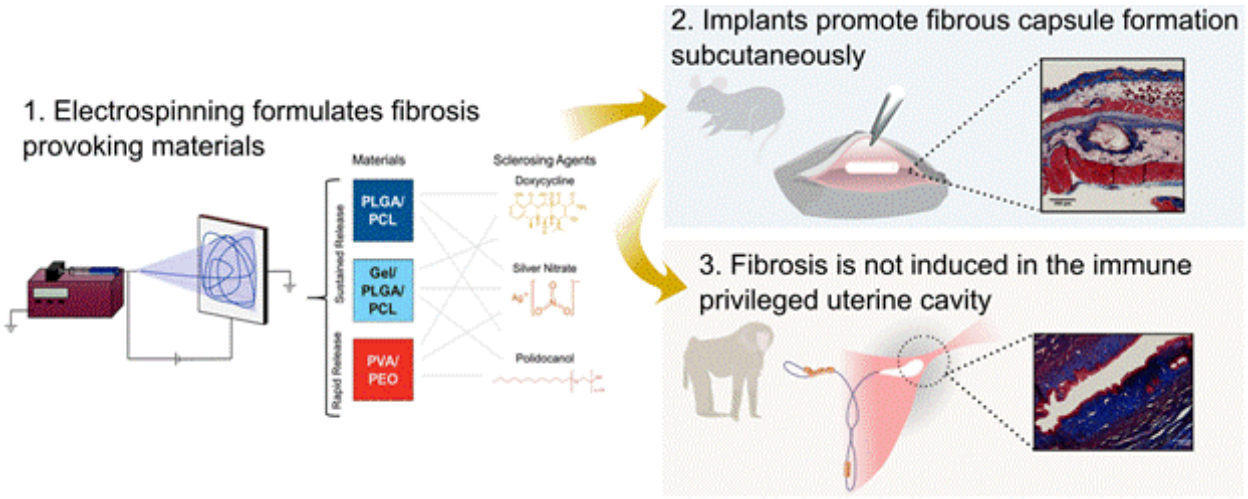

Figure 5.1. Graphical abstract for the effect of tissue microenvironment on fibrous capsule formation

5.2 INTRODUCTION

The foreign body reaction (FBR) describes the host response towards biomaterial implants.[170,177,178,194] The FBR begins with the spontaneous absorption of blood plasma proteins onto the biomaterial surface, forming a provisional matrix for FBR relevant cell types.[170,178,336–338] Although neutrophils are the first immune cells active in the FBR, macrophages are the primary arbiters of this response.[170,177,178] Polarized macrophages direct the local tissue response towards either a state of chronic inflammation or tissue remodeling,[170,177] which is further shaped by various cytokines that trigger migration of immune cells and fibroblasts. Fibroblasts aid in wound healing and are also responsible for the deposition of collagen-rich scar tissue known as the fibrous capsule[170,177,178] This pathology of the FBR is well characterized from the perspective of various biomaterial properties, but is less studied across different tissue microenvironments, including

differences in the local cellular, extracellular, chemical, and tissue mechanical properties at homeostasis.[170,194,206,268,339–341]

Biomaterial properties have been extensively investigated for their contributing role in the FBR. Hydrophobic materials show greater protein adsorption and macrophage adhesion, which may promote fibrotic encapsulation.[170,336,339,342–344] For hydrophilic materials, macrophages have shown greater adhesion to cationic surfaces as compared to anionic or nonionic implants.[170,343] Material topography has been shown to impact development of the FBR, with smooth and flat implants inducing greater foreign body giant cell (FBGC) adhesion and fibrotic capsule formation.[170,345] Mechanical mismatch between biomaterial and the local tissue has also been shown to provoke pro-inflammatory responses.[170,346,347] As such, strategies to prevent the FBR have focused on changing attributes of the biomaterial itself such as employing inert polymers, surface modifications, control of geometry, and patterning techniques to improve biocompatibility and tissue integration.[170,177,336,339,348] Although the FBR is well studied from the biomaterials engineering perspective, less is known about the role of different tissue microenvironments.[268,339,340,344] Sites of immune privilege are particularly interesting to consider given their immunosuppressive bias that is distinguished by large populations of regulatory T-cells[349], increased expression of anti-inflammatory cytokines,[350] and matrix metalloproteinases (MMPs).[243,244] Whether immune privilege alone can hinder development of the FBR induced by biomaterials has not been investigated, and could have important implications for future design of biomaterial implants.

The FBR has been best characterized within the subcutis due to the testability in mice and the minimally invasiveness of the procedure. While these factors have made the subcutaneous implant model the standard for assessing implant biocompatibility, it has narrowed our

understanding of microenvironmental factors that could be exploited for controlling the FBR.[194,344,351–354] In contrast to subcutaneous tissue, specific regions of the body exist that confer immune privilege in order to protect tissue function, including the eye, brain, and reproductive organs.[238] Immune privilege in the uterus prevents host recognition of haploid germ cells, paternal antigens in sperm cells, as well as embryos and fetuses.[238–240] Despite this privileged immune status, some biomaterial foreign bodies are known to provoke an immune response in the uterus. In fact, the contraceptive mechanism of intrauterine devices (IUDs) is due in part to inflammation generated towards a foreign body.[245–248] Although IUDs provoke an immune response, these devices are not subject to fibrous capsule formation and can be readily removed.[245] Intrauterine fibrosis is known to arise only under chronic provocation. For example, repeated exposure to *Chlamydia trachomatis* can cause chronic inflammation of the fallopian tube that leads to tubal occlusion and infertility.[250,252] Cytotoxic agents that cause sclerosis have also been administered within the uterine cavity as a method to induce scar tissue growth for permanent contraception.[250,251,355–357] The uterus is an interesting compartment to investigate microenvironmental effects on the FBR because it is a highly vascularized organ but, as described above and in contrast to the subcutis, shows differential responses to foreign bodies. Investigating microenvironmental effects in the uterus towards biomaterials previously described in the subcutis as either inert or capable of generating an inflammatory response could demonstrate a larger role for leveraging host factors to inhibit the FBR to biomaterial implants.[170,174,221]

Here, we investigated the relationship between the FBR resulting in fibrous capsule formation across the classical (subcutaneous) and immune privileged (uterine) environments. Biomaterials eluting various sclerosing agents were used to further provoke a FBR towards implants. Electrospinning was implemented as the material fabrication method for its known

ability to efficiently encapsulate physicochemically diverse agents, modulate drug release rates,[90,167,168,269,358] and for ease of integration onto an IUD. Materials were screened for a pro-fibrotic response both *in vitro* and in a subcutaneous mouse model, then highly fibrotic materials were placed *via* an IUD into an intrauterine baboon model. Although the biomaterials proved to be highly fibrotic in the subcutis, the same materials did not provoke a response within the uterine cavity. This is the first study to our knowledge showing that uterine immune privilege alone may hinder development of a fibrotic FBR. The foreign body response to biomaterials has been investigated primarily from the perspective of biomaterial attributes (e.g., surface chemistry, topology, mechanical, etc.), but only minor attention has been given to the role of host microenvironmental factors. We show that using biomaterials with a record of inducing a strong foreign body response, and even when combined with fibrotic inducers, fail to initiate fibrosis when transplanted into a site of immune privilege in the uterus. Our results suggest the importance of identifying host factors that could be leveraged in combination with biomaterials engineering to reduce the foreign body response to medical implants in non-immune privileged tissue microenvironments.

5.3 MATERIALS AND METHODS

5.3.1. Electrospinning fiber formulations

Poly(lactic-co-glycolic acid) (PLGA, 50:50 L:G, acid terminated, inherent viscosity = 0.55-0.75 dL/g, Lactel Absorbable Polymers) and polycaprolactone (PCL, Mw = 80,000, Sigma-Aldrich) were blended at a ratio of 80:20 (wt./wt.) in 15% (wt./v) hexafluoroisopropanol (HFIP, Oakwood Chemical). PLGA/PCL/Gelatin (Gel, Type A from porcine skin, Sigma-Aldrich) was created at a ratio of 64:16:20 (wt./wt./wt.). Sclerosing agents were added into the aqueous polymer

solution at defined weight percent loadings in respect to polymer mass. The tested sclerosing agents include doxycycline hyclate (Dox, MP Biochemicals), nonaethylene glycol monododecyl ether for polidocanol (PD, Sigma-Aldrich), and silver nitrate (SN, Sigma-Aldrich). Polymers were needle electrospun using a 1 mL glass syringe and 21 G, 1.5-inch needle. A voltage of 10-13 kV was applied, and polymer was extruded at a rate of 40 µL/min. Poly(vinyl alcohol) (PVA, 87-90% hydrolyzed, MW=30,000-70,000, Sigma-Aldrich) and poly(ethylene oxide) (PEO, Mw=400,000, Scientific Polymer Products, Inc.) blends were added at a ratio of 86:14 (wt./wt.) into 17.4% (wt./v) deionized water with 0.0224% (wt./v) sodium chloride. PVA/PEO materials were electrospun using an Elmarco Nanospider (Liberec, Czech Republic). The carriage rate was set to 350 mm/s, with an electrode distance of 200 cm, and with 100 kV voltage difference. Electrospun fibers were prepared into 10 mg, 1.5 cm long sections, UV sterilized for 30 minutes per side, and hand-rolled cylinders secured using 20% (wt./v) PVA/water glue.

5.3.2. Sclerosing agent release, encapsulation, and measurement

Release studies were conducted using the drug loading implemented for mouse studies and at sink conditions. Dox and PD used 1x DPBS (Mediatech, Inc.) as the release medium, and ultrapure water (Millipore Sigma) was used for SN. Release media samples were taken at specified timepoints starting at five minutes and out to two weeks. Percent release was quantified as a ratio of the measured sample signal (x_{Sample}) to the signal of full theoretical loading (x_{Theo}), with signal from the blank release media (x_{Blank}) subtracted out, as shown in the equation below [5.1]:

$$\%\ Release = 100 \times \frac{x_{Sample} - x_{Blank}}{x_{Theo} - x_{Blank}} \quad (5.1)$$

Encapsulation efficiency of drug within the materials was measured after dissolving polyester fibers in dimethyl sulfoxide (DMSO, BDH/VWR Analytical) and PVA/PEO fibers in water. Percent encapsulation (% EE) was calculated using the equation below [5.2]:

$$\% EE = 100 \times \frac{Measured\ drug\ mass\ in\ fiber\ sample}{Theoretical\ drug\ mass\ in\ fiber} \quad (5.2)$$

Dox was quantified by high-performance liquid chromatography (HPLC) (Simadzu Prominence) using a method referenced from Kogawa, *et al.*.[359] Briefly, we used a detector wavelength of 360 nm, injection volume of 20 µL, and A C18 column (Phenomenex Kinetex) for the stationary phase. The mobile phase 75:25 (v/v) water/ACN (HPLC grade, Fisher) with 0.1% (v/v) trifluoroacetic acid (TFA, Sigma-Aldrich) was used, resulting in a retention time of 10 minutes for Dox. SN release was quantified using inductively coupled plasma optical emission spectrometry (ICP-OES) (Perkin Elmer Optima 8300). Silver was detected using the preferred emission wavelength of 328.068 nm. PD approximation by thin-layer chromatography (TLC) was adapted from Hahn-Dienstrop (2007).[360] Samples, drug spiked positive control samples, blank fiber negative control samples, and PD standards were all spotted by glass capillary onto a single TLC plate (250 µm, particle size 10-12 µm, Millipore Sigma). The plate was dried (approximately 1 min), then saturated in Dragendorff's reagent (Sigma Life Science) for 1 minute, removed, and set flat to dry again. Once the color had developed, images of the plates were collected using a standard office scanner (Aficio MP 301, Ricoh, USA). Plate images were analyzed using ImageJ (FIJI/ImageJ 1.51s, National Institutes of Health, USA)[314] software to quantify spot pixel intensity in the blue channel

5.3.3 Cell culture assessment of cytokine expression and cell attachment

To assess the induction of inflammatory responses, RAW 264.7 macrophages were used as the cell model, (kindly gifted by Dr. James Bryers). Cells were cultured in Dulbecco's Modified Eagle Medium (DMEM, 4.5 g/L D-Glucose, L-glutamine, 110 mg/L sodium pyruvate, Gibco) supplemented with 10% (v/v) fetal bovine serum (FBS, Gibco) and 1% (v/v) penicillin-streptomycin (P/S, Gibco) and seeded 0.5x106 per well in a 6-well plate. Drug treated cells were

cultured with 10 mg of fiber, or drug spiked media at the equivalent dose. For a positive control, 100 ng/mL of lipopolysaccharide (LPS) was added to the media. Media was collected after 48 hours of culture, centrifuged at 1500 RPM for 10 minutes, and the supernatant was stored at -80°C until analysis. Expression of TNF-α, IL-1β, and IL-10 were determined via enzyme-linked immunosorbent assay (ELISA) kits purchased from PeproTech and used as instructed.

To test fibroblast attachment, fiber mats were controlled for surface area and mass, and delivered onto glass coverslips with a final fiber mass of 10 ± 0.1 mg. Collagen coated coverslips were used as a control for cell attachment and were created with 40 µL collagen (rat tail collagen type I, Corning) diluted to 50 µg/mL in 0.2 N acetic acid (Fisher Scientific). Cultured NIH 3T3 fibroblasts were resuspended in serum free, high-glucose DMEM with 1% P/S. Coverslips in a 6-well plate were seeded with 2.5x105 cells. After 24-hours of culture, the quantity of attached cells on the material was measured using Cell Titer Blue (Promega, used as instructed)

5.3.4. Subcutaneous implant surgeries

Murine research was approved by the Institutional Animal Care and Use Committee (IACUC) at the University of Washington, and all guidelines for care were followed. Implantation studies were conducted using 8 to 12-week-old female C57BL/6J mice (Jackson Laboratory). Mice were anesthetized using isoflurane delivered by a precision gas vaporizer and given a subcutaneous injection of buprenorphine hydrochloride (0.05 mg/kg) as an analgesic. Two incisions were made just off the midline of the dorsum. A single pocket was made from each incision in the subcutaneous space above each scapula using blunt dissection. One fiber/drug implant was placed in each pocket. After 28 days, entire pocket sections of the mouse were excised and fixed in a formalin solution made from 4% (v/v) paraformaldehyde (Electron Microscopy Sciences, 40%

aqueous solution). Tissues were sectioned and stained with Masson's trichrome. Images were captured using a Sakura VisionTek Digital Microscope.

5.3.5 Fiber IUD placement in baboons

Experiments conducted with baboons were approved by the IACUC at Oregon Health and Sciences University. We created drug-eluting fiber intrauterine devices (IUD) by integrating 10 mg of electrospun fiber materials onto each arm of a nitinol wire IUD frame (Figure 5.2*C).* The nitinol wire frames were supplied by ContraMed LLC, (Campbell, CA). Three healthy adult female baboons received IUDs; blank-fiber (PLGA/PCL/Gel) device (n=1, Papio hamadryas), and silver nitrate loaded fiber devices (loaded at 60% (wt./wt.) SN in PLGA/PCL/Gel Fibers) (n=2, one each P. hamadryas, P. Anubis). The females received general anesthesia and underwent transcervical placement of the IUDs using an insertion tube under ultrasound guidance. Successful placement of the devices was confirmed by contrast hysterosalpingogram using fluoroscopy. After 28-days, the animals underwent humane euthanasia and necropsy. A gross dissection of the extirpated reproductive tract was performed, with the uterine cavity opened to evaluate the position of the IUD arms in the cornual region. Tissue sections taken from this region, the intramural fallopian tube, the endometrium, and tubal isthmus were collected for histological analysis. These tissues were paraffin embedded, and representative sections stained with hematoxylin and eosin, and with Masson's trichrome.

5.3.6. Image analysis of histology to measure fibrotic response to study materials

Appendix C Figure C.5 illustrates our process for the quantitative image analysis of the murine subcutaneous histology. In the subcutis, we focused on measuring inflammation and collagen as correlates of the FBR. We first defined three regions of interest (ROI) to perform

unbiased measurements. The first ROI is defined by a line, intersecting the center point of the implant in the image of the implant cross-section, and drawn perpendicular to the skin surface (L1, solid white line). To approximate the implant location for materials dissolved by the study endpoint (PVA/PEO), the center ROI was determined to be at the center point of observed collagen or immune cell staining. Two additional ROIs are defined as parallel lines (solid white line) 1 mm to the left (L2) and right (L3) of L1. ImageJ was used to take three measurements at each of these ROIs: (1) subcutis length = length between the two muscle layers (dashed white line, Lsc), (2) inflammation = total length of accumulated immune cells stained within the subcutis, marked by red stain and additionally identified by cell morphology (dashed black line with in-turned black arrow heads, Li), and (3) fibrosis = total length of collagen blue stain (dashed black line with in-turned white arrow heads, Lf). Collagen deposition was defined as the length of both loose collagen (light blue with visible background white light) and dense collagen (dark blue) staining (not shown on image). The inflammatory or fibrotic response is calculated as a percent length of the total subcutis.

Supplementary assessment methods included scoring and capsule measurements (Appendix C, Figure C.3). Scoring analysis of the histology images is adapted from the scoring system used by Greenhalgh, *et al.*.[361] In brief, lower scores for either collagen deposition or inflammation would be given to histology images with minimal or no collagen staining or tissue sections with no immune cell accumulation. Scores closer to 12 would be given to tissue images with highly dense collagen staining or thick layers of inflammatory cells within the subcutis. Scorers were first shown two test images as a means of calibration, and additionally assessed sham control images for method validation (Figure 5.6O and Appendix C Figure C.4). A full description of scoring ranges, criteria, and example diagrams is shown in Appendix C Table C.1.

For images with an implant present at the study endpoint, we also collected measurements of the surrounding layer of inflammatory cells and the fibrous capsule. Inflammatory cells were stained red and identified at the interface of the implant. The collagen-rich fibrous capsule is stained blue and was defined from the interface of the inflammatory cell layer, until either the end of collagen staining or at an observable change in collagen density.

Fibrosis in the fallopian tube is best defined by the by the (1) absence of epithelium and (2) presence of collagen-rich scar tissue in the fallopian tube luminal space. Histology images were therefore visually assessed for these features. To quantify tubal patency in the baboon histology images (Figure 5.7), we additionally measured the perimeter of uninterrupted epithelium (yellow dashed line) using ImageJ.

5.3.7. Statistical analysis

Statistical analysis was conducted using GraphPad Prism 8 software. Statistical significance between for fiber diameter measurements, cytokine expression, histology scoring, and measurements was all determined using two-way ANOVA. One-way ANOVA was used to compare cytokine expression of controls and tested fiber/drugs.

5.4 RESULTS AND DISCUSSION

5.4.1. Design targets and attributes of electrospun fiber formulations to provoke fibrosis

To probe microenvironmental effects on the FBR, we selected polymers commonly employed in drug delivery systems with different timeframes of drug release. PVA and PEO have been used to study factors that impact the development of a fibrous capsule,[174] and to formulate solid dosage forms for short-timeframe mucosal drug delivery.[272,276] Polyesters such as PLGA and

PCL have been extensively studied as subcutaneous implants due to their biocompatibility, long-term biodegradability, and drug release.[321,362] Using these polymers, we formulated three different blends to elicit known mechanisms in the FBR that culminate in fibrous capsule formation, which is collagen rich, scar tissue growth at the implant surface. First, water-soluble PVA/PEO fibers, which exhibit rapid dissolution, were used to burst release sclerosants to only induce acute inflammation – the initial phase of the FBR. Second, we used a blend of PLGA and PCL to provide sustained sclerosant delivery and a material depot for inducing persistent and chronic inflammation. Finally, since fibroblasts play a critical role in fibrous capsule formation, PLGA/PCL fiber blends were modified to incorporate gelatin (Gel), which contains RGD-binding sequences shown to enhance fibroblast attachment[363] and macrophage fusion for foreign body giant cell (FBGC) formation.[170]

Polymers were formulated with three physicochemically and mechanistically diverse sclerosing agents used to further provoke an immune response and initiate fibrosis (Appendix C Table C.1, Figure 5.2). Sclerosing agents were also selected from drugs clinically used for fibrosis inducing therapies. Doxycycline (Dox) is a water soluble tetracycline derivative that has been shown to initiate fibrosis by inhibiting matrix metalloproteinases (MMPs), thereby allowing an overabundance of extracellular matrix (ECM) proteins to deposit.[364] Silver nitrate (SN) salt is a water soluble compound implicated in epithelial cell damage, which contributes to the acute and chronic inflammatory responses.[365–367] Topically delivered 0.5% SN solution is used clinically to treat burn wounds, which promotes tissue healing via stimulating an amplified immune response.[368] Polidocanol (PD) is a non-ionic liquid surfactant that is miscible with water and used intravenously as a 1% PD foam for varicose vein sclerotherapy mediated by endothelial cell

lysis.[356,369,370] These distinct agents were screened in our study to best identify an agent appropriate for inducing fibrosis and for probing the intrauterine response.

Table 5.1. Sclerosant fiber dosing for in vitro and in vivo studies.

Sclerosing Agent	**Molecular Weight** (g/mol)	**Aqueous Solubility/ Miscibility** (mg/mL)	**20% IC50 Cells** Free drug dose mg/mL (% loading in fibers formulation)	**10% LD50 Mice** Free drug dose mg/mL (% loading in fibers formulation)
Dox	1025.89 [371]	50 [371]	0.3 (3%)	2 (20%) [372,373]
SN	169.872 [367]	2450 [367]	0.001 (0.01%)	0.16 (1.6%) [373,374]
PD	494.71 [369]	100 [369]	0.01 (0.1%)	1.6 (16%) [373,375]

In vitro toxicity determined experimentally using 3T3 fibroblasts and TZM-bL epithelial cells (Appendix B Figure C.1). In vivo doses calculated from reported murine LD50 values.

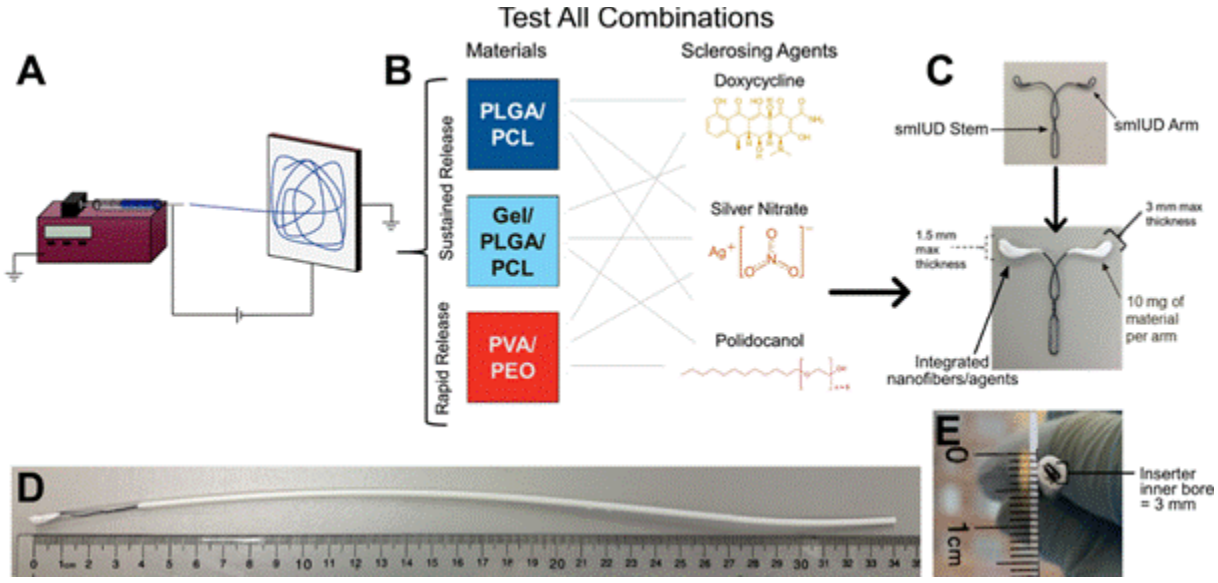

Figure 5.2. Fiber-integrated IUD device and material design.

(A) A schematic of the electrospinning process to develop these fibers, and (B) the material drug combinations tested throughout this study. (C) Image of the modified VeraCept® nitinol wire IUD frame (top) and the proposed combined IUD/fiber device with required dimensions for the wrapped electrospun fibers (bottom). Fiber dimensions were constrained by the IUD insertion tube required for placement of the (D) folded fiber-IUD. The (E) inner bore of the inserter is 3 mm in diameter.

Table 5.2. Sclerosant fiber properties and release profile.

Fiber Formulation		Fiber diameter (μm)	Observed Max Drug Loading (wt. drug/wt. polymer)	% Drug Encapsulation Efficiency	Time to max release
PLGA/PCL	No Drug	1.4± 0.47 (****)	-	-	-
	Dox	1.0 ± 0.19 (****, ###)	60%	98 ± 0.54%	7d
	SN	1.0 ± 0.37 (****, ####)	50%	~56%	10 d
	PD	2.1 ± 2.3	60%	~104%	7 d
PLGA/PCL/Gel	No Drug	0.96 ± 0.22 (****, ####)	-	-	-
	Dox	1.1 ± 0.19 (****, ##)	70%	81 ± 0.17%	10 d
	SN	0.94 ± 0.25 (****, ####)	60%	~100%	10 d
	PD	1.1 ± 0.22 (****, ##)	60%	~97%	3 d
PVA/PEO	No Drug	1.0 ± 0.37 (****, ####)	-	-	-
	Dox	1.1 ± 0.34 (****, ##)	70%	92 ± 7.0%	6 h
	SN	1.14 ± 0.32 (****)	40%	72 ± 3.5%	NA
	PD	0.99 ± 0.22 (****, ####)	30%	NA	NA

*Fiber diameters determined using the cell culture dose, with n=3 samples, n=3 images, and n=20 measurements. Representative fiber images are shown in Supporting Figure C.2. Encapsulation efficiency quantified for mouse implant dose, with n=3 samples, and n=3 measurements. Values reported as mean ± standard deviation. If encapsulation efficiency could not be quantified, the maximum percent drug released is reported. **** = significantly smaller fibers as compared to PLGA/PCL/PD fibers ($p < 0.0001$). ##, ###, and #### = significantly smaller fibers as compared to blank PLGA/PCL fibers ($p < 0.01$, $p < 0.001$, and $p < 0.0001$, respectively).*

We successfully electrospun all drugs and polymers into solid dosage forms. The PLGA/PCL/Gel polymer blend had the highest observed drug loading for all sclerosing agents and Dox showed the highest loading of up to 70 wt.% within the polymer compositions (Table 5.2). The higher loading in PLGA/PCL/Gel is likely a product of greater compatibility of the more

hydrophilic drugs with hydrophilic functional groups of gelatin. Similarly in a study of PCL/Gel electrospun fibers by Xue, *et al*., gelatin improved dispersion of hydrophilic metronidazole at higher drug loadings, specifically as an effect of hydrogen bonding between gelatin's amine and carboxyl functional groups with the drug and PCL.[363] The sclerosants SN and PD showed loss of electrospinnability at high loading and could only be formulated at 30-40 wt.% in PVA/PEO. This low drug loading is potentially due to high solution conductivity or changes in viscosity, which are factors known to affect Taylor cone formation of the charged polymer solution.[90] Overall, we electrospun sclerosants loaded at relevant doses that could be tested *in vitro* to identify highly immunogenic biomaterials for assessing microenvironment effects in vivo.

5.4.2. Electrospun materials formulate rapid or sustained sclerosing agent release profiles

As expected, PVA/PEO fiber blends showed rapid sclerosant release within an hour, which is consistent with their complete dissolution (Figure 5.3, Table 5.2). Similar studies of PVA fibers have achieved full drug release and material dissolution within 10-30 minutes.[272,276] In contrast, polyester blends showed biphasic release of sclerosants. Within the first 24 hours, an initial burst release from PLGA/PCL fibers accounted for approximately 98% total loaded Dox, 18% of SN, and 82% of PD. For PLGA/PCL/Gel fibers, the initial burst release accounted for 67% of total Dox, 30% of SN, and 60% of PD (Figure 5.3). After 24 hours, the second release phase yielded slower release out to a maximum of 10 days with pseudo-linear release rates of approximately 5.8 µg/day PLGA/PCL/Gel/Dox, 1.4 µg/day PLGA/PCL/Gel/SN, and 0.45 µg/day PLGA/PCL/SN) (Figure 5.3, Table 5.2).

Overall, we observed that release profiles were dominated by the material composition of the fiber formulations rather than the physicochemical properties of the sclerosants. That is, physicochemically disparate sclerosants like Dox and PD showed similar release from fibers with

the same polymer composition like PLGA/PCL (Table 5.2, Figure 5.3). While specific sclerosants such as SN showed some variability in the initial burst release phase from the polyester blends, the cumulative time to 100% release was ultimately the same as the other drugs. These findings are consistent with a study from Carson, *et al*., which determined the ratio of PLGA/PCL in electrospun fibers and hydrogen bonding between hydrophilic tenofovir and the polyester backbone mediated the controlled release of drug beyond 10 days.[167] Overall, we successfully developed polymer blends that achieve either rapid (≤24 hours) or sustained agent release (≥ 7 days) and material persistence. We think these materials are suitable for promoting the FBR since the acute inflammation phase occurs on the order of hours to days, whereas responses that progress to the chronic inflammatory phase occurs over multiple weeks.[170] Based on this understanding, we hypothesize that PLGA/PCL materials that release agent for 10-days will extend into the chronic inflammation phase. In contrast, the PVA/PEO materials would dissolve within hours following implantation and are expected to provide stimuli during the timeframe of the acute inflammation phase.

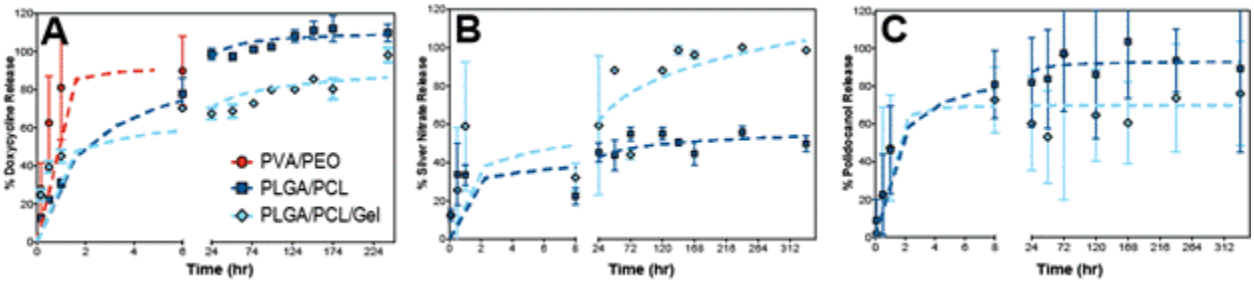

Figure 5.3. Different polymer compositions vary the release rate of sclerosing agents.
Release of (A) Dox, (B) SN, and (C) PD from all fiber blends as percent of total theoretical loading plotted over time from n = 3 fiber sections (mean ± standard deviation).

5.4.3. Polyester electrospun materials induce FBR relevant in vitro macrophage cytokine expression

Next, we sought to characterize the immune response generated to our different sclerosant formulations. Activated macrophages have been described to exist in classically (M1) or alternatively (M2) polarized states, both which are known to influence development of the FBR.[376] M1 macrophages are necessary for the destruction of pathogens, clearing cellular debris, and recruiting immune cells during the initial acute inflammatory phase, but this response also results in tissue damage. M2 macrophages attenuate inflammation, but also promote tissue remodeling and the synthesis of ECM proteins, such as collagen.[170,177,194] These two activation modes are phenotypically differentiated by the expression of specific cytokines.[170,177,194,377] Moreover, paracrine signaling of cytokines secreted from macrophages during the FBR shapes the response from additional cell types, including other immune cells and fibroblasts.[170,177] Here, we measured the cytokine expression from the murine macrophage cell line RAW 264.7 in response to our materials.[352,378] The cytokines tumor necrosis factor alpha (TNF-α) and interleukin 1 beta (IL-1β) were identified as markers of a pro-inflammatory response, characteristic of M1 macrophages. Interleukin 10 (IL-10) expression was quantified as a marker of M2 macrophages.[177] Jones, *et al*. has shown that biomaterial adherent macrophages are not at first fully classically activated but rather undergo a phenotypic change towards the alternative activation state characterized by secretion of higher concentrations of IL-10 over time.[377] We hypothesized that the FBR would require cytokine expression from both M1 and M2 activated macrophages, including TNF-α, IL-1β, and IL-10.[170,177,194,376,379,380]

For cell culture experiments, we decreased the drug loading within the fibers to be 0.01 - 3 wt.%, or 20% LD50 for each drug, to sustain greater than 90% cell viability (Table 5.1, Appendix C Figure C.1, Figure 5.4A-D). Cells treated with LPS as a positive control expressed the predicted

excess of measured cytokines, thereby validating that the cell assay could sufficiently capture the macrophage response. We found that all PVA/PEO fiber formulations induced TNF-α but not IL-1β or IL-10 (Figure 5.4). For both SN and PD, IL-1β and IL-10 expression were significantly lower when delivered by PVA/PEO, even when compared to free drug (Figure 5.4 K, L, O, & P). A minimal cytokine profile from the PVA/PEO fibers is consistent with our hypothesis that the rapid dissolution of the fibers can capture the early, pro-inflammatory phases of the FBR, but would not sustain a cytokine profile for excessive scar tissue growth or fibrous capsule formation.

Blank PLGA/PCL/Gel and PLGA/PCL/Gel/Dox fibers provoked higher TNF-α expression than other polymer blends (Figure 5.4 E & F). Additionally, blank PLGA/PCL/Gel fibers had significantly higher expression of IL-1β as compared to all control groups, and significantly higher IL-10 expression than the media control (Figure 5.4 I & M). This suggests that PLGA/PCL/Gel fibers alone could induce the initial inflammatory response leading to fibrotic capsule formation. These data support our hypothesis that material persistence could mediate large immune stimulation. Although these data support a drug-free implant, this study *in vitro* quantified the response from a single cell type at a single timepoint. Therefore, long-term *in vivo* studies of the materials were conducted to further assess the value of sclerosing agent enhanced implants.

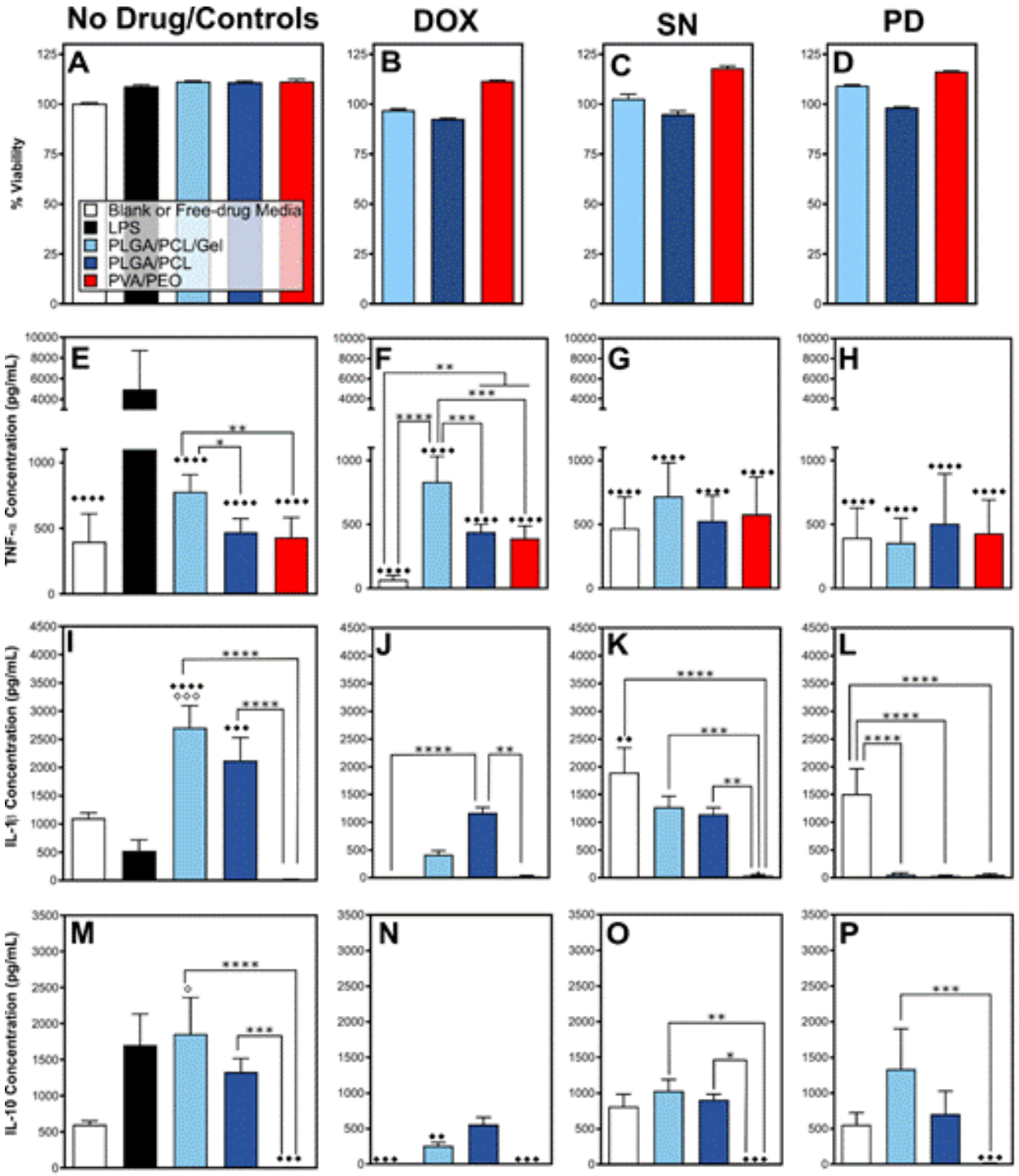

Figure 5.4. Fibers/drug blends affect the expression of pro- and anti-inflammatory cytokines by macrophages.

(A-D) Cell viability and expression of the proinflammatory cytokines (E-H) TNF-α,(I-L) IL-1β, and anti-inflammatory cytokine (M-P) IL-10 from RAW 264.7 macrophages 48-hours post treatment (mean + standard deviation). Viability results are measured for n=1 cultured fiber

*(Figure 5.4. continued) sections and n=3 assay replicates as a percent signal against untreated cells. Cytokine results are measured from n=3 fiber sections, n=3 assay replicates. Statistically significant different expression than media (◇) and LPS (◆) is marked on all plots. Statistical differences between material types (*) are specifically marked. For each symbol, * = $p \leq 0.05$, ** = $p \leq 0.01$, *** = $p \leq 0.001$, and **** = $p \leq 0.0001$.*

5.4.4. Gelatin supplemented polyester implants promote in vitro fibroblast attachment

We next assessed *in vitro* attachment of NIH-3T3 fibroblasts to our study materials as a factor in the progression of the FBR *in vivo*. Following the chronic inflammatory phase of the FBR, fibroblasts migrate to the implant surface and generate collagen-rich scar tissue growth to form a fibrous capsule. Fibroblast adhesion and proliferation onto a material surface can therefore inform the capability for implant-tissue integration.[363,381] Based on the cytokine data and slow material degradation, we hypothesized that the polyester fibers could enable cell attachment and thereby promote fibrosis.

Immediate dissolution of PVA/PEO fibers precluded any ability for cell attachment. Within the polyester blend, we investigated the addition of gelatin due to its (1) properties as a natural polymer with excellent biocompatibility, (2) electrospinnability, (3) RGD binding sequences that may promote cell adhesion, and (4) composition of amine and carboxyl functional groups that increase hydrophilicity of the material, which has been observed to promote fibroblast attachment and proliferation.[170,363,382] For these reasons, gelatin and synthetic polymer blends have been commonly electrospun and studied in tissue engineering applications and for drug delivery.[363,382] However, previous studies also indicate that hydrophilic materials yield less fibrotic encapsulation by decreasing macrophage activation.[170,177] Here, we observe comparable or higher macrophage cytokine expression with our gelatin materials, and stratified analysis of material and sclerosant as factors of attachment indicates that overall the addition of gelatin is a significant factor in

mediating fibroblast attachment ($p = 0.0073$). Indeed, gelatin blends increased fiber attachment up to four-fold compared to PLGA/PCL fibers. As expected, the sclerosing agents did not significantly affect cell attachment (Figure 5.5). Thus, we predict gelatin supplemented materials would generate enhanced fibroblast integration and fibrous capsule formation *in vivo*.

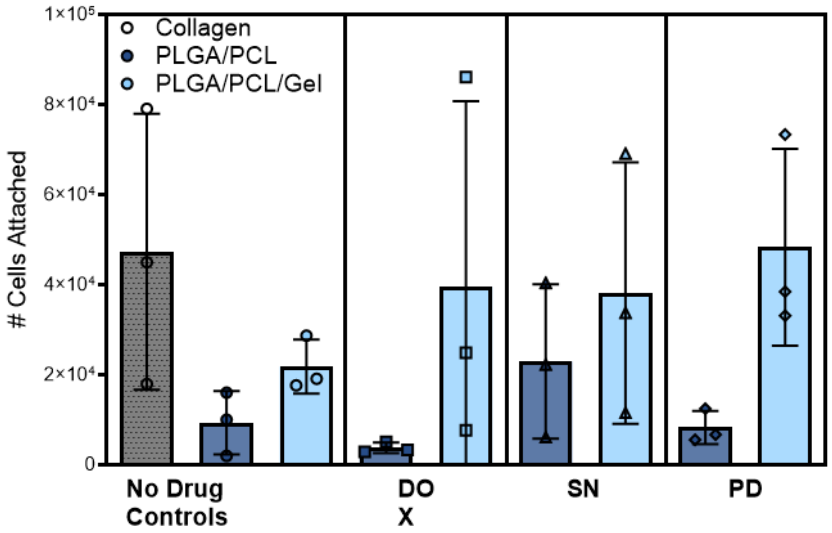

Figure 5.5. Fiber type contributes significantly to fibroblast attachment as determined by 2-way ANOVA.

Plot of the cell quantity cultured on the fibers after 24 hours as measured by a standard MTS assay. Collagen treated coverslip was used as an attachment control. Cell quantity attached measured on n=3 cultured material segments and is plotted as individual measurements and as the mean ± standard deviation.

5.4.5. PLGA/PCL/Gel/SN implants yield a strong fibrotic FBR within the mouse subcutis

Subcutaneous murine implantation is the standard for assessing the FBR,[221,352–354,383] and was used here as a primary outcome to identify study materials that could induce fibrous capsule formation prior to placement in the immune privileged uterine cavity. We assessed subcutaneous

histology for the presence of inflammation and collagen deposition. For this, collagen was differentiated between loose and dense deposition, the latter being more indicative of a fibrous capsule-type response.[170,221] End-point tissue response to our study materials were obtained 28-days after biomaterial implantation by taking measurements from representative histology images that captured a large cross-section of the implant (Figure 5.6, Appendix C Figure C.3, Figure C.4). We performed quantitative image analysis of the histology to rigorously define the fibrotic response to our study materials (Appendix C Figure C.5). As a secondary metric, histology was additionally interpreted via a scoring system (Appendix C Figure C.3 A-L, Table C.1). Both the quantitative image analysis and qualitative scoring were validated on histology images from our control groups (Figure 5.6 O and Figure C.4), and found that they had good congruency (Figure C.3).

As expected, the PVA/PEO fibers showed no indication of the implant in the pocket subcutis at the time of necropsy, indicating that they had completely dissolved. Capsule size was not measured for PVA/PEO implants due to the absence of an implant surface boundary (Appendix C Figure C.3 I-O). Inflammation towards PVA/PEO blends was largely undetected as measured by the minimal cellular staining in the adipose tissue, which at homeostasis is comprised of a loose extracellular matrix and dispersed immune cells. Loose collagen deposition was dominantly observed from PVA/PEO treated subcutis histology, with blank and Dox loaded PVA/PEO fibers resulting in quantitatively greater collagen deposition than the sham control (Figure 5.6 D, H, & P). As anticipated, PVA/PEO implants did partially initiate the FBR cascade, but comparably less than the resident implants (Figure 5.6 C, G, & K).

All polyester-based implants resulted in detectable inflammatory infiltrate of <25% of the subcutis (Figure 5.6 D, H, L, & P), which is greater than the sham control (Figure 5.6 O). We

observed that gelatin containing implants (PLGA/PCL/Gel) degraded more than PLGA/PCL implants (Figure 5.6 A-B, 5E-F, 5I-J, & 5M-N). Bulk degradation is desirable as it would increase implant porosity, which is a feature reported to improve healing responses and promoting greater M2 versus M1 macrophage adhesion.[132] Additionally, RGD-binding sequences present in gelatin are known to promote macrophage fusion, specifically IL-4 mediated macrophages associated with FBGC formation.[170,384] We would therefore expect greater inflammatory cell accumulation around the gelatin supplemented implants as compared to PLGA/PCL alone, which was observed but varied based on the specific combination of implant material and agent. Specifically, PLGA/PCL/Gel/PD and PLGA/PCL/Dox had the largest measurements of immune cell infiltration across the subcutis and surrounding the implant, as compared to the other material types (Figure 5.6 H & L, Appendix C Figure C.3 N & O). All polyester implants also yielded a detectable fibrous capsule (Figure 5.6). Specifically, the PLGA/PCL/Gel/SN implant resulted in the highest quantity of dense collagen and a clearly defined fibrous capsule (Figure 5.6 M & P). We hypothesize that the pro-inflammatory stimuli from SN and pro-healing factors from gelatin are contributing to the strong fibrotic response within the subcutaneous microenvironment. Based on this strong fibrotic response, the PLGA/PCL/Gel/SN combination was selected to probe the intrauterine fibrotic FBR.

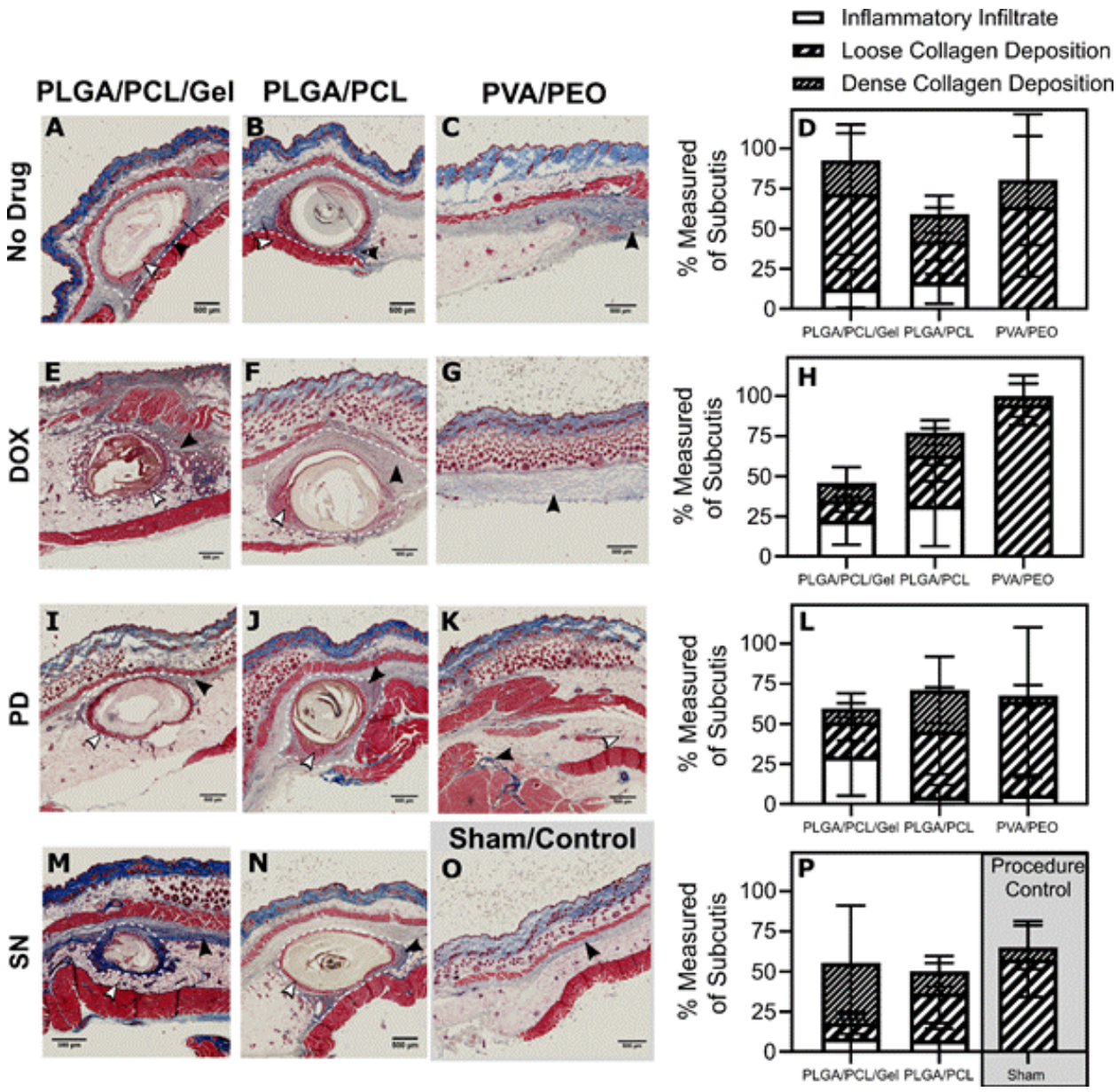

Figure 5.6. Fibers induce fibrosis as shown in representative histology images for all fiber/drug implant groups after 28 days.

Masson's Trichrome stained tissue sections for (A-C) fiber implants loaded (A-C) without drug, (E-G) doxycycline, (I-K) polidocanol, (M-N) silver nitrate, and (O) the sham/procedure control. Implants are composed of (A, E, I, and L) PLGA/PCL/Gel, (B, F, J, and N) PLGA/PCL, or (C, G, and K) PVA/PEO. Collagen deposition is visualized in blue, cell cytoplasm is stained pink/red. Regions of inflammation (white arrows) and collagen deposition (black arrows) are marked. Images were taken at 2.5x magnification. Quantitative analysis of the histology images is included for fibers with (D) no drug, (H) Dox, (L) PD, and (P) SN/sham. Implant studies were

(Figure 5.6. continued) conducted with n=1 mouse and n=2 implant pockets. Percent inflammatory infiltrate and total collagen deposition (loose and dense staining) of the subcutis were determined from representative implant images for each implant (n=3 sections). Implants for PLGA/PCL/PD and PLGA/PCL/Gel/Dox were only imaged for as n=1. For those samples, analysis was conducted using two images from a single implant replicate. Measurements are plotted as mean % ± standard deviation.

5.4.6. Intrauterine placement of biomaterials in NHPs yields negligible FBR

To probe the FBR in the uterine cavity, we designed an intrauterine device (IUD) composed of a nitinol wire frame integrated with our reactive biomaterials (Figure 5.2 C). Smaller animal models, such as rodents, have anatomically different reproductive tracts making intrauterine biomaterial placement difficult or impossible. We specifically selected baboons in this study due to anatomical similarities between the human and baboon cervix, which allows for transcervical placement of materials, and the presence of the intramural portion of the fallopian tube, which is absent in other NHPs.[251,357,385] In transitioning to the larger weight NHP animal model, the total sclerosing agent dose possible by our device was significantly below estimated toxic levels for all drugs. Therefore, the potency of silver nitrate and the high maximum 60% (wt./wt.) loading in the PLGA/PCL/Gel blend further supported the use of the PLGA/PCL/Gel/SN materials (Appendix C Figure C.1, Table 5.2).

One control and two silver nitrate loaded fiber devices were placed in three different baboons for our study to probe the intrauterine fibrotic response. The "fundus-seeking" property of the nitinol IUD consistently places the arms of the frame at the utero-tubal junction, where the fallopian tube diameter is thinnest and most susceptible to fibrosis and occlusion.[81,250] Fibers were therefore wrapped onto each arm of the IUD to target materials to the utero-tubal junction. The

materials added to the device could not exceed 1.5 mm thickness in order to accommodate the 3 mm diameter of the transcervical insertion tube, corresponding to 10 mg of fibers per arm (Figure 5.2 D & E). Initial tests of IUD placement showed that the human-scale nitinol wire frames placed the arms as expected within the utero-tubal junctions in both *Papio hamadryas* (hamadryas) and *Papio anubis* (anubis) (Appendix C Figure C.6). Details of the individual studied NHP subjects and fiber-IUD placement observations are included in Table 5.3. We evaluated the position of the IUD frames following placement using fluoroscopy with contrast (Isovue). In two NHPs (Control and SN-H), both of the IUD arms localized to one of the cornual regions, and in the third (SN-A) the arms deployed correctly (Table 5.3, Figure 5.7 A&B). This suggests that the adherence of the fibers may have prevented full expansion of the device.

We evaluated histologic sections from each cornual region proximal to the IUD arms and found no evidence of inflammation or collagen deposition in either the endometrium or intramural fallopian tube (Figure 5.7 D-I). First, at the 28-day study endpoint, no abnormal immune cell infiltration was observed. The wide-angle overview of the uterine cornual histology shows that the ECM is inherently collagen rich, which is supported by other studies of primate uterine tissue.[386,387] We did not observe any excess collagen deposition in these tissue sections as would be evident by tubal obstruction by scar tissue, as well as by a disruption of the tubal epithelium.[387] Rather, tubal epithelium was clearly present and intact in all histology sections (Figure 5.7 D-I). Additionally, the perimeter of uninterrupted fallopian tube epithelium was measured to be within a range of 1.16-9.62 mm for all treatment groups (Table 5.3). Considering human fallopian tubes have been reported to be as small as 0.4 mm in inner diameter[388] and up to 4 mm in diameter,[389] an epithelial perimeter within a range of approximately 1.26-12.6 mm would be considered typical for healthy human or baboon tubal tissue. PLGA/PCL/Gel fibers persisted beyond 28-days throughout our

study, and as anticipated these materials were present for the entirety of intrauterine placement. The absence of observable scar tissue integration onto the material further indicates that the materials did not undergo fibrotic encapsulation. Despite our observations of subcutaneous fibrotic encapsulation of PLGA/PCL/Gel/SN materials in the mouse, the same materials with an increased sclerosing agent dose did not induce a reaction within the uterine environment.

Table 5.3. Summary of NHP subjects and study observations

NHP	Baboon Species	Biomaterial Treatment	Device Conformation at Placement	Device Conformation at Necropsy	Measured Tubal Perimeter (mm)
Control	*Papio hamadryas*	2x – 10 mg PLGA/PCL/Gel Fiber	Both arms in right utero-tubal junction	Open, device arms local to each utero-tubal junction	1.94 ± 0.50
SN-H	*Papio hamadryas*	2x – 10 mg PLGA/PCL/Gel +60% SN Fiber	Both arms in left utero-tubal junction	Folded at left utero-tubal junction	5.44 ± 3.91
SN-A	*Papio anubis*	2x – 10 mg PLGA/PCL/Gel +60% SN Fiber	Open, device arms local to each utero-tubal junction	Open, device arms local to each utero-tubal junction	6.98 ± 0.51

Perimeter of tubal epithelium measured taken as n=3 measurements between n=2 fallopian tubes on n=1 animal.

One significant difference between the subcutaneous and uterine environments here is the procedure used to implant the materials. Blood and biomaterial interactions are implicated in the first stage of the FBR cascade, and thereby blood contact a necessary first step to fibrous capsule formation. Both the subcutis and tubal submucosa are highly vascularized,[390,391] but surgical implantation within the subcutis entails greater physical tissue damage than transcervical delivery

induces onto the utero-tubal junction. However, the material coated devices did contact blood caused from tissue damage during cervical dilation. Additionally, subcutaneous sham procedures, healed with negligible fibrosis (Appendix C Figure C.4 L). For these reasons, the differences between placement procedures are not expected to entirely account for the differences in the responses observed towards the biomaterials in the different compartments.

The delivered dose in our study had a comparably lower mass of total drug than other intrauterine sclerosing agent studies. However, the dose was expected to be sufficient for local epithelial toxicity due to targeted drug delivery to the utero-tubal junction and higher degree of sclerosant/material tissue contact and residence. We also do not think that the duration of dose release in this case to be the cause of the minimal response. In fact, we expect that prolonged exposure to silver nitrate could delay development of collagen deposition and remodeling. However, having a larger sclerosant dose could induce a stronger fibrotic response to the treatment. For example, our silver nitrate dose in the baboons was approximately 6 mg per utero-tubal junction and did not lead to a fibrotic FBR in the baboons. Neuwirth, *et al*. showed that a 10% silver nitrate ointment fully infused in pigtail macaque fallopian tubes induced scar tissue occlusion – a dose calculated to be 18.8 mg for an estimated 2 mm diameter by 6 cm long tube.[365] Knowing that fibrosis is a possible reaction of provoked uterine tissue, yet was not observed here in response to material implants confirmed to be reactive in the subcutis, emphasizes the ability of host factors to strongly dampen the fibrotic response.

Although the presence of uterine immune privilege towards foreign bodies such as paternal cells and fetuses has been well documented,[238–240] to the best of our knowledge ours if the first study to directly compare the FBR between the subcutis and the uterine environment and demonstrate a dampened fibrotic response in the uterine microenvironment to known fibrosis

provoking implants within the subcutaneous microenvironment. Our results illustrate the extent that uterine immune privilege has towards the tolerance of biomaterial foreign bodies. Previous studies have demonstrated that the FBR does vary in magnitude towards different biomaterial properties[170] and across different tissue implantation sites.[206] While it is true that fibrosis can be induced within the immune privileged uterine tissue environment, we showed that a fibrotic response within the uterus is significantly dampened in comparison to classical microenvironments and may require an acute stimulus to provoke. Examples of stimuli needed beyond the presence of a foreign body may include mechanical properties as is the case of the Essure contraceptive device,[249] large and repeated drug dosages for chemical tubal occlusion,[250,355,356,365] and chronic inflammation from sources such as sexually transmitted pathogens.[250,252]

Our work demonstrates the important role that the tissue microenvironment plays in the FBR. Studies are needed to identify the ques, or combination of ques, responsible for this dampened intrauterine fibrotic response. Once identified, these immunosuppressive factors from the uterine microenvironment could be used in a peripheral biomaterial implant model. Such studies would inform possible methods for translating this immune privilege to implants broadly. For example, both progesterone and estrogen are steroid hormones produced cyclically by the ovaries. Both hormones are known to regulate the quantity of macrophages present within the uterus, as well as the expression of these macrophages in the anti-inflammatory, M2 polarization state.[392] The expression of these hormones, as well as the local immune environment, changes dynamically throughout the menstrual cycle.[240,393,394] Some studies of progesterone and estrogen's effects on the FBR have already been studied,[395,396] but the direct effect of both hormones on a subcutaneous implant has not been considered. Additionally, the temporal effects of such hormones could be studied in the context of the FBR. The role of macrophages as an important

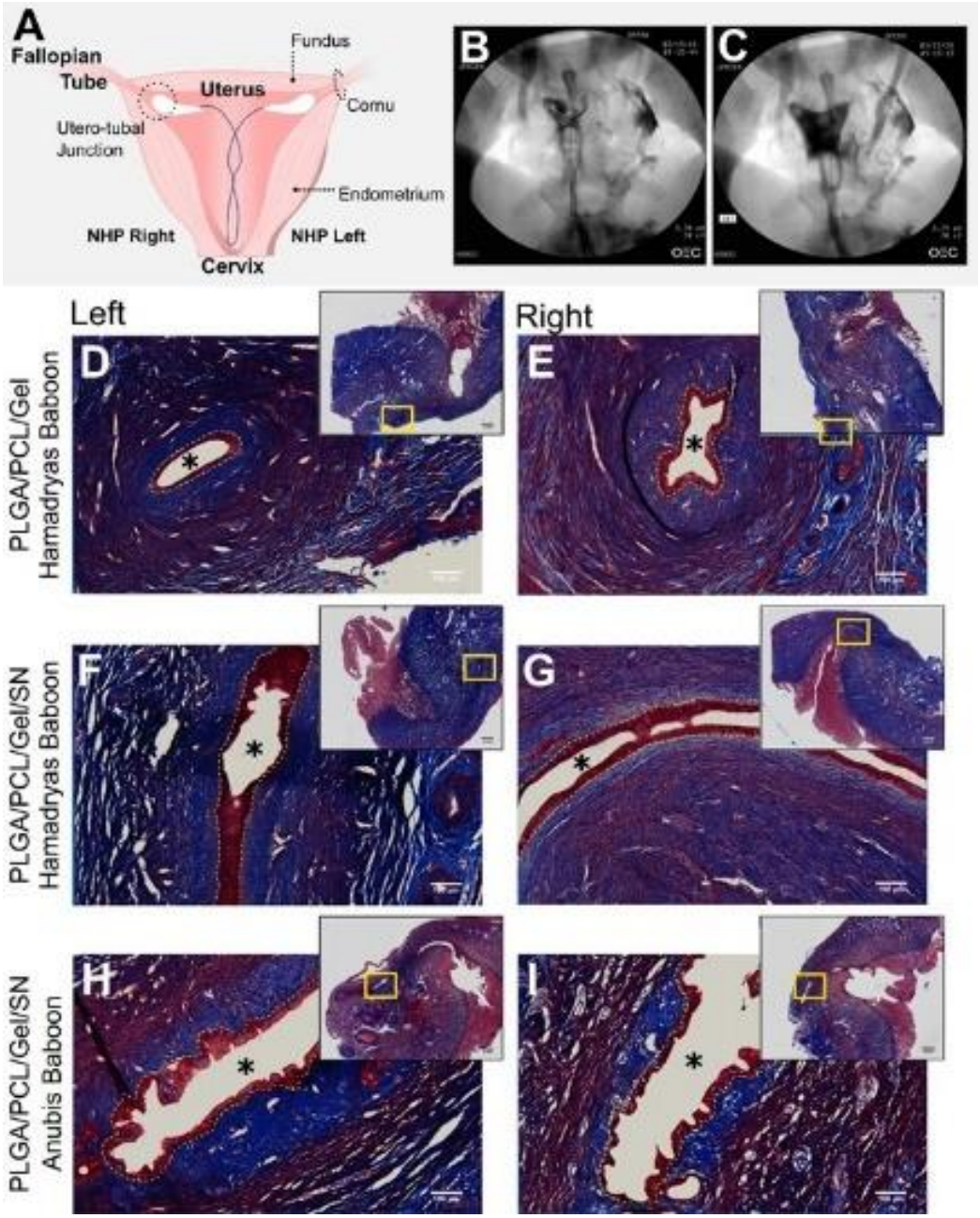

Figure 5.7. Fibers can be integrated onto IUD devices for intrauterine placement in a non-human primate model.

(A) Diagram of the fiber-IUD and relevant anatomical features of the female reproductive tract. Fluoroscopy images of fiber loaded IUD placed in an anubis baboon with active fibers (B) without and (C) with contrast to outline shape of uterine cavity. Resulting tissue sections of left and right cornu of the uterus stained with Masson's trichrome 28-days following treatment with (D&E) PLGA/PCL/Gel fibers without drug in an hamadryas baboon (n=1), (F & G) 60% (w/w)

(Figure 5.7 continued) SN loaded fibers in the anubis baboon (n=1), and (H&I) SN loaded fibers treated in the hamadryas baboon (n=1). Main images are captured at 10x magnification, and overview scan images of the tissue sections are included at the top right. Asterisks (*) mark the lumen of the fallopian tube, and yellow-dashed lines outline the tubal epithelium.

mediator in uterine immune privilege has already been identified, especially in the context of pregnancy. In the context of the current work, we expect that studies of macrophage polarization, specifically in response to various biomaterials, would further elucidate the presence of the intrauterine FBR dampening response.

5.5 CONCLUSION

In this study, we designed a novel biomaterial-IUD to investigate the fibrotic FBR within the uterine environment. Electrospun fibers were used for their ability to (1) formulate both hydrophilic or hydrophobic polymers, (2) incorporate ECM-like fiber matrices including natural polymers with RGD-binding sequences, and (3) be easily integrated onto an intrauterine device for direct delivery to the utero-tubal junction. These fibrous materials also showed high encapsulation efficiency of the physicochemically diverse agents Dox, SN, and PD.

Polyester fibers successfully released sclerosing agents up to 10 days. These materials additionally persisted as a fiber depot beyond 28 days. In contrast, PVA/PEO blend fibers fully dissolved and released the drug cargo within an hour as designed to capture only the initial phases of the FBR. In assessing the in vitro immune response, polyester blend fibers were shown to have higher pro-inflammatory (IL-1β) and pro-healing (IL-10) cytokine expression compared to than PVA/PEO fibers. This suggests that sustained polyester fiber blends, and even these fibers alone, are more likely to provoke the initial cell signaling needed to cause permanent fibrotic scar tissue

growth. Using the subcutaneous mouse implant model, the fibrotic reaction to these materials was also captured, showing high collagen-rich tissue encapsulation of PLGA/PCL/Gel/SN fibers. PLGA/PCL/Gel/SN was prioritized for assessing the fibrotic FBR in the intrauterine NHP model due to the relative potency of SN and the higher SN loading within the gelatin blend fibers.

Histological evidence from the NHP studies indicate that the materials optimized for initiating subcutaneous fibrosis did not cause excess intrauterine fibrotic tissue growth 28-days post placement. This study illustrates the significant role of the immunosuppressive tissue microenvironment on the FBR. Knowledge from this study highlights the importance of considering the tissue environment in designing biomaterials. Future studies could additionally seek out these mechanisms of protection or could investigate methods of bringing known elements of immune privilege to systemic implants.

5.6 ACKNOWLEDGEMENTS

We thank I. Suydam for his help with TLC and the method for PD detection. We also thank A. Roehrich for her assistance with ICP-OES and acknowledge the Spectroscopic and Analytical Instrumentation Facility at the University of Washington. Research is supported by the Bill and Melinda Gates Foundation grant to the Oregon Permanent Contraception Research Center [OPP1006248 to JTJ and KAW]; NIH/NIAID [R01-AI-150325 to KAW and JTJ]; ARCS (Achievement Rewards for College Scientists) foundation [to JH]; and the Howard Hughes Medical Institute (HHMI) [Gilliam Fellowship for Advanced Study to JH and KAW].

APPENDIX A: SUPPORTING FIGURES FOR CHAPTER 3

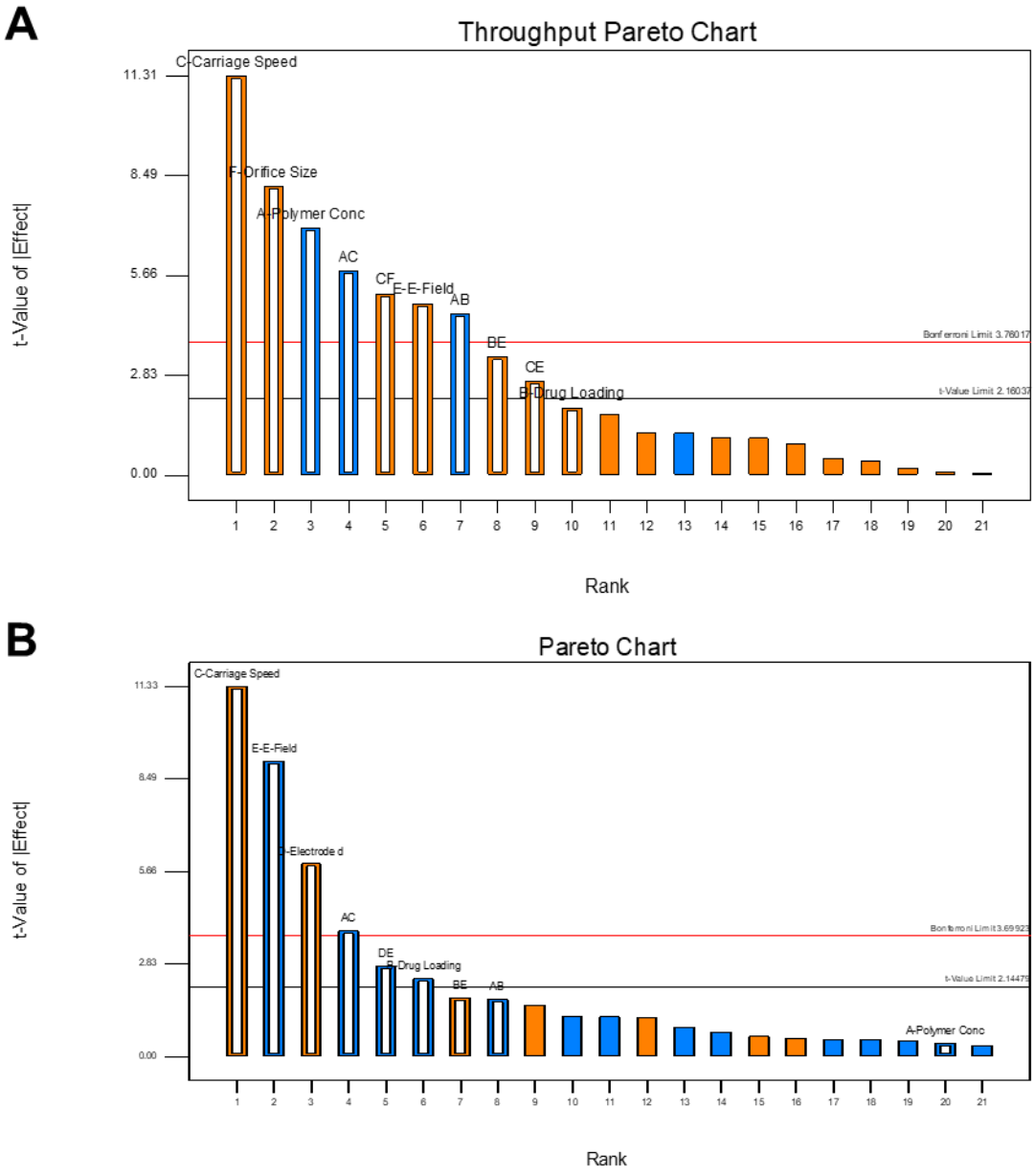

Figure A.1. Free-surface electrospinning parameters significantly affect fiber throughput and the spread of fiber distribution.

Pareto charts showing the effect of each factor and factor interaction for (A) throughput and (B) σ_s. Factors with t-values above the Bonferroni limit (red line) are determined to have significant impact, while values above the t-value limit (black line) are likely significant.

Table A.1. Throughput ANOVA Results

	Adjusted F-value	Model p-value	Unadjusted F-value	Model p-value
Model	46.86	< 0.0001	44.33	< 0.0001
Curvature	1.80	0.2031		
Lack of Fit	0.62	0.7591	0.67	0.7385
Factor	**Adjusted Coefficient Estimate**	**Model p-value**	**Unadjusted Coefficient Estimate**	**Model p-value**
Intercept	4.98		5.04	
A-Polymer Conc	-0.93	< 0.0001	-0.93	< 0.0001
B-Drug Loading	0.25	0.0788	0.26	0.0819
C-Carriage Speed	1.48	< 0.0001	1.49	< 0.0001
E-E-Field	0.65	0.0003	0.64	0.0003
F-Orifice Size	1.10	< 0.0001	1.10	< 0.0001
AB	-0.62	0.0005	-0.62	0.0005
AC	-0.78	< 0.0001	-0.78	< 0.0001
BE	0.45	0.0052	0.46	0.0051
CE	0.36	0.0196	0.36	0.0197
CF	0.69	0.0002	0.70	0.0002
Ctr Pt 1	0.49	0.2031		

Table A.2. σ_S ANOVA Results

	Adjusted F-value	Model p-value	Unadjusted F-value	Model p-value
Model	30.13	< 0.0001	31.90	< 0.0001
Curvature	0.17	0.6882		
Lack of Fit	0.69	0.7284	0.64	0.7517
Factor	**Adjusted Coefficient Estimate**	**Model p-value**	**Unadjusted Coefficient Estimate**	**Model p-value**
Intercept	2.97		2.97	
A-Polymer Conc	-0.022	0.6854	-0.022	0.6792
B-Drug Loading	-0.13	0.0320	-0.13	0.0273
C-Carriage Speed	0.62	< 0.0001	0.62	< 0.0001
D-Electrode d	0.32	< 0.0001	0.32	< 0.0001
E-E-Field	-0.49	< 0.0001	-0.49	< 0.0001
AB	-0.096	0.1009	-0.097	0.0883
AC	-0.21	0.0018	-0.21	0.0012
BE	0.099	0.0922	0.10	0.0802
DE	-0.15	0.0146	-0.15	0.0113
Ctr Pt 1	0.061	0.6882		

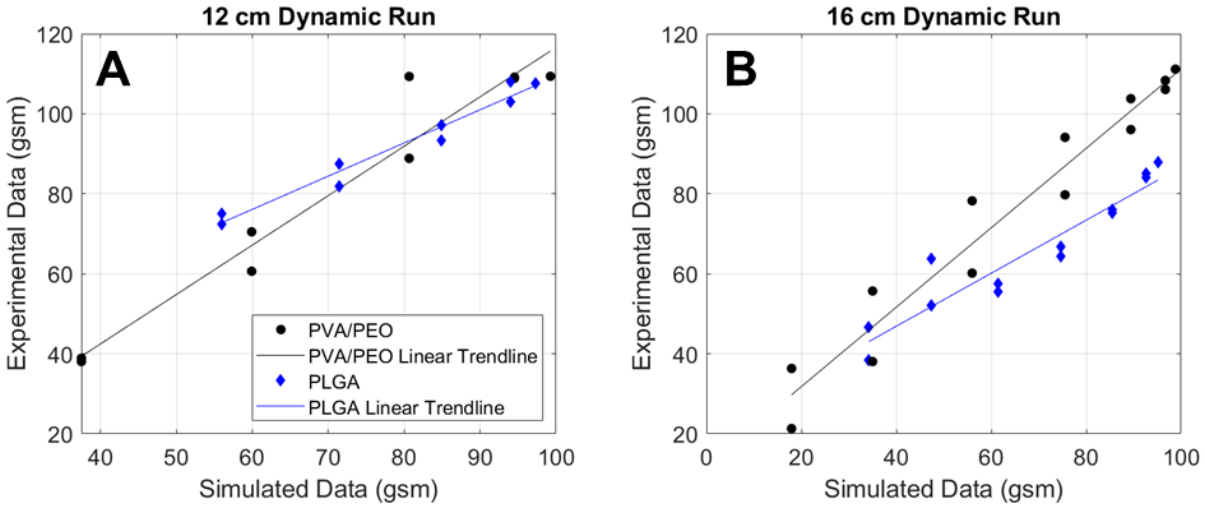

Figure A.2. Linear relationships between simulated and experimental results show that mass deposition patterns can be roughly predicted.

Experimental and simulated data are highly correlated for both PVA/PEO and PLGA formulations and for (A) 12 or (B) 16 cm dynamic run conditions.

Table A.3 Statistical comparisons of measured fiber mass, normal distribution, and simulated data

	Dynamic Path Length (DPL)	Optimized PVA/PEO	PLGA
Statistical analysis of gaussian distribution of fiber mass			
σ_{MD} (cm)	**Static (0 cm)**	3.787	6.443
Statistically non-normal? (D'Agostino-Pearson omnibus test, p-value)	**Static (0 cm)**	NS, 0.370	NS, 0.579
Statistical comparisons of simulated and measured dynamic runs			
r (correlation coefficient)	***12***	0.973	0.982
	16	0.974	0.946
RMSE	***12***	13.02	13.36
	16	13.28	9.038
R^2, linear fit of experimental vs simulated data	***12***	0.947	0.949
	16	0.965	0.894

Significance level $p \leq 0.05$, fiber mats measured with n=1 fiber mat, and up to n=4-5 samples per MD location at CD= -8, -4, 0, 4, and 8.
NS=non-significant
RMSE=root mean square error
R^2=coefficient of determination

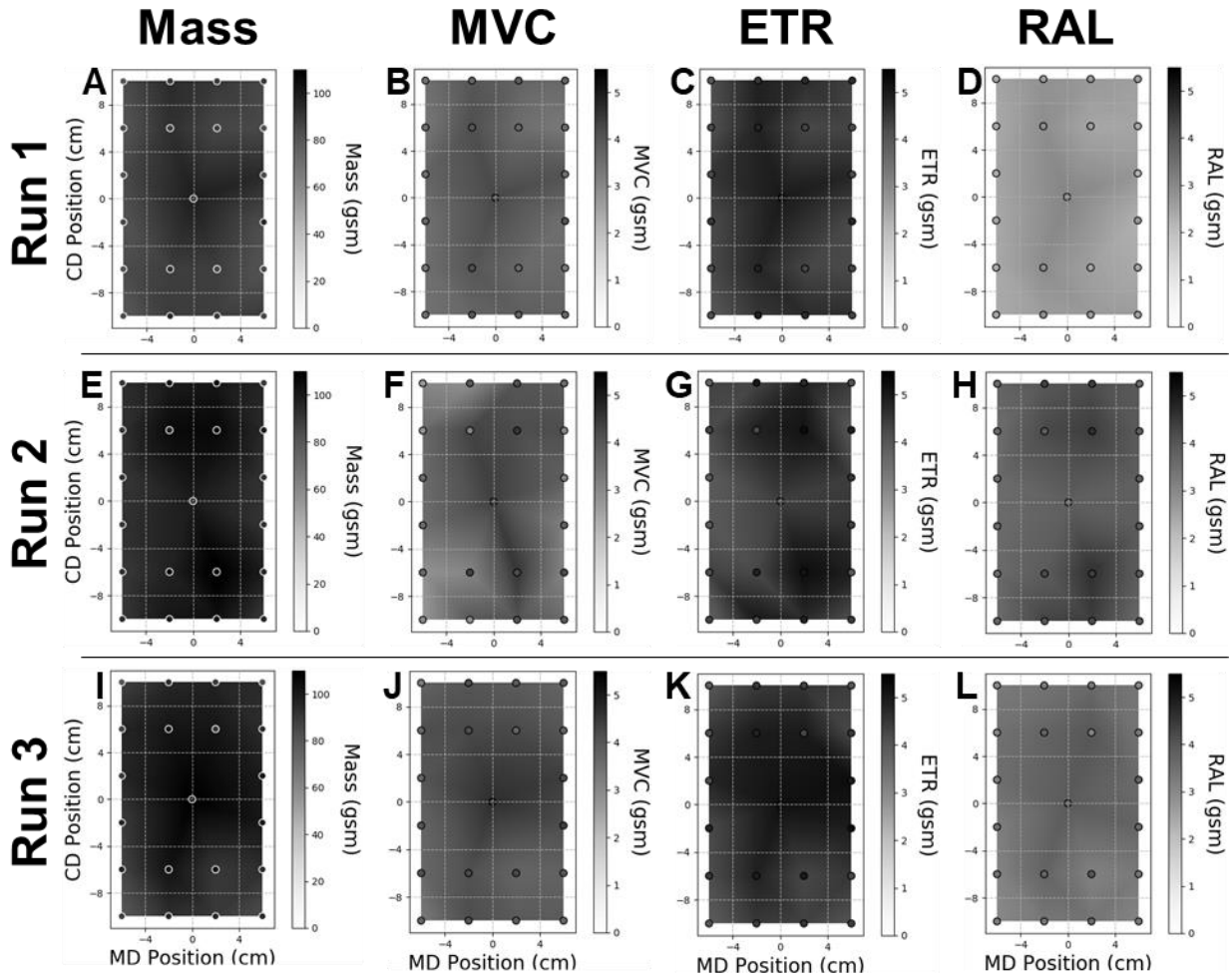

Figure A.3. Mass and drug distribution is mostly uniform across different fiber mats, with some regions of negligible variability.

Maps of linearly interpolated (A, E, & I) mass, and the co-formulated drugs (B, F, & J) MVC, (C, G, & K) RAL, and (D, H, & L) ETR show location-based changes of fiber deposition and drug loading across replicate fiber mats from a 20 cm dynamic run.

APPENDIX B: SUPPORTING FIGURES FOR CHAPTER 4

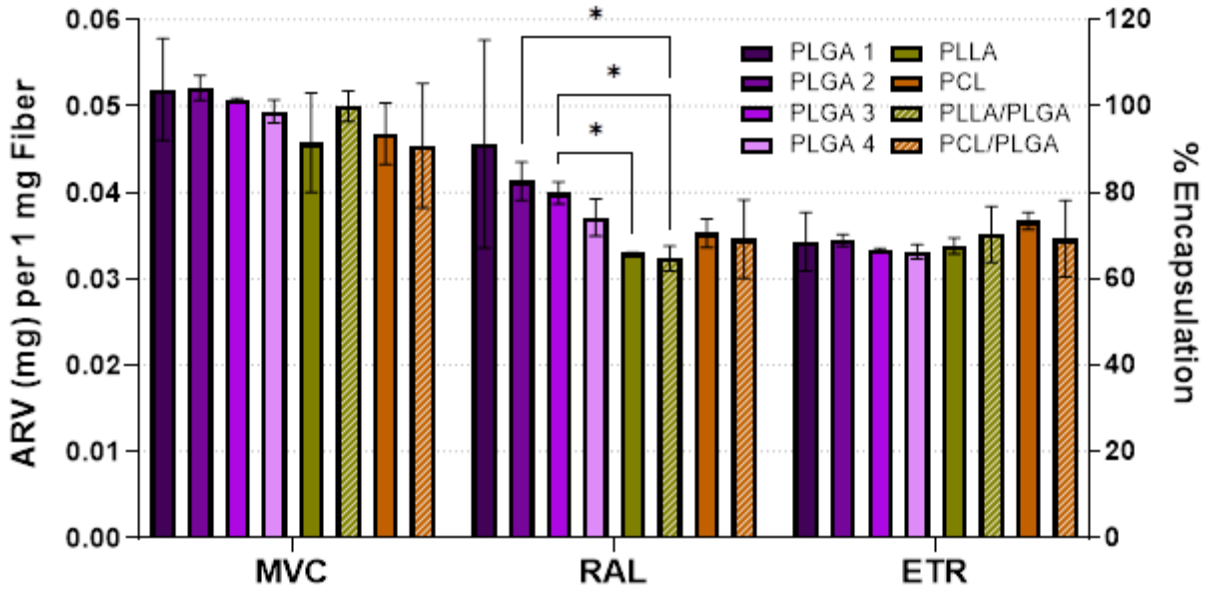

Figure B.1 All screened polymers can efficiently encapsulate 3ARVs when formulated using electrospinning, except for RAL formulated in PLLA materials.

*Measurements are plotted as average ± standard deviation. Significant differences are measured by repeated measures 2way ANOVA with Geisser-Greenhouse correction and Tukey's multiple comparisons test, where *=p<0.05.*

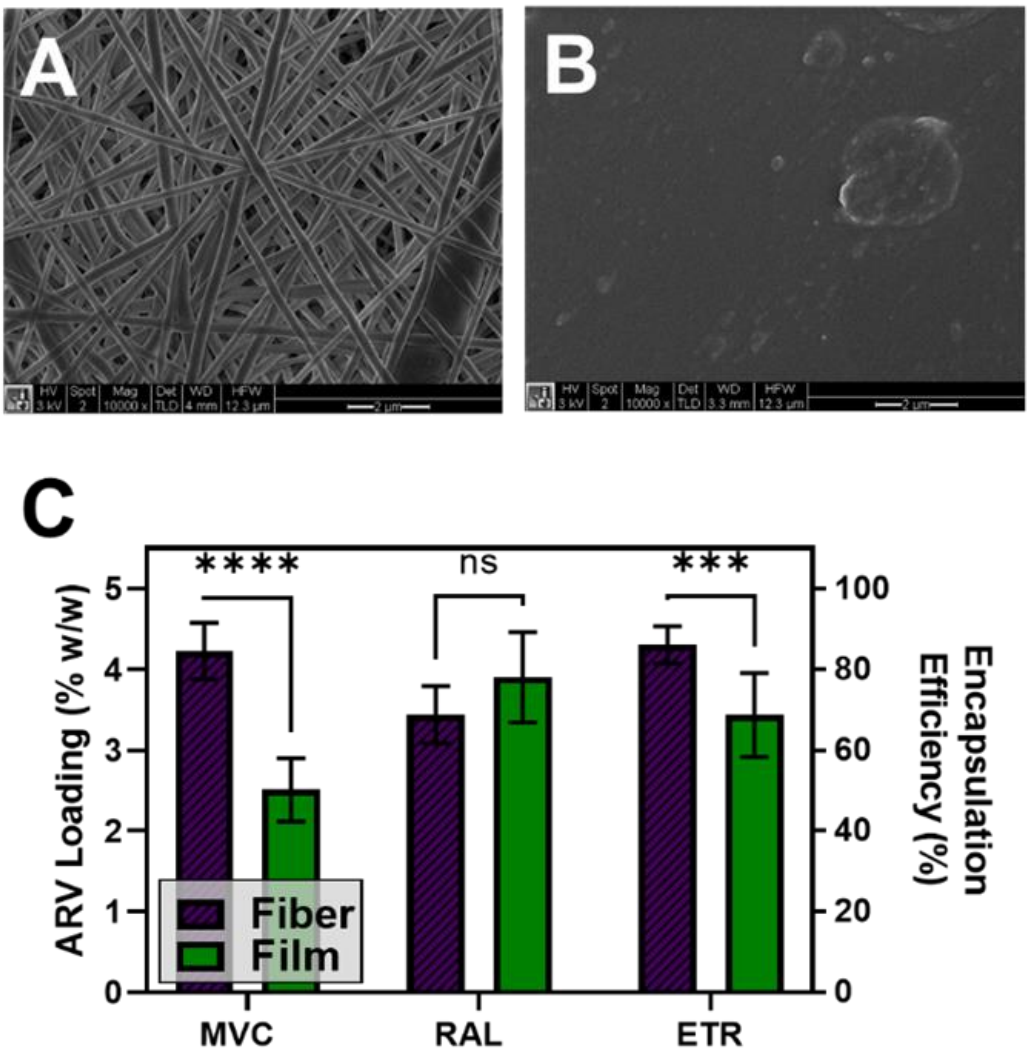

Figure B.2 Electrospinning and solvent casting methods create materials with different surface morphologies and varied MVC and ETR release.

*Surfaces of (A) electrospin fibers and (B) solvent cast films are SEM imaged at 10000x magnification. (C) Drug encapsulation is presented as total loading within material and as present of the theoretical drug loading. Drug measurements are measured from n=3 sheets of materials with n=3 location-separated samples. Values are plotted as mean ± standard deviation. Significant differences were determined by repeated measures 2way ANOVA with Geisser-Greenhouse correction followed by Šídák's multiple comparisons test, and are marked as ns= non-significant, ***=p<0.001 and ****=p<0.0001.*

Table B.1 Material characterization and comparisons between PLGA electrospun fibers and solvent cast films

	Fiber	Film
Contact Angle (º)	120.9 ± 10.6	73.2 ± 17.2
Fiber diameter (nm)	250.7 ± 79.2	NR
Pore size (nm)	139.8 ± 35.7	NR

NR = not relevant
Values reported as average ± standard deviation
Determined for n = 3 material replicates each with n=3 measurements for contact angle and n = 1 material and 3 images measurements for fiber and pore diameter measurements.

Table B.2 Pharmacokinetics for standard and washed fiber and film implants

		Fiber	Washed Fiber	Film	Washed Film
Initial release (t ≤ 24 h) PK					
	n	3	3	3	3
AUC_{24} **(h·ng/mL)**	MVC	6672.3 ± 699.4	1147.0 ± 107.3 (p=0.0541)	559.60 ± 316.97 (p=0.0234)	440.40 ± 347.23 (p=0.0196)
	RAL	9687.0 ± 2749.7	1097.7 ± 1065.3 (p=0.0005)	1031.7 ± 488.74 (p=0.0005)	514.13 ± 146.78 (p=0.0002)
	ETR	96.33 ± 166.85	3590.4 ± 5643.3 (p=0.5287)	1028.3 ± 1253.8 (p>0.9999)	331.00 ± 103.25 (p>0.9999)
$C_{MAX,24}$ **(ng/mL)**	MVC	1527.40 ± 163.41	171.5 ± 90.1 (p=0.0001)	115.81 ± 50.13 (p<0.0001)	165.63 ± 138.09 (p=0.0001)
	RAL	1852.45 ± 608.39	85.6 ± 62.0 (p<0.0001)	176.22 ± 53.89 (p<0.0001)	184.42 ± 213.15 (p<0.0001)
	ETR	8.421 ± 14.586	431.1 ± 641.2 (p=0.7527)	143.03 ± 74.15 (p>0.9999)	69.400 ± 49.153 (p>0.9999)
Long-acting release (7 d ≤ t ≤ 120 d) PK					
n		3	2	3	3
AUC_{LA} **(h·ng/mL)**	MVC	32346.3 ± 24503.9	19365.5 ± 5714.1 (p=0.9991)	14907.0 ± 3983.2 (p=0.9765)	20952.7 ± 6725.9 (p=0.9993)
	RAL	74322.7 ± 8294.6	132852.0 ± 60430.8 (p=0.0396)	98278.0 ± 10507.8 (p=0.8383)	83822.0 ± 1615.0 (p=0.9999)
	ETR	22534.0 ± 8132.0	34699.5 ± 14627.9 (p=0.9995)	28174.0 ± 13259.5 (p>0.9999)	20578.0 ± 2219.4 (p>0.9999)
$C_{MAX,LA}$ **(ng/mL)**	MVC	125.2 ± 68.3	64.1 ± 33.0 (p=0.9947)	37.47 ± 16.4 (p=0.8686)	46.3 ± 10.4 (p=0.9278)
	RAL	102.4 ± 13.4	279.8 ± 237.7 (p=0.1788)	156.7 ± 9.9 (p=0.9951)	127.1 ± 15.1 (p>0.9999)
	ETR	59.7 ± 3.0	109.5 ± 117.2 (p=0.9991)	76.8 ± 55.0 (p>0.9999)	19.3 ± 0.5 (p=0.9996)

Values reported at average ± standard deviation and p-values are reported for significant comparisons to fiber implants of the same drug determined by 3way ANOVA with Tukey multiple comparisons test.

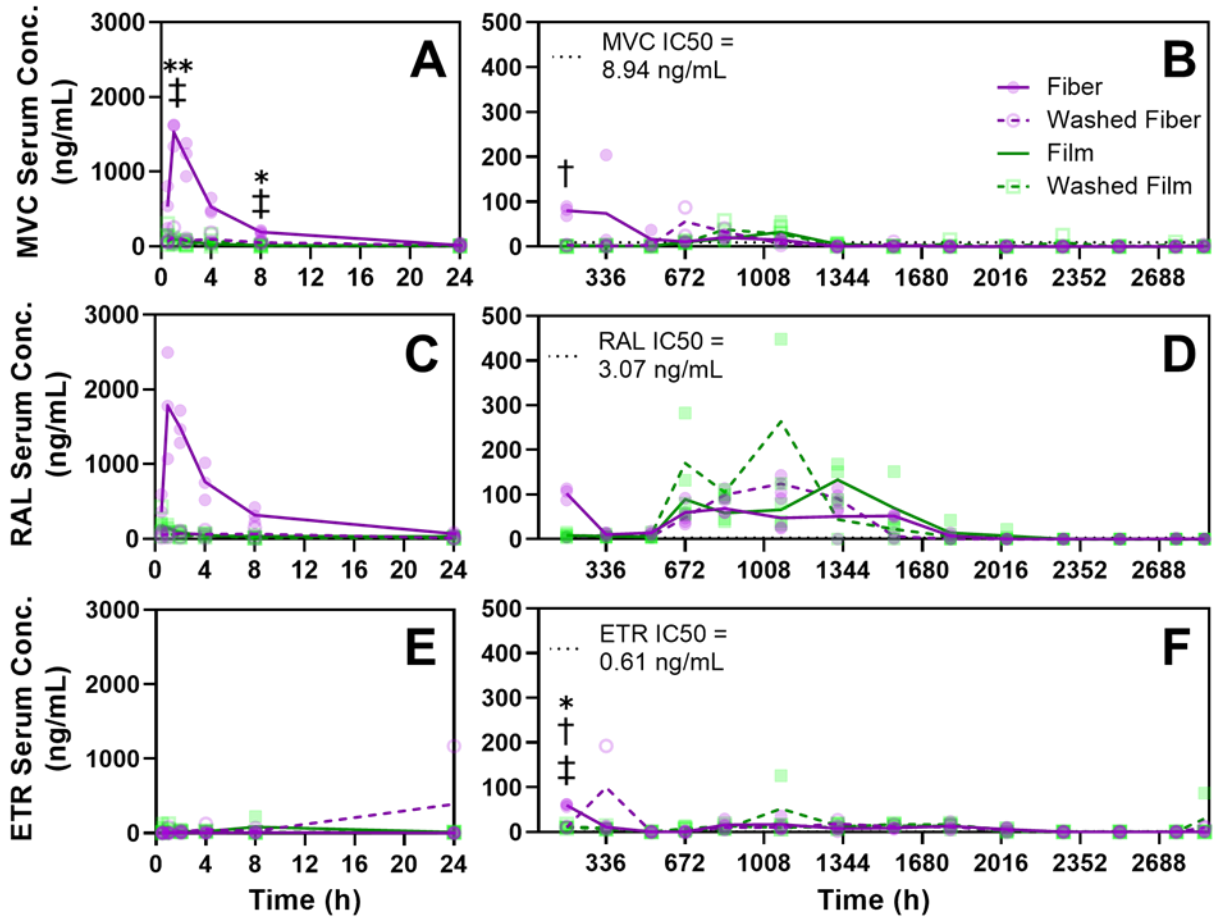

Figure B.3 Fiber and film PK comparisons for standard and pre-washed treatments indicate greater surface associated MVC and RAL on fiber materials which caused the burst release of these drugs.

*Initial (≤24 hour) drug release is shown for (A) MVC, (C) RAL, and (E) ETR shows the timeframe for drug burst release into blood serum. Long-acting drug release ($7 \leq t \leq 120$ days) is also plotted for (B) MVC, (D) RAL, and (F) ETR. All values are plotted as individual values, with a line representing the mean. Significant differences per drug and per timepoint are shown comparing material and treatments with: * = $p<0.05$ and ** = $p<0.01$ between fibers and washed fibers; † = $p<0.05$ between fibers and films; and ‡ = $p<0.05$ between fibers and washed films.*

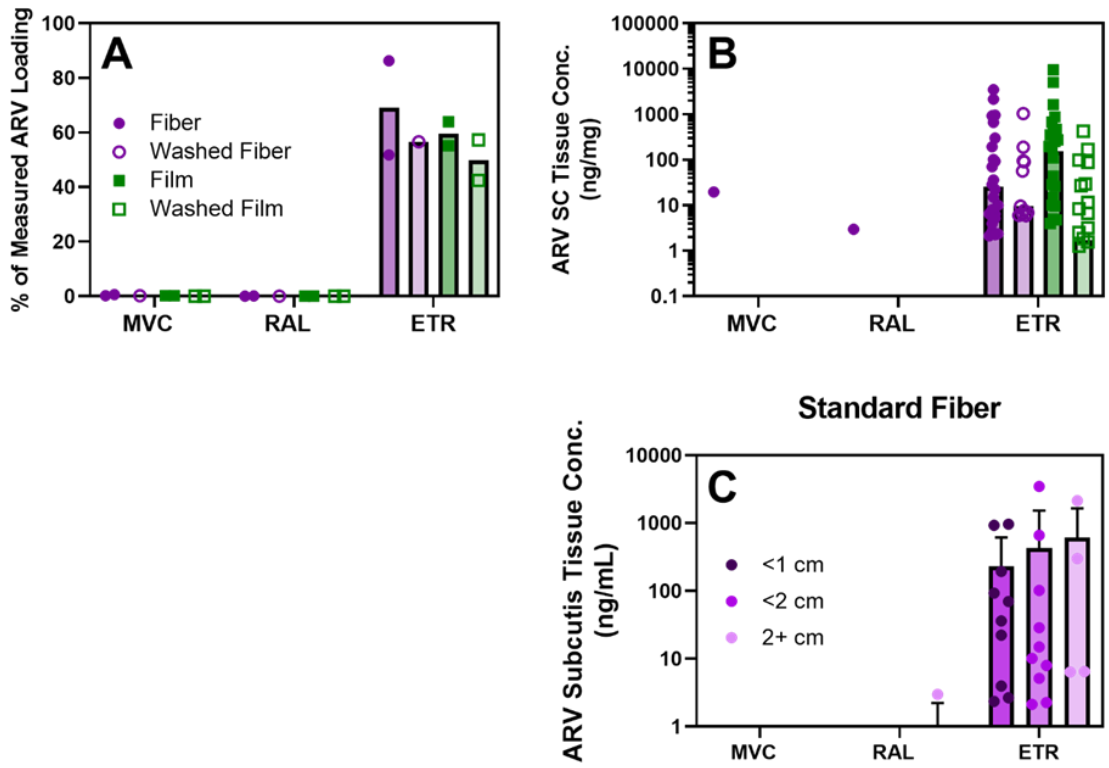

Figure B.4 ETR remains in high concentrations in all implants and surrounding tissues, with non-significant differences between treatment types and tissue concentrations not dependent on biopsy distance.

(A) ARV concentrations measured in remaining implant material at 120-days is calculated as a percent of the measured drug dosage determined by the encapsulated quantity of drug in the materials delivered. For each treatment, n=2 implants are measured. (B) ARVs are also measure in skin biopsies local to the implant site, (C) with samples taken at specified distances away from the implant ranging from the implant site to more than 2 cm away. For biopsy measurements, n=9 biopsies are collected for n=2 mice, and n=6 biopsies for n=1 mouse per each group. Washed fibers have n=2 mice total, so n=1 implant is measured, and n=1 mouse has n=9 or 6 biopsies. Individual vales are plotted individually, with bars that represent the mean. Values plotted by location just include the standard fiber group, and is additionally represented with error bars to represent the standard deviation.

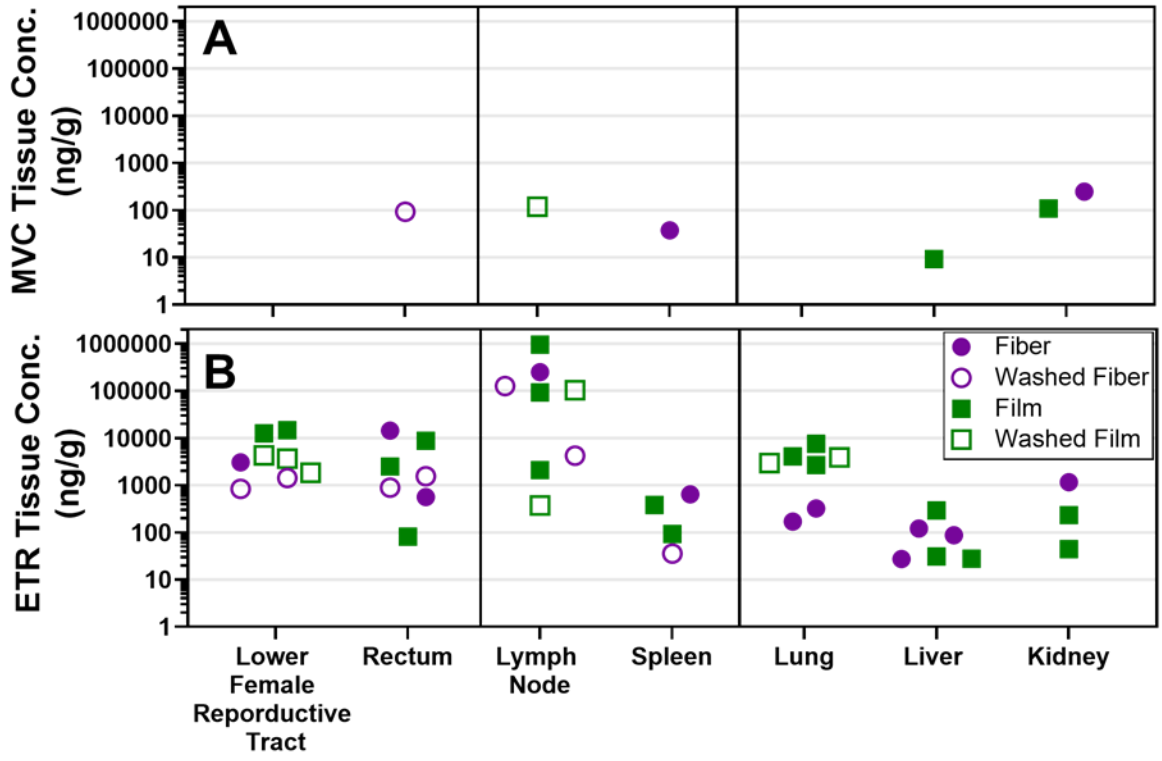

Figure B.5 All material implant groups show similar trends in ARV partitioning across organ tissues.

In samples collected from the lower female reproductive tract, the rectum, inguinal and lumbar lymph nodes, spleen, lung, liver, and kidney (A) MVC and (B) ETR concentrations are reported as individual values for each mouse. All samples had RAL signal below the limit of detection. All samples which had drug signal below 4x the background signal are excluded.

Table B.3 ETR organ tissue concentrations at 120-days for all implant treated mice.

Treatment/ Mouse	ETR tissue Conc. (ng/g)						
	Lower FRT	Rectum	Lymph node	Spleen	Lung	Liver	Kidney
Fiber							
1	ND	564.1	ND	ND	323.0	27.2	ND
2	ND	ND	ND	ND	ND	87.7	ND
3	3035.7	14316.4	247469.2	637.1	169.7	120.5	1151.9
Average ± SD	1011.9 ± 1752.7	4960.2 ± 8107.6	82489.7 ± 142876.4	212.4 ± 367.8	164.2 ± 161.5	78.4 ± 47.3	384.0 ± 665.1
Washed Fiber							
1	840.1	1544.3	4245.9	ND	ND	NM	NM
2	1426.1	893.2	126487.0	35.8	NM	NM	NM
Average± SD	1133.1 ± 414.4	1218.8 ± 460.4	65366.5 ± 86437.5	17.9 ± 25.3	NM	NM	NM
Film							
1	12475.1	2492.6	945816.9	92.4	4074.2	291.7	233.1
2	ND	81.3	2087.3	ND	2652.5	27.5	ND
3	14627.5	8708.9	92410.4	380.1	7553.3	31.0	44.5
Average± SD	9034.2 ± 7897.5	3760.9 ± 4451.5	346771.5 ± 520750.5	157.5 ± 198.2	4760.0 ± 2521.3	116.7 ± 151.5	92.5 ± 123.7
Washed Film							
1	1830.0	NM	371.2	NM	2924.9	NM	NM
2	3640.0	NM	ND	NM	NM	NM	NM
3	4296.4	NM	102828.0	NM	3902.6	NM	NM
Average ± SD	3255.5 ± 1277.4	NM	34399.7 ± 59260.9	NM	3413.8 ± 691.3	NM	NM

Averages calculated with ND values as zero.
ND = not detected; NM = not measured; ETR = etravirine; FRT = female reproductive tract; SD = standard deviation

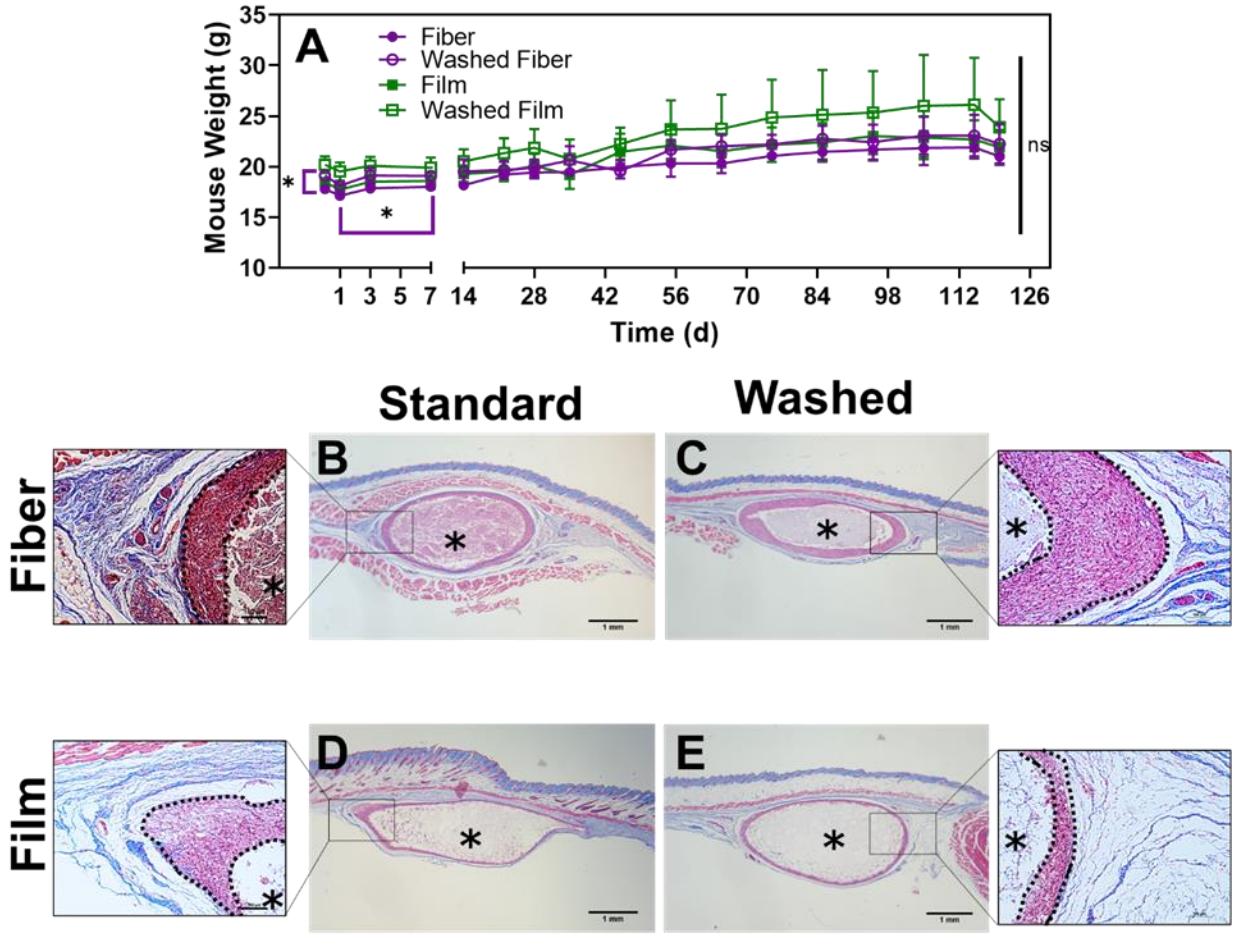

Figure C.6. Fiber and film implants are similarly well tolerated but show differences in local tissue response.

*Tolerability was monitored over the course of the study as measured by (A) mouse weights. Masson's trichrome stained histology sections for (B) fiber, (C) washed fiber, (D) film, and (E) washed film implants are shown at 2x (main) and 10x magnification (inset). Implants are denoted by *, and the surrounding inflammatory layer is outlined with a dashed line. All images show relatively low density of collagen accumulation but have defined regions of inflammatory cell adhesion. The inflammatory layer is 2.1x greater for fibers than films (113.4 +/- 46.9 um versus 53.8 +/- 26.2 um), and washed fibers have 3.1x greater inflammatory layer than washed films (243.1 +/- 136.8 um versus 78.5 +/- 30.0 um)*

APPENDIX C: *SUPPORTING FIGURES FOR CHAPTER 5*

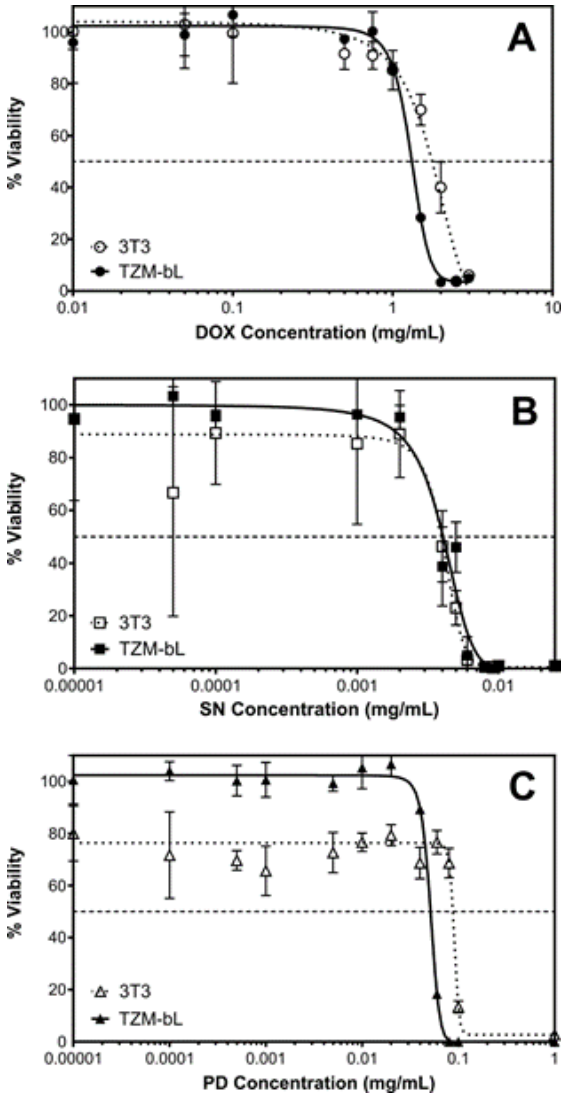

Figure C.1 Cell cytotoxicity of free drug to determine LD50 in vitro.

Dose-response curves for 3T3 fibroblasts and TZM-bL epithelial cells treated for 24 hours with (A) doxycycline, (B) silver nitrate, and (C) polidocanol (n=3). Viability was measured using a CellTiter Blue assay and calculated based on cell signal from untreated cells. Data is fit with a non-linear, log(agonist) vs response, least squares equation (using GraphPad Prism). LD50 values estimated at the intersection of the data fit at 50% viability.

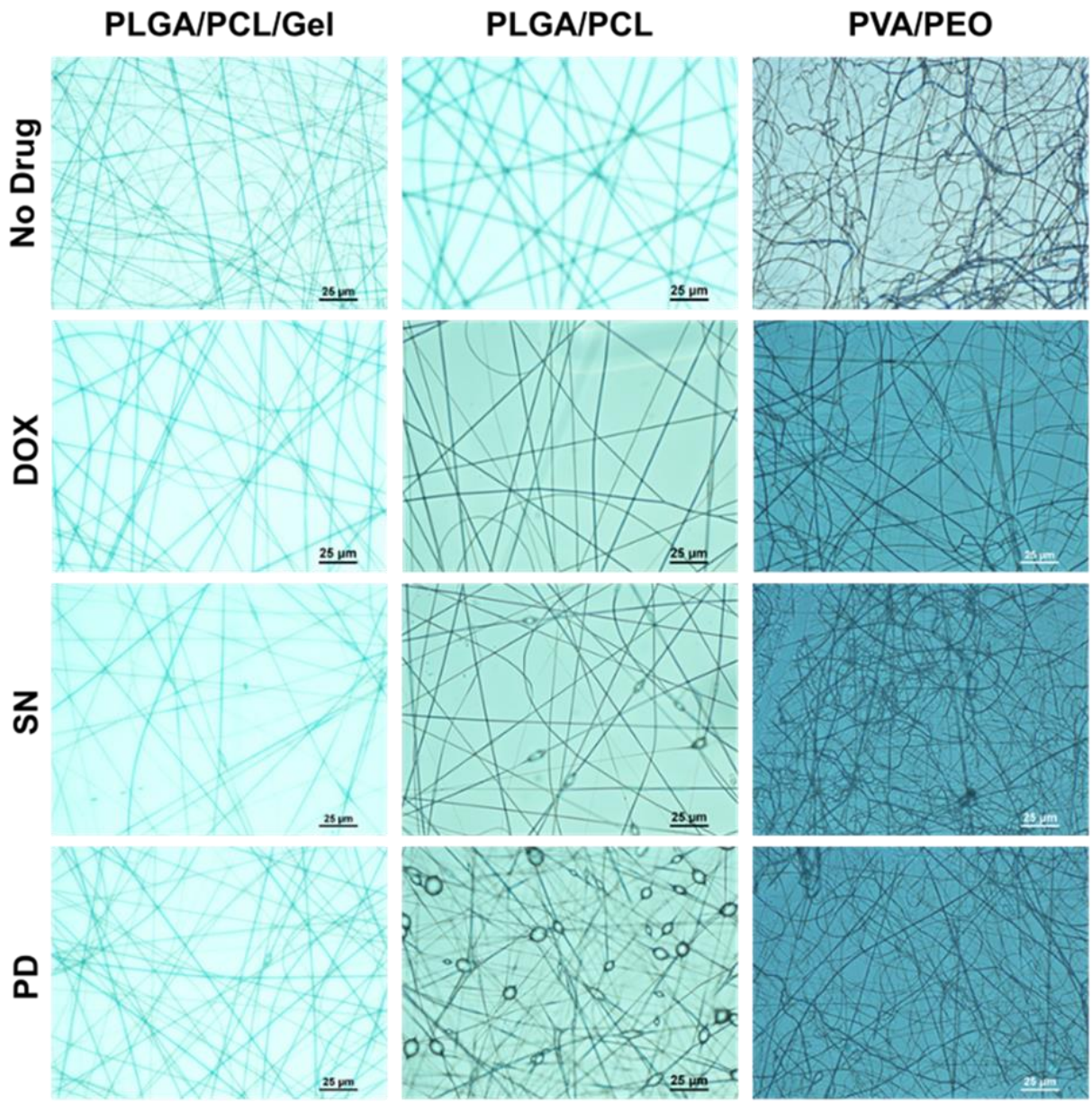

Figure C.2 Images of differences in fiber morphology.

Bright field images of the different fiber/drug combinations electrospun onto microscope slide coverslips captured at 40x magnification by a brightfield microscope (Nikon Eclipse Ti).

Table C.1. Table of descriptions and diagrams used to score histology images

Criteria: Collagen Deposition		
Score	**Description**	**Diagram Example**
1-3	Minimal collagen deposition. Loose deposition if at all.	
4-6	Thin layer of collagen deposition. Deposition of collagen is loose between muscle layers.	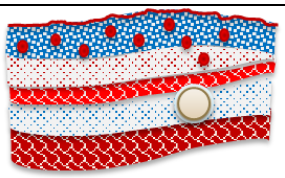
7-9	Thick collagen deposition around implant or between muscle layers. Some regions of thick deposition, but primarily loosely oriented.	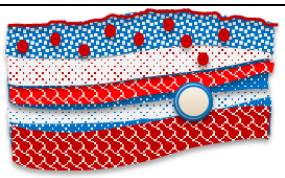
10-12	Extensive and dense collection of collagen found around implant or between muscle layers.	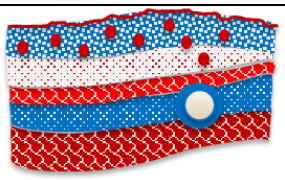
Criteria: Inflammatory Infiltrate		
Score	**Description**	**Diagram Example**
1-3	No Apparent accumulation of inflammatory cells.	
4-6	Few inflammatory cells are present in the pocket space or in adipose tissue.	
7-9	A thin layer of cells surrounds the implant or are accumulated in the pocket space.	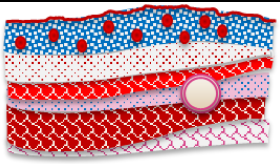
10-12	A thick layer of cells surrounds the implant or are accumulated in the pocket space.	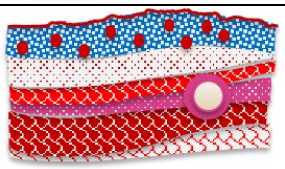

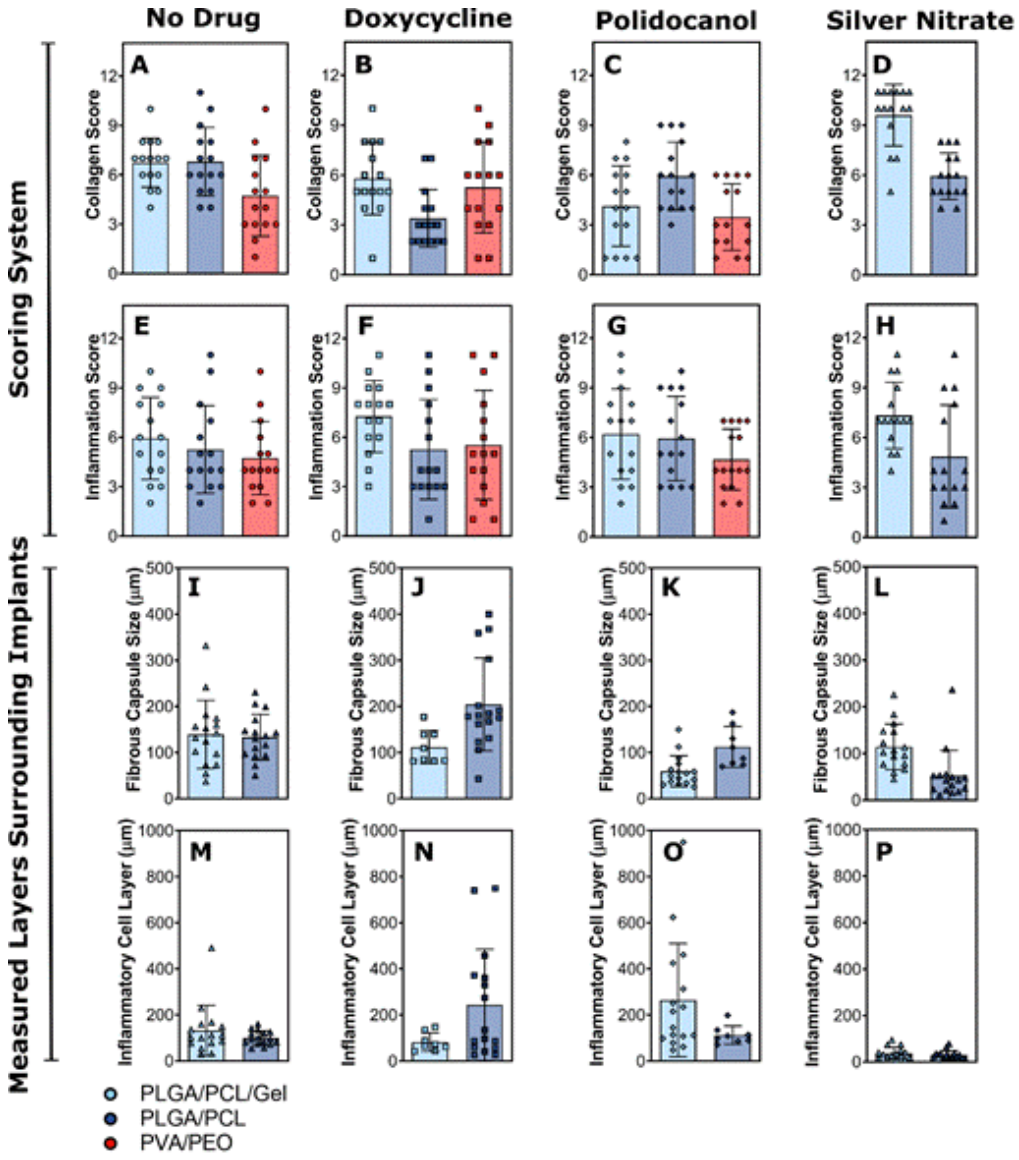

Figure C.3. Scores, Fibrous capsule, and cell layer measurements from implant histology.

Implants made of PLGA/PCL/Gel (light blue), PLGA/PCL (dark blude), and PVA/PEO (red) elute (A, E, I, & M) no drug, (B, F, J, & N) doxycycline, (C, G, K, & O) polidocanol, or (D, H, L, & P) silver nitrate. Scores for collagen deposition (A-D) and inflammation (E-H) were determined by the scoring system shown in supporting Table C.1

Table C.1. Table of descriptions and diagrams used to score histology images

. Scores were determined by n=8 scorers, and n=2 images of implants for n=1 mouse. Measurements of (I-L) fibrous capsule and inflammatory cell layers (M-P) taken from Masson's Trichrome histology images at the implant site. Biomaterial implants included in this measurement analysis were present at the time of sacrifice, and therefore are composed of PLGA/PCL or PLGA/PCL/Gel. Capsule quantifications were made using ImageJ and n=8 measurements of n=2 implants. Implants for PLGA/PCL/PD and PLGA/PCL/Gel/Dox were only imaged for as n=1 implant. Measurements are plotted as individual measurements as well as bars that represent the average ± the standard deviation.

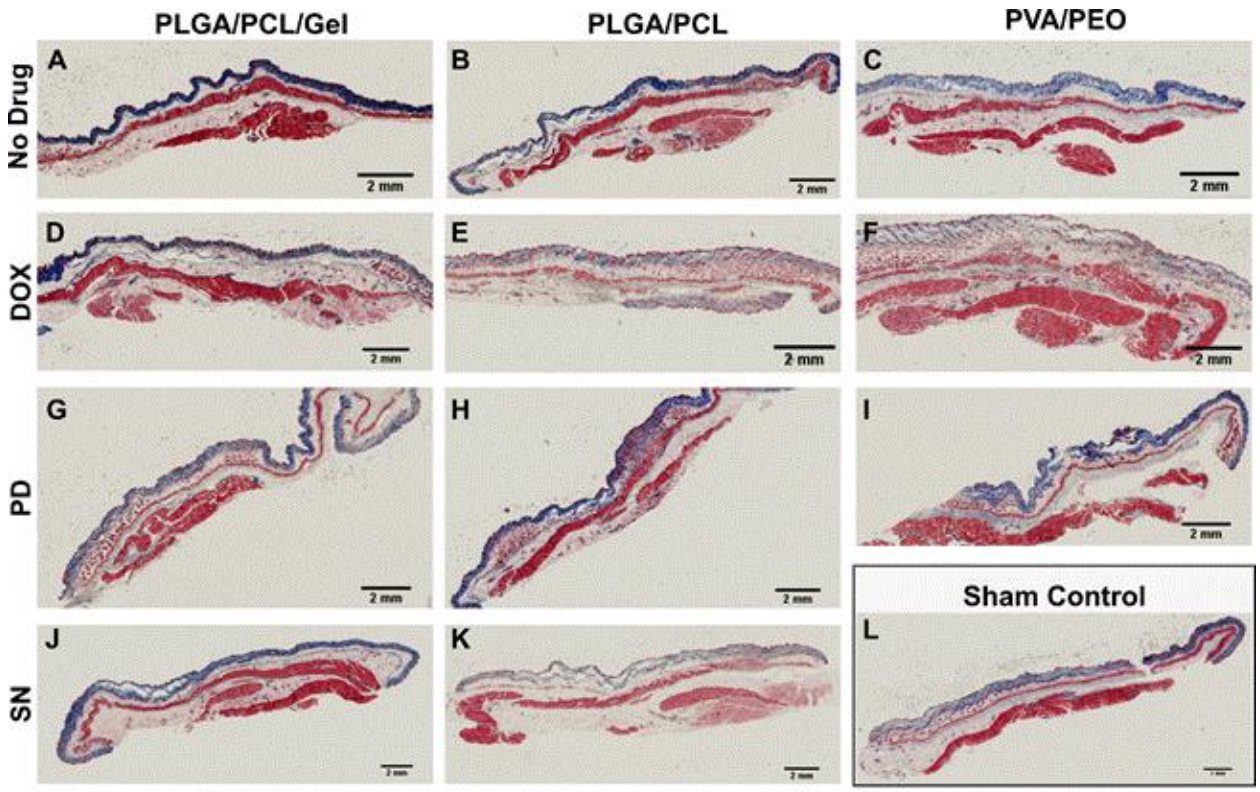

Figure C.4. Murine implant internal control histology sections.

Masson's Trichrome stained tissue sections sampled from implant pocket site, away from the location of the implants. Biomaterial implants are composed of (A, D, G, & J) PLGA/PCL/Gel, (B, E, H, & K) PLGA/PCL, and (C, F, & I) PVA/PEO and eluted (A-C) no drug, (D-F) Dox, (G-I) PD, or (J-K) SN. Histology taken from a (L) sham procedure control is additionally included. Images captured as scans using a Sakura VisionTek Digital Microscope.

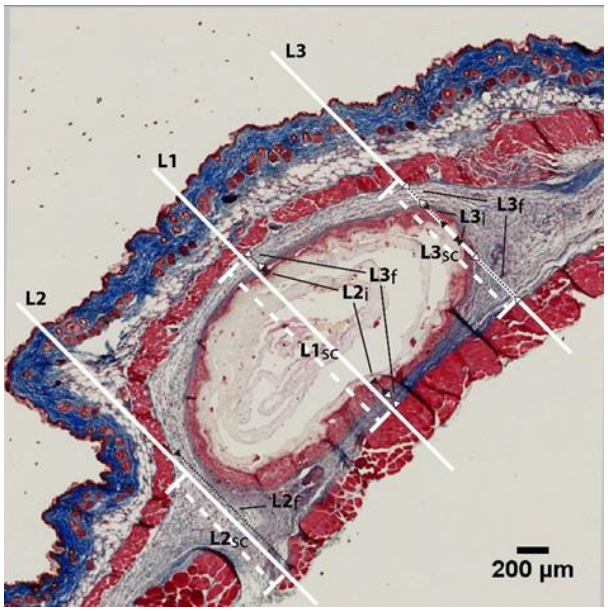

Figure C.5. Diagram of histology quantification method.

Masson's Trichrome stained PLGA/PCL/Gel no drug implant tissue is shown as an example for the quantification method. Three regions of interest (ROI) were defined to perform unbiased measurements. The first ROI is defined by a line, intersecting the center point of the implant in the cross-section image, and drawn perpendicular to the skin surface and through the lower layers of muscle (L1, solid white line). Two additional ROIs are defined as parallel lines (solid white line) 1 mm to the left (L2) and right (L3) of L1. ImageJ (FIJI/ImageJ 1.51s, National Institutes of Health, USA)50 was used to take three measurements at each of these ROIs: (1) subcutis length = length between the two muscle layers (dashed white line, Lsc), (2) inflammation = total length of accumulated immune cells stained red within the subcutis, and additionally identified by cell structure (dashed black line with in-turned black arrow heads, Li), and (3) fibrosis = total length of collagen blue stain (dashed black line with in-turned white arrow heads, Lf). Collagen deposition was defined as the length of both loose collagen (light blue) and dense collagen (dark blue) staining (not shown on image). The inflammatory or fibrotic response is calculated as a percent length of the total subcutis.

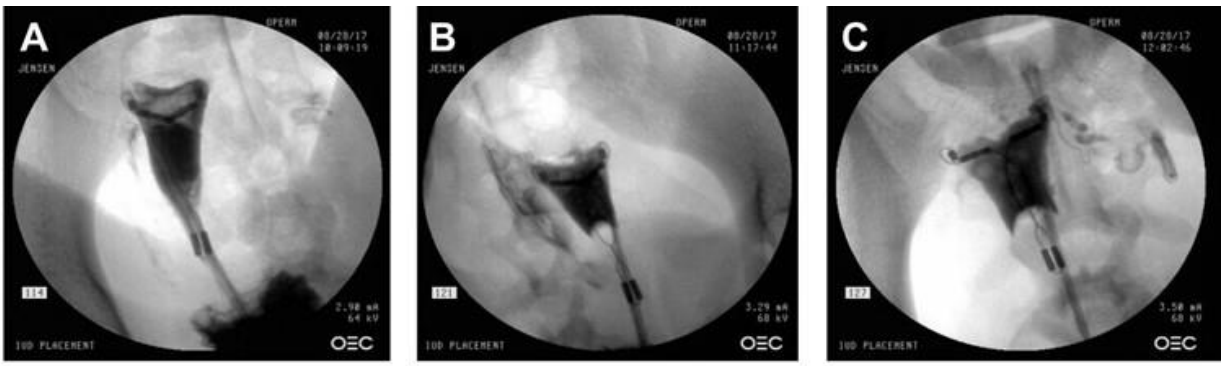

Figure C.6. X-ray images of ContraMed VeraCept IUDs placed in hemadryas (A & B) and Anubis (C) baboons.

The space of the uterine cavity was imaged using contrast agent.

APPENDIX D: CLINICALLY APPROVED ARVS

There are seven classes of FDA approved ARV drugs that inhibit the HIV lifecycle. Fusion inhibitors and CCR5 antagonists prevent HIV attachment to $CD4^+$ T-cells by blocking gp41 on the virus or CCR5 on the cell, respectively. Non-nucleoside reverse transcriptase inhibitors (NNRTIs) and nucleoside reverse transcriptase inhibitors (NRTIs) block viral reverse transcriptase, therefore preventing replication of viral DNA. Integrase inhibitors prevent the viral DNA from integrating into the cellular DNA. Protease inhibitors (PIs) block viral protease enzymes from assembling functional HIV replicates.[397] The newest class of ARVs is post attachment inhibitors, containing only Ibalizumab which was FDA approved in 2018.[398] Ibalizumab is an anti-CD4 antibody that also blocks HIV-1 entry.[398,399]

Table D.1 contains a list of various FDA approved ARV agents and drug properties. Solubility is reported as a known factor of drug release rate. Sustained drug release is typically achieved with the use of more hydrophobic drugs with lower water solubility values.[90] In addition to the timeframe which a drug can be released in the body, the amount that is needed to be effective must be considered. Greater drug potency can inhibit HIV at lower concentrations. Lower half maximal effective concentration (EC_{50}) or inhibitory concentration (IC_{50}) values are most ideal for long-acting, compliance independent drug dosing systems. Values for protein adjusted inhibitory concentrations for 90% (PA-IC_{90}) of the viral population were included if found in the literature. The PA-IC_{90} accounts for concentrations of the drug that will bind to plasma proteins and therefore is considered a more applicable measurement.[400] Half-life was included in this table as it is a widely reported value that can provide information on relative required dosing frequencies.[401]

Table D.1. List of FDA approved ARVs.

ARV[402]	Class[402]	Solubility in Water (mg/mL)	Potency (against wildtype HIV-1)	Terminal plasma half-life with Oral dosing ($t_{1/2}$)
Rilpivirine (RPV)	NNRTI	$2.0x10^{-5}$ (at pH 7)[403]	EC_{50} = 0.67 nM[403], 0.5 nM[404] PA-IC_{90} = 20.3 ng/mL[405]	34-55 hours[404]
Dapivirine (DPV)[403]	NNRTI	$1.5x10^{-4}$ (at pH 6.5)[403]	EC_{50} = 0.7 nM[403] IC_{99} = 3.3 ng/mL[45]	67 hours (from vaginal ring), 12-14 hours (after ring removal)[45]
Etravirine (ETR)	NNRTI	<< $1.0x10^{-3}$ (at pH 6.5)[403], 0.07 mg/mL in water[406]	EC_{50} = 1 nM[403], 1.4-4.8 nM[404] PA-IC_{90} = 116 ng/mL[405]	30-40 hours[407], 41 hours[404]
Efavirenz (EFV)	NNRTI	$6.8x10^{-2}$ (at pH 6.5)[403]	EC_{50} = 2 nM[403] PA-IC_{90} = 126 ng/mL[405]	26 hours[408] 40-50 hours[409]
Doravirine (DOR)	NNRTI	$1.9x10^{-2}$ (at pH 7)[410]	IC_{50} = 12 nM[403], 13 nM[410] IC_{95} = 19 nM[411]	12-21 hours[411]
Nevirapine (NVP)	NNRTI	0.167 (at pH 6.5)[403]	EC_{50} = 110 nM[403]	51-53.9 hours[412] 25-30 hours[409]
Tenofovir disoproxil fumerate (TDF)	NRTI	13.4 (at 25°C)[413]	EC_{50} = 5 nM[414] IC_{90} = 18 ng/mL[405]	12-14.4 hours[414] 6.64 hours[414] 71 hours (cervicovaginal fluids), 47 hours (Oral)[415]
Emtricitabine (FTC)	NRTI	112 (at 25°C)[416]	EC_{50} = 8.5 nM[417] IC_{90} = 50.2 ng/mL[405]	49 hours (blood) 40 hours (cervicovaginal fluids)[415]
Zidovudine (AZT)	NRTI	20.1 (at 25°C)[418]	EC_{50} = 55 nM[417]	1 hour[419] 1.2 hours[409]
Abacavir (ABC)	NRTI	77 (at 25°C)[420]	EC_{50} = 5000 nM[421]	1.5 hour[409]
Lamivudine (3TC)	NRTI	70 (at 20°C)[422]	EC_{50} = 12,800 nM[410], 110 nM[417]	5-7 hours (IV)[423] 5.9-9.8 hours (Oral)[423]

Table D.1 (Continued). List of FDA Approved ARVs

ARV[402]	Class[402]	Solubility in Water (mg/mL)	Potency (against wildtype HIV-1)	Terminal plasma half-life with Oral dosing ($t_{1/2}$)
Darunavir (DRV)	PI	$8.7x10^{-3}$ (at 25 °C)[424]	EC_{50} = 1-5 nM[425]	15 hours (in combination with RTV)[404]
Atazanavir (ATV)	PI	0.11 (at 25°C)[426]	EC_{50} = 2.6-5.3 nM[427] PA-IC_{90} = 60 ng/mL[405]	2.8-6.14 hours[427]
Saquinavir (SQV)	PI	2.2 (at 25°C)[428]	EC_{50} = 26 nM[429]	10-13 hours (IV), 6.1-7.7 hours (Oral)[430]
Ritonavir (RTV)	PI	$1.1x10^{-6}$ (at 25°C)[431]	EC_{50} = 65 nM[429]	4.8 hours (in combination with TPV)[404]
Tipranavir (TPV)	PI	$1.17x10^{-9}$ (at 25°C)[432]	EC_{50} = 500 nM[429]	4.8 hours (in combination with RTV)[404]
Enfuviritide (T-20)	Fusion Inhibitor	850-1420 (at pH 7.5)[433]	EC_{50} = 20-240 nM[434]	8.8 hours[435]
Maraviroc (MVC)	CCR5 Antago-nist	$6.57x10^{-6}$ (at 25°C)[436]	EC_{50} = 0.1-4.5 nM[437]	22.9 hours[404]
Dolutegravir (DTG)	Integrase Inhibitor	$9.5x10^{-2}$ (at 25°C)[438]	EC_{50} = 0.2-0.8 nM[439] PA-IC_{90} = 64 ng/mL (nanocrystalline)[37]	61.9 hours (nanocrystalline)[37] 12-15 hours[440]
Raltegravir (RAL)	Integrase Inhibitor	53.9 (at 25°C)[441]	EC_{50} = 3-8 nM[439] IC_{95} = 15 ng/mL[405]	7-12 hours[404] 9 hours[440]
Ibalizumab	Post-attachment Inhibitor	-	IC_{50} = 30 ng/mL[442]	3-3.5 days[399]

BIBLIOGRAPHY

1. Thomson, K. A. *et al.* Tenofovir-based Oral PrEP Prevents HIV Infection among Women. *Curr Opin HIV AIDS* **11**, 18–26 (2016).
2. Campaign, P. A. RISK OF SEXUAL TRANSMISSION OF HIV FROM A PERSON LIVING WITH HIV WHO HAS AN UNDETECTABLE VIRAL LOAD. (2019). Available at: https://www.preventionaccess.org/consensus. (Accessed: 20th August 2018)
3. UNAIDS. Global HIV & AIDS statistics - 2018 fact sheet. (2018). Available at: http://www.unaids.org/en/resources/fact-sheet.
4. Eakle, R., Venter, F. & Rees, H. Pre-exposure prophylaxis (PrEP) in an era of stalled HIV prevention: Can it change the game? *Retrovirology* **15**, 1–10 (2018).
5. Women, U. Facts and figures: HIV and AIDS. (2018). Available at: http://www.unwomen.org/en/what-we-do/hiv-and-aids/facts-and-figures.
6. Cottrell, M. L. *et al.* A Translational Pharmacology Approach to Predicting Outcomes of Preexposure Prophylaxis Against HIV in Men and Women Using Tenofovir Disoproxil Fumarate with or Without Emtricitabine. *J. Infect. Dis.* **214**, 55–64 (2016).
7. Kashuba, A. D. M. *et al.* Genital Tenofovir Concentrations Correlate With Protection Against HIV Infection in the CAPRISA 004 Trial: Importance of adherence for microbicide effectiveness. *J. Acquir. Immune Defic. Syndr.* **69**, 264–269 (2015).
8. Spreen, W. *et al.* GSK1265744 pharmacokinetics in plasma and tissue after single-dose long-acting injectable administration in healthy subjects. *J. Acquir. Immune Defic. Syndr.* **67**, 481–486 (2014).
9. Spreen, W. *et al.* Pharmacokinetics, Safety, and Monotherapy Antiviral Activity of GSK1265744, an HIV Integrase Strand Transfer Inhibitor. *HIV Clin. Trials* **14**, 192–203 (2013).
10. Trezza, C., Ford, S. L., Spreen, W., Pan, R. & Piscitelli, S. Formulation and pharmacology of long-acting cabotegravir. *Curr. Opin. HIV AIDS* **10**, 239–245 (2015).
11. Owen, A. & Rannard, S. Strengths, weaknesses, opportunities and challenges for long acting injectable therapies: Insights for applications in HIV therapy. *Adv. Drug Deliv. Rev.* **103**, 144–156 (2016).
12. Kovarova, M. *et al.* Ultra-long-acting removable drug delivery system for HIV treatment and prevention. *Nat. Commun.* **9**, 1–11 (2018).
13. Iyer, S. S., Barr, W. H. & Karnes, H. T. Profiling in vitro drug release from subcutaneous implants: A review of current status and potential implications on drug product development. *Biopharm. Drug Dispos.* **27**, 157–170 (2006).
14. Segura, S. & Requena, L. Anatomy and Histology of Normal Subcutaneous Fat, Necrosis of Adipocytes, and Classification of the Panniculitides. *Dermatol Clin* **26**, 419–424 (2008).
15. Weld, E. D. & Flexner, C. Long-acting implants to treat and prevent HIV infection. *Curr Opin HIV AIDS* **15**, 33–41 (2020).
16. Kovalevsky, G. & Barnhart, K. Norplant and Other Implantable Contraceptives. *Clin. Obstet. Gynecol.* **44**, 92–100 (2001).
17. Abdool Karim, S. S., Kashuba, A. D. M., Werner, L. & Abdool Karim, Q. Drug concentrations after topical and oral antiretroviral pre- exposure prophylaxis: implications for HIV prevention in women. *Lancet* **378**, 279–281 (2011).

18. Baeten, J. M. *et al.* Use of a vaginal ring containing dapivirine for HIV-1 prevention in women. *New Engl. J. Med.* **375**, 2121–2130 (2016).
19. Fredricks, D. N., Fiedler, T. L. & Marrazzo, J. M. Molecular Identification of Bacteria Associated with Bacterial Vaginosis. *N. Engl. J. Med.* **353**, 1899–1911 (2005).
20. Jagarapu, A., Piovoso, M. J. & Zurakowski, R. An Integrated Spatial Dynamics — Pharmacokinetic Model Explaining Poor Penetration of Anti-retroviral Drugs in Lymph Nodes. *Front. Bioeng. Biotechnol.* **8**, 1–15 (2020).
21. Burgunder, E. *et al.* Antiretroviral Drug Concentrations in Lymph Nodes: A Cross-Species Comparison of the Effect of Drug Transporter Expression, Viral Infection, and Sex in Humanized Mice, Nonhuman Primates, and Humans. *J. Pharmacol. Exp. Ther.* 360–368 (2019). doi:10.1124/jpet.119.259150
22. Hladik, F. & Hope, T. J. HIV infection of the genital mucosa in women. *Curr. HIV/AIDS Rep.* **6**, 20–8 (2009).
23. Hladik, F. & McElrath, M. J. Setting the stage: Host invasion by HIV. *Nat. Rev. Immunol.* **8**, 447–457 (2008).
24. Guay, L. A. *et al.* Intrapartum and neonatal single-dose nevirapine compared with zidovudine for prevention of mother-to-child transmission of HIV-1 in Kampala, Uganda: HIVNET 012 randomised trial. *Lancet* **354**, 795–802 (1999).
25. Grant, R. M. *et al.* Preexposure Chemoprophylaxis for HIV Prevention in Men Who Have Sex with Men. *N. Engl. J. Med.* **363**, 2587–2599 (2010).
26. Van Damme, L. *et al.* Preexposure Prophylaxis for HIV Infection among African Women. *N. Engl. J. Med.* **367**, 411–422 (2012).
27. UNAIDS. Global HIV & AIDS statistics - Fact sheet. (2020). Available at: https://www.unaids.org/en/resources/fact-sheet.
28. Dwyer-Lindgren, L. *et al.* Mapping HIV prevalence in sub-Saharan Africa between 2000 and 2017. *Nature* **570**, 189–193 (2019).
29. Estimates, Unaid. Prevalence of HIV, total (% of population ages 15-49). (2017). Available at: https://data.worldbank.org/indicator/SH.DYN.AIDS.ZS.
30. Celum, C. L. *et al.* Rethinking HIV prevention to prepare for oral PrEP implementation for young African women. *J. Int. AIDS Soc.* **18**, 1–10 (2015).
31. UNAIDS. *Joint United Nations Programme on HIV/AIDS*. (2017).
32. Estimates, U. Prevalence of HIV, female (% ages 15-24). (2017). Available at: https://data.worldbank.org/indicator/SH.HIV.1524.FE.ZS?view=chart.
33. Estimates, U. Prevalence of HIV, male (% ages 15-24). (2017). Available at: https://data.worldbank.org/indicator/SH.HIV.1524.MA.ZS?view=chart.
34. Corneli, A. L. *et al.* FEM-PrEP: Adherence Patterns and Factors Associated With Adherence to a Daily Oral Study Product for Pre-exposure Prophylaxis. *J Acquir Immune Defic Syndr* **66**, 324–331 (2014).
35. Pena-Cruz, V. *et al.* HIV-1 replicates and persists in vaginal epithelial dendritic cells. *J. Clin. Invest.* **128**, 3439–3444 (2018).
36. Aquaro, S. *et al.* Macrophages and HIV infection: Therapeutical approaches toward this strategic virus reservoir. *Antiviral Res.* **55**, 209–225 (2002).
37. Sillman, B. *et al.* Creation of a long-acting nanoformulated dolutegravir. *Nat. Commun.* **9**, 1–14 (2018).
38. Karim, S. S. A., Kashuba, A. D., Werner, L. & Karim, Q. A. Drug concentrations after topical and oral antiretroviral pre-exposure prophylaxis: Implications for HIV prevention

in women. *Lancet* **378**, 279–281 (2011).
39. Karim, Q. A. *et al.* Effectiveness and Safety of Tenofovir Gel, and Antiretroviral Microbicide, for the Prevention of HIV Infection in Women. *Science (80-.).* **329**, 1168–1174 (2010).
40. Marrazzo, J. M. *et al.* Tenofovir-Based Preexposure Prophylaxis for HIV Infection among African Women. *N. Engl. J. Med.* **372**, 509–518 (2015).
41. Murray, M. I. *et al.* Satisfaction and acceptability of cabotegravir long-acting injectable suspension for prevention of HIV: Patient perspectives from the ECLAIR trial. *HIV Clin. Trials* **19**, 129–138 (2018).
42. Margolis, D. A. *et al.* Long-acting intramuscular cabotegravir and rilpivirine in adults with HIV-1 infection (LATTE-2): 96-week results of a randomised, open-label, phase 2b, non-inferiority trial. *Lancet* **390**, 1499–1510 (2017).
43. Ferretti, F. & Boffito, M. Rilpivirine long-Acting for the prevention and treatment of HIV infection. *Curr. Opin. HIV AIDS* **13**, 300–307 (2018).
44. Nel, A. *et al.* Safety and Efficacy of a Dapivirine Vaginal Ring for HIV Prevention in Women. 2133–2143 (2016). doi:10.1056/NEJMoa1602046
45. Nel, A. *et al.* A safety and pharmacokinetic trial assessing delivery of dapivirine from a vaginal ring in healthy women. *AIDS* **28**, 1479–1487 (2014).
46. Williams, P. E., Crauwels, H. M. & Basstanie, E. D. Formulation and pharmacology of long-acting rilpivirine. *Curr. Opin. HIV AIDS* **10**, 233–238 (2015).
47. Markowitz, M. *et al.* Safety and tolerability of long-acting cabotegravir injections in HIV-uninfected men (ECLAIR): a multicentre, double-blind, randomised, placebo-controlled, phase 2a trial. *Lancet HIV* **4**, e331–e340 (2017).
48. Nicol, M. R., Corbino, J. A. & Cottrell, M. L. Pharmacology of Antiretrovirals in the Female Genital Tract for HIV Prevention. *J. Clin. Pharmacol.* **58**, 1381–1395 (2018).
49. Dumond, J. B. *et al.* Antiretroviral drug exposure in the female genital tract: implications for oral pre- and post-exposure prophylaxis. *AIDS* **21**, 1899–1907 (2007).
50. Rosen, R. K. *et al.* Acceptability of tenofovir gel as a vaginal microbicide among women in a phase I trial: A mixed-methods study. *J. Women's Heal.* **17**, 383–392 (2008).
51. Chen, B. A. *et al.* Phase 1 Safety, Pharmacokinetics, and Pharmacodynamics of Dapivirine and Maraviroc Vaginal Rings: a Double-Blind Randomized Trial Beatrice. *J Acquir Immune Defic Syndr* **70**, 242–249 (2015).
52. Else, L. J., Taylor, S., Back, D. J. & Khoo, S. H. Pharmacokinetics of antiretroviral drugs in anatomical sanctuary sites: The male and female genital tract. *Antivir. Ther.* **16**, 1149–1167 (2011).
53. Kerrigan, D. *et al.* Experiences with long acting injectable ART: A qualitative study among PLHIV participating in a Phase II study of cabotegravir + rilpivirine (LATTE-2) in the United States and Spain. *PLoS One* **13**, 1–11 (2018).
54. Cleland, J. Contraception in historical and global perspective. *Best Pract. Res. Clin. Obstet. Gynaecol.* **23**, 165–176 (2009).
55. Brooks, M. I. *et al.* Can community health workers increase modern contraceptive use among young married women? A cross-sectional study in rural Niger. *Reprod. Health* **16**, 1–10 (2019).
56. Speidel, J. J., Harper, C. C. & Shields, W. C. The potential of long-acting reversible contraception to decrease unintended pregnancy. *Contraception* **78**, 197–200 (2008).
57. Buhling, K. J., Zite, N. B., Lotke, P. & Black, K. Worldwide use of intrauterine

contraception: A review. *Contraception* **89**, 162–173 (2014).
58. Nations, U. *Trends in Contraceptive Use Worldwide*. (2015).
59. Ahmed, K. *et al.* HIV incidence among women using intramuscular depot medroxyprogesterone acetate, a copper intrauterine device, or a levonorgestrel implant for contraception: a randomised, multicentre, open-label trial. *Lancet* 1–11 (2019). doi:10.1016/S0140-6736(19)31288-7
60. Polis, C. B. *et al.* An updated systematic review of epidemiological evidence on hormonal contraceptive methods and HIV acquisition in women. *Aids* **30**, 2665–2683 (2016).
61. Morrison, C. S. *et al.* Hormonal Contraception and the Risk of HIV Acquisition: An Individual Participant Data Meta-analysis. *PLoS Med.* **12**, 1–26 (2015).
62. Ba, D. M., Ssentongo, P., Agbese, E. & Kjerulff, K. H. Prevalence and predictors of contraceptive use among women of reproductive age in 17 sub-Saharan African countries: A large population-based study. *Sex. Reprod. Healthc.* **21**, 26–32 (2019).
63. Wang, C. & Cao, H. Persisting Regional Disparities in Modern Contraceptive Use and Unmet Need for Contraception among Nigerian Women. *Biomed Res. Int.* 1–9 (2019). doi:10.1155/2019/9103928
64. United Nations, Department of Economic and Social Affairs, P. D. World Contraceptive Use 2019. (2019). Available at: https://www.un.org/en/development/desa/population/publications/dataset/contraception/wcu2019.asp.
65. Prevention, C. for D. C. and. Birth Control Methods. (2018). Available at: https://www.cdc.gov/reproductivehealth/contraception/index.htm.
66. Wall, K. M. *et al.* Rwandan stakeholder perspectives of integrated family planning and HIV services. *Int J Heal. Plann Mgmt* **33**, e1037–e1049 (2018).
67. Foundation, H. J. K. F. Intrauterine Devices (IUDs): Access for Women in the U.S. (2016). Available at: https://www.kff.org/womens-health-policy/fact-sheet/intrauterine-devices-iuds-access-for-women-in-the-u-s/.
68. Administration, U. S. F. and D. Drug Approval Package Mirena. (2004). Available at: https://www.accessdata.fda.gov/drugsatfda_docs/nda/2000/21-225_Mirena.cfm.
69. Administration, U. S. F. and D. Drugs@FDA: FDA Approved Drug Products.
70. Administration, U. S. F. and D. Depo-Provera Highlights of Prescribing Information. 1–22 (2010).
71. U.S. Food and Drug Administration. Drug Approval Package NuvaRing. (2001). Available at: https://www.accessdata.fda.gov/drugsatfda_docs/nda/2001/21-187_NuvaRing.cfm.
72. America, P. P. F. of. Birth Control - History of the Pill. 1–14 (2015).
73. Margulies, L. History of Intrauterine Devices. *Bull N Y Acad Med* **51**, 662–667 (1975).
74. P.G., C. Intrauterine devices and intrauterine systems. *Hum. Reprod. Update* **14**, 197–208 (2008).
75. Katz, B., Fujii, D., Matsumoto, S. & Peters, K. INVESTIGATOR'S BROCHURE : VeraCept. 0–26 (2017).
76. CooperSurgical. Paragard Intrauterine Copper Contraceptive Prescribing Information. 1–5 (2018).
77. Baldaszti, E., Wimmer-Puchinger, B. & Loöschke, K. Acceptability of the long-term contraceptive levonorgestrel-releasing intrauterine system (Mirena®): A 3-year follow-up study. *Contraception* **67**, 87–91 (2003).

78. Thonneau, P. F. & Almont, T. E. Contraceptive efficacy of intrauterine devices. *Am. J. Obstet. Gynecol.* **198**, 248–253 (2008).
79. Gemzell-Danielsson, K., Schellschmidt, I. & Apter, D. A randomized, phase II study describing the efficacy, bleeding profile, and safety of two low-dose levonorgestrel-releasing intrauterine contraceptive systems and Mirena. *Fertil. Steril.* **97**, 616-622.e3 (2012).
80. US National Library of Medicine. Evaluation of Efficacy, Safety and Tolerability of VeraCept IUD. *ClinicalTrials.gov* (2018). Available at: https://clinicaltrials.gov/ct2/show/NCT03633799. (Accessed: 17th August 2019)
81. Reeves, M. F., Katz, B. H., Canela, J. M., Hathaway, M. J. & Tal, M. G. A randomized comparison of a novel nitinol-frame low-dose-copper intrauterine contraceptive and a copper T380S intrauterine contraceptive. *Contraception* **95**, 544–548 (2017).
82. Reeves, M. F. A Randomized Single-Blinded Trial of VeraCept, a Novel Nitinol Low-Dose Copper Interuterine Contraceptive Compared With a Copper T380S Intrauterine Contraceptive. *Obstet. Gynecol.* **125**, 5S (2015).
83. Huber, J. Pharmacokinetics of Implanon®. *Contraception* **58**, 85S-90S (1998).
84. Mansour, D. Nexplanon®: what Implanon® did next. *J. Fam. Plan. Reprod. Heal. Care* **36**, 187–189 (2010).
85. Palomba, S., Falbo, A., Di Cello, A., Materazzo, C. & Zullo, F. Nexplanon: The new implant for long-term contraception. A comprehensive descriptive review. *Gynecol. Endocrinol.* **28**, 710–721 (2012).
86. Wong, R. C., Bell, R. J., Thunuguntla, K., McNamee, K. & Vollenhoven, B. Implanon users are less likely to be satisfied with their contraception after 6 months than IUD users. *Contraception* **80**, 452–456 (2009).
87. Uhrich, K. E., Cannizzaro, S. M., Langer, R. S. & Shakesheff, K. M. Polymeric Systems for Controlled Drug Release. *Chem. Rev.* **99**, 3181–3198 (1999).
88. Lyu, S. P., Sparer, R., Hobot, C. & Dang, K. Adjusting drug diffusivity using miscible polymer blends. *J. Control. Release* **102**, 679–687 (2005).
89. Perego, G., Cella, G. D. & Bastioli, C. Effect of molecular weight and crystallinity on poly(lactic acid) mechanical properties. *J. Appl. Polym. Sci.* **59**, 37–43 (2004).
90. Chou, S. F., Carson, D. & Woodrow, K. A. Current strategies for sustaining drug release from electrospun nanofibers. *J. Control. Release* **220**, 584–591 (2015).
91. Ribeiro, C., Sencadas, V., Costa, C. M., Gómez Ribelles, J. L. & Lanceros-Méndez, S. Tailoring the morphology and crystallinity of poly(L-lactide acid) electrospun membranes. *Sci. Technol. Adv. Mater.* **12**, (2011).
92. Fang, J. & Jadhav, P. R. From in vitro EC50 to in vivo dose – response for antiretrovirals using an HIV disease model. Part II: Application to drug development. *J Pharmacokinet Pharmacodyn* **39**, 369–381 (2012).
93. Jilek, B. L. *et al.* A quantitative basis for antiretroviral therapy for HIV-1 infection. *Nat. Med.* **18**, 446–451 (2012).
94. Jiang, Y. *et al.* Nanoparticle-Based ARV Drug Combinations for Synergistic Inhibition of Cell-Free and Cell − Cell HIV Transmission. *ACS Mol. Pharm.* **12**, 4363–4374 (2015).
95. Sleep, D., Cameron, J. & Evans, L. R. Albumin as a versatile platform for drug half-life extension. *Biochim. Biophys. Acta* **1830**, 5526–5534 (2013).
96. Boffito, M. *et al.* Protein Binding in Antiretroviral Therapies. *AIDS Res. Hum. Retroviruses* **19**, 825–835 (2003).

97. Rosenthal, L. D. & Burchum, J. R. Pharmacokinetics, Pharmacodynamics, and Drug Interactions. in *Lehne's Pharamacotherepeutics for Advanced Practice Providers* 80–127 (Elsevier, 2018).
98. Larsen, M. T., Kuhlmann, M., Hvam, M. L. & Howard, K. A. Albumin-based drug delivery: harnessing nature to cure disease. *Mol. Cell. Ther.* **4**, 1–12 (2016).
99. Zhang, W. *et al.* In vivo irreversible albumin-binding near-infrared dye conjugate as a naked- eye and fluorescence dual-mode imaging agent for lymph node tumor metastasis diagnosis. *Biomaterials* **217**, 119279 (2019).
100. Tsopelas, C. & Sutton, R. Why Certain Dyes Are Useful for Localizing the Sentinel Lymph Node. *J. Nucl. Med.* **43**, 1377–1382 (2002).
101. Liu, H. *et al.* Structire-based programming of lymph-node targeting in molecular vaccines. *Nature* **507**, 519–522 (2014).
102. Akers, M. J. Excipient-drug interactions in parenteral formulations. *J. Pharm. Sci.* **91**, 2283–2300 (2002).
103. Wais, U., Jackson, A. W., He, T. & Zhang, H. Nanoformulation and encapsulation approaches for poorly water-soluble drug nanoparticles. *Nanoscale* **8**, 1746–1769 (2016).
104. Gao, L., Zhang, D. & Chen, M. Drug nanocrystals for the formulation of poorly soluble drugs and its application as a potential drug delivery system. *J. Nanoparticle Res.* **10**, 845–862 (2008).
105. Junyaprasert, V. B. & Morakul, B. Nanocrystals for enhancement of oral bioavailability of poorly water-soluble drugs. *Asian J. Pharm. Sci.* **10**, 13–23 (2015).
106. Haugen, H. J. & Bertoldi, S. *Characterization of morphology — 3D and porous structure*. (2017).
107. Rouquerol, J. *et al. Recommendations for the characterization of porous solids*. *Pure & Appl. Chem.* **66**, (1994).
108. Mishra, R., Militky, J. & Venkataraman, M. *Nanoporous materials*. (2018).
109. Sayed, E. *et al.* Porous Inorganic Drug Delivery Systems — a Review. *AAPS PharmSciTech* **18**, 1507–1525 (2017).
110. Ngo, T. D., Kashani, A., Imbalzano, G., Nguyen, K. T. Q. & Hui, D. Additive manufacturing (3D printing): A review of materials, methods, applications and challenges. *Compos. Part B* **143**, 172–196 (2018).
111. Yan, Q. *et al.* A Review of 3D Printing Technology for Medical Applications. *Engineering* **4**, 729–742 (2018).
112. He, F. *et al.* A novel layer-structured scaffold with large pore sizes suitable for 3D cell culture prepared by near-field electrospinning. *Mater. Sci. Eng. C* **86**, 18–27 (2018).
113. Tylek, T. *et al.* Precisely defined fiber scaffolds with 40 μm porosity induce elongation driven M2-like polarization of human macrophages. *Biofabrication* **12**, 025007 (2020).
114. Li, S. *et al.* Liquid-induced topological transformations of cellular microstructures. *Nature* **592**, 386–391 (2021).
115. Saltzman, W. M. & Langer, R. Transport rates of proteins in porous materials with known microgeometry A9t. *Biophys. J.* **55**, 163–171 (1989).
116. Gunathilake, T. M. S. U., Ching, Y. C., Ching, K. Y. & Chuah, C. H. Biomedical and Microbiological Applications of Bio-Based Porous Materials: A Review. *Polymers (Basel).* **9**, 1–16 (2017).
117. Annabi, N., Nichol, J. W., Ph, D., Zhong, X. & Ji, C. Controlling the Porosity and Microarchitecture of Hydrogels for Tissue Engineering. *Tissue Eng. Part B* **16**, 371–383

(2010).
118. Garg, T. & Goyal, A. K. Biomaterial-based scaffolds – current status and future directions. *Expert Opin. Drug Deliv.* **11**, 767–789 (2014).
119. Braunecker, J., Baba, M., Milroy, G. E. & Cameron, R. E. The effects of molecular weight and porosity on the degradation and drug release from polyglycolide. *Int. J. Pharm.* **282**, 19–34 (2004).
120. Kumari, P. V. K., Sharmila, M. & Rao, Y. S. Super Porous Hydrogels: A Review. *J. Pharm. Res. Int.* **32**, 153–165 (2020).
121. Oh, D. S., Joon, Y., Hong, M., Han, M. & Kim, K. Effect of capillary action on bone regeneration in micro-channeled ceramic scaffolds. *Ceram. Int.* **40**, 9583–9589 (2014).
122. Long, T. J., Takeno, M., Sprenger, C. C., Plymate, S. R. & Ratner, B. D. Capillary Force Seeding of Sphere-Templated Hydrogels for Tissue-Engineered Prostate Cancer Xenografts. *Tissue Eng. Part C* **19**, 738–744 (2013).
123. Rnjak-Kovacina, J. & Weiss, A. S. Increasing the Pore Size of Electrospun Scaffolds. *Tissue Eng. Part B* **17**, 365–372 (2011).
124. von Recum, A. F. *et al.* Surface Roughness, Porosity, and Texture as Modifiers of Cellular Adhesion. *Tissue Eng.* **2**, 241–253 (1996).
125. Bota, P. C. S. *et al.* Biomaterial topography alters healing in vivo and monocyte/macrophage activation in vitro. *J. Biomed. Mater. Res. A* **95A**, 649–657 (2010).
126. Cox, S. C. *et al.* Surface Finish has a Critical Influence on Biofilm Formation and Mammalian Cell Attachment to Additively Manufactured Prosthetics. *ACS Biomater. Sci. Eng.* **3**, 1616–1626 (2017).
127. Xu, L., Bauer, J. & Siedlecki, C. A. Proteins, Platelets, and Blood Coagulation at Biomaterial Interfaces. *Colloids Surf B Biointerfaces* **124**, 49–68 (2014).
128. Ozpinar, E. W., Frey, A. L., Cruse, G. & Freytes, D. O. Mast Cell – Biomaterial Interactions and Tissue Repair. *Tissue Eng. Part B* **00**, 1–14 (2021).
129. Doloff, J. C. *et al.* The surface topography of silicone breast implants mediates the foreign body response in mice, rabbits and humans. *Nat. Biomed. Eng.* (2021). doi:10.1038/s41551-021-00739-4
130. Ribas, R. G. *et al.* Current advances in bone tissue engineering concerning ceramic and bioglass scaffolds: A review. *Ceram. Int.* **45**, 21051–21061 (2019).
131. Sussman, E. M., Halpin, M. C., Muster, J., Moon, R. T. & Ratner, B. D. Porous Implants Modulate Healing and Induce Shifts in Local Macrophage Polarization in the Foreign Body Reaction. *Ann. Biomed. Eng.* **42**, 1508–1516 (2014).
132. Garg, K., Pullen, N. A., Oskeritzian, C. A., Ryan, J. J. & Bowlin, G. L. Macrophage functional polarization (M1/M2) in response to varying fiber and pore dimensions of electrospun scaffolds. *Biomaterials* **34**, 4439–4451 (2013).
133. Karp, R. D. *et al.* Tumorigenesis by Millipore Filters in Mice: Histology and Ultrastructure of Tissue Reactions as Related to Pore Size. *Natl Cancer Inst* **51**, 1275–1285 (1973).
134. Bezuidenhout, D., Davies, N. & Zilla, P. Effect of Well Defined Dodecahedral Porosity on Inflammation and Angiogenesis. *ASAIO J.* **48**, 465–471 (2002).
135. Wesolowski, S. A., Fries, C. C., Karlson, K. E., Bakey, M. De & Sawyer, P. N. Porosity: Primary determinant of ultimate fate of synthetic vascular grafts. *Plast. Reconstr. Surg.* **29**, 131–132 (1962).
136. Brauker, J. H. *et al.* Neovascularization of synthetic membranes directed by membrane

microarchitecture. *J. Biomed. Mater. Res.* **29**, 1517–1524 (1995).
137. Milleret, V., Hefti, T., Hall, H., Vogel, V. & Eberli, D. Influence of the fiber diameter and surface roughness of electrospun vascular grafts on blood activation. *Acta Biomater.* **8**, 4349–4356 (2012).
138. Sclafani, A. P., Thomas, J. R., Cox, A. J. & Cooper, M. H. Clinical and Histologic Response of Subcutaneous Expanded Polytetrafluoroethylene (Gore-Tex) and Porous High-Density Polyethylene (Medpor) Implants to Acute and Early Infection. *Arch Otolaryngol Head Neck Surg* **123**, 328–336 (1997).
139. Gouda, R., Baishya, H. & Qing, Z. Application of Mathematical Models in Drug Release Kinetics of Carbidopa and Levodopa ER Tablets. *J. Dev. Drugs* **6**, 1–8 (2017).
140. Siepmann, J. & Peppas, N. A. Higuchi equation: Derivation, applications, use and misuse. *Int. J. Pharm.* **418**, 6–12 (2011).
141. Khanafer, K. & Vafai, K. The role of porous media in biomedical engineering as related to magnetic resonance imaging and drug delivery. *Heat Mass Transf. und Stoffuebertragung* **42**, 939–953 (2006).
142. Korsmeyer, R. W., Gurny, R., Doelker, E., Buri, P. & Peppas, N. A. Mechanisms of solute release from porous hydrophilic polymers. *Int. J. Pharm.* **15**, 25–35 (1983).
143. Guan, J., Fujimoto, K. L., Sacks, M. S. & Wagner, W. R. Preparation and characterization of highly porous, biodegradable polyurethane scaffolds for soft tissue applications. *Biomaterials* **26**, 3961–3971 (2005).
144. Agrawal, C. M., Mckinney, J. S., Lanctot, D. & Athanasiou, K. A. Effects of fluid flow on the in vitro degradation kinetics of biodegradable scaffolds for tissue engineering. *Biomaterials* **21**, 2443–2452 (2000).
145. Lu, L. *et al.* In vitro degradation of porous poly (L -lactic acid) foams. *Biomaterials* **21**, 1595–1605 (2000).
146. Chen, S., Li, R., Li, X. & Xie, J. Electrospinning: An enabling nanotechnology platform for drug delivery and regenerative medicine. *Adv. Drug Deliv. Rev.* **132**, 188–213 (2018).
147. Persano, L., Camposeo, A., Tekmen, C. & Pisignano, D. Industrial upscaling of electrospinning and applications of polymer nanofibers: A review. *Macromol. Mater. Eng.* **298**, 504–520 (2013).
148. Doshi, J. & Reneker, D. H. Electrospinning Process and Applications of Electrospun Fibers. *J. Electrostat.* **35**, 151–296 (1995).
149. Yarin, A. L., Koombhongse, S. & Reneker, D. H. Taylor cone and jetting from liquid droplets in electrospinning of nanofibers. *J. Appl. Phys.* **90**, 4836–4846 (2001).
150. Yoo, H. S., Kim, T. G. & Park, T. G. Surface-functionalized electrospun nanofibers for tissue engineering and drug delivery. *Adv. Drug Deliv. Rev.* **61**, 1033–1042 (2009).
151. Pilehvar-Soltanahmadi, Y., Akbarzadeh, A., Moazzez-Lalaklo, N. & Zarghami, N. An update on clinical applications of electrospun nanofibers for skin bioengineering. *Artif. Cells, Nanomedicine Biotechnol.* **44**, 1350–1364 (2016).
152. Ardila, D. C., Tamimi, E., Doetschman, T., Wagner, W. R. & Vande Geest, J. P. Modulating smooth muscle cell response by the release of TGFβ2 from tubular scaffolds for vascular tissue engineering. *J. Control. Release* **299**, 44–52 (2019).
153. Ball, C., Krogstad, E., Chaowanachan, T. & Woodrow, K. A. Drug-Eluting Fibers for HIV-1 Inhibition and Contraception. *PLoS One* **7**, (2012).
154. Jordan, S. W., Fligor, J. E., Janes, L. E. & Dumanian, G. A. Implant Porosity and the Foreign Body Response. *Plast. Reconstr. Surg.* **141**, 103–112 (2017).

155. Vaquette, C. & Cooper-white, J. J. Increasing electrospun scaffold pore size with tailored collectors for improved cell penetration. *Acta Biomater.* **7**, 2544–2557 (2011).
156. Rnjak-Kovacina, J. *et al.* Tailoring the porosity and pore size of electrospun synthetic human elastin scaffolds for dermal tissue engineering. *Biomaterials* **32**, 6729–6736 (2011).
157. Leong, M. F., Rasheed, M. Z., Lim, T. C. & Chian, K. S. In vitro cell infiltration and in vivo cell infiltration and vascularization in a fibrous , highly porous poly (D, L-lactide) scaffold fabricated by cryogenic electrospinning technique. *J Biomed Mater Res* **91A**, 231–240 (2008).
158. Wright, L. D., Andric, T. & Freeman, J. W. Utilizing NaCl to increase the porosity of electrospun materials. *Mater. Sci. Eng. C* **31**, 30–36 (2011).
159. U.S. National Library of Medicine. EktoTherix™ Regenerative Tissue Scaffold for Repair of Surgical Excision Wounds. *ClinicalTrials.gov* (2017). Available at: https://clinicaltrials.gov/ct2/show/NCT02409628?term=electrospun&rank=2. (Accessed: 20th September 2008)
160. Denchai, A., Tartarini, D. & Mele, E. Cellular response to surface morphology: Electrospinning and computational modeling. *Front. Bioeng. Biotechnol.* **6**, 1–11 (2018).
161. U.S. National Library of Medicine. Antimicrobial Effect of Modified Antibiotic Nanofibers for Regenerative Endodontics Procedures. *ClinicalTrials.gov* (2018). Available at: https://clinicaltrials.gov/ct2/show/NCT03690960?term=electrospun&rank=1. (Accessed: 19th August 2019)
162. Blakney, A. K., Ball, C., Krogstad, E. A. & Woodrow, K. A. Electrospun fibers for vaginal anti-HIV drug delivery. *Antiviral Res.* **100**, S9–S16 (2013).
163. Huang, C. *et al.* Electrospun cellulose acetate phthalate fibers for semen induced anti-HIV vaginal drug delivery. *Biomaterials* **33**, 962–969 (2012).
164. Hua, D. *et al.* pH responsive polyurethane (core) and cellulose acetate phthalate (shell) electrospun fibers for intravaginal drug delivery. *Carbohydr. Polym.* **151**, 1240–1244 (2016).
165. Ball, C. & Woodrow, K. A. Electrospun solid dispersions of maraviroc for rapid intravaginal preexposure prophylaxis of HIV. *Antimicrob. Agents Chemother.* **58**, 4855–4865 (2014).
166. Ball, C., Chou, S. F., Jiang, Y. & Woodrow, K. A. Coaxially electrospun fiber-based microbicides facilitate broadly tunable release of maraviroc. *Mater. Sci. Eng. C* **63**, 117–124 (2016).
167. Carson, D., Jiang, Y. & Woodrow, K. A. Tunable Release of Multiclass Anti-HIV Drugs that are Water-Soluble and Loaded at High Drug Content in Polyester Blended Electrospun Fibers. *Pharm. Res.* **33**, 125–136 (2016).
168. Blakney, A. K., Krogstad, E. A., Jiang, Y. H. & Woodrow, K. A. Delivery of multipurpose prevention drug combinations from electrospun nanofibers using composite microarchitectures. *Int. J. Nanomedicine* **9**, 2967–2978 (2014).
169. Crawford, L., Wyatt, M., Bryers, J. & Ratner, B. Biocompatibility Evolves: Phenomenology to Toxicology to Regeneration. *Adv. Healthc. Mater.* **2002153**, 1–21 (2021).
170. Klopfleisch, R. & Jung, F. The pathology of the foreign body reaction against biomaterials. *J. Biomed. Mater. Res. - Part A* **105**, 927–940 (2017).

171. Isenhath, S. N. *et al.* A mouse model to evaluate the interface between skin and a percutaneous device. *J. Biomed. Mater. Res. Part A* **83**, 915–922 (2007).
172. Fukano, Y. *et al.* Characterization of an in vitro model for evaluating the interface between skin and percutaneous biomaterials. *Wound Rep Reg* **14**, 484–491 (2006).
173. Fukano, Y. *et al.* Epidermal and dermal integration into sphere-templated porous poly (2-hydroxyethyl methacrylate) implants in mice. *J. Biomed. Mater. Res. A* **94A**, 1172–1186 (2010).
174. Ward, W. K., Slobodzian, E. P., Tiekotter, K. L. & Wood, M. D. The effect of microgeometry, implant thickness and polyurethane chemistry on the foreign body response to subcutaneous implants. *Biomaterials* **23**, 4185–4192 (2002).
175. Gori, M., Vadalà, G., Giannitelli, S. M., Denaro, V. & Pino, G. Di. Biomedical and Tissue Engineering Strategies to Control Foreign Body Reaction to Invasive Neural Electrodes. *Front. Bioeng. Biotechnol.* **9**, 1–26 (2021).
176. Orenstein, S. B., Saberski, E. R., Kreutzer, D. L. & Novitsky, Y. W. Comparative analysis of histopathologic effects of synthetic meshes based on material, weight, and pore size in mice. *J. Surg. Res.* **176**, 423–429 (2012).
177. Bryers, J. D., Giachelli, C. M. & Ratner, B. D. Engineering biomaterials to integrate and heal: The biocompatibility paradigm shifts. *Biotechnol. Bioeng.* **109**, 1898–1911 (2012).
178. Anderson, J. M., Rodriguez, A. & Chang, D. T. Foreign body reaction to biomaterials. *Semin. Immunol.* **20**, 86–100 (2008).
179. Hady, T. F. *et al.* Uniform 40-μm-pore diameter precision templated scaffolds promote a pro-healing host response by extracellular vesicle immune communication. *J Tissue Eng Regen Med* **15**, 24–36 (2020).
180. Haase, T. *et al.* In vivo biocompatibility assessment of poly(ether imide) electrospun scaffolds. *J. Tissue Eng. Regen. Med.* **11**, 1034–1044 (2017).
181. Rosengren, A. & Bjursten, L. M. Pore size in implanted polypropylene filters is critical for tissue organization. *J. Biomed. Mater. Res. - Part A* **67**, 918–926 (2003).
182. Yin, Y. *et al.* Pore size-mediated macrophage M1-to-M2 transition influences new vessel formation within the compartment of a scaffold. *Appl. Mater. Today* **18**, 100466 (2020).
183. Saino, E. *et al.* Effect of Electrospun Fiber Diameter and Alignment on Macrophage Activation and Secretion of Proinflammatory Cytokines and Chemokines. *Biomacromolecules* **12**, 1900–1911 (2011).
184. Lucke, S. *et al.* The in vivo inflammatory and foreign body giant cell response against different poly (L-lactide-co-D/L-lactide) implants is primarily determined by material morphology rather than surface chemistry. *J Biomed Mater Res Part A* **106A**, 2726–2734 (2018).
185. Feng, G. *et al.* Bacterial attachment and biofilm formation on surfaces are reduced by small-diameter nanoscale pores: How small is small enough? *npj Biofilms Microbiomes* **1**, 15022 (2015).
186. Braem, A. *et al.* Staphylococcal biofilm growth on smooth and porous titanium coatings for biomedical applications. *J. Biomed. Mater. Res. A* **102A**, 215–224 (2014).
187. Merritt, K., Shafer, J. W. & Brown, S. A. Implant Site Infection Rates with Porous and Dense Materials. *J. Biomed. Mater. Res.* **13**, 101–108 (1979).
188. Arciola, C. R., Campoccia, D. & Montanaro, L. Implant infections: adhesion, biofilm formation and immune evasion. *Nat. Rev. Microbiol.* **16**, 397–409 (2018).
189. Lord, M. S., Foss, M. & Besenbacher, F. Influence of nanoscale surface topography on

protein adsorption and cellular response. *Nano Today* **5**, 66–78 (2010).
190. Jansson, E. & Tengvall, P. Adsorption of albumin and IgG to porous and smooth titanium. *Colloids Surfaces B Biointerfaces* **35**, 45–51 (2004).
191. Richert, L., Variola, F., Rosei, F., Wuest, J. D. & Nanci, A. Surface Science Adsorption of proteins on nanoporous Ti surfaces. *Surf. Sci.* **604**, 1445–1451 (2010).
192. Woo, K. M., Chen, V. J. & Ma, P. X. Nano-fibrous scaffolding architecture selectively enhances protein adsorption contributing to cell attachment. *J Biomed Mater Res A* **67**, 531–537 (2003).
193. van Tienen, T. G. *et al.* Tissue ingrowth and degradation of two biodegradable porous polymers with different porosities and pore sizes. *Biomaterials* **23**, 1731–1738 (2002).
194. Klopfleisch, R. Macrophage reaction against biomaterials in the mouse model – Phenotypes, functions and markers. *Acta Biomater.* **43**, 3–13 (2016).
195. Adusei, K. M., Ngo, T. B. & Sadtler, K. T lymphocytes as critical mediators in tissue regeneration, fibrosis, and the foreign body response. *Acta Biomater.* (2021). doi:10.1016/j.actbio.2021.04.023
196. Rodriguez, A., MacEwan, S. R., Meyerson, H., Kirk, J. T. & Anderson, J. M. The foreign body reaction in T-cell-deficient mice. *J. Biomed. Mater. Res. - Part A* **90**, 106–113 (2009).
197. Bartneck, M. *et al.* Inducing healing-like human primary macrophage phenotypes by 3D hydrogel coated nanofibres. *Biomaterials* **33**, 4136–4146 (2012).
198. Klinge, U. *et al.* Impact of polymer pore size on the interface scar formation in a rat model. *J. Surg. Res.* **103**, 208–214 (2002).
199. Conze, J. *et al.* Polypropylene in the intra-abdominal position: Influence of pore size and surface area. *Hernia* **8**, 365–372 (2004).
200. Galperin, A., Long, T. J. & Ratner, B. D. Degradable, Thermo-Sensitive Poly (N-isopropyl acrylamide)-Based Scaffolds with Controlled Porosity for Tissue Engineering Applications. *Biomacromolecules* **11**, 2583–2592 (2010).
201. Galperin, A., Long, T. J., Garty, S. & Ratner, B. D. Synthesis and fabrication of a degradable poly (N-isopropyl acrylamide) scaffold for tissue engineering applications. *J. Biomed. Mater. Res. A* **101A**, 775–786 (2012).
202. Ratner, B. D. A pore way to heal and regenerate: 21st century thinking on biocompatibility. *Regen. Biomater.* **3**, 107–110 (2016).
203. Brodbeck, W. G. *et al.* Influence of biomaterial surface chemistry on the apoptosis of adherent cells. *J. Biomed. Mater. Res.* **55**, 661–668 (2001).
204. Ghanaati, S. *et al.* Influence of b-tricalcium phosphate granule size and morphology on tissue reaction in vivo. *Acta Biomater.* **6**, 4476–4487 (2010).
205. Barbeck, M. *et al.* Heterogeneity of biomaterial-induced multinucleated giant cells : Possible importance for the regeneration process ? *Biomed Mater Res Part A* **104A**, 413–418 (2015).
206. Reid, B. *et al.* PEG hydrogel degradation and the role of the surrounding tissue envrionment. *J. Tissue Eng. Regen. Med.* **9**, 315–318 (2015).
207. Saleh, L. S. & Bryant, S. J. In vitro and in vivo models for assessing the host response to biomaterials. *Drug Discov. Today Dis. Model.* **24**, 13–21 (2018).
208. Whitaker, R., Hernaez-Estrada, B., Hernandez, R. M., Santos-Vizcaino, E. & Spiller, K. L. Immunomodulatory Biomaterials for Tissue Repair. *Chem. Rev.* **121**, 11305–11335 (2021).

209. Krombach, F. *et al.* Cell size of alveolar macrophages: an interspecies comparison. *Environ. Health Perspect.* **105 Suppl**, 1261–1263 (1997).
210. Invitrogen. *Countess Cell Data Sheet NIH/3T3*.
211. Keller, N. *et al.* Study of Biofilm Growth on Slippery Liquid-Infused Porous Surfaces Made from Fluoropor. *ACS Appl. Mater. Interfaces* **11**, 4480–4487 (2019).
212. Hardy, L., Cerca, N., Jespers, V., Vaneechoutte, M. & Crucitti, T. Bacterial biofilms in the vagina. *Res. Microbiol.* **168**, 865–874 (2017).
213. Donlan, R. M. & Costerton, J. W. Biofilms: Survival Mechanisms of Clinically Relevant Microorganisms. *Clin. Microbiol. Rev.* **15**, 167–193 (2002).
214. Busscher, H. J. *et al.* Biomaterial-associated infection: Locating the finish line in the race for the surface. *Sci. Transl. Med.* **4**, 153rv10 (2012).
215. Wang, X. *et al.* A nanofibrous encapsulation device for safe delivery of insulin-producing cells to treat type 1 diabetes. *Sci. Transl. Med.* **13**, 1–19 (2021).
216. Hernandez, J. L. *et al.* Effect of tissue microenvironment on fibrous capsule formation to biomaterial-coated implants. *Biomaterials* **273**, 120806 (2021).
217. Luttikhuizen, D. T. *et al.* The correlation between difference in foreign body reaction between implant locations and cytokine and MMP expression. *Biomaterials* **27**, 5763–5770 (2006).
218. Sharkawy, A. A., Klitzman, B., Truskey, G. A. & Reichert, W. M. Engineering the tissue which encapsulates subcutaneous implants . I. Diffusion properties. *J. Biomed. Mater. Res.* **37**, 401–412 (1996).
219. Sharkawy, A. A., Klitzman, B., Truskey, G. A. & Reichert, W. M. Engineering the tissue which encapsulates subcutaneous implants. II. Plasma – tissue exchange properties. *J. Biomed. Mater. Res.* **40**, 586–597 (1997).
220. Woodard, L. N. & Grunlan, M. A. Hydrolytic Degradation and Erosion of Polyester Biomaterials. *ACS Macro Lett.* **7**, 976–982 (2018).
221. Ward, W. K. A review of the foreign-body response to subcutaneously-implanted devices: The role of Macrophages and cytokines in biofouling and fibrosis. *J. Diabetes Sci. Technol.* **2**, 768–777 (2008).
222. Chen, W., Yung, B. C., Qian, Z. & Chen, X. Improving long-term subcutaneous drug delivery by regulating material-bioenvironment interaction ☆. *Adv. Drug Deliv. Rev.* **127**, 20–34 (2018).
223. Kleiner, L. W., Wright, J. C. & Wang, Y. Evolution of implantable and insertable drug delivery systems. *J. Control. Release* **181**, 1–10 (2014).
224. Cohen, J. Once-a-year implant shows promise against HIV. *Science* **365**, 309 (2019).
225. Dammerman, R., Kim, S., Adera, M. & Schwarz, A. Pharmacokinetics and Safety of Risperidone Subcutaneous Implants. *Clin. Pharmacol. Drug Dev.* **7**, 298–310 (2018).
226. Barrett, S. E. *et al.* Extended-Duration MK-8591-Eluting Implant as a Candidate for HIV Treatment and Prevention. *Antimicrob. Agents Chemother.* **62**, 1–13 (2018).
227. Siegel, R. A., Kost, J. & Lange, R. Mechanistic studies of macromolecular drug release from macroporous polymers. I. Experiments and preliminary theory concerning completeness of drug release. *J. Control. Release* **8**, 223–236 (1989).
228. Wood, R. C., Lecluyse, E. L. & Fix, J. A. Assessment of a model for measuring drug diffusion through implant generated fibrous capsule membranes. *Biomaterials* **16**, 957–959 (1995).
229. Schneider, C., Langer, R., Loveday, D. & Hair, D. Applications of ethylene vinyl acetate

copolymers (EVA) in drug delivery systems. *J. Control. Release* **262**, 284–295 (2017).
230. Almeida, A. *et al.* Ethylene vinyl acetate as matrix for oral sustained release dosage forms produced via hot-melt extrusion. *Eur. J. Pharm. Biopharm.* **77**, 297–305 (2011).
231. Grandi, G., Timò, A., Sammarini, M., Chiara Del Savio, M. & Facchinetti, F. Surface roughness of different contraceptive vaginal rings: evaluation by scanning electron microscope (SEM). *Eur. J. Contracept. Reprod. Heal. Care* **25**, 60–64 (2020).
232. Miller, L., Macfarlane, S. A. & Materi, H. L. A scanning electron microscopic study of the contraceptive vaginal ring. *Contraception* **71**, 65–67 (2005).
233. Frodel, J. L. & Lee, S. The Use of High-Density Polyethylene Implants in Facial Deformities. *Arch Otolaryngol Head Neck Surg* **124**, 1219–1223 (1998).
234. Alvarez, F., Brache, V., Faundes, A., Jorge, A. & Sousa, M. H. Local side effects observed among long-term users of Norplant contraceptive implants. *Contraception* **68**, 111–115 (2003).
235. López del Cerro, E. *et al.* Influence of age on tolerability, safety and effectiveness of subdermal contraceptive implants. *J. Obstet. Gynaecol. (Lahore).* **38**, 979–984 (2018).
236. Ramdhan, R. C. *et al.* Complications of Subcutaneous Contraception: A Review. *Cureus* **10**, 1–10 (2018).
237. Su, J. T. *et al.* A Subcutaneous Implant of Tenofovir Alafenamide Fumarate Causes Local Inflammation and Tissue Necrosis in Rabbits and Macaques. *Anitmicrobial Agents Chemother.* **64**, 1–17 (2020).
238. Niederkorn, J. Y. See no evil, hear no evil, do no evil: The lessons of immune privilege. *Nat. Immunol.* **7**, 354–359 (2006).
239. Fijak, M. & Meinhardt, A. The testis in immune privilege. *Immunol. Rev.* **213**, 66–81 (2006).
240. Lee, S. K., Kim, C. J., Kim, D. & Kang, J. Immune Cells in the Female Reproductive Tract. *Immune Netw.* **15**, 16–26 (2015).
241. Clark, G. F. & Schust, D. J. Manifestations of immune tolerance in the human female reproductive tract. *Front. Immunol.* **4**, 1–14 (2013).
242. Rose, W. A. *et al.* Commensal Bacteria Modulate Innate Immune Responses of Vaginal Epithelial Cell Multilayer Cultures. *PLoS One* **7**, 1–11 (2012).
243. Nothnick, W. B. Regulation of uterine matric metalloproteinase-9 and the microRNAs. *Semin Reprod Med* **26**, 494–499 (2008).
244. Curry Jr., T. E. & Osteen, K. G. The Matrix Metalloproteinase System: Changes, Regulation, and Impact throughout the Ovarian and Uterine Reproductive Cycle. *Endocr. Rev.* **24**, 428–465 (2003).
245. Gupta, P. K., Malkani, P. K. & Bhasin, K. Cellular response in the uterine cavity after IUD insertion and structural changes of the IUD. *Contraception* **4**, 375–384 (1971).
246. Chou, C. H. *et al.* Divergent endometrial inflammatory cytokine expression at peri-implantation period and after the stimulation by copper intrauterine device. *Sci. Rep.* **5**, 1–9 (2015).
247. Sheppard, B. L. Endometrial morphological changes in IUD users: A review. *Contraception* **36**, 1–10 (1987).
248. Sahwi, S. El & Moyer, D. L. Antifertility effects of the intrauterine foreign body. *Contraception* **2**, 1–28 (1970).
249. Thurmond, A. S. *et al.* Nonsurgical Sterilization Using the ESSURE Device in the Fallopian Tubes: Results in Rabbits. *J. Women's Imaging* **6**, 75–80 (2004).

250. Growe, R. G., Luster, M. I., Fail, P. A. & Lippes, J. Quinacrine-induced occlusive fibrosis in the human fallopian tube is due to a unique inflammatory response and modification of repair mechanisms. *J. Reprod. Immunol.* **97**, 159–166 (2013).
251. Jensen, J. T. *et al.* Characterization of tubal occlusion after transcervical polidocanol foam (PF) infusion in baboons. *Contraception* **92**, 96–102 (2015).
252. Patton, D. L., Cosgrove Sweeney, Y. T. & Kuo, C.-C. Demonstration of Delayed Hypersensitivity in Chlamydia trachomatis Salpingitis in Monkeys : A Pathogenic Mechanism of Tubal Damage. *J. Infect. Dis.* **169**, 680–683 (1994).
253. Leidy, L. E. Possible Role of the Pessary in the Etiology of Toxic Shock Syndrome. *Med. Anthropol. Q.* **8**, 198–208 (1994).
254. Schlievert, P. M. & Davis, C. C. Device-associated menstrual toxic shock syndrome. *Clin. Microbiol. Rev.* **33**, e00032-19 (2020).
255. Hill, D. R. *et al.* In vivo assessment of human vaginal oxygen and carbon dioxide levels during and post menses. *J. Appl. Physiol.* **99**, 1582–1591 (2005).
256. Tatum, H. J., Schmidt, F. H., Mccarty, M. & Leary, W. M. O. The Dalkon Shield Controvery: Structural and Biological Studies of IUD Tails. *JAMA* **231**, 711–717 (1975).
257. Bank, H. L. & Williamson, H. O. Scanning electron microscopy of Dalkon Shield tails. *Fertil. Steril.* **40**, 334–339 (1983).
258. Sivin, I. Another look at the Dalkon Shield: Meta-analysis underscores its problems. *Contraception* **48**, 1–12 (1993).
259. Britton, L. E., Alspaugh, A., Greene, M. Z. & McLemore, M. R. An Evidence-Based Update on Contraception: A Detailed Review of Hormonal and Non Hormonal Methods. *Am J Nurs* **120**, 1–22 (2020).
260. Pabuccu, R. *et al.* Efficiency and pregnancy outcome of serial intrauterine device-guided hysteroscopic adhesiolysis of intrauterine synechiae. *Fertil. Steril.* **90**, 1973–1977 (2008).
261. Cai, Y. *et al.* Porous scaffolds from droplet microfluidics for prevention of intrauterine adhesion. *Acta Biomater.* **84**, 222–230 (2019).
262. Jahanbani, Y., Davaran, S., Ghahremani-Nasab, M., Aghebati-Maleki, L. & Yousefi, M. Scaffold-based tissue engineering approaches in treating infertility. *Life Sci.* **240**, 117066 (2019).
263. MacDonald, S., Terlecki, R., Costantini, E. & Badlani, G. Complications of Transvaginal Mesh for Pelvic Organ Prolapse and Stress Urinary Incontinence: Tips for Prevention, Recognition, and Management. *Eur. Urol. Focus* **2**, 260–267 (2016).
264. Mukherjee, S. *et al.* Electrospun Nanofiber Meshes With Endometrial MSCs Modulate Foreign Body Response by Increased Angiogenesis, Matrix Synthesis, and Anti-Inflammatory Gene Expression in Mice: Implication in Pelvic Floor. *Front. Pharmacol.* **11**, 1–18 (2020).
265. Feng, X. *et al.* Electrospun polymer micro/nanofibers as pharmaceutical repositories for healthcare. *J. Control. Release* **302**, 19–41 (2019).
266. Deitzel, J. M., Kleinmeyer, J., Harris, D. & Tan, N. C. B. The effect of processing variables on the morphology of electrospun nanofibers and textiles. *Polymer (Guildf).* **42**, 261–272 (2001).
267. Wang, K. *et al.* Overcoming foreign-body reaction through nanotopography: Biocompatibility and immunoisolation properties of a nanofibrous membrane. *Biomaterials* **102**, 249–258 (2016).
268. Xue, J., Wu, T., Dai, Y. & Xia, Y. Electrospinning and electrospun nanofibers: Methods,

materials, and applications. *Chem. Rev.* **119**, 5298–5415 (2019).
269. Sill, T. J. & von Recum, H. A. Electrospinning: Applications in drug delivery and tissue engineering. *Biomaterials* **29**, 1989–2006 (2008).
270. Stoddard, R. J., Steger, A. L., Blakney, A. K. & Woodrow, K. A. In pursuit of functional electrospun materials for clinical applications in humans. *Ther. Deliv* **7**, 387–409 (2016).
271. Krogstad, E. A. & Woodrow, K. A. Manufacturing scale-up of electrospun poly(vinyl alcohol) fibers containing tenofovir for vaginal drug delivery. *Int. J. Pharm.* **475**, 282–291 (2014).
272. Krogstad, E. A. *et al.* Nanoparticle-releasing nanofiber composites for enhanced in vivo vaginal retention. *Biomaterials* **144**, 1–16 (2017).
273. Laborde, N. D. *et al.* Perceptions of the 'fabric' - An exploratory study of a novel multi-purpose technology among women in Sub Saharan Africa. *PLoS One* **13**, 1–13 (2018).
274. Lancina, M. G., Singh, S., Kompella, U. B., Husain, S. & Yang, H. Fast Dissolving Dendrimer Nanofiber Mats as Alternative to Eye Drops for More Efficient Antiglaucoma Drug Delivery. *ACS Biomater. Sci. Eng.* **3**, 1861–1868 (2017).
275. Yu, D., Shen, X. & Branford-white, C. Oral fast-dissolving drug delivery membranes prepared from electrospun polyvinylpyrrolidone ultrafine fibers. *Nanotechnology* **20**, 1–9 (2009).
276. Vrbata, P. *et al.* Electrospun drug loaded membranes for sublingual administration of sumatriptan and naproxen. *Int. J. Pharm.* **457**, 168–176 (2013).
277. Nagy, Z. K. *et al.* High speed electrospinning for scaled-up production of amorphous solid dispersion of itraconazole. *Int. J. Pharm.* **480**, 137–142 (2015).
278. Balogh, A. *et al.* Melt-Blown and Electrospun Drug-Loaded Polymer Fiber Mats for Dissolution Enhancement: A Comparative Study. *J. Pharm. Sci.* **104**, 1767–1776 (2015).
279. Frizzell, H., Ohlsen, T. J. & Woodrow, K. A. Protein-loaded emulsion electrospun fibers optimized for bioactivity retention and pH-controlled release for peroral delivery of biologic therapeutics. *Int. J. Pharm.* **533**, 99–110 (2017).
280. Tuin, S. A., Pourdeyhimi, B. & Loboa, E. G. Creating tissues from textiles: scalable nonwoven manufacturing techniques for fabrication of tissue engineering scaffolds Creating tissues from textiles : scalable nonwoven manufacturing techniques for fabrication of tissue engineering scaffolds. *Biomed. Mater.* **11**, 1–14 (2016).
281. LeCorre-Bordes, D. S., Jaksons, P. & Hofman, K. Mind the gap: Ensuring laboratory-scale testing of an electrospinning product meets commercial-scale needs. *J. Appl. Polym. Sci.* **44836**, 1–8 (2017).
282. Huang, Y., Song, J., Yang, C., Long, Y. & Wu, H. Scalable manufacturing and applications of nanofibers. *Mater. Today* **28**, 98–113 (2019).
283. Stoddard, R. & Chen, X. Electrospinning of ultra-thin nanofibers achieved through comprehensive statistical study. *Mater. Res. Express* **3**, 055022 (2016).
284. Zhang, X., Yang, X. & Chase, G. G. Filtration performance of electrospun acrylonitrile-butadiene elastic fiber mats in solid aerosol filtration. *Sep. Purif. Technol.* **186**, 96–105 (2017).
285. Skiena, S. S. *The Algorithm Design Manual*. (Springer, 2008). doi:10.1007/978-1-84800-070-4
286. Collins, G., Federici, J., Imura, Y. & Catalani, L. H. Charge generation, charge transport, and residual charge in the electrospinning of polymers: A review of issues and complications. *J. Appl. Phys.* **111**, 1–18 (2012).

287. National Center for Biotechnology Information. PubChem Compound Summary for CID 54671008, Raltegravir. *PubChem* Available at: https://pubchem.ncbi.nlm.nih.gov/compound/54671008%0A. (Accessed: 12th October 2021)
288. John, J. & Liang, D. Oral liquid formulation of etravirine for enhanced bioavailability. *J. Bioequivalence Bioavailab.* **6**, 46–52 (2014).
289. National Center for Biotechnology Information. PubChem Compound Summary for CID 3002977, Maraviroc. *PubChem* Available at: https://pubchem.ncbi.nlm.nih.gov/compound/Maraviroc#section=UNII%0Ahttp://www.vcclab.org/lab/alogps/%0Ahttps://hmdb.ca/metabolites/HMDB0015584%0A. (Accessed: 12th October 2021)
290. Yu, D. G. *et al.* A modified coaxial electrospinning for preparing fibers from a high concentration polymer solution. *eXPRESS Polym. Lett.* **5**, 732–741 (2011).
291. Forward, K. M. & Rutledge, G. C. Free surface electrospinning from a wire electrode. *Chem. Eng. J.* **183**, 492–503 (2012).
292. Vass, P. *et al.* Scale-up of electrospinning technology: Applications in the pharmaceutical industry. *WIREs Nanomed Nanobiotechnol* **12**, 1–24 (2020).
293. Bhattacharyya, I., Molaro, M. C., Braatz, R. D. & Rutledge, G. C. Free surface electrospinning of aqueous polymer solutions from a wire electrode. *Chem. Eng. J.* **289**, 203–211 (2015).
294. Yu, D.-G., Zhu, L.-M., White, K. & Branford-White, C. Electrospun nanofiber-based drug delivery systems. *Health (Irvine. Calif).* **01**, 67–75 (2009).
295. Kadam, V. *et al.* Electrospun bilayer nanomembrane with hierarchical placement of bead-on-string and fibers for low resistance respiratory air filtration. *Sep. Purif. Technol.* **224**, 247–254 (2019).
296. Matulevicius, J. *et al.* Design and Characterization of Electrospun Polyamide Nanofiber Media for Air Filtration Applications. *J. Nanomater.* 1–14 (2014).
297. Yu, S., Wang, X. & Wu, D. Microencapsulation of n-octadecane phase change material with calcium carbonate shell for enhancement of thermal conductivity and serving durability: Synthesis, microstructure, and performance evaluation. *Appl. Energy* **114**, 632–643 (2014).
298. Wang, Y., Li, W., Xia, Y., Jiao, X. & Chen, D. Electrospun flexible self-standing γ-alumina fibrous membranes and their potential as high- efficiency fine particulate filtration media. *J. Mater. Chem. A.* **2**, 15124–15131 (2014).
299. Matulevicius, J., Kliucininkas, L., Prasauskas, T., Buivydiene, D. & Martuzevicius, D. The comparative study of aerosol filtration by electrospun polyamide, polyvinyl acetate, polyacrylonitrile and cellulose acetate nanofiber media. *J. Aerosol Sci.* **92**, 27–37 (2016).
300. Opálková Šišková, A., Frajová, J. & Nosko, M. Recycling of poly(ethylene terephthalate) by electrospinning to enhanced the filtration efficiency. *Mater. Lett.* **278**, 2–4 (2020).
301. Wu, Y., Carnell, L. A. & Clark, R. L. Control of electrospun mat width through the use of parallel auxiliary electrodes. *Polymer (Guildf).* **48**, 5653–5661 (2007).
302. Feltz, K. P., Growney Kalaf, E. A., Chen, C., Martin, R. S. & Sell, S. A. A review of electrospinning manipulation techniques to direct fiber deposition and maximize pore size. *Electrospinning* **2**, 46–61 (2017).
303. Wang, B., Zhou, W., Chang, M. W., Ahmad, Z. & Li, J. S. Impact of substrate geometry on electrospun fiber deposition and alignment. *J. Appl. Polym. Sci.* **134**, 1–11 (2017).

304. Creighton, R. L., Phan, J. & Woodrow, K. A. In situ 3D-patterning of electrospun fibers using two-layer composite materials. *Sci. Rep.* **10**, 1–14 (2020).
305. Kupiec, T. C., Vu, N. & Branscum, D. Homogeneity of Dosage Forms. *Int. J. Pharm. Compd.* **12**, 340–343 (2008).
306. French, R. S. *et al.* Levonorgestrel-releasing (20 uL/day) intrauterine systems (Mirena) compared with other methods of reversible contraceptives. *Br. J. Obstet. Gynaecol.* **107**, 1218–1225 (2000).
307. Commandeur, S., Beusekom, H. Van & Giessen, W. J. Van Der. Polymers, Drug Release, and Drug-Eluting Stents. *J. Interv. Cardiol.* **19**, 500–506 (2006).
308. Flexner, C. Antiretroviral implants for treatment and prevention of HIV infection. *Curr. Opin. HIV AIDS* **13**, 374–380 (2018).
309. Dybul, M. *et al.* Evaluation of Lymph Node Virus Burden in Human Immunodeficiency Virus – Infected Patients Receiving Efavirenz-Based Protease Inhibitor – Sparing Highly Active Antiretroviral Therapy. *J. Infect. Dis.* **181**, 1273–1279 (2000).
310. Lappe, S., Mulac, D. & Langer, K. Polymeric nanoparticles – Influence of the glass transition temperature on drug release. *Int. J. Pharm.* **517**, 338–347 (2017).
311. Omelczuk, M. O. & McGinity, J. W. The influence of polymer glass transition temperature and molecular weight on drug release from tablets containing poly(DL-lactic acid). *Pharm. Res.* **9**, 26–32 (1992).
312. Kalepu, S. & Nekkanti, V. Insoluble drug delivery strategies: review of recent advances and business prospects. *Acta Pharm. Sin. B* **5**, 442–453 (2015).
313. Catiker, E., Gumusderelioglu, M. & Guner, A. Degradation of PLA , PLGA homo- and copolymers in the presence of serum albumin: a spectroscopic investigation. *Polym. Int.* **734**, 728–734 (2000).
314. Schindelin, J. *et al.* Fiji: an open-source platform for biological-image analysis. *Nat. Methods* **9**, 676–682 (2019).
315. Blakney, A. K., Jiang, Y., Whittington, D. & Woodrow, K. A. Simultaneous measurement of etravirine, maraviroc and raltegravir in pigtail macaque plasma, vaginal secretions and vaginal tissue using a LC–MS/MS assay. *J. Chromatogr. B* **1025**, 110–118 (2016).
316. Malcolm, R. K. *et al.* Pharmacokinetics of a CCR5 inhibitor in rhesus macaques following vaginal, rectal and oral application. *J. Antimicrob. Chemother.* **69**, 1325–1329 (2014).
317. Minuto, J. J. & Haubrich, R. Etravirine: a second-generation NNRTI for treatment-experienced adults with resistant HIV-1 infection. *Futur HIV Ther* **2**, 525–537 (2008).
318. Akil, A. *et al. Development and Characterization of a Vaginal Film Containing Dapivirine, a Non- nucleoside Reverse Transcriptase Inhibitor (NNRTI), for prevention of HIV-1 sexual transmission*. *Drug Deliv Transl Res* **1**, (2011).
319. Antoniou, T. *et al.* Pharmacokinetics of Maraviroc, Raltegravir, Darunavir, and Etravirine in the Semen of HIV-Infected Men. *J Aquir Immune Defic Syndr* **62**, 58–60 (2013).
320. Hirenkumar, M. & Steven, S. Poly Lactic-co-Glycolic Acid (PLGA) as Biodegradable Controlled Drug Delivery Carrier. *Polymers (Basel).* **3**, 1–19 (2012).
321. Dash, T. K. & Konkimalla, V. B. Poly-ε-caprolactone based formulations for drug delivery and tissue engineering: A review. *J. Control. Release* **158**, 15–33 (2012).
322. Shenoy, S. L., Bates, W. D., Frisch, H. L. & Wnek, G. E. Role of chain entanglements on fiber formation during electrospinning of polymer solutions : good solvent , non-specific polymer – polymer interaction limit. *Polymer (Guildf).* **46**, 3372–3384 (2005).
323. Park, P. I. P. & Jonnalagadda, S. Predictors of Glass Transition in the Biodegradable Poly-

lactide and Poly-lactide- co -glycolide Polymers. *J. Appl. Polym. Sci.* **100**, 1983–1987 (2006).
324. Abouelmagd, S. A., Sun, B., Chang, A. C., Ku, Y. J. & Yeo, Y. Release Kinetics Study of Poorly Water-Soluble Drugs from Nanoparticles: Are We Doing It Right? *Mol. Pharm.* **12**, 997–1003 (2015).
325. Peschka, R., Dennehy, C. & Szoka, F. C. A simple in vitro model to study the release kinetics of liposome encapsulated material. *J. Control. Release* **56**, 41–51 (1998).
326. Deb, P. K., Al-attraqchi, O., Prasad, M. R. & Tekade, R. K. *Protein and Tissue Binding : Implication on Pharmacokinetic Parameters*. *Dosage Form Design Considerations* (Elsevier Inc., 2018). doi:10.1016/B978-0-12-814423-7.00011-3
327. Kovarova, M. *et al.* A long-acting formulation of the integrase inhibitor raltegravir protects humanized BLT mice from repeated high-dose vaginal HIV challenges. *J. Antimicrob. Chemother.* **71**, 1586–1596 (2016).
328. Landovitz, R. J., Kofron, R. & McCauley, M. The Promise and Pitfalls of Long Acting Injectable Agents for HIV Prevention. *Curr Opin HIV AIDS* **11**, 122–128 (2016).
329. Woollard, S. M. & Kanmogne, G. D. Maraviroc: A review of its use in HIV infection and beyond. *Drug Des. Devel. Ther.* **9**, 5447–5468 (2015).
330. Guarnieri, M., Tyler, B. M., Detolla, L., Zhao, M. & Kobrin, B. Subcutaneous implants for long-acting drug therapy in laboratory animals may generate unintended drug reservoirs. *J. Pharm. Bioallied Sci.* **6**, 38–42 (2014).
331. Litterst, C. L., Mimnaugh, E. G., Reagan, R. L. & Gram, T. E. Comparison of in vitro drug metabolism by lung, liver, and kidney of several common laboratory species. *Drug Metab. Dispos.* **3**, 259–265 (1975).
332. De Kanter, R. *et al.* Drug-metabolizing activity of human and rat liver, lung, kidney and intestine slices. *Xenobiotica* **32**, 349–362 (2002).
333. Karunakaran, D. *et al.* Design and Testing of a Cabotegravir Implant for HIV Prevention. *J. Control. Release* **330**, 658–668 (2021).
334. Scholler-Gyure, M., Kakuda, T. N., Raoof, A., Smedt, G. De & Hoetelmans, R. M. W. Clinical Pharmacokinetics and Pharmacodynamics of Etravirine. *Clin Pharmacokinet* **48**, 561–574 (2009).
335. McLennan, D. N., Porter, C. J. H. & Charman, S. A. Subcutaneous drug delivery and the role of the lymphatics. *Drug Discov. Today Technol.* **2**, 89–96 (2005).
336. Mariani, E., Lisignoli, G., Borzì, R. M. & Pulsatelli, L. Biomaterials: Foreign bodies or tuners for the immune response? *Int. J. Mol. Sci.* **20**, 1–42 (2019).
337. Monopoli, M. P. *et al.* Physical-Chemical aspects of protein corona: Relevance to in vitro and in vivo biological impacts of nanoparticles. *J. Am. Chem. Soc.* **133**, 2525–2534 (2011).
338. Serpooshan, V. *et al.* Protein Corona Influences Cell-Biomaterial Interactions in Nanostructured Tissue Engineering Scaffolds. *Adv. Funct. Mater.* **25**, 4379–4389 (2015).
339. Fournier, E., Passirani, C., Montero-Menei, C. N. & Benoit, J. P. Biocompatibility of implantable synthetic polymeric drug carriers: Focus on brain biocompatibility. *Biomaterials* **24**, 3311–3331 (2003).
340. Tang, S. W., Tong, W. Y., Pang, S. W., Voelcker, N. H. & Lam, Y. W. Deconstructing, Replicating, and Engineering Tissue Microenvironment for Stem Cell Differentiation. *Tissue Eng. Part B* **00**, 1–15 (2020).
341. Rani, B. *et al.* Role of the tissue microenvironment as a therapeutic target in

hepatocellular carcinoma. *World J Gastroenterol* **20**, 4128–4140 (2014).
342. Seong, S. & Matzinger, P. Hydrophobicity: an ancient damage-associated molecular pattern that initiates innate immune responses. *Nat. Rev. Immunol.* **4**, 469–478 (2004).
343. Arai, T. & Norde, W. The behavior of some model proteins at solid-liquid interfaces 2 . Sequential and competitive adsorption. *Colloids and Surfaces* **51**, 17–28 (1990).
344. Anderson, J. M. Exploiting the inflammatory response on biomaterials research and development. *J Mater Sci Mater Med* **26**, 1–2 (2015).
345. Hakelius, L. & Ohlsen, L. Tendency to Capsular Contracture around Smooth and Textured Gel-Filled Silicone Mammary Implants: A 5-Year Follow-Up. *Plast. Reconstr. Surg.* **100**, 1566–1569 (1997).
346. Chen, R., Canales, A. & Anikeeva, P. Neural recording and modulation technologies. *Nat. Rev. Mater.* **2**, 1–16 (2017).
347. Hilborn, J. & Bjursten, L. M. A new and evolving paradigm for biocompatibility. *J. Tissue Eng. Regen. Med.* **1**, 110–119 (2007).
348. Veiseh, O. *et al.* Size- and shape-dependent foreign body immune response to materials implanted in rodents and non-human primates. *Nat. Mater.* **14**, 643–651 (2015).
349. Aluvihare, V. R., Kallikourdis, M. & Betz, A. G. Tolerance , suppression and the fetal allograft. *J Mol Med* **83**, 88–96 (2005).
350. Wahl, S. M., Wen, J. & Moutsopoulos, N. TGF-b: a mobile purveyor of immune privilege. *Immunol. Rev.* **213**, 213–227 (2006).
351. Avula, M. N., Rao, A. N., McGill, L. D., Grainger, D. W. & Solzbacher, F. Foreign body response to subcutaneous biomaterial implants in a mast cell-deficient Kitw-Sh murine model. *Acta Biomater.* **10**, 1856–1863 (2014).
352. Blakney, A. K., Swartzlander, M. D. & Bryant, S. J. The effects of substrate stiffness on the in vitro activation of macrophages and in vivo host response to poly(ethylene glycol)-based hydrogels. *J. Biomed. Mater. Res. - Part A* **100 A**, 1375–1386 (2012).
353. Voskerician, G. *et al.* Biocompatibility and biofouling of MEMS drug delivery devices. *Biomaterials* **24**, 1959–1967 (2003).
354. Voskerician, G. *et al.* In Vivo Inflammatory and Wound Healing Effects of Gold Electrode Voltammetry for MEMS Micro-Reservoir Drug Delivery Device. *IEEE Trans. Biomed. Eng.* **51**, 627–635 (2004).
355. Lippes, J. Quinacrine sterilization (QS): Time for reconsideration. *Contraception* **92**, 91–95 (2015).
356. Jensen, J. T. *et al.* Blockade of tubal patency following transcervical administration of polidocanol foam: Initial studies in rhesus macaques. *Contraception* **89**, 540–549 (2014).
357. Jensen, J. T. *et al.* Transcervical administration of polidocanol foam prevents pregnancy in female baboons. *Contraception* **94**, 527–533 (2016).
358. Blakney, A. K., Simonovsky, F. I., Suydam, I. T., Ratner, B. D. & Woodrow, K. A. Rapidly Biodegrading PLGA-Polyurethane Fibers for Sustained Release of Physicochemically Diverse Drugs. *ACS Biomater. Sci. Eng.* **2**, 1595–1607 (2016).
359. Kogawa, A. C. & Salgado, N. Quantification of Doxycycline Hyclate in Tablets by HPLC – UV Method. *J. Chromatogr. Sci.* **40**, 919–925 (2013).
360. Hahn-Deinstrop, E. *Applied Thin-Layer Chromatography: Best Practice and Avoidance of Mistakes*. (Wiley, 2007).
361. Greenhalgh, D. G., Sprugel, K. H., Murray, M. J. & Ross, R. PDGF and FGF stimulate wound healing in the genetically diabetic mouse. *Am. J. Pathol.* **136**, 1235–1246 (1990).

362. Jain, R. A. The manufacturing techniques of various drug loaded biodegradable poly(lactide-co-glycolide) (PLGA) devices. *Biomaterials* **21**, 2475–2490 (2000).
363. Xue, J. *et al.* Fabrication and evaluation of electrospun PCL–gelatin micro-/nanofiber membranes for anti-infective GTR implants. *J. Mater. Chem. B* **2**, 6867–6877 (2014).
364. Hurewitz, A. N., Lidonicci, K., Wu, C. L., Reim, D. & Zucker, S. Histologic Changes of Doxycycline Pleurodesis in Rabbits. *Chest* **106**, 1241–1245 (1994).
365. Neuwirth, R. S., Richart, R. M. & Taylor, H. D. Chemical Induction of Tubal Blockade in the Monkey. *Obstet. Gynecol.* **38**, 51–54 (1971).
366. Vargas, F. S. *et al.* Effectiveness of silver nitrate compared to talc slurry as pleural sclerosing agent in rabbits. Influence of concomitant intrapleural lidocaine. *Rev. Hosp. Clin. Fac. Med. Sao. Paulo.* **54**, 199–208 (1999).
367. US National Library of Medicine. Silver Nitrate. *PubChem* Available at: https://pubchem.ncbi.nlm.nih.gov/compound/24470. (Accessed: 18th April 2019)
368. Atiyeh, B. S., Costagliola, M., Hayek, S. N. & Dibo, S. A. Effect of silver on burn wound infection control and healing: Review of the literature. *Burns* **33**, 139–148 (2007).
369. US National Library of Medicine. Heptaethylene glycol monododecyl ether. *PubChem* Available at: https://pubchem.ncbi.nlm.nih.gov/compound/76459. (Accessed: 18th April 2019)
370. Eckmann, D. M. Polidocanol for endovenous microfoam sclerosant therapy. *Expert Opin. Investig. Drugs* **18**, 1919–1927 (2009).
371. US National Library of Medicine. Doxycycline. *PubChem* Available at: https://pubchem.ncbi.nlm.nih.gov/compound/54671203. (Accessed: 18th April 2019)
372. Nostrandt, A. C., Osterberg, R. E., Soreth, J. & Milstein, J. *Pharmacology Review Application Number: 50-795*. (Center for Drug Evaluation and Research, 2004).
373. Nair, A. B. & Jacob, S. A simple practice guide for dose conversion between animals and human. *J. basic Clin. Pharm.* **7**, 27–31 (2016).
374. *The dictionary of substances and their effects (DOSE)*. (The Royal Society of Chemistry, 1999).
375. Brown, P. C. *Pharmacology Review(s) Application Number: 21-201s000*. (2009).
376. Witherel, C. E., Abebayehu, D., Barker, T. H. & Spiller, K. L. Macrophage and Fibroblast Interactions in Biomaterial-Mediated Fibrosis. *Adv Healthc. Mater* **8**, 1–35 (2019).
377. Jones, J. A. *et al.* Proteomic analysis and quantification of cytokines and chemokines from biomaterial surface-adherent macrophages and foreign body giant cells. *J. Biomed. Mater. Res. Part A* **83**, 585–596 (2007).
378. Villa, A., Rizzi, N., Vegeto, E., Ciana, P. & Maggi, A. Estrogen accelerates the resolution of inflammation in macrophagic cells. *Sci. Rep.* **5**, 1–14 (2015).
379. Brundu S, F. A. Polarization and Repolarization of Macrophages. *J. Clin. Cell. Immunol.* **06**, 1–10 (2015).
380. Alvarez, M. M. *et al.* Delivery strategies to control inflammatory response: Modulating M1-M2 polarization in tissue engineering applications. *J Control Release* **240**, 349–363 (2016).
381. Xue, J. *et al.* Drug loaded homogeneous electrospun PCL/gelatin hybrid nanofiber structures for anti-infective tissue regeneration membranes. *Biomaterials* **35**, 9395–9405 (2014).
382. Zhang, Y., Ouyang, H., Chwee, T. L., Ramakrishna, S. & Huang, Z. M. Electrospinning of gelatin fibers and gelatin/PCL composite fibrous scaffolds. *J. Biomed. Mater. Res.* -

Part B Appl. Biomater. **72**, 156–165 (2005).
383. Voskerician, G., Gingras, P. H. & Anderson, J. M. Macroporous condensed poly(tetrafluoroethylene). I. In vivo inflammatory response and healing characteristics. *J. Biomed. Mater. Res. - Part A* **76**, 234–242 (2006).
384. McNally, A. K. & Anderson, J. M. Phenotypic expression in human monocyte-derived interleukin-4 induced foreign body giant cells and macrophages in vitro: Dependence on material surface properties. *J Biomed Mater Res Part A* **103A**, 1380–1390 (2014).
385. Hafez, E. S. E. & Jaszczak, S. Comparative Anatomy and Histology of the Cervix Uteri in Non-Human Primates. *Primates* **13**, 297–298 (1972).
386. Goldsmith, L. T. *et al.* Relaxin regulation of endometrial structure and function in the rhesus monkey. *Proc. Natl. Acad. Sci. U. S. A.* **101**, 4685–4689 (2004).
387. Lee, D. O. *et al.* Polidocanol foam induces collagen deposition. *Fertil. Steril.* **102**, e141 (2014).
388. Ryan, T. P. Historical perspective on procedures to ligate the fallopian tube for sterilization. *Crit. Rev.* **CR75**, (2000).
389. Rezvani, M. & Shaaban, A. M. Fallopian tube disease in the nonpregnant patient. *Radiographics* **31**, 527–548 (2011).
390. Verco, C. J. Mammalian oviduct vasculature and blood flow. **239**, 229–239 (1991).
391. Findlay, M. W. & Gurtner, G. C. Engineering Niches for Skin and Wound Healing. in *Biology and Engineering of Stem Cell Niches* 559–579 (2017).
392. Chambers, M. *et al.* Macrophage Plasticity in Reproduction and Environmental In fl uences on Their Function. *Front. Immunol.* **11**, 1–16 (2021).
393. Osteen, K., Igarashi, T. & Bruner-tran, K. Progesterone action in the human endometrium: Induction of a unique tissue environment which limits matrix metalloproteinase (MMP) expression. *Front. Biosci.* **8**, 78–86 (2003).
394. Salamonsen, L. A., Zhang, J. & Brasted, M. Leukocyte networks and human endometrial remodelling. **57**, 95–108 (2002).
395. Lescure, F., Glu, R., Doelker, E. & Anderson, J. M. Long-term histopathological study of new polypeptidic biomaterials. **13**, 1009–1011 (1992).
396. Salem, M. L., Hossain, M. S. & Nomoto, K. Mediation of the Immunomodulatory Effect of ß-Estradiol on Inflammatory Responses by Inhibition of Recruitment and Activation of Inflammatory Cells and Their Gene Expression of TNF-alpha and IFN-gamma. *Int Arch Allergy Immunol* **82**, 235–245 (2000).
397. Arts, E. J. & Hazuda, D. J. HIV-1 Antiretroviral Drug Therapy. *Cold Spring Harb. Perspect. Med.* **2**, 1–23 (2012).
398. Bettiker, R. L., Koren, D. E. & Jacobson, J. M. Ibalizumab. *Curr. Opin. HIV AIDS* **13**, 354–358 (2018).
399. Bruno, C. J. & Jacobson, J. M. Ibalizumab: an anti-CD4 monoclonal antibody for the treatment of HIV-1 infection. *J. Antimicrob. Chemother.* **65**, 1839–1841 (2010).
400. Delille, C. A. *et al.* Effect of protein binding on unbound atazanavir and darunavir cerebrospinal fluid concentrations. *J. Clin. Pharmacol.* **54**, 1063–1071 (2014).
401. Rowland, M., Benet, L. Z. & Graham, G. G. Clearance Concepts in Pharmacokinetics. *J. Pharmacokinet. Biopharm.* **1**, 123–124 (1973).
402. US Department of Health and Human Services. FDA-Approved HIV Medicines. (2019). Available at: https://aidsinfo.nih.gov/understanding-hiv-aids/fact-sheets/21/58/fda-approved-hiv-medicines. (Accessed: 30th July 2019)

403. Huang, B., Kang, D., Yang, J., Zhan, P. & Liu, X. Expert Opinion on Therapeutic Patents Novel diarylpyrimidines and diaryltriazines as potent HIV-1 NNRTIs with dramatically improved solubility : a patent evaluation of. *Expert Opin. Ther. Pat.* **26**, 281–289 (2016).
404. Hughes, C. A., Robinson, L., Tseng, A. & Macarthur, R. D. New antiretroviral drugs: a review of the efficacy , safety , pharmacokinetics , and resistance profile of tipranavir , darunavir , etravirine , rilpivirine , New antiretroviral drugs : a review of the efficacy , safety. *Expert Opin. Pharmacother.* **10**, 1744–7666 (2009).
405. Rajoli, R. K. R., Back, D. J., Flexner, C., Owen, A. & Siccardi, M. Physiologically Based Pharmacokinetic Modelling to Inform Development of Intramuscular Long-Acting Nanoformulations for HIV. *Clin. Pharmacokinet.* **54**, 639–650 (2015).
406. Ramesh, K., Shekar, B. C. & Khadgapathi, P. Formulation and evaluation of poorly soluble Etravirine by Spray drying method. *Int. J. Pharm. Pharm. Sci.* **7**, 98–103 (2015).
407. Perri, G. Di *et al.* Pharmacokinetics and Pharmacodynamics of Etravirine 400 mg Once Daily in Treatment-Naïve Patients. *HIV Clin. Trials* **14**, 92–98 (2013).
408. Ribaudo, H. J. *et al.* Pharmacogenetics of Plasma Efavirenz Exposure after Treatment Discontinuation: An Adult AIDS Clinical Trials Group Study. *HIV/AIDS* **42**, 401–407 (2006).
409. Donnerer, J., Kronawetter, M., Kapper, A., Haas, I. & Kessler, H. H. Therapeutic Drug Monitoring of the HIV/AIDS Drugs Abacavir , Zidovudine, Efavirenz, Nevirapine, Indinavir, Lopinavir, and Nelfinavir. *Pharmacology* **69**, 197–204 (2003).
410. Wang, Z. *et al.* Design, synthesis and biological evaluation of novel acetamide-substituted doravirine and its prodrugs as potent HIV-1 NNRTIs. *Bioorg. Med. Chem.* **27**, 447–456 (2019).
411. Anderson, M. S. *et al.* Original article Safety , tolerability and pharmacokinetics of doravirine , a novel HIV non-nucleoside reverse transcriptase inhibitor , after single and multiple doses in healthy subjects. **405**, 397–405 (2015).
412. L'homme, R. F. A., Dijkema, T., Ven, A. J. A. M. van der & Burger, D. M. Enzyme Inducers Reduce Elimination Half-Life After a Single Dose of Nevirapine in Healthy Women. *J. Acquir. Immune Defic. Syndr.* **43**, 193–196 (2006).
413. US National Library of Medicine. Tenofovir Disoproxil Fumerate (Compound). *PubChem* Available at: https://pubchem.ncbi.nlm.nih.gov/compound/Tenofovir-Disoproxil-Fumarate#section=Color-Form. (Accessed: 30th July 2019)
414. Fung, H. B., Stone, E. A. & Piacenti, F. J. Tenofovir Disoproxil Fumarate: A Nucleotide Reverse Transcriptase Inhibitor for the Treatment of HIV Infection. *Clin. Ther.* **24**, 1515–1548 (2002).
415. Patterson, K. B. *et al.* Penetration of Tenofovir and Emtricitabine in Mucosal Tissues : Implications for Prevention of HIV-1 Transmission. **3**, (2011).
416. US National Library of Medicine. Emtricitabine (Compound). *PubChem* Available at: https://pubchem.ncbi.nlm.nih.gov/compound/Emtricitabine#section=Melting-Point. (Accessed: 30th July 2019)
417. Richman, D. D. Antiretroviral activity of emtricitabine , a potent nucleoside reverse transcriptase inhibitor P otency of emtricitabine. 83–88
418. US National Library of Medicine. Zidovudine (Compound). *PubChem* Available at: https://pubchem.ncbi.nlm.nih.gov/compound/Zidovudine#section=Solubility. (Accessed: 30th July 2019)
419. Kornhauser, D. M. *et al.* Probenecid and Zidovudine Metabolism. *Lancet* **334**, 473–475

(1989).
420. US National Library of Medicine. Abacavir (Compound). *PubChem* Available at: https://pubchem.ncbi.nlm.nih.gov/compound/Abacavir#section=Melting-Point. (Accessed: 30th July 2019)
421. Balzarini, J., Haller-meier, F., Clercq, E. De & Meier, C. Antiviral activity of cyclosaligenyl prodrugs of acyclovir , carbovir and abacavir. *Antivrial Chem. Chemother.* **12**, 301–306 (2002).
422. US National Library of Medicine. Lamivudine (Compound). *PubChem* Available at: https://pubchem.ncbi.nlm.nih.gov/compound/Lamivudine#section=Solubility. (Accessed: 30th July 2019)
423. Johnson, M. A., Moore, K. H. P., Yuen, G. J., Bye, A. & Pakes, G. E. Clinical Pharmacokinetics of Lamivudine. *Clin. Pharmacokinet.* **36**, 41–66 (1999).
424. US National Library of Medicine. Darunavir (Compound). *PubChem* Available at: https://pubchem.ncbi.nlm.nih.gov/compound/Darunavir#section=Computed-Properties. (Accessed: 30th July 2019)
425. McKeage, K., Perry, C. M. & Keam, S. J. Darunavir A Review of its Use in the Management of HIV Infection in Adults. *Drugs* **69**, 477–503 (2009).
426. US National Library of Medicine. Atazanavir (Compound). *PubChem* Available at: https://pubchem.ncbi.nlm.nih.gov/compound/Atazanavir#section=Physical-Description. (Accessed: 30th July 2019)
427. Goldsmith, D. R. & Perry, C. M. Atazanavir. *Drugs* **63**, 1679–1693 (2003).
428. US National Library of Medicine. Saquinavir. *PubChem* Available at: https://pubchem.ncbi.nlm.nih.gov/compound/Saquinavir. (Accessed: 30th July 2019)
429. Ali, A. *et al.* Molecular Basis for Drug Resistance in HIV-1 Protease. *Viruses* **2**, 2509–2535 (2010).
430. Kupferschmidt, H. H. T., Fattinger, K. E., Ha, H. R., Follath, F. & Krahenbuhl, S. Grapefruit juice enhances the bioavailability of the HIV protease inhibitor saquinavir in man. *Br. J. Clin. Pharmacol.* **45**, 355–359 (1998).
431. US National Library of Medicine. Ritonavir (Compound). *PubChem* Available at: https://pubchem.ncbi.nlm.nih.gov/compound/Ritonavir. (Accessed: 30th July 2019)
432. US National Library of Medicine. Tipranavir. *PubChem* Available at: https://pubchem.ncbi.nlm.nih.gov/compound/Tipranavir. (Accessed: 30th July 2019)
433. Roche Pharmaceuticals. *Fuzeon*. (2003).
434. Greenberg, M., Cammack, N., Salgo, M. & Smiley, L. HIV fusion and its inhibition in antiretroviral therapy. *Rev. Med. Virol.* **14**, 321–337 (2004).
435. Dwyer, J. J. *et al.* Design of helical , oligomeric HIV-1 fusion inhibitor peptides with potent activity against enfuvirtide-resistant virus. **104**, (2007).
436. US National Library of Medicine. Maraviroc. *PubChem* Available at: https://pubchem.ncbi.nlm.nih.gov/compound/Maraviroc#section=Solubility. (Accessed: 30th July 2019)
437. US Department of Health and Human Services. Maraviroc. *Inxight: Drugs* Available at: https://drugs.ncats.io/ginas/app/drug/MD6P741W8A. (Accessed: 30th July 2019)
438. US National Library of Medicine. Dolutegravir. *PubChem* Available at: https://pubchem.ncbi.nlm.nih.gov/compound/Dolutegravir#section=Solubility. (Accessed: 30th July 2019)
439. Heredia, A. *et al.* Monotherapy with either dolutegravir or raltegravir fails to durably

suppress HIV viraemia in humanized mice. *J. Antimicrob. Chemother.* **72**, 2570–2573 (2017).
440. Adams, J. L., Greener, B. N. & Kashuba, A. D. M. Pharmacology of HIV integrase inhibitors. *Curr. Opin. HIV AIDS* **7**, 390–400 (2012).
441. US National Library of Medicine. Raltegravir. *PubChem* Available at: https://pubchem.ncbi.nlm.nih.gov/compound/Raltegravir#section=Computed-Properties. (Accessed: 30th July 2019)
442. Pace, C. S. *et al.* Anti-CD4 Monoclonal Antibody Ibalizumab Exhibits Breadth and Potency Against HIV-1 , With Natural Resistance Mediated by the Loss of a V5 Glycan in Envelope. *J Acquir Immune Defic Syndr* **62**, 1–9 (2013).